Nanoparticle Self-Assembly for the Synthesis and Processing of Ordered Nanocomposite Solids

by
Margaret Sandra Lee

M.S. Chemistry, University of Chicago (2017)
B.S. Chemistry, University of Chicago (2017)

Submitted to the Department of Materials Science and Engineering
and the Program in Polymers and Soft Matter
in Partial Fulfillment of the Requirements for the Degree of

Doctor of Philosophy
at the
MASSACHUSETTS INSTITUTE OF TECHNOLOGY

May 2022

Signature of Author ……...
Department of Materials Science and Engineering
April 19, 2022

Certified by ……...
Robert J. Macfarlane
Associate Professor of Materials Science and Engineering
Thesis Supervisor

Accepted by …….
Frances M. Ross
Professor of Materials Science and Engineering
Chair, Departmental Committee on Graduate Studies

Nanoparticle Self-Assembly for the Synthesis and Processing of Ordered Nanocomposite Solids

by
Margaret Sandra Lee

Submitted to the Department of Materials Science and Engineering
on April 19, 2022 in partial fulfillment of the
requirements for the degree of
Doctor of Philosophy in Materials Science and Engineering
and the Program in Polymers and Soft Matter

Abstract

Nanoparticle self-assembly has emerged in recent years as a promising strategy for generating nanocomposite materials, with a focus on developing methods that are capable of controlling structure and composition at the nanoscale and ideally beyond, as natural nanocomposites have demonstrated how hierarchical ordering of constituent materials leads to enhanced properties in the composite. Nanocomposite tectons (NCTs) are a class of scalable nanoscale building blocks capable of self-assembly into ordered superlattices in solution through the use of dynamic supramolecular binding interactions. However, while dynamic interparticle interactions are key for enabling reversible binding and preventing kinetic traps during the assembly process, they render assembled structures susceptible to dissociation upon changes in the solution environment, limiting their processability outside of these narrow conditions. This work presents various methods for improving NCT superlattice stability and processability into polymer nanocomposites. These methods include the addition of free polymer to the assembly solution as a simple means to controllably increase the stability of nanoparticle superlattices against thermal dissociation in solution, as well as a method for embedding ordered nanoparticle superlattices into a polymer gel matrix, a medium that stabilizes the embedded arrays against disruption while still allowing dynamic lattice manipulation. Further stabilization can be obtained with complete solvent removal to bind nanoparticle arrays within a solid polymer matrix. The NCT design space is expanded by demonstrating a unary NCT-small molecule linker system capable of undergoing a reversible order-to-order phase transition between FCC and BCC, as well as demonstrating how solvent quality can be used to obtain ordered assemblies without the need for thermal annealing.

Thesis Supervisor: Robert J. Macfarlane
Title: Associate Professor of Materials Science and Engineering

Acknowledgements

My thanks go first and foremost to my parents for their unwavering and unconditional support, and for encouraging my interest in science while also making sure that I had fun with it. I would not have made it this far without their support, teaching of basic life skills, and willingness to accept progressively earlier phone calls as I moved progressively further across the country for university and graduate school. I would also like to thank my undergraduate friends, particularly Ellen and Elaine, for the exchange of moral support as we each went through PhD programs in our respective fields. Despite the fact that our fields of research rarely overlapped, we frequently found commonalities in the overall graduate school experience. Thank you to the Boston Bruins for being the first sports team I have been emotionally invested in since the Chargers left my hometown, and to my cactus Strawberry for braving many Boston winters.

I would like to thank numerous people at MIT for making my graduate experience a memorable one, including my classmates, PPSM cohort, lab-mates, and co-workers at the Thirsty Ear and the Language Conversation Exchange – I had not anticipated making this many friends at MIT and I was happy to be proven wrong. I would be amiss if I did not give particular thanks to the members of the Macfarlane Lab, both past and present. Thank you to everyone in the lab for listening me talk about San Diego, but in particular thank you to PJ for excellent mentorship, Paul for inviting us to his chorus performances, Yuping for educating me about Pokémon, Diana for always being right, Marla for being the best post-dogtoral scholar and best dog in general, Josh for shenanigans and introducing me to the existence of "yinz", Leo for being my Duolingo buddy and for even more shenanigans, Daryl for late night commiseration, Matt for letting me drag him to a Bruins game even though he's a Leafs fan, and Joyce for being a fantastic UROP. Thank you to Rob for going beyond his role of providing support as a research advisor by also putting up with our antics, funding deep dish pizza on Argonne trips, allowing us to sneak multiple Christmas trees into his office, and supplying us with baked goods. Thank you to my thesis committee, Alfredo and Jeremiah, for providing advice on my research throughout my years at MIT.

Professional Acknowledgements

I acknowledge support from MIT with the T.S. Lin Fellowship, as well as additional support through research assistant and teaching assistant appointments. This work was supported by an NSF CAREER Grant, award number CHE-1653289 and made use of the MRSEC Shared Experimental Facilities at MIT, supported by NSF Award DMR 14-19807. SAXS experiments at beamline 12-ID-B at the Advanced Photon Source at Argonne National Laboratory were supported by the U.S. Department of Energy, Office of Science, Office of Basic Energy Sciences, under contract DE-AC02-06CH11357. Additional thanks go to Charlie Settens at MIT and Byeongdu Lee, Xiaobing Zuo, and Ivan Kuzmenko at Argonne for their expertise and assistance with SAXS.

Table of Contents

List of Figures

List of Tables

Chapter 1: Nanoparticle Assembly as a Materials Development Tool

Adapted from Lee, M. S., Yee, D. W., Ye, M. & Macfarlane, R. J. Nanoparticle Assembly as a Materials Development Tool. J. Am. Chem. Soc. 144, 3330–3346 (2022).

The concept of nanoparticles (NPs) as "artificial atoms" has been a valuable framework for both interrogating and understanding the unique chemical and physical properties that arise from matter confined to the ~1–100 nm length scale.[1,2] Initial comparisons to atoms were drawn when it was observed that these tiny bits of nanoscale matter exhibited discrete optical and electrical characteristics, and that those characteristics could be easily analogized to the properties of atoms that are governed by the filling of their electron orbitals.[3–5] Thus, well-understood topics from general chemistry provided a useful common language to describe the properties of nanoparticles as chemists, physicists, and materials scientists began to explore this emerging field. As colloidal synthesis methods advanced and nanoparticles of various sizes, shapes, compositions, and ligand coatings propagated through the community, the "NPs as atoms" analogy expanded to

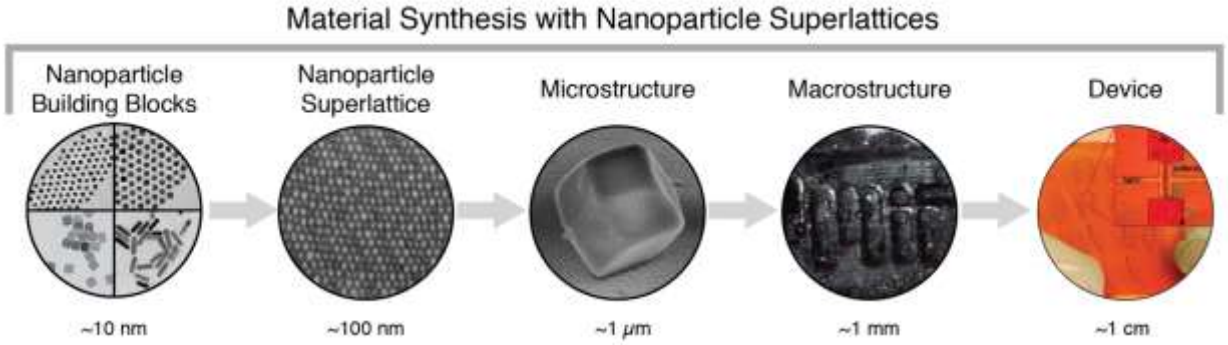

Figure 1.1. Material synthesis with nanoparticle superlattices allows for hierarchical structural control across multiple length scales. Nanoparticle building blocks (~10 nm) can be assembled into microscopic nanoparticle superlattices (~100 nm – 1 μm), which can be processed into macroscopic structures (~1 mm) and ultimately devices (≥1 cm). Adapted from ref. 80, 160.

encompass materials synthesis as well (Figure 1.1).[6–13] Ligand interactions between NPs became "bonds", and both discrete clusters (i.e., "molecules") and extended superlattices ("crystals") could be generated by controlling nanoscale bonding. This analogy allows decades of chemical research to inform our intuition on how NPs might assemble, and also permits the nomenclature and terms used in conventional chemistry to facilitate our description of NP-based materials. In many ways, however, using NPs as fundamental units of materials synthesis provides several advantages not found when starting with individual atomic species, the most obvious of which lie in their compositional variation. At the time of writing, there are only 118 named elements that can be selected as building blocks for materials synthesis; practically, this number is even smaller, as many elements are either too rare or too unstable to be commonly used. Conversely, NPs have significantly greater variety in terms of their elemental makeup, size, shape, and surface coatings, leading to potentially thousands of unique material synthons. Nevertheless, our understanding of the use of NP "artificial atoms" to build materials is still in its infancy compared with conventional chemical synthesis, and it remains a daunting challenge to establish basic scientific principles in NP assembly that are as well-understood as chemical bond formation. The previous decades have built up an impressive (and still expanding) library of NP tools and assembly methods for materials synthesis that has benefitted from analogizing their behavior to textbook-level chemical knowledge – the next challenges for this field lie in writing our own textbooks and design rules.

In this introduction, we will highlight key advancements in NP materials synthesis of the past decades, noting specific milestones in their development and the new functionality or structures they have enabled. We will also describe the properties that have been induced in these NP assemblies, and note current or potential applications that enable novel functionality not achievable in traditional bulk materials. These advancements will allow us to draw a roadmap of

future work for NP assembly, and highlight challenges and limitations that must be addressed to both increase our scientific understanding of the assembly process and provide utility for NP materials in functional devices.

History and Current Methods of Nanoparticle Assembly

Multiple strategies have been established for building structures out of NPs. Here we highlight the history of materials containing NPs, ranging from the formation of random aggregates to advances in directly controlling NP organization within an extended structure.

Aggregation and Uncontrolled Precipitation

The use of nanoparticles as additives to improve the mechanical performance of polymer composites has been an industrially relevant strategy since the twentieth century. For example, modern transportation as we know it would not exist without durable tire rubbers, which were achieved by combining rubbers with carbon black reinforcing fillers to improve tensile strength and resistance to abrasion.[14,15] Since the performance of nanomaterials and nanocomposites is determined not only by particle composition, but also by how individual particles are distributed and arranged, in order to obtain functional nanomaterials it is essential to develop methods of controlling nanoparticle assembly and arrangement.[16]

The most basic category of nanoparticle assembly is uncontrolled aggregation, which occurs when dispersed particles in solution assemble into disordered clusters or films. For example, the aggregation of noble metal nanoparticles, particularly gold, is of interest both as a model system for understanding nanoparticle aggregation, more broadly, and as a practical system with applications in optical sensing.[17] These nanoparticles are typically synthesized with a capping

ligand such as citrate or cetyl trimethylammonium bromide (CTAB) to achieve stable colloidal dispersions via classic Derjaguin-Landau-Verwey-Overbeek theory, which explains colloidal aggregation in aqueous solutions as the result of van der Waals attraction and electrostatic repulsion.[18–20] The stabilizing effect of the charged capping ligand can be disrupted either by replacing the surface ligand to lower the surface potential or by screening or neutralizing the surface charge,[21,22] allowing surface ligands to induce assembly upon introduction of a specific external stimulus like light, heat, solution ionic strength, or solution pH. This aggregation can be irreversible or reversible, depending on if permanent bonds are formed between neighboring particles. An example of the former is the chemical cross-linking of thymine-functionalized gold nanoparticles using UV light irradiation, while an example of the latter is the use of bridging cations to induce aggregation of carboxylate-functionalized gold nanoparticles.[23,24] Since the color and localized surface plasmon resonance of gold nanoparticles in solution changes in response to the aggregation state, this aggregation can be monitored using UV-visible absorption spectroscopy, allowing both the aggregation state and the kinetics of aggregation to be tracked.[25]

Nanoparticles can also be deposited on surfaces to form films, which are useful in situations where functional surfaces with a high surface-area-to-volume ratio are desired, such as solar cells and hydrophobic coatings.[26,27] Common wet deposition methods for generating nanoparticle films include Langmuir-Blodgett (LB) technique, dip coating, spin coating, and layer-by-layer (LbL) deposition. With the LB technique, nanoparticles are first assembled at an air-water interface, compressed to the desired packing density, and then transferred to a solid substrate using vertical dipping to deposit a monolayer, with subsequent layers formed by additional dipping rounds.[28] Dip coating is performed by immersing a substrate in a nanoparticle solution, followed by steady withdrawal of the substrate and removal of excess liquid via drainage or washing.[29] Spin coating

is done by applying the nanoparticle solution to the center of a substrate, followed by spinning at high speeds until a film of the desired thickness is obtained.[30] The latter two methods can also be used in conjunction with LbL deposition, where multilayer films are made by depositing alternating layers of oppositely charged nanoparticles, interspersed with wash steps to remove excess particles and ensure layers of uniform thickness.[31] Each of these techniques offers some degree of control over the quality of the deposited film (e.g., particle density, particle distribution, particle coverage, film thickness, etc.) using assembly handles such as solution viscosity, nanoparticle concentration, substrate withdrawal rate, or substrate pretreatment.

The main advantage of uncontrolled nanoparticle aggregation and deposition techniques lies in their simplicity. Since long-range order is often not a goal for these rapid material syntheses, uncontrolled aggregation and deposition methods are tolerant of high nanoparticle size and shape dispersity, allowing for almost any kind of nanoparticle to be used. These aggregation and deposition methods are also amenable to large-scale production, making them attractive for industrially relevant coatings. However, the inability to manipulate NP ordering means that the emergent properties that often arise from precisely dictated interparticle distances and coordination environments either are not seen in these simple materials or exhibit limited ability to be controlled.

Drop Casting and Evaporation-Driven Assembly

Evaporation-based self-assembly relies on solvent evaporation to drive the assembly of nanoparticles into two-dimensional (2-D) arrays ranging in complexity from “coffee-rings” to highly ordered binary nanoparticle thin films. The “coffee-ring effect,” so named for the characteristic thin brown rings that form upon the evaporation of coffee droplets, is one of the most well-known and ubiquitous examples of evaporation-based self-assembly. This phenomenon

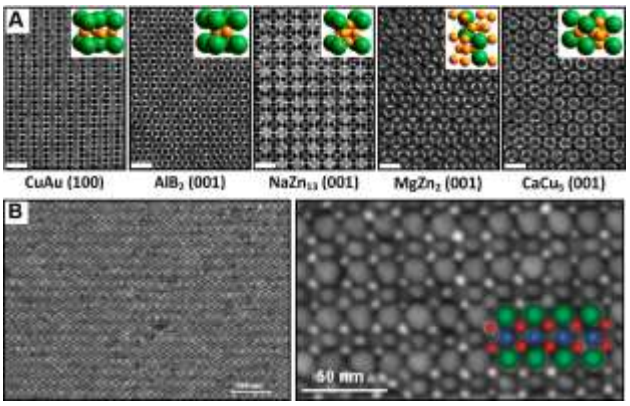

Figure 1.2. Evaporation-driven assembly of ordered nanoparticle arrays presents a simple means of generating complex nanoscale architectures. A) Binary nanoparticle superlattices assembled with different crystal symmetries based on variations in particle sizes and ligand chemistries. Scale bars are 20 nm. B) Ternary nanoparticle superlattices assembled using co-crystallization of 3 particle types. Adapted from ref. 41, 44.

occurs due to capillary flow – as a droplet dries, liquid carrying coffee particles from the droplet interior flows outward to replace liquid evaporating at the edge, concentrating the particles into a dense ring.[32] While the "coffee-ring effect" does not always result in ordered structures, it provides an easy method for creating arrays of thin, uniformly sized rings of nanoparticles, which can be utilized in applications such as printing transparent conductive arrays with silver nanoparticles.[33]

Solvent evaporation can be used on its own or in conjunction with a variety of other directing factors to generate ordered 2-D nanoparticle superlattices. The most basic of these superlattices, ordered hexagonal arrays of close-packed spheres, can be simply made by drop casting a small volume of hydrocarbon-capped nanoparticles in a solvent onto a substrate and letting the solvent gradually evaporate.[34] More complex unary particle close-packed patterns can be obtained by using anisotropic particles such as rods, rectangles, and cubes, which introduce a shape-direction element into the evaporation-driven assembly process[35]. In addition to capillary forces from solvent evaporation, attractive van der Waals forces between particles, and shape-mediated packing geometries, ligand interactions also play a role in determining how anisotropic

particles align. For example, while CTAB prevents particle aggregation in solution via electrostatic repulsion, upon drying, CTAB ligands assist close-packing by pulling particles closer together to facilitate counterion sharing or alkyl tail interdigitation between adjacent particles.[35,36] Further control over particle alignment can be achieved by combining the application of an external electric field with solvent evaporation, such as in the assembly of perpendicularly oriented nanorod superlattices.[37] Nanorods in solution are aligned in the direction of the applied electric field and then confined into hexagonally close-packed arrays during solvent evaporation. Since nanorod orientation is controlled by the direction of the electric field, this method makes it possible to obtain nanorod arrays oriented perpendicular to the substrate, in contrast to nanorod arrays oriented parallel to the substrate that typically result from solvent evaporation.

Some of the most impressive advances in the development of evaporation-based assembly relate to the synthesis of binary nanocrystal superlattices (BNSLs), complex ordered arrays composed of two types of nanoparticles. A large library of BNSLs have been demonstrated using various small-molecule-capped inorganic nanoparticles evaporated onto either a canted surface or a liquid interface (Figure 1.2A).[38–40] Upon gradual solvent evaporation under reduced pressure, ordered BNSL films are formed at the receding solvent–substrate interface. Assembly of BNSLs is governed by a combination of competing short-range Coulombic, dipolar, and van der Waals interactions dictated by the various ligands on the particles' surfaces; this competition allows for a broad range of crystal symmetries. These ligand interactions have been studied extensively, and the enthalpic and entropic contributions arising from both ligand packing and ligand–ligand binding are now well-understood enough to enable highly reproducible and large-area crystalline features, and to explain the fundamental nature of the interparticle bonding interactions driving assembly (Figure 1.2A).[41,42] Recently, this BNSL approach has been expanded to the use of

polymer ligands, which provides a much broader design space to explore, at the cost of typically more complicated and technically demanding assembly protocols.[43] Ternary NPSLs have also been made, but the number of examples remains limited due to the technical challenge of forming a ternary NPSL in a reproducible manner; such syntheses are often prone to forming different BNSLs containing only two of the three nanoparticle components on different regions of the substrate (Figure 1.2B).[44,45]

Close-packed nanoparticle arrays can also be assembled from nanoparticle solutions via sedimentation. Gravitational sedimentation is generally not of practical use in the context of nanoparticle assembly since the assembly behavior of particles less than 100 nm in size is not significantly influenced by gravity.[9] However, the gravitational sedimentation of colloidal particles in the 100-1000 nm size range to form close-packed arrays is one of the simplest methods for fabricating artificial opals and inverse opals, which are of interest as photonic crystals.[46,47] Centrifugation can be used to speed up the assembly process and exert greater control over the rate of sedimentation during colloidal crystallization.[48] Sedimentation can also be induced in nanoparticle systems by introducing a nonsolvent or depletant. The gradual diffusion of miscible nonsolvent into a nanoparticle solution slowly decreases the solvent quality, causing nucleation, growth and sedimentation with enough time for particles to assemble into ordered superlattices.[49] Depletants can be used to overcome the electrostatic repulsion between neighboring particles and drive assembly via depletion attraction.[50,51]

The main advantages of evaporation-based techniques lie in their low cost and ability to generate highly ordered 2-D films of varying composition with different kinds of nanoparticles. These films are potentially of interest for applications like optical coatings or devices (see section on emergent properties below). Drawbacks to these techniques include a limited ability to

accommodate particle dispersity and the difficulty of achieving nonclose-packed structures. Specifically, BNSLs require nanoparticles with very low dispersity in shape and size to achieve good long-range ordering, which restricts their composition to nanomaterials that can be synthesized with typically <5% size dispersity.[52] Lastly, while evaporation-based assembly is an excellent method for generating ordered 2-D superlattices, it is not as robust in generating materials with NPSLs of arbitrary 3-D geometries.

Biomolecule Assembly

Biomolecules represent a complex ligand for nanoparticle assembly, as their macromolecular structures enable sophisticated interactions that can be significantly more complicated than those of a small molecule ligand, or even a synthetic polymer. DNA is arguably the most versatile biomolecule for particle assembly, capable of producing structures ranging from simple aggregates to intricate 3-D origami complexes with an unprecedented degree of control over particle arrangement and spacing. Since initial work in the late 1990s that showed the potential of DNA as a ligand for reversible, programable nanoscale self-assembly, hundreds of thousands of papers have been published exploring the vast design space available to DNA-grafted nanoparticle (DNA-NP) self-assembly.[7,10,53,54] (Figure 1.3A). Watson–Crick base-pairing interactions between complementary DNA strands are capable of producing a virtually infinite number of pairwise DNA interactions, making it possible to utilize both strand length and nucleobase sequence to program the formation of different crystallographic symmetries and lattice parameters using a wide range of NP compositions. Importantly, in all of these syntheses, the NP assembly process shows remarkable similarity to atomic crystallization, leading to the description of these DNA-grafted NPs as "Programmable Atom Equivalents" (PAEs).[7] A series of design rules

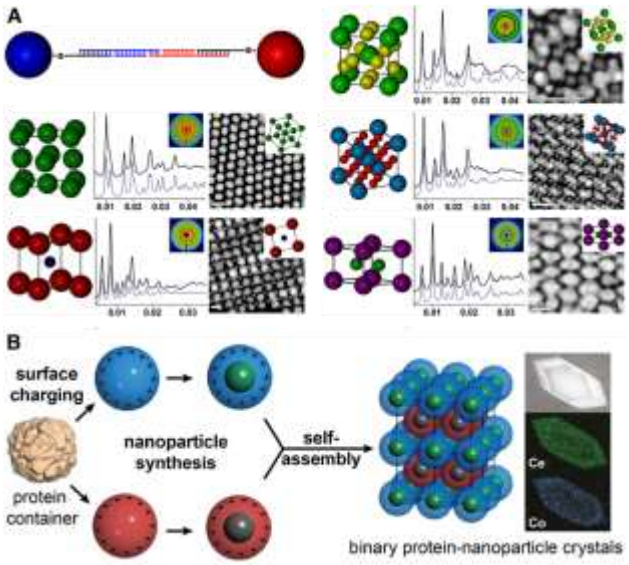

Figure 1.3. Biomolecule complexity can be used to precisely tune the organization of nanoparticles in 3-D arrays. A) DNA-mediated self-assembly provides a means to both predict and program superlattice crystal structure as a function of nucleobase sequence. X-ray scattering plots show the superlattice structure factor (y axis, arbitrary units) versus scattering vector q (x axis, $Å^{-1}$) for each crystal structure. B) Protein cages with encapsulated nanoparticles can assemble into BNSLs via electrostatic attraction. Adapted from ref. 54, 72.

(analogized to Pauling's design rules for ionic lattices) has even been established for these PAEs, using the overarching hypothesis that the most stable particle lattice is the organization that maximizes the number of DNA duplexes formed.[54] Moreover, assembling PAEs at equilibrium enables the synthesis of faceted single crystals with the same well-defined microscale shapes predicted for atomic crystals of the same symmetry.[55,56]

In addition to generating single crystal nanoparticle superlattices in solution, by tailoring the balance between particle-particle and particle-surface interactions DNA-NPs can be used to form single crystal substrate-bound nanoparticle superlattices.[56] DNA-NP thin films can be fabricated using a variety of methods, such as confined microdroplet evaporation to form free-standing nanoparticle superlattice sheets or layer-by-layer epitaxial growth on a template to form ordered multilayer films of arbitrary shape and size.[57,58] Anisotropic nanoparticles can be used to introduce a shape-directing element to the self-assembly process, expanding the library of

available structures beyond what can be achieved with spherical DNA-NPs.[59] Anisotropy can also be added to spherical DNA-NPs by heterogeneously functionalizing the particle surface, resulting in patchy particles capable of site-selective binding.[60] The incorporation of DNA origami (nanostructures made by utilizing complementary binding to fold DNA into a desired shape) enables further control over nanoparticle positioning beyond what can be dictated with the DNA-NP itself, such as in the use of tetrahedral DNA origami cages to assemble DNA-NPs into low packing fraction diamond lattices.[61] For additional information on DNA-mediated self-assembly, we refer the reader to other sources dedicated to the topic.[10,62]

Proteins can also drive NP assembly, though their more complex structures mean that they form a distinct set of lattice or cluster types compared to DNA-driven assembly. These biopolymers are composed of polypeptides composed of amino acids that spontaneously fold into four levels of structure via non-covalent interactions to generate the protein's overall 3-D structure.[63] Both natural and recombinant proteins can be used to guide nanoparticle self-assembly. For example, patchy protein cages formed from native cowpea chlorotic mottle virus and recombinant ferritin can be used to encapsulate RNA or iron oxide nanoparticles respectively. These protein cages with negatively charged directional patches can then be assembled into binary superlattices with positively charged gold nanoparticles by tuning the electrostatic interactions between them to obtain ordered structures.[64] Biotemplating with protein templates provides another method of utilizing the structural organization present in biological materials to direct nanoparticle assembly. Natural proteins can be extracted from bacteria to be used as templates for the adsorption and assembly of gold nanoparticles and CdSe/ZnS core/shell quantum dots into 2-D arrays.[65] Protein templates can also be engineered to covalently bind to nanoparticles, such as

by modifying chaperonins (double-ring structures) with cysteine to create binding sites for metal nanoparticles during assembly.[66]

The main advantage of biomolecule assembly is the ability to exploit the natural structural organization of these molecules, which is typically far more complex than simple small molecules. DNA-mediated programmable nanoscale self-assembly can achieve a level of structural control that is essentially unmatched by any other assembly method, particularly in the fabrication of nonclose-packed ordered arrays. In addition, biomolecular coatings on the NPs could make these assemblies more suited to use in applications that require biocompatibility. However, a significant drawback to biomolecule assembly is its high cost compared to nonbiological molecules or macromolecules, making such assemblies difficult to scale-up or produce in macroscopic quantities.

Supramolecular Assembly

Reversible noncovalent interactions (e.g., hydrogen bonding, pi–pi stacking, hydrophobic interactions, host–guest binding) are ideal means to drive the assembly of ordered NP materials.[67] Although weaker than permanent covalent bonds, the transient nature of noncovalent intermolecular forces allows particles to rearrange their organization during the assembly process and avoid kinetic traps.

While electrostatic interactions can be used to maintain colloidal stability when all particles are functionalized with like charges, ordered patterns can be generated from sets of NPs grafted with oppositely charged ligands.[68,69] BNSLs can use NP size, surface ligand length, and solution salt concentration to modulate the screening length, surface charge, and degree of electrostatic attraction between particles in solution, thereby regulating the formation of different NPSL

structures.[69–71] Electrostatic interactions can also be engineered on particle surfaces using protein shells (Figure 1.3B).[72]

Hydrogen bonding is a common means of supramolecular-driven NP assembly, as these bonds are typically thermally addressable, and are easily incorporated into ligands with polar functional groups.[73] Polymer-grafted nanoparticles with hydrogen-bonding groups can be assembled into robust nanocomposites with high filler content, and both crystallization and self-healing in these materials can be triggered simply by heating up the material to allow hydrogen bonds to dynamically exchange with one another.[74] For example, nanocomposite tectons (NCTs), a nanocomposite building block composed of an inorganic core functionalized with a dense brush of polymers terminated with supramolecular binding groups (Figure 1.4A), use hydrogen bonding between complementary particles to form body-centered cubic (BCC) NPSLs, where crystal lattice parameters are dictated by both the NP diameter and the polymer length (Figure 1.4B).[75,76] By using polymers rather than short alkyl chains, a much higher dispersity in polymer length and core size can be accommodated without negatively affecting lattice ordering, unlike assembly systems that require highly monodisperse particles to achieve ordered structures.[77] By using different nanoparticle core materials or introducing additional binding chemistries with coloading, it is possible to combine hydrogen bonding with other assembly stimuli to further direct the organization and stability of the final structure.[78–81]

Host-guest chemistry is another branch of supramolecular chemistry that can be used to drive nanoparticle self-assembly via interactions between a host molecule and a guest molecule. Host-guest chemistry can be used in conjunction with LbL to fabricate multilayer films with alternating monolayers of host-functionalized and guest-functionalized particles on a substrate.[82] The reversible nature of host-guest interactions can also be leveraged to make nanostructures

capable of dynamic attachment. For example, β-cyclodextrin-functionalized particles (host) and ferrocenyl-functionalized particles (guest) can be reversibly adsorbed and desorbed from a surface by using electrochemical oxidation to control the oxidation state (and complexation ability) of the redox-active ferrocenyl groups.[83] Guest molecules can also be introduced as small molecules in solution rather than functionalized to a particle or substrate surface to facilitate the 3-D self-assembly of non-close-packed NPSLs.[84]

The main advantage of supramolecular assembly methods lies in their customizability. Since supramolecular interactions can be incorporated into materials ranging from proteins to short alkyl chains, there exists a large design space to tailor both the composition and binding chemistry of the final nanoparticle assembly for the desired application. Multiple stimuli can be used to trigger assembly in supramolecular assembly systems, while the reversible nature of noncovalent interactions makes it possible to synthesize materials with self-healing and dynamic responses. Although supramolecular assembly techniques cannot match the level of structural control exhibited by biomolecule assembly methods or some evaporation-driven BNSLs, they are typically more amenable to both large-scale and 3-D material fabrication. While future advances in supramolecular chemistry may enable the same level of sophistication in intermolecular interactions that is currently found in complex biomacromolecules, research in this area requires additional effort (see "future challenges" section below).

Additional Assembly Methods

The diversity of available NP and ligand chemistries also enables opportunities for assembly methods that do not easily fit into the categories above. The ever-expanding range of nanoparticle materials, surface chemistries, and assembly stimuli available for creating

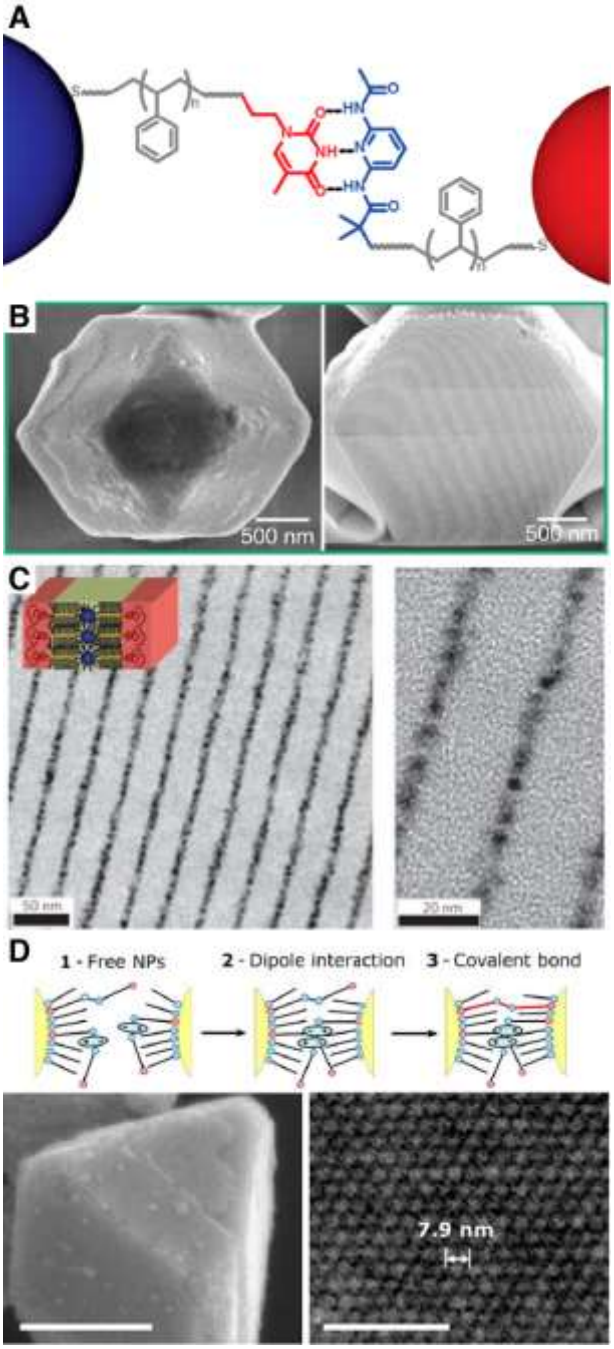

Figure 1.4. Reversible supramolecular interactions via nanoparticle surface ligands provide multiple means of tuning particle assembly as a function of different stimuli. A) Hydrogen bonding interactions between polymer-grafted nanoparticles (so-called Nanocomposite Tectons) rapidly assemble nanoparticles into both polycrystalline and B) single crystal superlattices with well-defined, faceted microscale shapes. C) BCPs form lamellar domain structures in which nanoparticles can organize using reversible supramolecular bonding. D) Light irradiation modulates both covalent and non-covalent interactions between photoresponsive ligands. Scale bars are 200 nm (left) and 50 nm (right). Adapted from ref. 77, 80, 88, 97.

nanoparticle self-assembly systems has allowed for the creation of a diverse library of self-assembly methods to achieve the desired structure or composition.

Block copolymers (BCPs) are a versatile class of polymers that can be used either as a polymer matrix or as a nanoparticle ligand to drive nanoparticle self-assembly. These linear polymers, which are composed of two or more blocks of distinct monomer compositions, phase separate into domains whose size and morphology can be controlled by varying the molecular weight of each block and the size ratio between adjacent blocks.[85] Nanoparticles can be incorporated into the polymer matrix and their location within the ordered domains controlled enthalpically by modifying their surface functionalization. For example, in a symmetric diblock copolymer such as poly(styrene-b-2 vinyl pyridine) (PS-PVP) that forms a lamellar structure, functionalizing nanoparticles with either PS or PVP localizes them within PS or PVP domains respectively, while functionalizing nanoparticles with a blend of PS and PVP localizes them at the interface between domains.[86] Along with surface functionalization, nanoparticle size can also be used to control whether nanoparticles preferentially organize in the center of a domain or at the interface between domains.[87] The addition of small molecules capable of favorably interacting non-covalently with both BCPs and nanoparticles is another strategy for making ordered BCP nanocomposites, and can also be used to introduce stimuli-responsiveness to the nanocomposite(Figure 1.4C).[88] Nanoparticles functionalized with block copolymers are typically used for the self-assembly of vesicles, micelles, and other discrete structures rather than ordered arrays, but can be dried to produce nanoparticle thin films with interparticle spacing determined by the molecular weight of the BCP ligand.[89–91]

Templated self-assembly methods are particularly well-suited for generating ordered 2-D nanoparticle arrays and in recent decades have garnered interest for their potential for largescale

nanoscale device fabrication. These techniques vary widely in cost and precision, depending on the template material or patterning process used, and templates can be used to direct both nanoparticle synthesis and nanoparticle self-assembly. Nanosphere lithography is a low-cost technique that uses colloidal nanosphere masks to generate ordered 2-D metal nanoarrays.[92] Nanospheres are first deposited in a hexagonally close-packed array on a substrate, followed by metal deposition and then mask removal, leaving behind a pattern formed by the metal deposited through the mask. The pattern design can be modified by changing the mask thickness and metal deposition angle but is generally limited to periodic arrays. To achieve more complex nanoscale patterning on a substrate, chemical e-beam lithography is a powerful method combining top-down lithography and bottom-up nanoparticle self-assembly. For example, gold nanoparticles can be deposited in an arbitrary pattern on a silicon substrate by using e-beam irradiation to selectively reduce functional groups on the substrate surface, creating regions for nanoparticles to bind to during the assembly process.[93] Biological materials can also be used for templated nanoparticle self-assembly. DNA-templated nanoparticle self-assembly utilizes the programmability of DNA to create DNA scaffolds with nanoscale precision over individual nanoparticle placement by placing single-stranded DNA at each desired nanoparticle site to bind to a complementary DNA-functionalized nanoparticle.[94,95] Protein lattices, in addition to providing a pattern for nanoparticles to bind to (see Section 1.3), can also be used as templates for generating nanoparticle arrays by directly synthesizing nanoparticles from a precursor added to protein cavities arrayed in an ordered 2-D pattern.[96]

External stimuli such as light and magnetic fields can be used either on their own to drive nanoparticle self-assembly, or in conjunction with another self-assembly technique to add additional structural complexity or responsiveness to the resulting ordered nanostructure. In an

example of the former, nanoparticles functionalized with light-responsive ligands and covalent cross-linkers can be either reversibly or irreversibly self-assembled into nanoparticle superlattices via light-induced dipole-dipole interactions followed by covalent cross-linking, with the degree of reversibility determined by the surface density of light-responsive ligands (Figure 1.4D).[97] In an example of the latter, DNA-nanoparticle superlattices can be stabilized against denaturation by modifying DNA strands with a photosensitive compound that, upon UV irradiation, forms interstrand chemical bonds.[98] Evaporation-driven assembly of maghemite nanocubes in the absence of a magnetic field generates monolayers with no long-range order, but applying a field perpendicular to the surface results in highly ordered, defect-free superlattices.[99] It has also been shown that an applied magnetic field can affect both the crystal symmetry and micro- to macroscopic shape of the assembled lattice, generating complex superlattice crystal habits like elongated rods or twisted ribbons.[100,101]

Emergent Properties of Nanoparticle Assemblies

Materials development is often driven by the desire to generate and understand new emergent properties, as well as applications that benefit from these new characteristics. In NPSLs, such properties can include those that stem from the inherent large surface-area-to-volume ratios possessed by nanoscale objects, such as a larger number of catalytic active sites, or specific surface facets that expose low-coordination number atomic species. NP properties also inherently include emergent phenomena that arise when matter is confined to the nanometer length scale, such as the size- and shape-dependent plasmonic absorption of noble metal NPs or quantum confinement effects in luminescent semiconductor particles. Self-assembly of ordered arrays offers the possibility to control the coupling of particles' individual properties to generate exotic

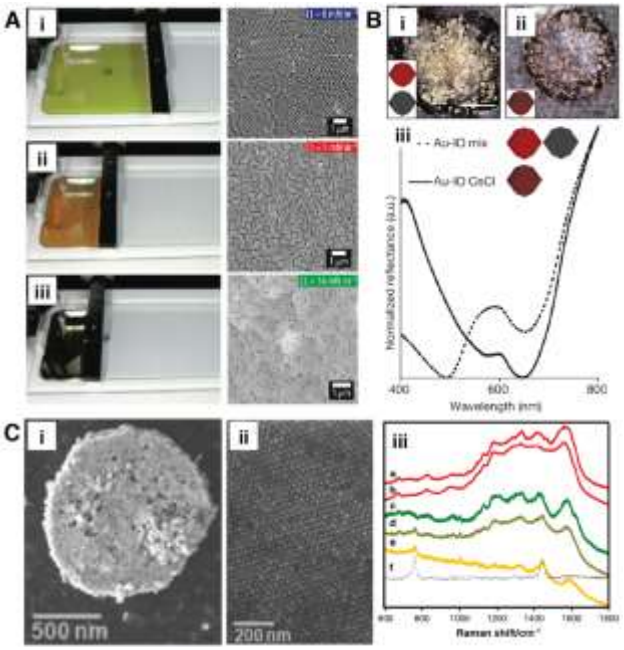

Figure 1.5. Emergent plasmonic properties in NPSLs. A) Changes to surface pressure (increasing from images i to iii) in Langmuir-Blodgett assembly of NPs changes the plasmon response via reduction of interparticle spacing. B) Macroscopic solids made from i) a blend of gold NPSLs and iron oxide NPSLs and ii) BNSLs of gold and iron oxide nanoparticles exhibit significantly different optical responses (iii). C) i,ii) Gold nanorod superlattices as SERS substrates for the detection of prions in blood. iii) SERS spectra of a) blood, b) prion spiked blood, c) plasma, d) prion spiked plasma, e) prion spiked plasma with plasma background subtracted, and f) the scrambled prion. Adapted from ref. 80, 107, 113.

metamaterial behaviors based on the hierarchical organization of the NPs. Here we will note multiple different properties and potential applications enabled by recent advances in controlling the organization of NPs in multiple dimensions.

Plasmonic Properties of NPSLs

A quintessential example of how nanostructure can generate or tune an emergent physical property is localized surface plasmon resonance (LSPR), in which an incident photon is in resonance with coherently oscillating surface electrons of metallic NPs, leading to strong absorption and scattering of the incident light.[102] As the LSPR spectrum is sensitive to multiple

factors including the composition of the surrounding environment, plasmonic nanoparticles have found significant application as ultrasensitive sensors.[103] One well-known application of this is in surface-enhanced Raman scattering (SERS), where the enhanced electromagnetic field around plasmonic particles amplifies the Raman scattering signal of adsorbed molecules.[104]

The organization of plasmonic nanoparticles into clusters or arrays can also be used to further control their optical responses, as bringing plasmonic particles in close proximity to each other allows their surface plasmons to couple, generating hybridized plasmon modes that change their extinction spectra. For example, when spherical nanoparticles are coupled into 1-D chains, their LSPR frequency splits into a transverse and a longitudinal plasmon mode; such splitting can even be used to further the "artificial atoms" analogy, as this splitting can be described in a manner similar to the splitting of orbitals in molecular orbital theory.[105,106] NPSL films of silver cuboctahedra nanocrystals have also shown that the coupling between nanoparticles can be controlled by changing the interparticle spacing, density, and packing symmetry to tune their optical response over the entire visible range (Figure 1.5A).[107] Similarly, the collective plasmonic response of BNSLs can be tuned across the entire visible spectrum by varying the composition and symmetry of the superlattice.[108] Macroscopic solids of NPSLs also exhibit composition and symmetry dependent plasmonic properties. For example, a blend of gold BCC NPSLs and iron oxide BCC NPSLs exhibits a plasmonic response, whereas CsCl-type BNSLs of gold and iron oxide nanoparticles do not, as the iron oxide particles act as spacers that suppress plasmonic coupling between gold NPs (Figure 1.5B).[80]

Coupling between plasmonic nanoparticles also results in significant enhancements of the electromagnetic field in the regions between the nanoparticles. These regions, commonly referred to as "hot spots", have fields that are of 10 orders of magnitude stronger than those of isolated

nanoparticles,[109] which enable a variety of plasmon-enhanced molecular spectroscopy techniques.[110] For example, in plasmon-enhanced Raman spectroscopy, the enhanced electric fields in the "hot spots" allow samples there to produce Raman signals that are 10^6–10^{12} times stronger than when in the free state.[111,112] In one example, gold nanorod superlattices were used as SERS substrates for the rapid detection of prions at concentrations even as low as 10^{-10} M (Figure 1.5C).[113] Similarly, gold nanorod superlattices coated with SiO_2 could be used to detect bacteria-produced pyocyanin at 10^{-14} M,[114] and Au/Ag bimetallic nanocuboid superlattice-based SERS substrates, have been used to detect water treatment chemicals at 10^{-12} M.[115]

Photonic Properties of NPSLs

One of the most common photonic applications of particle assembly is the formation of photonic band gaps via periodic alteration of the refractive index throughout a lattice.[116] However, because most demonstrations of this type of self-assembled photonic crystal use particles that are >200 nm, such structures are outside the scope of this perspective; we refer the reader to recent reviews for additional details.[11,117]

Nevertheless, plasmonic NPs are able to open a photonic band gap via strong coupling between surface plasmons and photonic modes of a microscale crystallite of defined shape. DNA-functionalized gold nanoparticles assembled into BCC rhombic dodecahedra single crystals exhibited a band gap in the visible range despite having interparticle distances that were <50 nm. The strong coupling between the surface plasmons of the gold nanoparticles and the photonic modes enabled by the size and geometry of the crystal led to the creation of plasmon polaritons with anticrossing behavior in the dispersion diagram, prohibiting the propagation of certain photonic modes.[118] Additionally, the effective refractive index of a plasmonic assembly can be

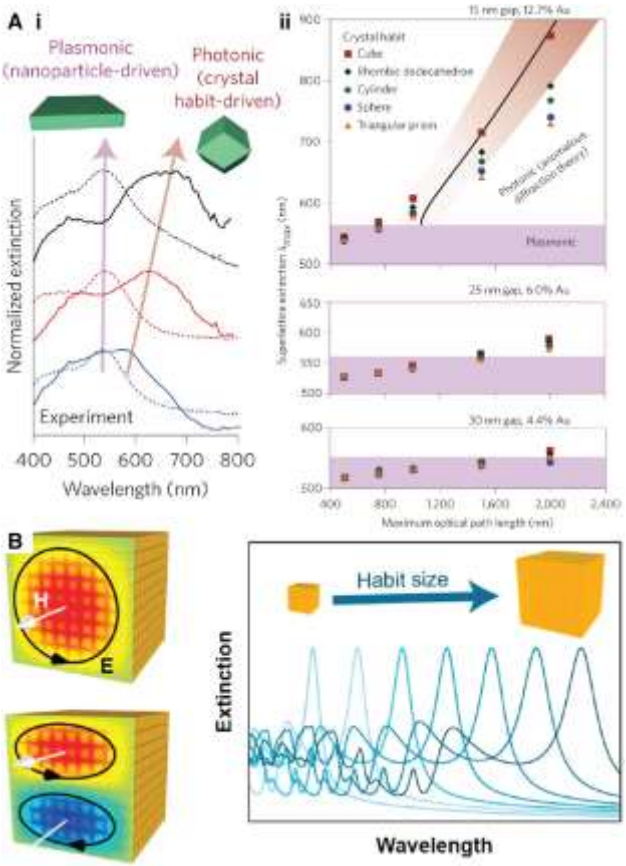

Figure 1.6. Emergent photonic properties in NPSLs. A) Photonic band gaps can be realized via strong coupling between surface plasmons and photonic modes in 3-D NPSL crystals. i) Extinction spectra for NPSL thin films (dashed) and 3-D crystals (solid) of similar composition differ significantly due to the presence of coupled photonic modes in the 3-D crystals. ii) The extinction wavelength of a 3-D NPSL crystal can be plasmonic or photonic in nature depending on its interparticle spacing, size, and crystal habit. B) Gold nanocubes assembled into NPSLs with cubic symmetry can exhibit multipolar Mie resonances which can be tuned by increasing the habit size of the crystal. Adapted from ref. 119, 122.

tuned by controlling the interparticle distance of the constituent nanoparticles. In thin films (~150 nm) that are unable to accommodate significant phase shifts in the transmitted light, extinction is primarily due to plasmon absorption. However, when light travels through NPSLs with 3-D geometries (~1 μm), sufficient phase interference between light on the interior and exterior of the structure results in light scattering (Figure 1.6A).[119] A set of design guidelines for the fabrication of intentionally designed plasmonic photonic crystals with designer stopband locations has even been developed by using the fundamental principles developed from these observations.[120]

The assembly of anisotropic ellipsoid nanoparticles into NPSLs has been computationally predicted to produce dichromatic crystals that exhibit birefringence. In addition, when assembled into NPSLs with anisotropic crystal habits, depending on their orientation, the crystals displayed a skin depth approaching that of pure metals or were able to directionally confine waves.[121] NPSLs with cubic symmetry, assembled using gold nanocubes, have exhibited multipolar Mie resonances and refractive indices as high as 8 in the mid-infrared (Figure 1.6B); rationally designed arrays of these NPSLs crystals could exhibit negative refractive indices due to their overlapping Mie resonances.[122]

While NPs are typically too small on their own to produce photonic crystals, coating NPs in thick polymer shells can be used to produce spacings large enough to assemble with visible photonic band gaps. Assemblies of ~70 nm SiO_2 NPs produced structural coloration, where the wavelength of reflected light scaled with the thickness of the polymer coating.[123] In 2-D arrays of plasmonic nanoparticles, hybridization of plasmonic and photonic modes can produce hybrid modes termed surface lattice resonances (SLRs). These SLRs are delocalized over large distances and exhibit narrow resonance widths and enhanced electric fields.[124] Plasmonic arrays fabricated via lithography processes can exhibit SLRs with high quality factors of order 100 (resonance wavelength/width of resonance),[125] although they are challenging to fabricate. Self-assembly approaches have been able to generate SLRs by encapsulating 100 nm plasmonic nanoparticles in a soft hydrogel shell, and assembling them into hexagonally ordered NPSL films with an interparticle spacing of ~500 nm (similar to the LSPR wavelengths of the plasmonic NP cores). Once the films were coated with an index-matched polymer, SLRs with quality factors of 25.7 were observed.[126] Similar methods using gold NPSL films demonstrated SLRs with quality factors ~20.[127]

Magnetic Properties of NPSLs

Magnetically responsive NPs below a critical size typically prefer a single-magnetic-domain structure, as domain formation is not energetically favorable in these small particles. These monodomain nanoparticles can be considered "superspins" with magnetic moments of $\sim 10^3$–10^5 μ_B.[128] Assembly of such NPs offers significant potential to tune the collective magnetic response of NP arrays as the structural organization of the NPSL can control the strength of dipole coupling between particles as a function of interparticle distance and coordination environment.

For example, in well-ordered NPSLs, each nanoparticle has the same spatial distribution of NP neighbors, and consequently experiences the same dipole–dipole interactions, leading to a narrower distribution of blocking temperatures. Furthermore, long-range order enhances the magnetic anisotropy of the whole assembly. As a result, NPSLs exhibit narrower magnetization peaks during zero-field cooling, a more gradual approach to saturation, and higher coercivity compared to their disordered counterparts (Figure 1.7A).[129]

Depending on the strength of dipolar correlations, superspin ensembles can exist in superparamagnetic (SPM), superspin glass (SSG), or superferromagnetic (SFM) phases, the study of which collectively comprise the field of "supermagnetism".[128] Monte Carlo simulations have been used to examine these different material properties by constructing a phase diagram for face-centered cubic (FCC) NPSLs in the temperature-anisotropy plane.[130] In the SPM phase, the dipoles are uncorrelated or only weakly correlated, so each nanoparticle has an independently fluctuating moment and the whole ensemble follows the same relaxation dynamics as its constituents.[131] In the SSG phase, moments are randomly oriented but frozen. Even without structural disorder, magnetic disorder in SSG NPSLs is still possible due to frustration from the random distribution

of easy axis orientations.[130] Co NPs assembled into 3-D FCC multilayers, for instance, have shown characteristic features of the SSG phase, including aging and memory effects. However, significant contributions of mesoscopic structural order to the SSG behavior have yet to be observed.[132]

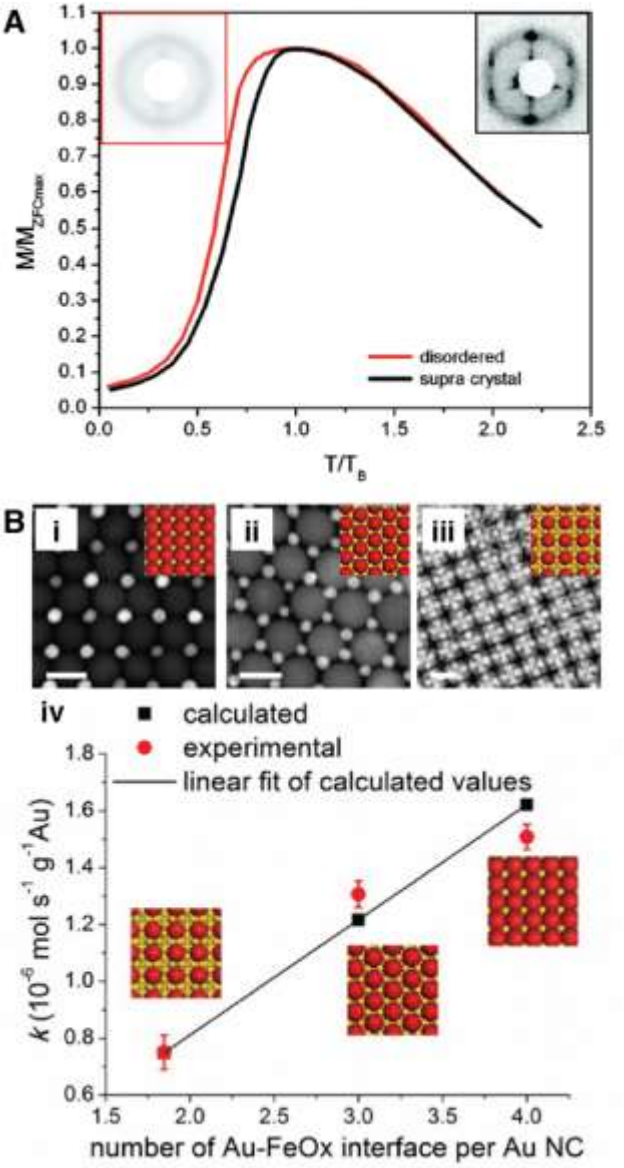

Figure 1.7. Emergent magnetic and catalytic properties in NPSLs. A) Structural ordering of Co NPs causes a narrowing of the zero-field cooled magnetization peak compared to disordered aggregates. B) BNSLs of gold and iron oxide nanoparticles with i) AB, ii) AB_2, and iii) AB_{13} Au-FeO_x symmetries exhibited iv) catalytic activities toward CO oxidation that was proportional to the number of Au-FeO_x contacts per gold nanoparticle. Scale bars are 20 nm (i, iii) and 10 nm (ii). Adapted from ref. 129, 141.

In contrast to the SPM and SSG states, the superspins in the SFM state are strongly correlated and exhibit long-range magnetic order, which indicates that lattice organization should have significant effects on collective magnetic behavior. An illustration of predicted order-induced effects is that, in the strongly coupled regime, the ground state of an NPSL material has been predicted to be antiferromagnetic in simple cubic arrays, but ferromagnetic in FCC and BCC arrays.[133] However, directly measuring such a result experimentally is challenging, as there are many additional factors that influence the dipole configuration in NPSLs, including the dimensionality of the superlattice, finite-size effects, and temperature. Thus, evidence of SFM ordering has been limited to 2-D close-packed arrays[134] and the exact relationship between structural ordering and magnetic ordering remains an open question.[135] Significantly more effort in NP-based materials is required to elucidate the scope of opportunities for NPSLs in this area.

Catalytic Properties of NPSLs

Nanomaterials often exhibit size-dependent catalytic properties that arise due to increased surface-area-to-volume ratios and an increased number of high energy active sites.[136,137] NPs can also be used in photocatalytic applications by using their optical properties (e.g., plasmon resonances) as a means of injecting energy into a system.[138] Many catalytic nanomaterials are often used in tandem with other (nano)materials because the formation of an interface between distinct compositions both enables new catalytic properties and provides a design handle to control catalytic behavior as a function of factors like distances between different materials.[139] As NPSLs are able to precisely structure shaped-nanomaterials together, they provide a unique platform to engineer these interfacial contacts in a deterministic and predictable manner to control emergent catalytic properties. It is important to note that while surface ligands are critical for the assembly

of NPs into NPSLs, their presence passivates the NP surface and prevents the formation of interfacial contacts between NPs. As such, the ligands generally need to be removed before any emergent catalytic properties can be observed.[140]

One instance of these emergent catalytic properties has been observed in Pt octahedra bound by (111) facets coassembled with Pd nanospheres to form binary NPSL films with ico-AB_{13} symmetry; these arrays exhibit four times more catalytic activity in reducing oxygen to water than either the pure Pt NPs or random arrangements of the Pt and Pd NPs.[140] This dramatic increase was attributed to combining the high catalytic activities of the Pt(111) planes with the synergistic catalytic effects of Pd and Pt. In a subsequent study, the well-known synergistic effects of Au and Fe_3O_4 in catalyzing CO oxidation were exploited by synthesizing Au–Fe_3O_4 binary NPSLs. The crystal symmetry of the NPSLs controlled the number of interfacial contacts between the two nanoparticle types and thus could be used as a design handle to tune catalytic activity (Figure 1.7B).[141]

NPSLs are also unique in that they can be used to design multifunctional catalytic materials by integrating different types of catalysts together. In one instance, carbon coated Co–Mn oxide (CoMnO) NPSLs were used as efficient bifunctional water splitting electrocatalysts, with the CoMnO nanoparticles and their nitrogen-doped carbon coating acting as oxygen evolution reaction and hydrogen evolution reaction catalysts, respectively. Importantly, the NPSLs had significantly better catalytic activities than their disordered counterparts, confirming that ordering of the nanoparticles resulted in emergent catalytic properties.[142] Tandem catalysts have also been developed by first assembling a monolayer of Pt nanocubes onto a silicon substrate and then assembling CeO_2 nanocubes on top of the Pt structures. In doing so, two different interfaces were generated that catalyzed sequential reactions to allow for the formation of propanal from ethylene

and methanol. When the reaction was conducted using physical mixtures of Pt-CeO_2 and Pt-SiO_2 catalysts instead, no propanal was formed, which indicated that the precise interfacial contact afforded by the NPSLs was key to enabling the tandem catalysis. In addition, when surface ligands were left on the nanocube bilayers, no reaction was observed as well, indicating that the removal of the ligands was indeed necessary for the formation of the CeO_2–Pt and Pt-SiO_2 interfaces.[143] Additional research has also shown that ordering in NPSLs can improve both mass activity and charge transfer properties.[144,145] Collectively, NPSLs therefore offer significant potential for generating new catalytic materials based not only on the composition of the NP building blocks, but also how they are organized in 3-D space.

Mechanical Properties of NPSLs

Because there are multiple methods and ligand interactions that can be used to govern their assembly, different NPSLs have been found to exhibit a wide range of mechanical properties depending on their composition and processing conditions:[146] Young's moduli can range from 100 kPa for hydrated PAE lattices,[147] to 100 MPa for dried hydrogen-bonded polymer-grafted nanoparticles,[74] to 64 GPa for dried NPSLs with cross-linked molecular ligands.[148] In general, however, the mechanical properties of most NPSLs to date have been determined to be comparable to that of glassy polymers, with Young's moduli between 1–10 GPa and hardness on the order of 100 MPa. However, they are typically brittle, with fracture toughness values around 40 $kPa/m^{1/2}$.[146]

Considering that most NPSLs are held together by weak van der Waals interactions between molecular ligands, the large Young's modulus and hardness values observed suggests that there are some collective emergent mechanical properties that arise from their ordering. Indeed,

when compared to amorphous nanoparticle assemblies, the mechanical properties of ordered NPSLs were found to be at least 2-fold greater.[149]

Multiple hypotheses have been put forth to account for this behavior. One possible factor is that the ligands interdigitate and interact strongly with each other when confined to the nanoparticle surfaces and the interstitial spaces, which increases their modulus significantly.[150] On the other hand, recent computational work suggests that it is the deflection of the ligands rather than their interdigitation during compression that is primarily responsible for the high stiffness

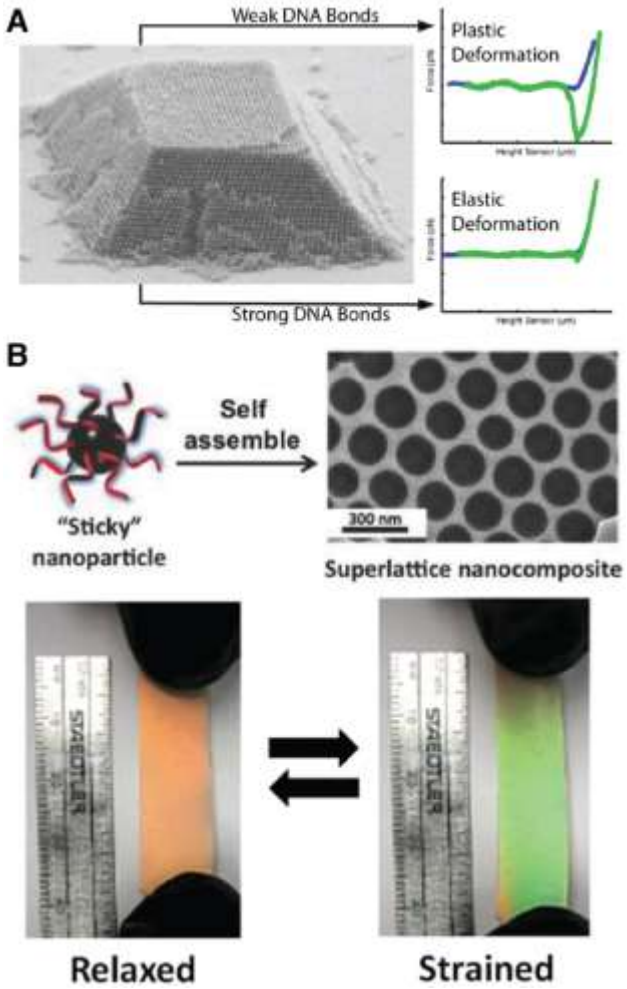

Figure 1.8. Emergent mechanical properties in NPSLs. A) The Young's modulus and yield strength of DNA-based NPSLs can be decoupled and independently tuned by varying the type of DNA used to drive assembly. B) Interparticle spacing-dependent photonic properties can be used to imbue mechanochromic properties to the material, such as reversible color changes upon mechanical strain. Adapted from ref. 74, 147.

values observed.[151] The presence of residual compressive stress in the NPSL has also been suggested to play a role, as ligands that are kinetically trapped in nonequilibrium conformations induce a compressive stress in the superlattice, which resists bulk compression and artificially inflates the elastic modulus.[152] However, because multiple factors may influence both the packing of surface ligands and the strength of their interactions with one another, it is difficult to definitively state how they govern the observed mechanical behaviors.[153–156]

Aside from exhibiting exceptional mechanical properties, NPSLs have also been able to demonstrate other unusual mechanical behaviors. In DNA-based NPSLs, the yield strength and Young's modulus can be decoupled and independently tuned, which is difficult to achieve in conventional bulk materials;[147] this decoupling means that the stiffness and mode of deformation (i.e., elastic vs plastic) can be independently dictated (Figure 1.8A). NPSLs assembled via hydrogen bonding have been shown in computational studies to exhibit an anomalous pressure softening due to the compression-induced buckling of the ligands.[157] Additionally, interparticle spacing-dependent photonic properties of NPSLs have been used to introduce mechanochromic properties (Figure 1.8B).[74] Collectively, these unique properties indicate that a wealth of new properties and structure–property relationships could be obtained via NP assembly, and thus this emerging area of research should be thoroughly explored in the near future.

Future Challenges in Nanoparticle-Based Materials

Given the wide design space afforded by materials synthesis via NP assembly, it is likely that new technologies and applications will continue to emerge that exploit the properties described in the previous section.[8,62,117] In addition to making new NP-based materials and investigating their structure–property relationships, however, there are multiple additional challenges that are just

beginning to become apparent (Figure 1.9). Here, we will explicitly note the areas of research we believe to be critical to enabling such technological transitions, and provide examples that provide preliminary insight on how these advancements might be accomplished (Figure 1.10).

Scale Up and Macroscopic Fabrication

If we define the term "device" as a specific structure tailored to take advantage of a material's properties for a desired effect, then devices can constitute a wide array of functional forms. Because most NPSL synthetic methods currently produce predominantly microscopic structures[55,69,158] or nominally 2-D films,[39,43,107] the most immediate applications for NPSLs involve devices with either small or planar form factors. For example, the size- and shape-dependent plasmonic and photonic phenomena of DNA-programmed NP assemblies discussed above would make them suitable for waveguiding in microelectronics due to their micron-scale assembly sizes and precise nanoscale structure control.[56,118] Conversely, the 2-D films generated in evaporation-driven BNSL assembly are well-suited for the synthesis of large-scale coatings for mechanical protection or for modification of the properties of an underlying substrate.[34,159–161] Technologies are also emerging for the use of NPSL films in light absorption and emission, applications for which the planar shape of these BNSL arrays is ideal.[162,163]

These types of microscale or planar geometries are likely to continue to be the main devices in the near future, as one of the predominant remaining challenges for NPSLs is their scale up to larger quantities. Compared with bulk atomic, molecular, or macromolecular materials, NPSLs can only be made in limited amounts, primarily due to the challenges of producing large volumes of low-dispersity NPs via colloidal synthesis, and in precisely regulating assembly conditions across large volumes to produce uniform materials.[164–166] However, as synthetic procedures

continue to improve, methods to produce large quantities of particles suitable for NPSL assembly are becoming more common, making multiple NP compositions (e.g., noble metals, oxides, semiconductors) readily available for purchase and enabling their use by researchers in a variety of disciplines outside just chemistry and materials science. Additional efforts to expand both the variety and quantity of nanoparticles available could also be improved by researching higher throughput batch processing or flow chemistry methods for continuous NP synthesis.[167–169]

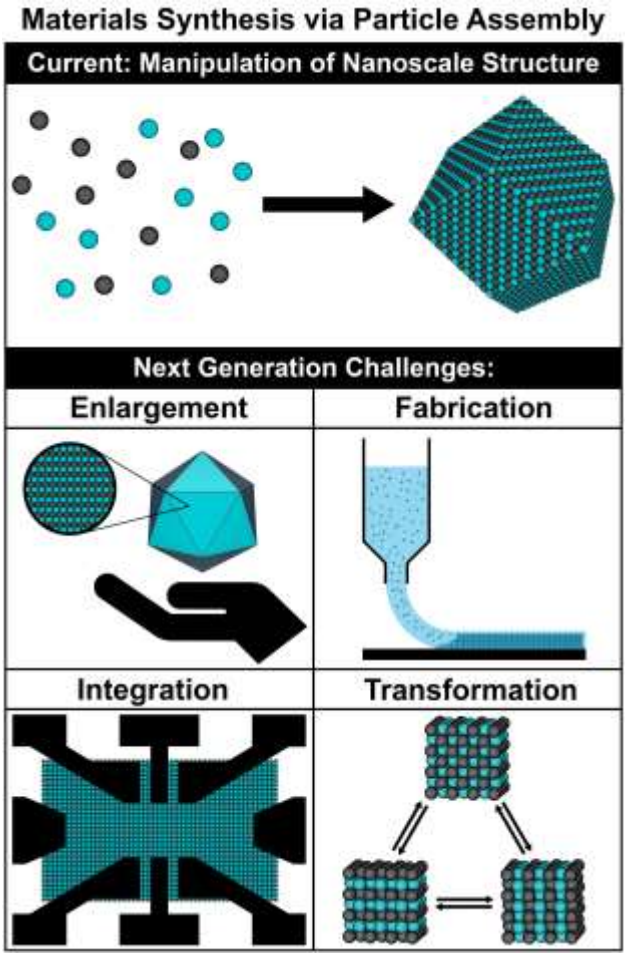

Figure 1.9. Advancements in nanoparticle assembly have provided a wealth of unique materials for study. Now that myriad assembly techniques have been developed, new challenges are beginning to emerge. Significant opportunities for both basic scientific investigation of structure-property relationships and functional device fabrication for NP assembly methods capable of being: produced at macroscopic scales; patterned into arbitrary shapes; integrated with traditional bulk materials and devices; intentionally toggled between different organization states.

It is important to note, though, that the process of scaling up a material's synthesis constitutes a bigger challenge than simply "making more" of it. Once enough material can be produced that the structures exist at the micron, centimeter, or larger size regimes, those length scales also become relevant for dictating material properties and behavior, and must be considered as part of the synthetic process.[80,170] For example, as chemists, we often view the formation of perfect crystals as the ultimate in material structure control. However, we also know from traditional atomic materials that defects and microstructural deviations are often key for generating or controlling material performance.[171] Substitutional defects or vacancies can be used to dope semiconductors and control their band gaps,[172] dislocations and grain boundaries affect mechanical properties by enabling or limiting slip planes,[171] and surface defects are often the most active sites of a catalyst.[173] Point defects, line defects, and grain boundaries are already commonly observed in NPSLs, though our ability to intentionally generate them is still in its infancy.[58,174] Nevertheless, the fact that NPs can be assembled independently of their composition allows for intentional programming of point defects like vacancies (e.g., "hollow" PAEs that graft DNA brushes to an empty polymer nanoparticle shell[175]) or substitutional defects by assembling NPSLs using a batch of NPs that incorporates small amounts of NPs with the same size and ligand chemistry, but different composition.[80,176] Methods to control 2-D and 3-D defects are more difficult to envision, but still potentially possible. Templated assembly is one potential path to generating these more complex microstructural features, by patterning a specific defect into an underlying substrate that propagates as the material is assembled on top of the pattern. Other methods such as post-assembly treatment of the assemblies with an external force (e.g., thermal gradients, solvent flow, or optical energy) that induce reorganization of NPs are also a potential route to controlling 2-D and 3-D microstructure.[177,178] Significantly greater effort needs to be put

into techniques to induce these defects in a controlled manner, and also to determine if such defects and microstructuring affect the collective properties of NPSLs in the same manner as their atomic analogues. In this regard, computational efforts will be critical both to guide the development of these new techniques, and to help understand the emergent properties as they arise. Computational efforts for hierarchical materials that span multiple length scales will undoubtedly be increasingly difficult as the scale of these assemblies increases, as coarse-grained models are required to make large systems or long timeframes computationally tractable. As such, methods must be developed to coordinate simulations or calculations and interpolate data across the wide range of time and length scales associated with molecular bonding, nanoscale assembly, and macroscopic shaping.[42,179]

Processing of NPSLs into Functional Forms

A key step in synthesizing materials for both fundamental structure–property measurements and device fabrication is the ability to shape the material into the correct functional form. For example, optical interrogation of a film can be hampered if factors like surface roughness, film thickness, or uniformity across the light source's cross-sectional diameter are not properly controlled. Similarly, mechanical measurements can be significantly affected by the shape of the object being compressed or extended. For advancing both our understanding of NP material synthesis and use of these materials in different applications, it is important to consider how we process the as-synthesized material into the appropriate shape for examination and use. However, the types of conventional materials processing strategies that can be employed with NPSLs are currently limited. Some NPSLs are only stable in solution,[54,180,181] others are mechanically brittle once assembled and dried,[182,183] and many are easily disrupted at elevated

temperatures;[10,76] processing techniques that require high temperatures or application of mechanical force are therefore likely to ruin the ordering generated by self-assembly. Thus, advancement of NPSL synthesis to generate materials with controlled micro- or macroscopic forms requires that we develop compatible processing steps that do not disturb their ordering, or develop protection methods that stabilize the lattice structure post-assembly.

For example, drop casting is a simple processing method to generate coatings, and sedimentation of NPSL via solvent evaporation can be thought of as a simultaneous assembly and processing step, for 2-D structures.[9] Also in the context of films and substrate-bound assemblies, it is possible to use plasmon thermalization as a means of simultaneously crystallizing and macroscopically shaping a material by irradiating plasmonic nanoparticle superlattices with a laser

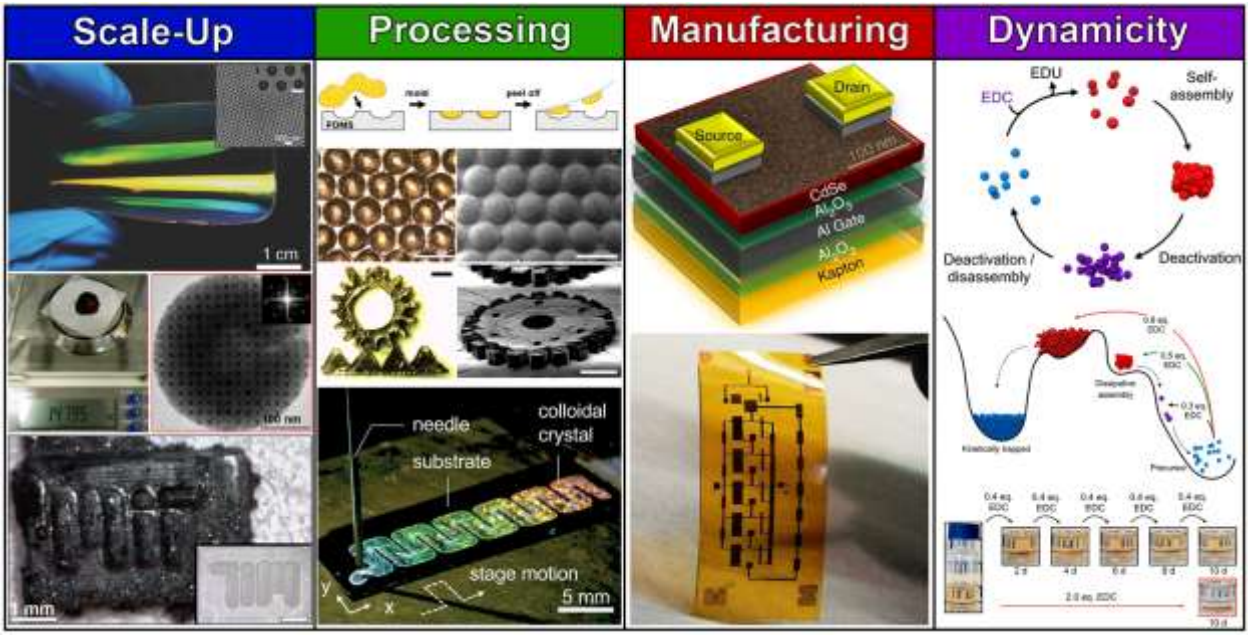

Figure 1.10. In order to address the challenges outlined in figure 9, four key areas of research in NP assembly must be undertaken. Successful advancements in these areas will lead to the establishment of NP assembly as a materials synthesis method that is potentially as well-understood and useful as traditional chemical syntheses. These include: scale-up of NP assembly methods, development of processing techniques to control micro- and macrostructural features, integration of NP-based materials with conventional bulk structures, and introduction of design handles to make dynamic or stimuli responsive assemblies. Initial research results in each of these areas indicate that the field is rapidly progressing towards accomplishing this goal. Adapted from ref. 80, 158, 159, 170, 184, 188, 199.

and allowing the local thermal gradient to induce NPSL reorganization and diffusion.[177] For macroscopic 3-D NPSL structures, appropriate control over the thermodynamics of interparticle interactions can allow for bulk quantities of NPSL crystallites to be "sintered" into free-standing structures of arbitrary shapes via compression molding.[80,184] Shear alignment during solvent flow has also been shown to control particle organization in colloidal structures,[185–187] meaning that extrusion or compression could be fruitful avenues for exploration,[183,188] provided that we can fully understand and manipulate the chemical interactions between the NPs and the surrounding fluid; computation is certainly a key factor to enabling such understanding.[189] To enable these methods, assembly within different solvents must be investigated, including the use of more viscous alternatives than small molecule liquids, such as homopolymer or block copolymer melts.[81,88] With regards to protection of the superlattice post-assembly, methods to sinter NPSLs into covalently connected solids via chemical, thermal, or optical stimulus have been developed, where weak intermolecular forces between NP ligands are replaced or reinforced with permanent chemical bonds.[161,190–192] It is also possible to embed NPSLs into different materials like metals, oxides, or cross-linked polymers and gels, where the superlattices act as a scaffold around which these other materials can be grown.[193–195]

Another area of NPSL processing research that remains underinvestigated is the establishment of methods to use NPSLs as additives in other bulk materials. By using the NPSLs as components of a material (as opposed to the entirety of a macroscopic structure), the physical properties induced by NP assembly can be exploited while minimizing the amount of NPSLs that must be synthesized. Examples of block copolymers with embedded, isolated NPs have already been demonstrated,[86,88,196] but encapsulation of fully formed NPSLs is less common. New chemical strategies to stabilize these assemblies so that they can be mixed with bulk polymers or

other materials should be a key focus of our community's research efforts. In this regard, it will be important to research both the stability of lattices (pre- and post-protected) during macroscopic processing methods, and to understand how the interfaces between NPSLs and bulk material around them affect the emergent properties of the lattices, such as optical refraction or phonon transport.

Integration with Other Devices

Although great examples have been shown of devices made solely from NPSLs,[118,160] most technological applications of these materials will require them to be properly integrated with other types of materials.[159,197] The ability both to interrogate the properties enabled by NPSL assembly and to use those properties in a given application therefore requires that we can either deposit assembled lattices at the site of interest, or that we can directly assemble them at a desired location within a preformed device. This research advancement also requires that the sizes, shapes, and orientations of the structure be controlled so that the other instrument or device components can properly interact with the NPSL. Thus, key areas of investigation must include means to break the symmetry of assembled materials to induce the formation of complex microscale and macroscale geometries. Given that the forces governing interparticle interactions often provide limited means of controlling structure beyond each NP's nearest neighbors, advancement in this area will require multidisciplinary approaches that combine chemical synthesis and NP assembly with top-down fabrication.

As an example, assembly on patterned substrates is a well-explored method to achieve the goal of macroscopic positioning, as lithography can easily create arbitrarily shaped and oriented patterns in an intentional manner.[58,93] Some examples are discussed in the earlier sections of this

perspective, such as DNA-programmed assembly on patterned and DNA-grafted substrates, or deposition of particles into specifically shaped wells. However, many of these methods are either tedious in their preparation or limited in their ability to fully control NPSL structure, requiring further study and advancement. The next stages for NPSL assembly therefore include developing a better understanding of how such confined assembly techniques affect assembly thermodynamics and kinetics, as well as how the underlying pattern affects the stability of different NPSL lattice types; it may even be possible to use these larger patterns as a way to "frustrate" crystallization to specifically manipulate crystal symmetry or microstructure.[198] More research is needed to fully understand how top-down patterning at the micro- to macroscopic scale affects the behavior of NPs as they form ordered arrays with nanoscale repeat structures.

Dynamic/Living Systems

The majority of NPSLs that have been synthesized to date are intentionally targeted thermodynamic products. The key advantage of assembling particles into their thermodynamically favored arrangement is that it simplifies the synthetic process if the desired crystallographic symmetry represents the thermodynamic minimum for the selected set of NP building blocks, then assembly is just a matter of applying enough time and energy to allow the NPs to reorganize into the appropriate state. Kinetically driven or out-of-equilibrium structures are thus more rare,[180,199] as both the NP building blocks and the assembly conditions must be more tightly controlled in order to reproducibly generate, isolate, and stabilize these inherently transient or intermediate species. Nevertheless, such structures offer the possibility of generating more complex organizations with broken or lower symmetry than thermodynamic products often

provide, as well as specific microstructural features or nonequilibrium properties that would open up new applications like energy storage or harvesting.

In order to induce such kinetic structures, design principles for NP assembly must be more refined to describe all relevant parameters (including factors like rates of assembly or relative stability of intermediate species) and the assembly pathways need to be better characterized and modeled. Properly controlling such kinetic products requires significantly more fundamental research. Important avenues of exploration are the establishment of new computational techniques to simulate dynamic colloids as they reorganize, coupled with methods to extrapolate the thermodynamic stability of different points in this complex phase space.[200] Additionally, experimental methods would be aided by the development of tools from traditional materials science to describe and explain crystallization phenomena (e.g., time–temperature-transition diagrams).[201] New instrumentation and technologies to track these formation processes in real time must also be established, such as in situ TEM or X-ray based techniques.[202,203] In situ TEM is particularly attractive for monitoring and understanding dynamic assembly processes, as NP crystallization occurs on a much slower time scale than traditional atomic or molecular crystal formation, and thus NPSLs could be used as model systems to directly monitor crystallization phenomena in a manner not accessible to lattices built from atomic species.

An additional goal for dynamic systems is the development of NPSLs that can reprogram their structures upon application of an external stimulus, as this offers the opportunity to toggle properties on the fly.[75,97,181,199,204,205] Additionally, because self-assembly is inherently based on the concept of designing building blocks that spontaneously form a predetermined structure upon application of a stimulus, dynamic NPSLs would in principle permit materials to reorganize and self-heal any mechanical damage by simply reapplying the initial assembly conditions (e.g.,

thermally reannealing the disrupted structure). However, many current reorganization methods require excessive amounts of time to reorganize upon introduction of a stimulus as they are limited by the rates of diffusion of either the molecule stimuli or the NPs themselves. Additionally, many reorganization processes are order–disorder–order transitions, where an initial stimulus changes the thermodynamically preferred state of a lattice and causes a loss of ordering that requires reassembling the structure to generate the new ordered array. The next challenges for dynamic NPSLs therefore lie in improving the switching rates for these materials by employing processes not driven by a chemical stimulus (e.g., lattices that switch with the use of thermal, magnetic, optical, or electrical stimuli), or developing methods to generate order-to-order transitions that do not require an intermediate annealing or reorganization step. The difficulty of establishing such processes lies in determining methods to force NP reorganization without the need for long-range mass transport, as diffusion of either the stimulus or of the NPs themselves would inherently result in a significantly slower process than one guided by solely local reorganization of individual NPs.

NPSLs are an exciting class of material, with significant potential for enabling both basic scientific research into understanding the chemistry of crystallization, and the exploration and use of new emergent properties controlled by NP organization in 3-D space. These nanoscale "artificial atoms" can use principles that have been quantified and explored in atomic systems as a guide, but they are not bound by the same limitations imposed by the limited palette of available atomic species selectable from the periodic table. This opportunity comes with significant challenges, though, as their assembly is in many ways far more complex than atomic crystallization. Nevertheless, the multitude of available NP building blocks and assembly methods, combined with our continually growing knowledge of the fundamental principles governing NP assembly, make

it not unreasonable to predict that in the foreseeable future we will be able to explain, predict, and control the formation of a host of new materials by design.

The impact of these NPSLs on the future of chemistry and materials science is dependent upon our ability to both use the structures and properties we have already generated and invent new ways of scaling up, integrating, and controlling the larger-scale structures of these NPSLs to enable advances in both fundamental science and engineering applications. Ultimately, the extent to which NPSLs affect the chemistry and materials science communities will be defined by our ability to identify key properties that can be best (or only) produced with NPSLs, as well as our ability to control NPSL structure from the molecular to macroscopic scale simultaneously. Scientific insight is necessary to define design principles for controlling and explaining NP assembly to the same levels of complexity and precision as the atomic precursors chemistry has studied for decades, and pairing these scientific insights with engineering research into integrating and using NP structures will enable multiple applications in a wide range of disciplines.

Chapter 2: Nanoparticle Assembly in High Polymer Concentration Solutions Increases Superlattice Stability

Adapted from Lee, M. S., Alexander-Katz, A. & Macfarlane, R. J. Nanoparticle Assembly in High Polymer Concentration Solutions Increases Superlattice Stability. Small 17, 2102107 (2021).

Polymer nanocomposites are made by combining a nanoscale filler with a polymer matrix, where polymer-particle interactions can enhance matrix properties and introduce behaviors distinct from either component. Manipulating particle organization within a composite potentially allows for better control over polymer-particle interactions, and the formation of ordered arrays can introduce new, emergent properties not observed in random composites. However, self-assembly of ordered particle arrays typically requires weak interparticle interactions to prevent kinetic traps, making these assemblies incompatible with most conventional processing techniques. As a result, more fundamental investigations are needed into methods to provide additional stability to these lattices without disrupting their internal organization. The authors show that the addition of free polymer chains to the assembly solution is a simple means to increase the stability of nanoparticle superlattices against thermal dissociation. By adding high concentrations (>50 mg/mL) of free polymer to nanoparticle superlattices, it is possible to significantly elevate their thermal stability without adversely affecting ordering. Moreover, polymer topology, molecular weight, and concentration can also be used as independent design handles to tune this behavior. Collectively, this work allows for a wider range of processing conditions for generating future nanocomposites with complete control over particle organization within the material.

Background

Multiple strategies for colloidal assembly have been developed using a diverse set of stimuli to precisely control the organization of particles in three dimensions.[9,43,206] In principle, the use of additives within the solution can provide additional design parameters to tune particle behavior by affecting the motion of the particles or the strength of the interactions driving their assembly.[50,51,207–213] While approaches that employ such a strategy (such as the addition of polymer to induce flocculation in colloidal dispersions) have been well-studied, these methods are most commonly studied in the formation of disordered aggregates or close-packed structures, and limited examples exist that fully explain how similar approaches can affect more robust or versatile assembly techniques capable of driving particle crystallization. Additionally, while numerous studies have focused on interactions between free particles and polymer in solution, interactions between nanoparticle assemblies and dissolved polymer chains remain an important area of investigation.[214–218] Design principles for using macromolecular additives to control nanoparticle assembly could even allow for the incorporation of these materials in different applications or processing techniques like additive manufacturing that often employ solution-dispersed or molten polymers. The extrusion of thermoplastics containing nanoscale filler is a common method used to generate polymer nanocomposites in additive manufacturing. However, the incorporation of filler into the polymer feed introduces additional processing variables that must be addressed in order to obtain a functional composite, including but not limited to filler dispersion, filler compatibility with the polymer matrix, and filler alignment.[219–221] Stabilizing ordered nanoparticle assemblies in polymer-rich environments at high temperatures would enable the use of nanofillers with complex ordering in the additive manufacturing of polymer nanocomposites. Here, we examine the supramolecular chemistry-driven assembly of nanoparticle superlattices in the

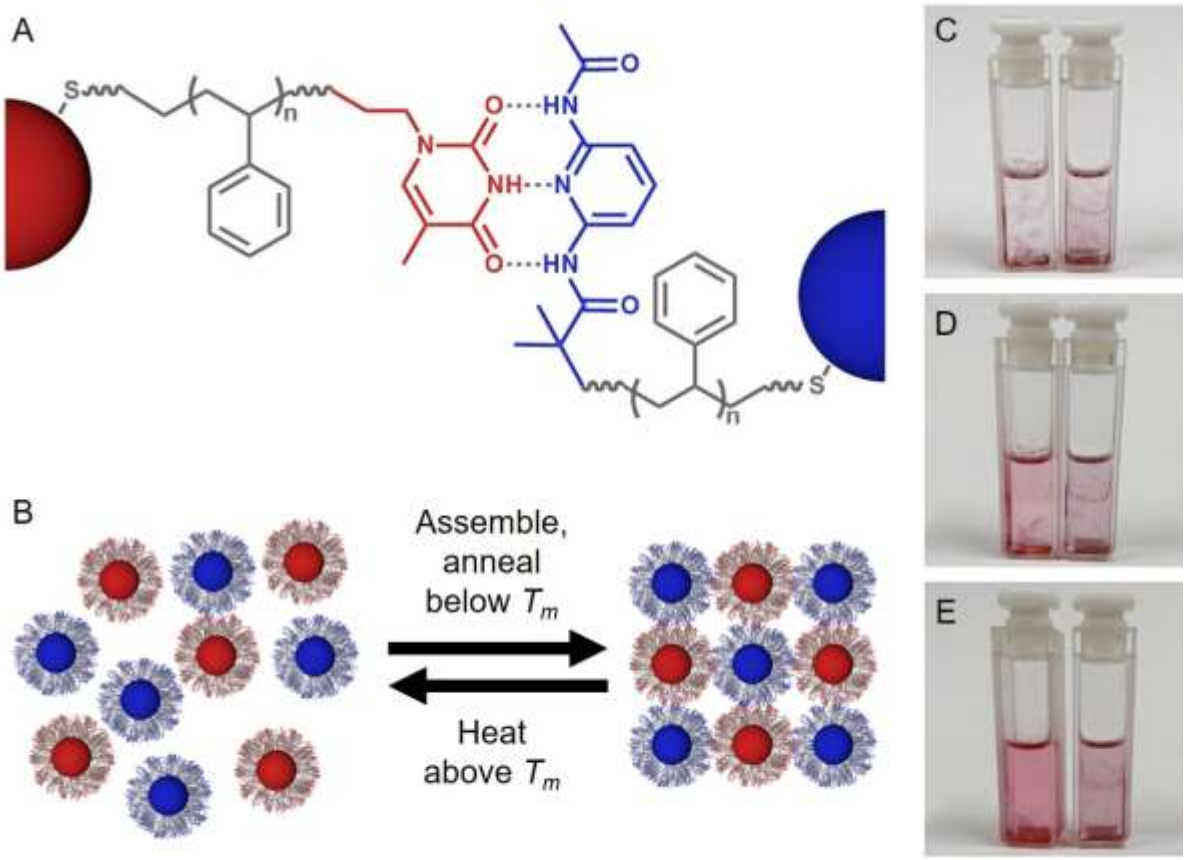

Figure 2.1. Nanocomposite tectons (NCTs) consist of (A) three components: a nanoparticle core, dense polymer shell, and supramolecular binding group. The binding groups on complementary NCTs form hydrogen bonds, allowing NCTs (B) to reversibly assemble into ordered structures with gentle thermal annealing and heating. Free particles appear pink in solution, while assembled structures appear purple. (C-E) The presence of free polymer in solution increases the thermal stability of NCTs. NCTs in pure toluene (left) and NCTs in a 200 mg/mL polymer solution (right) are both assembled at (C) 25 °C, but at (D) 50 °C and (E) 80 °C only NCTs in the polymer solution remain assembled, as indicated by the purple color of the solution. NCTs in pure toluene have disassembled into free particles, resulting in a bright pink solution.

presence of free polymer and show that free polymer can be used to control the thermodynamics and kinetics of particle assembly in a rational, readily understood manner. As a result, these particle superlattices can be rendered significantly more stable against thermal dissociation, potentially allowing them to be processed at higher temperatures that would enable compatibility of self-assembled nanoparticle superlattices with a wider range of fabrication techniques.

Nanocomposite tectons (NCTs) are a unique set of nanoscale building blocks that can be used to construct ordered arrays of polymer-grafted nanoparticles.[76,80] NCTs are composed of three distinct parts: an inorganic nanoparticle core, a dense polymer brush coating, and supramolecular binding groups attached to the ends of the polymer chains. The hard inorganic core dictates the overall shape and general size of the NCT, while the soft, deformable polymer chains control the solvent compatibility of the particles, as well as the distance between particles once assembled. Interactions between the supramolecular groups of different particles drive the assembly of NCTs into larger aggregates, where the most stable configuration of NCTs comprises an aggregate that maximizes the number of enthalpically favorable supramolecular linkages while minimizing the extent of entropically unfavorable polymer chain confinement. Because each individual supramolecular bond is weak and therefore dynamic, NCTs can easily be thermally annealed to induce particle reorganization into thermodynamically preferred ordered lattices (Figure 2.1). Moreover, each of the three components of an NCT can be independently modified to customize the overall material composition and nanoscale structure of the final assembly.[77–79]

While this level of control and programmability makes NCTs a promising tool for generating ordered nanocomposites, they are currently restricted to a narrow range of processing conditions that precludes many common processing methods used in polymer composite manufacturing.[222–224] This limitation arises from the fact that the formation of ordered particle arrays requires the NCT assembly process to be mediated by weak reversible bonds to allow for particle reorganization and prevent kinetic traps. However, the weak bonding interactions necessary to drive particle ordering also cause NCTs to disassociate at elevated temperatures. For example, hydrogen-bonded NCTs typically dissociate at temperatures of 40–50 °C (depending on NCT design), making them incompatible with common material processing methods that operate

at higher temperatures.[225] In order for NCTs and NCT arrays to be incorporated into polymer composite materials that can be used as stable solids, a method of processing assembled NCTs at higher temperatures without affecting the quality of the ordered superlattices is required. We hypothesized that assembling NCTs in the presence of a high-polymer content solution could be used to provide such added stability, as free polymer in solution should slow NCT diffusion away from the main assembly during the disassembly process. Additionally, alteration of the local solvent environment around each NCT has been demonstrated to affect their overall stability; we therefore also predicted that the addition of free polymer chains should provide design handles to control the thermodynamics of the supramolecular interactions driving NCT assembly.

Results and Discussion

Examination of the effects of a high-concentration polymer environment on NCT assembly was conducted using previously established NCT designs. NCTs consisted of 17 nm gold nanoparticles (AuNPs) grafted with a dense layer of 11 kDa polystyrene (PS) chains. Each polymer chain on an individual particle brush was terminated in either diaminopyridine (DAP) or thymine (Thy) supramolecular binding groups; DAP and Thy form a complementary hydrogen bonding pair (Figure 2.1A). When these complementary NCTs were combined, they rapidly assembled and precipitated from solution. The characteristic melting temperatures (T_m, the temperature at which the NCT aggregate dissociates) of the NCT assemblies were monitored via UV–vis absorption at 520 nm, which increases as particles dissociate away from an aggregate. Upon thermal annealing at a temperature just below their T_m, NCTs reorganized into ordered body-centered cubic (BCC) superlattices, as confirmed with small angle X-ray scattering (SAXS) (Figure 2.2A, B, Figure S2.2, Supporting Information). These synthesis and characterization protocols have been developed

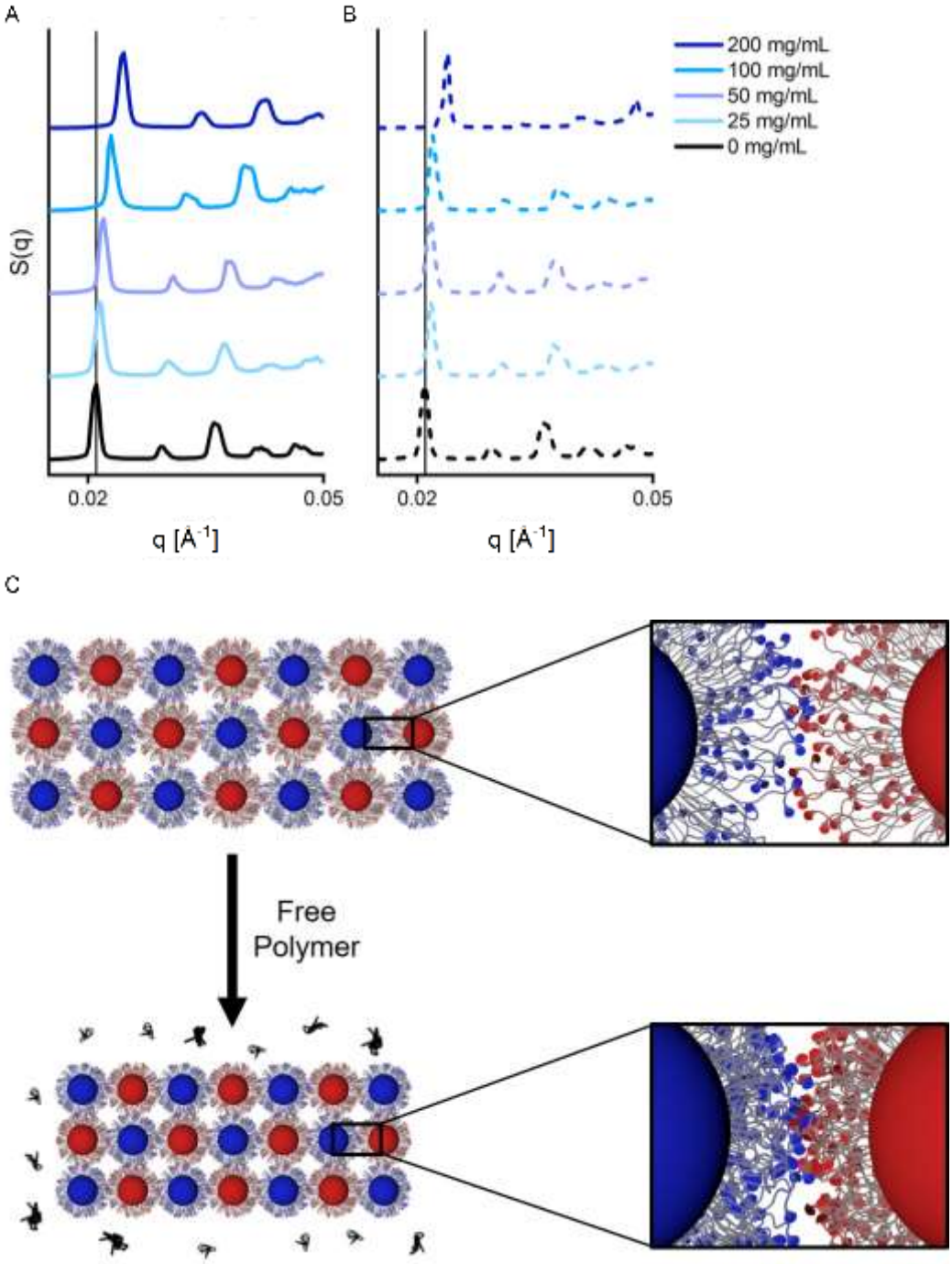

Figure 2.2. SAXS diffraction patterns of NCTs in varying concentrations of (A) linear PS and (B) star PS of the same molecular weight (26 kDa) show that NCTs retain their ordering quality in the presence of free polymer in solution while also exhibiting a decrease in the lattice parameter, indicated by peak shifting to higher q values (corresponding to smaller interparticle distances). (C) The presence of free polymer in solution generates an osmotic pressure that compresses NCT lattices, increasing the local binding group density between NCTs, which causes an increase in the NCT T_m.

previously, and allow for both monitoring of the overall strength of the supramolecular connections between particles, as well as confirmation of the nanoscale organization of assembled particles.[75–78] The effects of increasing the content of free polymer in solution was first examined by adding known quantities of linear PS (26 kDa) to the assembled and annealed NCTs.

To obtain the NCT T_m, fixed-rate melt curves were measured by heating NCTs in linear PS solutions of varying concentrations at a controlled rate of 0.25 °C/min while vigorously stirring (Figure S2.4, Supporting Information). Since adding free polymer increases the solution viscosity and lowers the rate of particle diffusion, we hypothesized that NCT T_m would increase as free polymer was added. It is also important to note that PS does not possess any functional groups that might interfere with the hydrogen bonds linking NCTs together. Thus, the net effect of adding free PS chains to the NCT solution was predicted to be an increased T_m directly correlated to the amount of PS added. Indeed, T_m was observed to increase in the presence of free polymer (Figure 2.3A); this elevated T_m was observed for NCT solutions containing different PS chains of varied Mn (26–60 kDa), with more significant effects being observed for longer polymers (Figure 2.3B). Because NCT binding occurs via multiple reversible supramolecular connections between particles, NCT melting is a second order phase transition. As a result, the dissociation of NCT assemblies occurs gradually as temperature is increased, and there is a broad temperature window over which there is a dynamic equilibrium of particles dissociating from and reincorporating into these extended aggregates. The slowed diffusion increases the time necessary for particles to reach thermodynamic equilibrium in this dynamic process, increasing the apparent T_m when following a fixed-rate heating profile.

While the observed increased T_m in viscous solutions is consistent with slowed diffusion kinetics, it does not preclude the possibility of free polymer also affecting the thermodynamics of

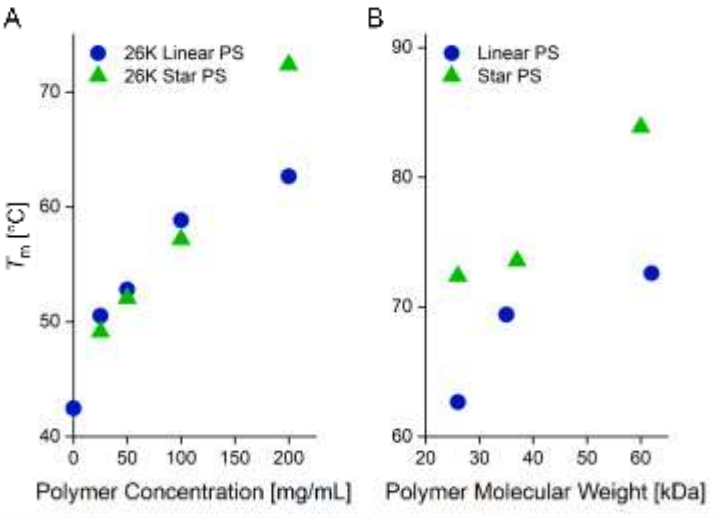

Figure 2.3. Fixed-rate melt curves were generated to measure the T_m for NCTs in polymer solutions of (A) varying polymer concentration at a constant molecular weight (26 kDa linear PS) and (B) varying molecular weight and morphology at a constant polymer concentration (200 mg/mL). Increasing the polymer concentration led to greater T_m elevation, as did increasing the polymer molecular weight. For the same concentration and molecular weight, at high polymer concentrations (200 mg/mL), NCTs in solutions of star PS exhibited greater T_m elevation than NCTs in solutions of linear PS.

supramolecular assembly. Prior work has demonstrated that the dynamic hydrogen bonding interactions between DAP and Thy-terminated polymer chains on NCTs are significantly affected by their chemical environment.[75,80] Therefore, to probe if the origins of the melting temperature elevation were solely kinetic in nature, forced-equilibrium melts were performed to determine if a thermodynamic effect was also present (Figure 2.4). In contrast to the prior fixed-rate melts where samples were subjected to a continuous heating rate, samples in a forced-equilibrium melt were subjected to temperature jumps of ≈10 °C, then held at that temperature until equilibrium was reached (noted as the point at which the UV-Vis absorption remained constant) (Figure S2.5, Supporting Information). Relative to the timescale of NCT dynamics, NCTs had an effectively infinite amount of time to reach the thermodynamically favored state, allowing for the influence of any kinetic effects to be removed from observations of the NCT melting process. Thus, if the

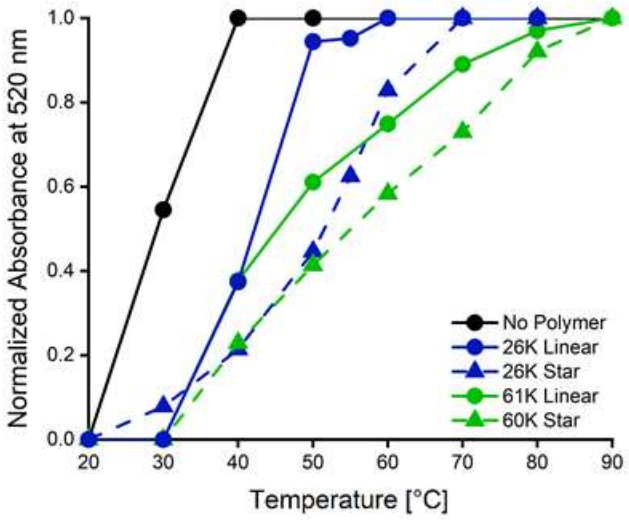

Figure 2.4. Forced-equilibrium melts were run at a constant polymer concentration (200 mg/mL) in toluene for varying molecular weights and morphologies to determine NCT T_m in the absence of any kinetic effects. The absorbance of assembled NCTs is normalized to 0, and the absorbance of fully dissociated NCTs is normalized to 1. NCT T_m elevation was present but to a lesser degree than in the corresponding fixed-rate melts, indicating that both kinetic and thermodynamic effects contribute to the observed T_m elevation.

melting temperature elevation was caused solely by kinetic effects, differences in T_m for the NCTs in high polymer concentration solutions would be expected to disappear, leaving all samples with the same melting temperature. However, the measured melting temperatures were still elevated to varying amounts as a function of both the amount of polymer and the Mn of the polymer added, with larger effects being observed with increased free polymer concentration and molecular weight. These data indicate that there is indeed an increase in thermodynamic stability for NCT lattices in solutions with free polymer, although the amount of melting temperature increase was lower than observed in the prior melting analyses. Together, these data indicate that the melting of NCT arrays in these high polymer content solutions is subject to both kinetic and thermodynamic effects.

While the kinetic effects on NCT melting are hypothesized to be a result of differences in NCT diffusion rates, the origin of the thermodynamic effects was not as readily apparent. To

determine the origin of this increase in T_m, additional melts were run with solutions containing 4-arm star PS using the same conditions as the samples with added linear PS (Figure 2.3B). These star polymers possess identical chemical compositions and molecular weights to the linear PS, but have a branched structure and central core that alters their conformation in solution, causing them to behave as a hybrid between soft linear polymers and hard spherical colloids.[226,227] Interestingly, at polymer concentrations of 100 mg/mL or less, NCT melting temperatures were more elevated for linear polymers than for star polymers of the same molecular weight and concentration, while the reverse was true at higher polymer concentrations. Since star polymers are more compact than linear polymers, a solution of linear polymer would have a viscosity higher than that of a star polymer at the same molecular weight and concentration.[228] If NCT T_m elevation in the presence of free polymer were due exclusively to alterations in solution viscosity, the star polymer-containing solutions would be predicted to exhibit lower elevation of T_m in comparison to linear polymer-containing solutions, regardless of the polymer concentration. These surprising results therefore indicate that the structure of the free polymer in solution must play a role in determining the degree of melting temperature elevation.

It has previously been shown that the melting temperature of NCT assemblies directly correlates to the local concentration of supramolecular groups around each particle.[75] It could therefore be hypothesized that these changes in T_m could be due to structural changes in the NCT lattice that affect the ability of DAP and Thy groups on adjacent particles to form linkages with one another. For example, changes to the distance between particles in an assembly alter the local concentration of DAP and Thy groups, which would in turn affect both the number of supramolecular connections between particles and the entropy associated with polymer chain confinement between bonded NCTs. To determine if these changes in T_m were induced by

structural alterations to the assemblies, SAXS was used to probe the crystal structure of NCTs in varying polymer solutions (Figure 2.2A, B and Table S2.2, Supporting Information). Importantly, the presence of free polymer was not observed to affect the quality of ordering in the crystal, as all samples formed highly ordered BCC arrays of particles with nearly identical SAXS peak breadth (an indicator of the degree of ordering within the sample). Thus, each NCT within an assembly possessed an identical number of nearest neighbors regardless of free polymer concentration. However, different amounts of added PS were observed to have noticeable effects on the interparticle distances within a lattice. In the presence of free polymer, all BCC arrays exhibited a decrease in their lattice parameters compared to the control sample with no free polymer. The amount of compression was more pronounced with increasing polymer concentrations, but less significant with increasing polymer molecular weight. Additionally, the amount of compression was greater for solutions containing linear polymers than for those containing star polymers of equal concentration and molecular weight (Figure S2.3, Supporting Information).

Based on these results, the origin of this compression was hypothesized to be due to an increase in osmotic pressure. Osmotic pressure is defined as the minimum pressure required to prevent solvent flow through a semipermeable membrane from pure solvent to a solution containing polymer dissolved in the same solvent. The virial expansion to determine osmotic pressure is:

$$\Pi = cRT\left(\frac{1}{\mathrm{M_n}} + Bc \ldots\right) \quad (1)$$

where Π is the osmotic pressure, c is the polymer concentration (g/mL), R is the ideal gas constant, T is temperature, M_n is the number average molecular weight, and B is the second virial coefficient.

In this equation, Π is proportional to polymer concentration but inversely proportional to polymer molecular weight, consistent with the observations noted above. B is a constant that provides an indication of the favorability of solvent–solute interactions for a given solvent and polymer. When solvent–solute interaction is preferred over solute–solute interaction, $B > 0$, and mixing is favored. In this case, toluene is a good solvent for PS, so B should be positive for both star and linear PS. However, it is important to note that despite having the same chemical composition, these polymers have different values of B, since solvent–solute interactions are affected by polymer morphology.[229] Due to their architecture of multiple low molecular weight arms radiating from a central core, star polymers behave more like spherical colloidal particles in comparison to the random coil behavior of linear polymers. The more compact, less penetrable structure of star polymers leads to smaller values of B than for linear polymers of the same molecular weight. Since Π is proportional to B, larger osmotic pressure values would be obtained for linear polymers than for the corresponding star polymer. These observations therefore lead to the hypothesis that the increased thermodynamic stability of particle superlattices in high polymer concentration solutions can be explained as an effect of depletion forces induced by compaction of the particle arrays.[230]

Depletion interactions are often seen in colloidal systems when the entropic penalty from pushing larger particles closer together is offset by the entropic gain from increasing the free volume available to the free polymer depletants in solution, resulting in colloidal flocculation.[231] In the system studied here, a reduction in the interparticle distance between assembled NCTs causes compression of the polymer brush between NCT cores, increasing the polymer brush density and also increasing the binding group density at each NCT–NCT interface, since each polymer chain is terminated with a binding group. In other words, the free-polymer-induced lattice compression increases the local binding group density between NCTs by reducing the volume

available to each polymer chain and forcing chains into a tighter packing configuration (Figure 2.2C). The increased hydrogen bonding between particles therefore increases the amount of energy needed to break NCT assemblies into free particles, resulting in an increase in the melting temperature. Based on this, the greater the lattice compression, the greater the expected T_m elevation, and linear polymers would therefore be expected to be the more effective T_m elevating additive.

While this correlation between compression and T_m elevation is seen experimentally at lower polymer concentrations, at high polymer concentrations the reverse is seen—despite exhibiting less compression, the addition of star polymer results in a greater increase in T_m in comparison to the addition of an equivalent amount of linear polymer. This deviation is due to the fact that NCTs are not hard spheres, but rather soft penetrable spheres. In the more commonly studied classic hard sphere Asakura–Oosawa model, entropy contributions are dominated by the balance between reducing the excluded volume of the colloidal hard spheres in favor of increasing the free volume available to the depletant.[232,233] However, in systems with soft particles, it is important to take into account an additional entropic contribution from the conformational entropy of the polymer brush coating.[234,235] While compressing the polymer brush increases the binding group density between NCTs, it also decreases the conformational entropy of the polymer brush, incurring an entropy penalty. Due to the surface curvature of the NCT particle core, there is a maximum binding group density that can be achieved between NCTs, while the entropic penalty continually increases with increased polymer chain compression.[59,75] Thus, once the maximum binding group density has been achieved, further compression will actually reduce the thermodynamic contribution to T_m elevation, as the enthalpic contribution from binding remains constant but the entropic penalty from polymer compression continues to increase.

Based on these factors, the thermodynamic contribution to T_m elevation would be expected to increase, reach a maximum, and then decrease as the concentration of free polymer in solution

Table 2.1. The lattice percent compression, thermodynamic contribution to NCT T_m elevation, and overall NCT T_m elevation upon the addition of free polymer.

Polymer	Polymer Concentration (mg/mL)	Lattice % Compression	Thermodynamic Contribution to T_m Elevation (°C)	Overall T_m Elevation (°C)
26K Linear	25	2.60%	2.3 ± 0.3	8.1 ± 0.4
26K Star	50	3.32%	4.0 ± 0.3	9.6 ± 0.5
26K Linear	50	4.46%	6.3 ± 0.3	10.3 ± 0.4
26K Linear	100	8.92%	7.7 ± 0.3	16.4 ± 0.4
60K Star	200	10.16%	12.6 ± 1.3	41.4 ± 0.4
26K Star	200	11.91%	9.0 ± 3.9	29.9 ± 0.7
61K Linear	200	12.75%	2.8 ± 0.3	30.1 ± 0.4
26K Linear	200	14.28%	0.8 ± 1.3	20.2 ± 0.4

is increased. In contrast, the kinetic contribution to T_m elevation should always increase as the concentration of free polymer in solution is increased, as higher solution viscosity always results in decreased particle diffusion rates, and the overall amount of T_m elevation would still be expected to increase. The thermodynamic contribution to T_m elevation was measured by performing forced-equilibrium melts for polymer concentrations of up to 200 mg/mL (higher concentrations resulted in viscosities that exceeded UV–vis stirring capabilities) (Table 2.1 and Figure S2.6, Supporting Information).

As can be noted in the data, the thermodynamic contribution to T_m elevation increases with lattice compression up to ≈10% compression. Beyond this point, the entropic penalty of polymer chain compression begins to outweigh the enthalpic gain from increased binding group density, and thus the thermodynamic contribution to T_m elevation begins to decrease as lattice compression increases. Since (for the same concentration and molecular weight) star polymers cause less compression than linear polymers, for polymer concentrations that result in lattice compression greater than 10%, the addition of star polymer causes greater NCT T_m elevation than the addition of an equivalent amount of linear polymer. Overall, the total amount of T_m elevation still increases with increasing polymer molecular weight and concentration since the kinetic contribution from reduced particle diffusion rates accounts for the majority of the T_m elevation, outweighing the decrease in the thermodynamic contribution. The corresponding trends that arise from these two factors can be seen in the growing gap between the thermodynamic contribution to T_m elevation and the overall T_m elevation.

Conclusion

NCTs are nanocomposite building blocks that can be readily assembled when suspended in organic solvents, and can further be rapidly organized into ordered lattice structures via gentle thermal annealing. While the thermal sensitivity of NCTs allows for this colloidal crystallization to occur via dynamic reorganization of the supramolecular bonds linking NCTs together, it also represents a processing challenge, as many materials processing methods require temperatures beyond those ordered NCTs in pure solvent can tolerate. By introducing high concentrations of free polymer into solution, the melting temperature of NCTs is elevated through a combination of thermodynamic and kinetic factors in a controllable and readily explainable manner. The addition

of free polymer in solution therefore provides a simple method for reliably increasing the processability of NCTs at higher temperatures without adversely affecting their nanostructural ordering. The observations presented here provide a greater understanding of particle assembly and supramolecular chemistry in viscous environments that are commonly used for the processing of polymer nanocomposites. This knowledge should better enable the incorporation of both ordered colloidal arrays and multivalent supramolecular building blocks in complex, next generation composites and metamaterials.

Chapter 3: Improving Nanoparticle Superlattice Stability with Deformable Polymer Gels

Adapted from the forthcoming work: Lee, M. S.; Kubiak, J. M.; Yee, D. W.; Santos, P. J.; Macfarlane, R. J. Improving Nanoparticle Superlattice Stability with Deformable Polymer Gels.

As the use and study of nanomaterials has grown, so too has interest in nanoparticle self-assembly as a promising strategy for providing control over both composition and particle ordering at the nanoscale in the bottom-up fabrication of complex nanomaterials. Nanocomposite tectons (NCTs) are a class of scalable nanoscale building blocks capable of self-assembly into ordered superlattices in solution through the use of dynamic supramolecular binding interactions. However, while dynamic interparticle interactions are key for enabling reversible binding and preventing kinetic traps during the assembly process, they render assembled structures susceptible to dissociation upon changes in the solution environment. Assembled NCTs can be stabilized against dissociation by removing them from solution, but doing so eliminates the dynamicity that they possess in solution, inhibiting further structure manipulation. Here, we present a method for embedding ordered nanoparticle superlattices into a polymer gel matrix, a medium that stabilizes the embedded arrays against disruption while still allowing dynamic lattice manipulation. Further stabilization can be obtained with complete solvent removal to bind nanoparticle arrays within a solid polymer matrix. This embedding method makes it possible to incorporate ordered colloidal arrays into a polymer matrix as either dynamic or static structures, expanding their potential for use in responsive materials.

Background

A key feature of nanoparticle self-assembly is its ability to precisely control particle organization from the bottom up, making it possible to generate ordered nanomaterials in one-, two-, and three-dimensions.[9,206,236] This precision in material structure formation is typically achieved by using weak interparticle interactions in order to prevent kinetic traps and facilitate particle mobility and rearrangement.[54,71,73,97] While dynamic interactions between particle are crucial for the formation of highly ordered particle arrays, they also make the final structures prone to dissociation upon changes in the environment (e.g. temperature, solvent polarity, ion concentration).[59,70,237,238] This limitation is typically overcome by the use of post-assembly processing methods that either crosslink the particles via less labile interactions (e.g. covalent bonds), or encapsulate them in a more robust material, although a drawback to such methods is the reduction or elimination of particle dynamicity.[98,193] In principle, a crosslinking or encapsulation method that prevented dissociation of the assembly while still allowing for modulation of particle positions during the stabilization process would allow for additional handles to modulate their structural organization. Such materials could either be kept in this state to allow for continued dynamic modulation using the forces applied during the stabilization process, or further processed to lock these new structures into a permanent state. Here, we present a method of embedding ordered nanoparticle superlattices in a crosslinked polymer gel matrix that stabilizes assemblies against lattice dissociation while still allowing for dynamic lattice manipulation. The nanoparticle polymer gel can then be further processed into a solid to obtain a fully stable polymer nanocomposite solid. Together, the solution, gel, and solid states provide a spectrum of dynamicity and stability, expanding the conditions under which ordered nanoparticle superlattices can be assembled and incorporated into functional materials.

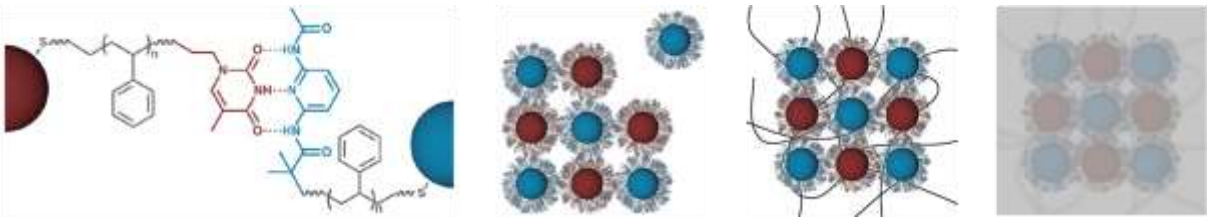

State	Solution	Gel	Solid
Dynamic Ability	High	Intermediate	Low
Stability	Low	Intermediate	High

Figure 3.1. NCTs are nanoscale building blocks that consist of a nanoparticle core grafted with a dense polymer brush terminated with supramolecular binding groups. In solution, NCTs can be reversibly self-assembled into ordered superlattices with gentle thermal annealing and heating. Assembled NCT crystals in solution can then be embedded in a polymer gel for increased stability while still maintaining a degree of dynamicity, or further processed into a polymer solid to fix NCTs in place. Each medium provides a different level of NCT dynamicity and stability and can be used as needed to suit the given processing conditions.

Nanocomposite tectons (NCTs) are nanoscale building blocks that can be self-assembled into ordered nanoparticle superlattices (Figure 3.1).[76] NCTs are composed of 3 distinct parts, containing an inorganic nanoparticle core, a polymer brush, and supramolecular binding groups at the terminus of each polymer chain; each of these components can be independently modified to control the composition and nanoscale organization of the assembled materials.[77–79] The supramolecular binding chemistry that mediates the NCT assembly process uses weak, reversible bonds to allow for easy particle reorganization, allowing NCTs to readily assemble into ordered particle arrays upon thermal annealing (typically at temperatures of ~30-50 °C).[75] However, the types of interactions used in this assembly process (e.g. hydrogen bonding) make the NCT assemblies susceptible to dissociation when heated above these temperatures, or when subjected to stimuli like polar solvents, UV light, or shifts in solution pH. Additionally, NCTs are also

susceptible to uncontrolled collapse upon sudden solvent removal, since solvent plays a structural role in supporting the polymer chains between NCT cores.

To combat this inherent fragility of the ordered NCT arrays, multiple methods have been developed to lock NCT positions in a lattice after the ordered superlattices have formed. For example, by adding free polymer to the solution in which NCT assemblies are suspended, it is possible to significantly elevate the thermal stability of NCTs without adversely affecting their ordering.[81] We hypothesized that this added stability would also make the NCT assemblies less susceptible to dissociation upon introduction of different chemical stimuli, and would therefore permit additional chemical reactions to occur within and around the NCT lattices without disrupting particle organization. Thus, a free polymer with crosslinkable functional groups added to a solution of assembled NCTs could allow for the formation of a gel matrix encapsulating the assemblies. Previous work has shown that such a strategy is possible for DNA-linked nanoparticle lattices, though this prior method relied on electrostatic interactions between the gel matrix and the DNA strands to sufficiently stabilize the particle arrays.[194] A more materials-general method that did not rely on such interactions between the matrix and the particle assembly components could therefore be used in a versatile manner to generate a range of different materials with varied dynamicity of the particle positions. NCTs are ideal for exploration of this kind of encapsulation process, as the composition of the NCT polymer brush and supramolecular group, as well as the solvent in which assembly occurs have been demonstrated to be compatible with multiple material compositions.

Results and Discussion

Experiments were conducted using previously established NCT designs, consisting of a gold nanoparticle core grafted with a dense layer of polystyrene (PS) chains. Each polymer chain was terminated in either a diaminopyridine (DAP) or thymine (Thy) supramolecular binding group; the two binding groups were chosen for their formation of a complementary hydrogen bonding pair (Figure 3.1). To obtain assembled NCTs, complementary DAP NCTs and Thy NCTs were combined in solution to produce rapidly assembled aggregates. These aggregates were heated

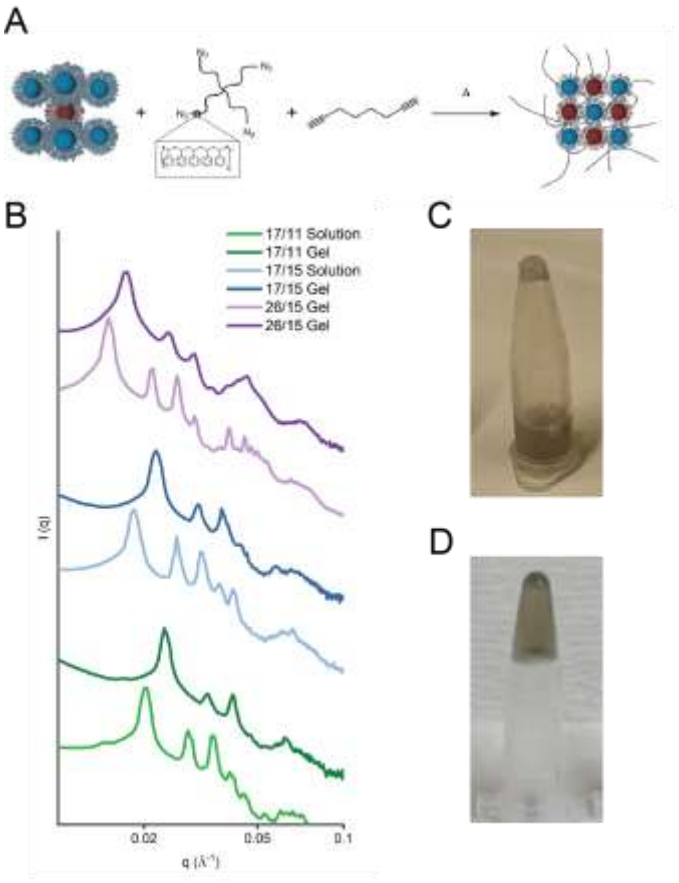

Figure 3.2. A) NCT crystals can be stabilized using CuAAC chemistry to embed NCTs into a crosslinked polymer gel matrix composed of azide-functionalized 4-arm star polymer and a small molecular dialkyne . B) SAXS diffraction patterns of NCTs in solution and embedded within a gel show that the gelation process preserves ordering and can be used with NCTs of varying core size and polymer brush length. NCTs C) pre- and D) post-gelation exhibit the purple color indicative of assembled NCTs.

above and then thermally annealed through their dissociation temperature to allow NCTs to reorganize into ordered body-centered cubic (BCC) superlattices whose ordering can be confirmed using Small Angle X-Ray Scattering (SAXS).[76]

To increase their stability against dissociation, assembled NCTs were embedded into polymer gels using copper(I)-catalyzed azide cycloaddition (CuAAC) chemistry, a click reaction well known for its versatility. The CuAAC reaction provides high yield, little to no byproducts, can be run under a wide range of temperatures, and is compatible with a variety of functional groups.[239,240] Importantly for NCT stability, neither azides nor alkynes, the key functional groups involved in the CuAAC reaction, will interfere with the hydrogen bonding between assembled NCTs. In addition, a variety of copper catalysts and coordinating ligands can be used in the CuAAC reaction, which allows for a catalyst-ligand combination optimized for NCT compatibility. Polydentate nitrogen-containing compounds such as PMDETA and TBTA are common coordinating ligands in CuAAC, used to prevent the formation of unreactive Cu(I) complexes and increase reaction rates by facilitating the coordination of alkyne to copper. CuCl was chosen as the copper(I) source, due to the chemical incompatibility of CuI with gold and the slower reaction rates of CuBr, while non-polydentate triphenylphosphine (PPh_3) was selected as the coordinating ligand to prevent the lone pairs present in nitrogen-containing polydentate ligands from interfering with the hydrogen bonding between DAP and Thy NCTs and disrupting ordering in assembled NCTs.[241]

Azide-terminated 4-arm star PS was used to form the polymer matrix, along with 1,7-octadiyne, a small molecule dialkyne cross-linker (Figure 3.2A). To form the gel, assembled NCTs were mixed with azide-terminated 4-arm star PS, 1,7-octadiyne, and CuCl/PPh_3 in toluene (Figure 3.2C), then heated at 65 °C to yield the NCT polymer gel (Figure 3.2D). The star PS serves a dual

purpose: prior to gelation, it elevates the NCT T_m, and post-gelation, it forms the polymer matrix of the gel, eliminating the need for the addition of extraneous polymer.[81] The ability of free polymer to elevate the thermal stability of assembled NCTs allowed gelation to be run at 65 °C, a temperature greater than the T_m of the NCTs used in these gels, without adversely affecting NCT ordering. Heating at 65 °C significantly reduced gelation times – gels were obtained in 3.5 hours or less, whereas at room temperature gels took 3-5 days to form. This straightforward procedure is not limited to a single NCT design – NCTs of varying core size and polymer length can be embedded into polymer gels using the same gelation process. SAXS shows that NCT lattices in gels exhibit a decrease in the lattice parameter compared to NCTs in solution, but that the ordering quality is retained (Figure 3.2B). The former is indicated by peak shifting to larger q values (corresponding to smaller interparticle distances), while the latter is indicated by peak sharpness. This decrease in the NCT lattice parameter post-gelation is due to solvent loss during the gelation process, as well as compression from the surrounding polymer matrix. In contrast to NCTs in the solution state, where solvent removal causes a loss of ordering from uncontrolled polymer brush collapse, solvent loss does not adversely affect NCTs during the gelation process, as the structural support originally provided solely by solvent is now supplemented by the polymer matrix.

Once embedded in a polymer gel matrix, ordered NCT lattices exhibit improved stability against a variety of external environment changes since, in contrast to ordered NCT lattices in solution, NCT ordering no longer relies exclusively on the weak supramolecular bonds between neighboring particles. Enabling NCT exposure to a wider range of environments while maintaining their stability is key for being able to process NCTs into functional materials, as accessible processing conditions are limited for NCTs in their solution state. For example, assembled NCTs in solution must be kept in nonpolar solvents such as toluene, as polar solvents weaken the

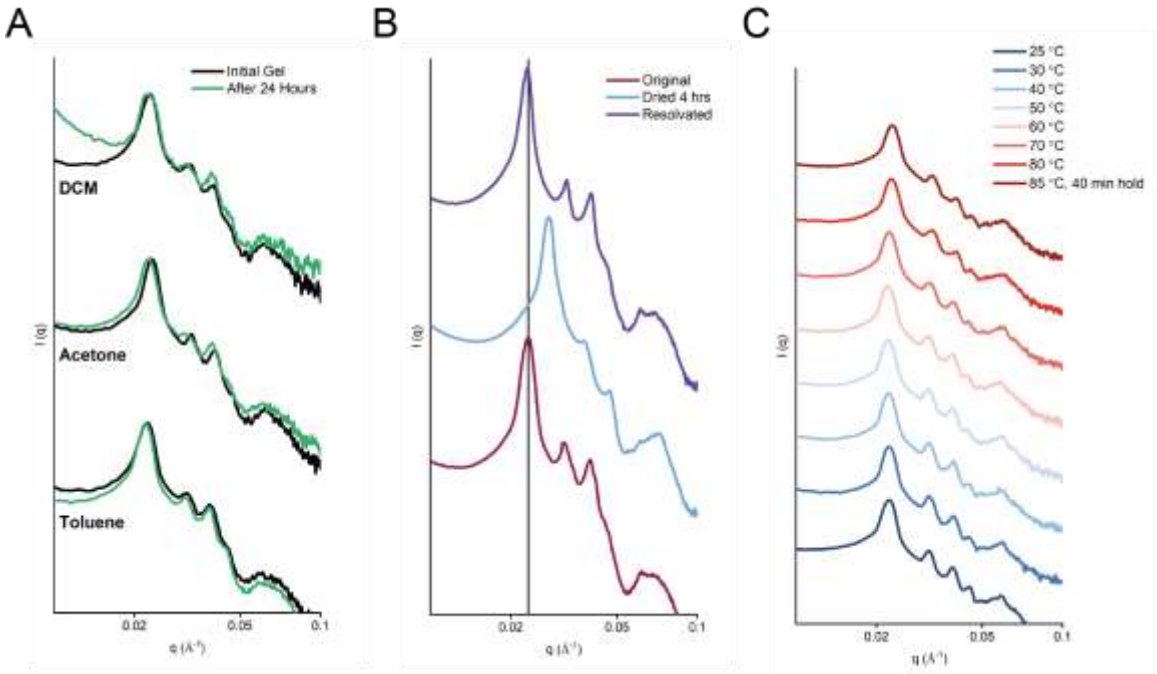

Figure 3.3. SAXS diffraction patterns of NCT polymer gels show that NCTs in polymer gels remain ordered after being A) exposed to polar solvents, B) dried under vacuum and resolvated, and C) heated to 85 ºC. Exposure to each of these external environmental changes would cause NCTs in solution to dissociate, demonstrating that NCTs in polymer gels exhibit improved stability in comparison to NCTs in solution.

hydrogen bonding between complementary DAP and Thy binding groups, causing assemblies to rapidly dissociate into free particles within a few minutes, whereas in a gel, the crosslinked polymer matrix stabilizes NCT assemblies by restricting particle movement to prevent dissociation, even if interparticle bonds are weakened. To demonstrate the resistance of NCT polymer gels to polar solvents, NCT polymer gels originally solvated with toluene were exposed to either toluene (control), acetone, or dichloromethane (DCM) for 24 hours. SAXS of the gels before and after polar solvent exposure (Figure 3.3A) showed that NCT ordering remained present and the lattice parameter unchanged, confirming that the gel embedding process provided increased stability against NCT dissociation in the presence of polar solvent.

In comparison to NCTs in solution, once embedded in polymer gels, NCTs also exhibit less reliance on the presence of solvent to retain ordering. Polymer gels containing NCTs can be

reversibly dried and re-solvated without losing ordering, while NCT crystals in toluene lose ordering upon the removal of solvent. The latter behavior is due to the fact that solvent plays a structural role in NCT lattice ordering – interparticle spacing is determined by polymer brush length, which is in turn determined by the solvent quality and presence. When solvent is directly removed from assembled NCTs in solution, the polymer brush collapses unevenly, resulting in the loss of long-range order. However, this is avoided in NCT polymer gels, as structural support is provided by both solvent and the polymer matrix, with the latter still present to help preserve ordering even after solvent removal. Furthermore, the polymer gel also slows the rate of solvent evaporation during drying, allowing for the NCT polymer brush to collapse more gradually and uniformly to preserve ordering. To demonstrate this, NCTs embedded in a polymer gel were dried under vacuum for 4 hours, then re-solvated, with each step monitored using SAXS (Figure 3.3B). The reduction in the interparticle spacing upon drying was fully recovered after re-solvation, as indicated by the recovery of the q_0 peak to its initial position. Ordering quality was also unaffected by solvent replacement after drying.

The thermal stability of NCTs is also greatly improved upon being embedded into a polymer matrix, even moreso than the T_m elevation seen in solution in the presence of free polymer. In-situ thermal SAXS of an ordered gel was performed to monitor NCT stability at sustained high temperatures (Figure 3.3C). During heating and after 40 minutes of heating at 85 ºC, the NCT lattice quality remained unaffected within the gel. For comparison, a sample of assembled NCTs in solution without any polymer present was heated to 85 ºC, as was an un-crosslinked sample containing the same reaction mixture as the ordered gel but without dialkyne (to prevent gelation) (Figure S3.2). As expected, since they were heated beyond their T_m, the NCTs in solution were completely disassembled at 85 ºC, with no structure factor and only the form factor of the free

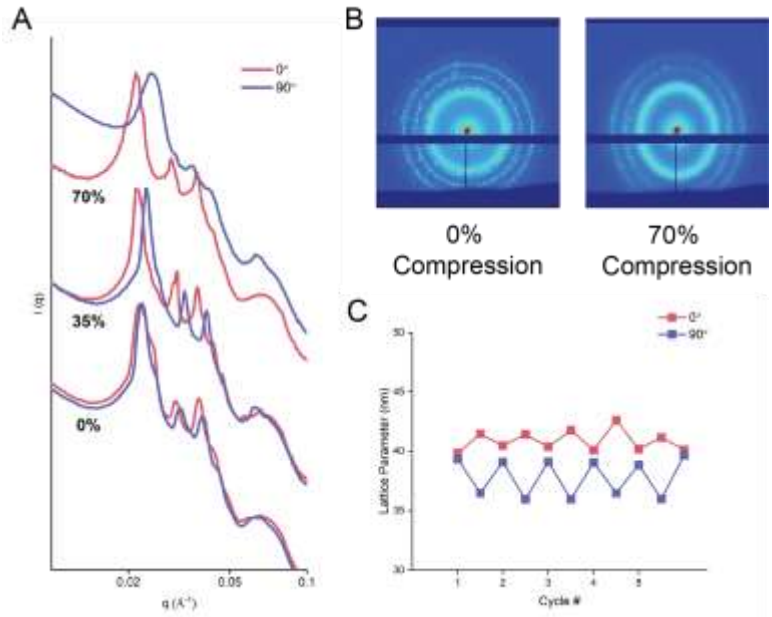

Figure 3.4. A) 1-D SAXS diffraction patterns obtained by sector averaging B) 2-D SAXS scattering data at various stages of compression show how interparticle spacing in orthogonal directions diverges with increasing compression. C) When NCT polymer gels are cycled between 0% compression and 70% compression, interparticle spacing increases in the plane perpendicular to the direction of compression (red) and decreases in the plane parallel to the direction of compression (blue), with spacing in both planes returning to initial values once compressive force is removed.

particles present. While NCTs in the un-crosslinked pre-gel mixture remained assembled at 85 ºC, ordering quality was diminished, as indicated by the weakening intensity and loss of higher order peaks. The improved retainment of NCT ordering in the gel in comparison to in the uncrosslinked pre-gel solution shows that the crosslinked polymer matrix has a positive effect on NCT thermal stability, and that the observed stability at high temperatures is not merely due to melting temperature elevation from the presence of high weight percentages of polymer.

A key advantage of the polymer gel matrix as a stabilizing medium lies not only in the way it improves NCT stability against multiple kinds of external environment changes, but also in its ability to do so without eliminating NCT dynamicity with the complete removal of solvent. This makes it possible to easily and reversibly mechanically manipulate NCT lattices simply by

deforming the surrounding polymer matrix. In contrast, NCTs in the solid state can be handled but lack the dynamicity for reversible mechanical deformation, while NCTs in solution can be reversibly assembled and disassembled, but cannot be easily mechanically manipulated. To study how NCT lattices embedded in a polymer gel responded to compressive force, NCT gels were placed on a linear compression stage and monitored in real-time using SAXS. Initially, before compression, gels displayed a circular 2-D SAXS pattern (Figure 3.4B), showing that lattice spacing was the same along orthogonal axes, as expected for a BCC crystal. As the gel was compressed, NCTs experienced anisotropic deformation. This was reflected in the shift of the 2-D SAXS from a circular to an oval pattern (Figure 3.4B), indicating lattice compression and expansion along orthogonal axes. To further quantify the changes in NCT ordering during gel compression, 2-D SAXS scattering patterns were averaged in sectors to obtain 1-D SAXS patterns at 0° (perpendicular to the direction of compression) and 90° (parallel to the direction of compression) (Figure 3.4A). At 0% compression, the BCC lattice was the same in all directions, and 1-D SAXS patterns for the 0° and 90° sectors overlapped. As the gel was compressed, spacing between particles in the plane perpendicular to the direction of compression was expected to increase (0°), while spacing between particles in the plane parallel to the direction of compression was expected to decrease (90°), corresponding to lattice expansion and lattice compression, respectively. This was seen experimentally as the 1-D SAXS patterns for the 0° and 90° sectors diverged with increasing compression – q_0 values decreased for the 0° sector and increased for the 90° sector, corresponding to increased and decreased lattice parameter values, respectively.

Deformation of the gel and its embedded NCTs was also shown to be reversible. Upon removal of the applied compressive force, NCTs within the gel recovered their initial ordering and spacing, regaining full symmetry and returning from an oval to the original circular 2-D SAXS

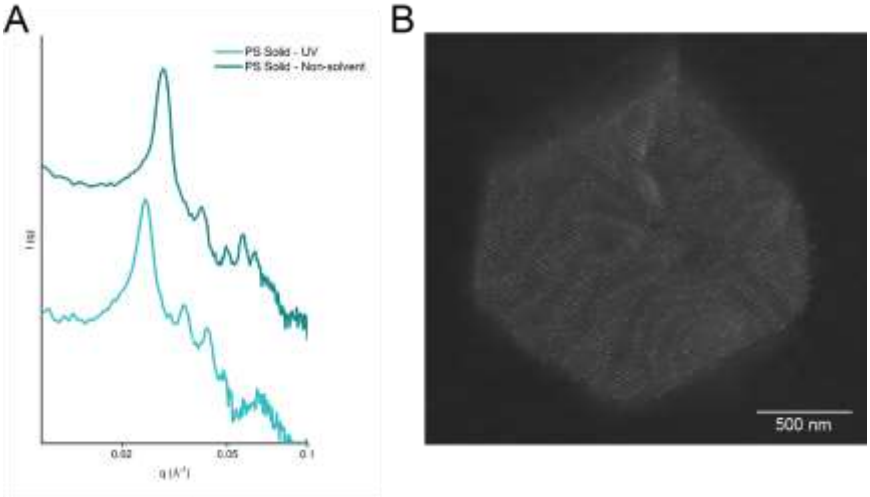

Figure 3.5. A) SAXS of NCT polymer solids prepared from NCT polymer gels show that during the transition from the gel to solid state, embedded NCT crystallites retain their ordering while undergoing a reduction in the lattice parameter. B) SAXS of a single NCT crystal embedded in a polymer matrix shows nanoscale ordering as well as the microscale shape expected of BCC NCT Wulff polyhedra.

scattering pattern. NCT gels were also robust enough to undergo multiple rounds of mechanical compression without permanent deformation. To demonstrate this, an NCT gel was cycled in the linear compression stage between 0% compression and 70% compression for 5 rounds, and the lattice parameter measured in orthogonal directions (Figure 3.4C). As compressive force was alternately applied and removed, lattice parameter values in orthogonal directions diverged and returned to initial values correspondingly. Thus, embedding NCTs within a gel provides multiple benefits – assembled NCTs are not only stabilized against polar solvents, uncontrolled solvent loss, and high temperatures, they can also be reversibly mechanically deformed to obtain anisotropic crystal lattices.

Once NCTs are embedded within a polymer gel, they can be further processed into a solvent-free form to obtain a fully stable ordered nanocomposite solid. Transitioning from the gel to solid state without disrupting NCT ordering can be done by two different methods, either by replacing the solvent within the gel with additional polymer, or by controllably removing the

solvent contained within the gel. The former was achieved via photopolymerization while the latter was achieved by solvent exchange with a non-solvent.[80] In the photopolymerization solidification process, gels were soaked in monomer to allow monomer diffusion into the gel, followed by exposure to UV light (254 nm) to photopolymerize the monomer within the gel into a polymer solid. In the non-solvent exchange process, a non-solvent for the polymer was gradually introduced to expel toluene from the gel, leaving a polymer solid. The photopolymerization method prevents NCT disruption from the loss of solvent by replacing the volume originally occupied by solvent with additional polymer to prevent NCT polymer brush collapse. In contrast, the non-solvent exchange method prevents NCT disruption by gradually eliminating the volume originally occupied by solvent, allowing enough time for both the polymer matrix and the polymer brush on the NCTs to contract without losing ordering. As expected, due to the greater reduction in total volume with the non-solvent exchange method in comparison to the photopolymerization method, NCT polymer solids obtained using the using the non-solvent exchange method exhibited a smaller interparticle distance than NCT polymer solids obtained using the photopolymerization method (Figure 3.5A). Once in solid form, NCTs are locked into place within the polymer matrix, free of solvent and fully stabilized against dissociation. The solid form, in addition to providing full stabilization, also enables the use of characterization methods that require a solvent-free state, such as scanning electron microscopy (SEM), making it possible to visually confirm the nanostructure of NCTs embedded within the polymer solid (Figure 3.5B). As a final note, while all polymer gels and solids were done using PS in this paper, the CuAAC gelation, photopolymerization, and non-solvent methods are general enough to be used to generate polymer gels and solids of other composition, such as PnBA (Figure S3.3).

Conclusion

The thermal sensitivity of NCTs in solution allows them to be readily and reversibly assembled, with gentle thermal annealing, into ordered nanoparticle superlattices. While this thermal responsiveness is useful for facilitating dynamic bond reorganization during the initial NCT assembly process, it becomes a detriment in subsequent processing of the assembled nanostructures, as it limits the maximum temperature that assembled NCTs can be exposed to without losing their ordering. Incorporating NCT crystals into a polymer gel matrix provides a simple method for greatly improving the thermal and chemical stability of assembled NCTs while still preserving a degree of dynamicity in the embedded nanocrystals. This makes it possible to not only heat assembled NCTs beyond their T_m without losing their ordering, but also to reversibly deform NCT crystals and manipulate their interparticle spacing simply by deforming the surrounding polymer matrix, neither of which can be done when the crystals are in solution. Removing the remaining solvent in the gel results in an ordered polymer nanocomposite solid, with NCT crystals locked in place within the polymer matrix. These three environments – solution, gel, and solid –allow assembled NCTs to exhibit a spectrum of dynamicity and stability, making it possible to expand the conditions under which NCT crystals can be processed after their initial assembly in solution. The ability to incorporate ordered colloidal arrays as either dynamic or static structures within a polymer matrix are a step towards the use of these nanomaterials in advanced composites, and also introduces their potential as for smart, responsive materials.

Chapter 4: Reversible Diffusionless Phase Transitions in 3D Nanoparticle Superlattices

Adapted from the forthcoming work: Yee, D. W.*; Lee, M. S.*; An, J.; Macfarlane, R. J. Reversible Diffusionless Phase Transitions in 3D Nanoparticle Superlattices.

The ability to control both the chemical composition and spatial ordering of materials from the bottom up is a key aim in the development of nanoparticle self-assembly systems. Nanocomposite tectons (NCTs) are a class of nanoscale building blocks capable of self-assembly whose components can be independently modified to obtain ordered nanoparticle superlattices of varying composition and structure. In this work, we introduce a small-molecule linker, compatible with existing NCT chemistries, to drive the self-assembly of a unary NCT system into face-centered cubic (FCC) superlattices. By changing the quality of the solvent, these assemblies can undergo a reversible martensitic FCC to body-centered cubic (BCC) phase transition. The phase transition is thermoreversible and can be kinetically suppressed, allowing both polymorphs to be obtained in the solid form. BCC superlattices were observed to maintain the same crystal habit as the parent FCC phase, but exhibit significant transformation twinning, similar to that seen in martensitic alloys.

Background

Nanoparticle superlattice (NPSL) crystallization processes have often been guided by chemical intuition derived from the formation of traditional bulk or atomic crystals.[55,56,242] As such, chemical concepts that guide atomic crystal formation can often be directly analogized to structural features in NPSL synthesis.[243–246] The successful use of concepts from atomic crystallization to

describe and predict the stability of NPSL crystal types suggests that similar concepts detailing more complex aspects of crystallization like microstructure formation or dynamic phase transitions could also be used to guide more sophisticated NPSL design. If such analogies indeed extended beyond simply the prediction of stable lattice unit cells, fundamental investigations of NPSL structures with higher-order structural control could potentially serve as useful models to provide generalizable insight into the mechanisms through which crystals generate defects or alter their symmetry. Moreover, because microstructural features in atomic lattices are often produced via the use of different processing conditions or the application of external stimuli to modulate material structure[247–249], methods to dynamically alter NPSL packing in an analogous manner could be a direct route to investigating these phenomena in nanoparticle assemblies. Nevertheless, techniques to induce alterations to NPSL packing post-assembly remain limited, with only a few examples of controllable NPSL phase transitions in the literature.[246,250–253] NPSL assembly methods that provide design handles that enable post-synthetic tailoring of material design factors beyond just crystal symmetry or habit are therefore critical for advancing the field.

Here, we report the synthesis of a single component NPSL that is capable of exhibiting a diffusionless phase transition between a face-centered cubic (FCC) and a body-centered cubic (BCC) structure when the solvent quality is changed. Importantly, these structural changes are rapid, fully reversible, and appear to proceed through an order-to-order crystal transition that induces unique microstructural features analogous to those observed in atomic martensitic transformations. Thus, NCTs provide both a unique method for rapid phase change NPSLs and for fundamental study of crystal defect formation in a generalizable manner.

The building blocks for these NPSLs are the recently developed nanocomposite tectons (NCTs). NCTs are polymer brush coated nanoparticles that have supramolecular recognition

groups at the polymer chain-ends; reversible, multivalent interactions between these groups direct the NCTs to assemble into NPSLs, where their crystal structure is determined by the configuration that balances the favorable enthalpic contributions from forming supramolecular linkages and the disfavorable conformational entropy penalties incurred from restricting polymer chains upon forming a linkage.[75,76,79,254] Previous NCT assemblies have predominantly used binary systems where each NCT in the binary pair contained a supramolecular group that was complementary to the opposite NCT.[76,79]

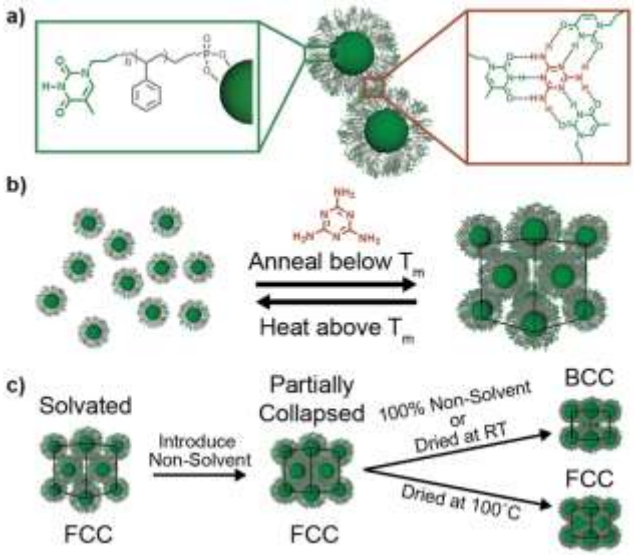

Figure 4.1. A) Nanocomposite tectons (NCTs) are polymer grafted nanoparticles that have a supramolecular recognition group at the chain end. Melamine (brown) is used to mediate the association of thymine (green) functionalized NCTs. B) On annealing, the thymine-melamine NCTs assemble into FCC crystals. C) These crystals exhibit an FCC to BCC phase transition when non-solvent is introduced but rapid removal of the solvent can kinetically trap the FCC phase.

Here, a new, unary NCT system is presented that is capable of forming ordered crystallites by functionalizing particles with thymine (Thy)-terminated polymer brushes and then using melamine (MA), a small molecule capable of bridging multiple Thy molecules[255], to assemble them into NPSLs (Figure 4.1). Because all particles should be able to form MA-mediated hydrogen bonding interactions with one another, an FCC lattice is predicted to be the thermodynamically

preferred arrangement of Thy-MA mediated NCT assembly, as it should maximize the number of nearest neighbors for each NCT, and thus maximize the potential for forming hydrogen bonds.

Results and Discussion

To test this hypothesis, Thy-NCTs were prepared using two sizes of iron oxide nanoparticles (10nm and 24nm) and three molecular weights of Thy-functionalized polystyrene (PS) chains (8kDa, 10kDa, 13kDa) (Figure S4.1). When MA was added to the Thy-NCTs in toluene, a good solvent for polystyrene, rapid assembly was observed (Figure S4.2), which upon thermal annealing formed NPSLs with the predicted FCC symmetry, as confirmed by small-angle X-ray scattering (SAXS) (Figure 4.2 and S4.3).

When NCT assembly occurs, however, it is important to note that the formation of enthalpically favored hydrogen bonds between particles also significantly restricts the motion of these linked polymer chains, inducing an entropic penalty. The most stable arrangement of NCTs must therefore balance the favorable enthalpic and disfavorable entropic factors that result from the formation of supramolecular linkages. The entropic penalty should in principle depend heavily on the initial conformation of the polymer brush, and thus could be significantly altered via design handles that altered brush configuration. One such example would be transferring NCT assemblies from a good solvent to a non-solvent for the polymer chains, which has been shown to significantly decreases the crystallites' lattice parameters due to collapse of the polymer brush.[80] In similar nanoparticle systems using DNA or small molecule ligands to guide assembly, alterations to design factors that affected ligand entropy without significantly altering the enthalpy of ligand interactions have shifted the relative importance of these two thermodynamic parameters, resulting in the formation of different crystalline phases. While these prior methods required separate

ligands to achieve different crystal phases, we hypothesized that the reversible alteration to polymer brush configurations observed for NCTs transferred between different solvents may allow for dynamic switching between different crystalline symmetries.

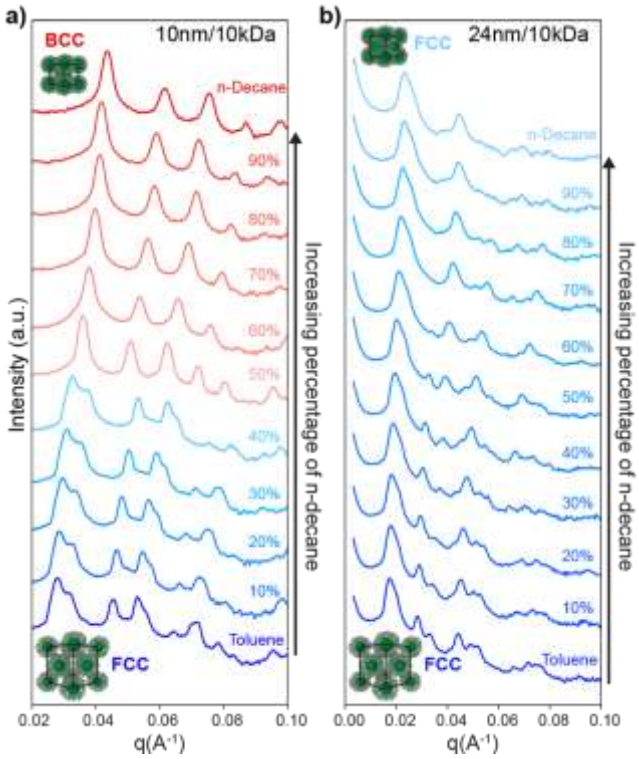

Figure 4.2. A) SAXS data showing the phase transition of the 10nm/10kDa assemblies from FCC (blue) to BCC (red) as a function of n-decane vol%. B) SAXS data showing that the larger 24nm/10kDa assemblies remained FCC (blue tones) throughout the collapse process.

To determine if a phase transition would occur when the solvent quality was changed, n-decane, a non-solvent, was gradually introduced to the assembled Thy-MA FCC NPSLs. In solutions with up to 40 vol% n-decane, the 10nm/10kDa NCT assemblies were observed to exhibit FCC symmetry with decreasing interparticle spacing (Figure 4.2A, blue traces, the other 10nm systems are shown in Figure S4.5), indicative of polymer brush collapse as noted in previous systems.[80] However, above 40 vol%, the diffraction pattern clearly changed to reflect that of a BCC structure (Figure 4.2A, red traces), indicating that the NPSLs underwent an FCC-to-BCC

phase transition. This FCC-to-BCC transition has been previously observed in NPSLs formed via evaporation-driven assembly[256–259], but has not been observed in systems with strong enthalpically-driven binding interactions between particles.

A closer inspection of the 10nm/10kDa NCTs at smaller n-decane vol% intervals around the observed transition point revealed FCC and BCC coexistence points at approximately 48 vol% n-decane with no readily observable disordered phase intermediate (Figure S4.6, similar coexistence points are seen for the other 10 nm assemblies); these experiments occurred ~25 °C below the melting transition of the NCTs, meaning that no thermal annealing was possible during this transition. Taken together, the SAXS data suggest that the phase transition is a diffusionless, order-to-order transformation, which is highly uncommon in NPSL assembly. Additionally, the lack of a body-centered tetragonal (BCT) phase also indicates that the transformation did not proceed via the Bain pathway[260], as observed in some other systems[256,259].

The fact that the phase transition only occurs after a certain vol% of the non-solvent is introduced is consistent with the hypothesis that interactions between polymer ligands (and not just the hydrogen bonding groups) can be used to drive the transformation. As the polymer chains collapse with decreasing solvent quality, the conformational entropy of the chains decreases. It is thus likely that when the loss in chain conformational entropy becomes too large, the FCC to BCC transition occurs to minimize the overall entropy loss of the system. This increase in configurational entropy would be expected to occur because the more open lattice of the BCC phase allows the ligands to sample more of the configurational space, and thus have a higher packing entropy, as suggested by existing computational and theoretical studies.[261,262] Furthermore, the more spherically symmetric BCC Wigner-Seitz cell has been theorized to have less of an entropic penalty on the conformations of ligand distribution[263].

In analyzing these systems, the attractive Van der Waals (VDW) interactions between the 10 nm iron oxide cores were ignored because the long polymers effectively screen some of those interactions.[78,264] As such, the supramolecular linkages and the interactions between the polymers drives the assembly and dictates the crystal symmetry. With larger core sizes, the NCTs should behave more like hard spheres with the VDW interactions dominating and favoring close-packed structures.[264–266] As expected, the larger 24 nm Thy-MA NCT assemblies formed FCC structures when assembled in toluene and maintained that symmetry even in n-decane (Figure 4.2B and S7).

Given that polymer-solvent interactions often become more favorable at higher temperatures, we hypothesized that the phase transition should be thermoreversible. Structural changes to BCC-ordered 10nm/10kDa Thy-MA NCT assemblies near the transition point (50 vol% n-decane) were thus observed as a function of temperature via in-situ thermal SAXS. The NCT assemblies remained BCC until 60 °C, where a phase transition occurred and both BCC and FCC phases were detected (Figure 4.3A and S8). Upon further heating, NCT assemblies transformed completely to FCC, confirming that the phase transition was indeed thermoreversible. Holding the FCC assemblies at 110 °C for 60 minutes resulted in no change to the crystal structure, indicating that FCC was the equilibrium phase at this temperature. Interestingly, cooling the assemblies back to room-temperature (RT) did not result in an immediate transformation back to BCC (Figures 4.3A, B). The fact that the d-spacing of the RT assemblies immediately after cooling (21.7 nm) was larger than that of the initial structure (21.1 nm) suggested that the FCC phase was kinetically trapped. Indeed, the FCC phase transformed almost completely back to the BCC phase within ~24 hours at 25 °C (Figure 4.3B). The 10nm/8kDa and 10nm/13kDa assemblies also exhibited similar thermoreversible phase transitions (Figures S9-10). Replacing the non-solvent with a good solvent also reversed the phase transition back to the FCC phase (Figure 4.3C and

S11), consistent with the fact that the transformation is governed by the degree of polymer-solvent interactions.

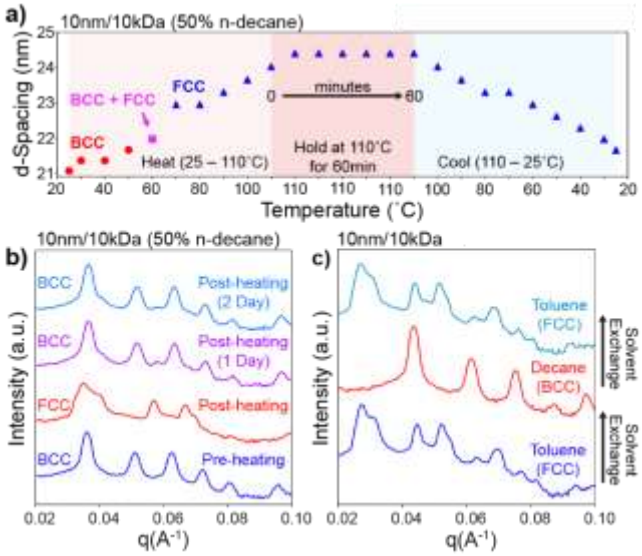

Figure 4.3. d-Spacing and crystal symmetry of the 10nm/10kDa assemblies in A) 50 vol% n-decane. B) SAXS data showing the reversion of the kinetically trapped FCC phase post-heating back to the equilibrium BCC phase within one day at RT. C) SAXS data showing that the phase transition is reversible with respect to solvent quality.

Because FCC to BCC transitions in atomic systems often occur via the formation of different microstructural features, we hypothesized that similar features might be governing this unusual and uncommon order-to-order nanoparticle superlattice transition as well. Because SAXS does not allow for direct imaging of microstructure, dried solids were prepared for microscopy analysis using modifications to previously established techniques to ensure that the FCC and BCC arrangements observed in SAXS were retained prior to imaging (see SI for additional discussion).

Scanning electron microscopy (SEM) imaging of the dried FCC NPSLs revealed faceted single crystals with habits similar to those observed for atomic FCC nanocrystals with stacking faults[267,268] (Figures 4.4B and S14-18), which is consistent with the fact that the NPSLs contained numerous stacking faults and twins (Figure S4.14-18). Notably, multiply twinned structures with

five-fold symmetry elements, a hallmark of FCC materials[49,269], were also observed (Figure 4.4C). Close-packed (111) planes could be observed on the surfaces of the FCC crystals (Figure S4.14-18).

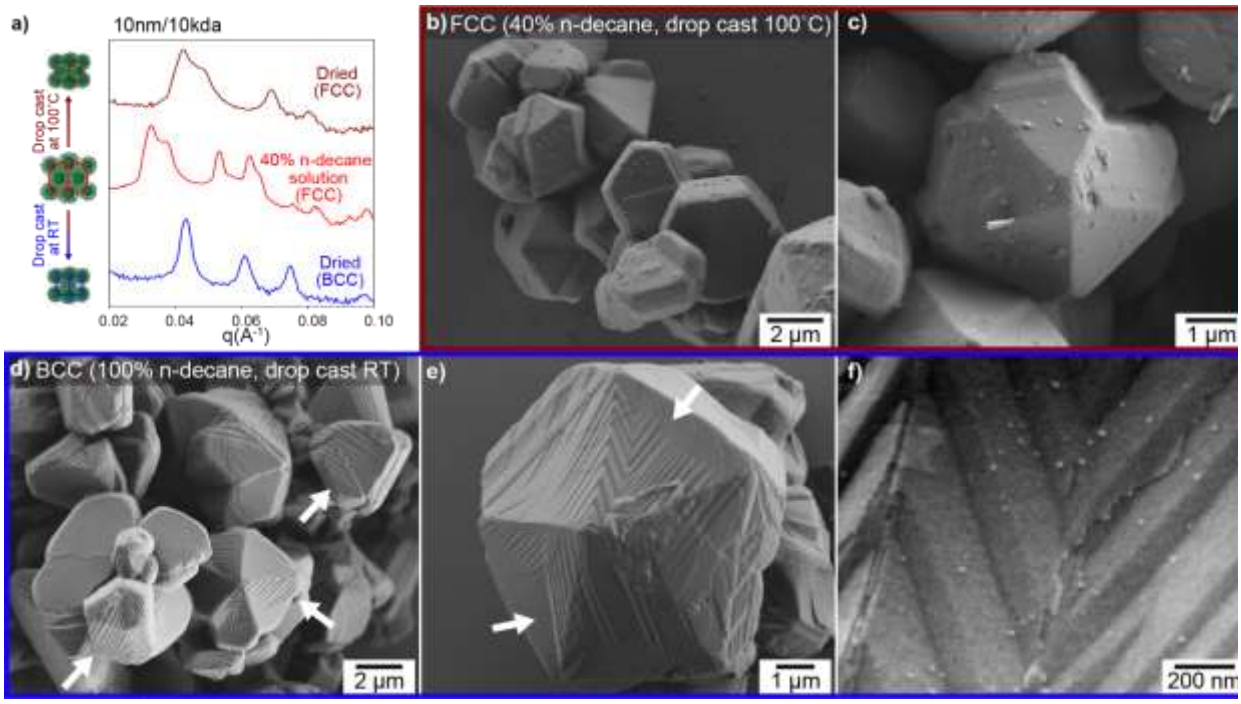

Figure 4.4. A) SAXS patterns of partially collapsed 10nm/10kDa FCC assemblies that are dried using different methods. B) SEM images of kinetically trapped 10nm/10kDa FCC crystals that show C) multiply twinned structures. SEM images of 10nm/10kDa BCC crystals that were D-F) drop cast after being in n-decane for two months. White arrows denote the transformation twins. F) High-resolution image of the transformation twins.

Interestingly, the BCC structures were also single crystalline and exhibited the same crystal habits as the FCC lattices. This lack of change in crystal habit is consistent with a diffusionless phase transition process that occurs without annealing, as a diffusionless method would not easily permit long-range motion of particles to re-shape the crystal habit. However, a significant number of twins could now be observed on the facets of these crystallites that were twin-free in the FCC assemblies (Figures 4.4D, E, and S19-22). These twins are remarkably similar to those observed

in twinned martensitic alloys[260,270], which suggests that the twins here were formed to relieve the strain associated with the phase transition. Phase transitioned BCC assemblies left in decane for two months prior to drying were qualitatively observed to exhibit more transformation twins as compared to the BCC assemblies immediately drop cast from 40 vol% n-decane, suggesting a kinetic aspect to their formation (Figure S4.20-21). As multiply twinned structures are typically only observed in FCC or diamond cubic crystals[271], the presence of multiply twinned BCC crystals that exhibit significant transformation twinning further confirms the martensitic diffusionless, order-to-order nature of the phase transition from the FCC phase (Figures 4.4E, F, and S23). The 10nm/8kDa and 10nm/13kDa phase-transitioned crystals also exhibited similar microstructural features (Figures S20-23). These transformation twins have not been previously observed in NPSLs and are likely due to the attractive supramolecular linkages between the NCTs hindering particle rearrangement. The exact mechanism for the formation of these transformation twins is the subject of a future investigation but their presence indicates that NCTs may indeed be ideal models for the observation and investigation of microstructural changes in crystalline systems, providing valuable information that could be generalized to other crystallization processes.

Conclusion

In conclusion, we have demonstrated a single-component NCT system that is capable of undergoing a reversible diffusionless FCC to BCC phase transition. Phase transitioned BCC structures were observed to exhibit the same crystal habits as their parent FCC phase, but were accompanied by significant amounts of twinning, similar to that seen in martensitic alloys. Given the importance of phase transitions and twinning in atomic materials, the ability to replicate them

in NPSLs represents a step forward in not only understanding their formation, but also in being able to control their appearance, which should better enable the engineering of complex materials.

Chapter 5: Using Solvent Quality to Drive Nanoparticle Self-Assembly

Background

Nanoparticle self-assembly is a powerful tool for generating ordered nanomaterials, and a field that has developed a wide variety of stimuli to mediate the assembly process.[9,206,236] One such method is solvent-mediated self-assembly. In recent years, advances in ligand chemistry as well as a greater understanding of the role of ligand-solvent interactions in colloidal assembly have made it possible to expand beyond using solvent to toggle between the dispersed and aggregated states, and have led to the development of various solvent-mediated self-assembly methods for generating ordered assemblies.[237,258,272,273] Here, we present a solvent-mediated self-assembly method for making ordered NCT crystallites, where neither supramolecular binding groups nor thermal annealing is required to assemble NCTs into ordered FCC superlattices at ambient temperatures (Figure 5.1). By eliminating the need for supramolecular binding groups, we greatly simplify the synthetic procedure for the NCT polymer brush. Using solvent to mediate the assembly structure also introduces an additional handle for modifying NCT structure without needing to modify NCT chemistry.

Nanocomposite tectons (NCTs) are nanoscale building blocks that can be self-assembled into ordered nanoparticle superlattices (Figure 2.1).[76] NCTs are composed of 3 distinct parts containing an inorganic nanoparticle core, a polymer brush, and supramolecular binding groups at the terminus of each polymer chain; each of these components can be independently modified to control the composition and nanoscale organization of the assembled materials.[77–79] The greater the number of available materials and binding chemistries, the greater the versatility of NCTs as a

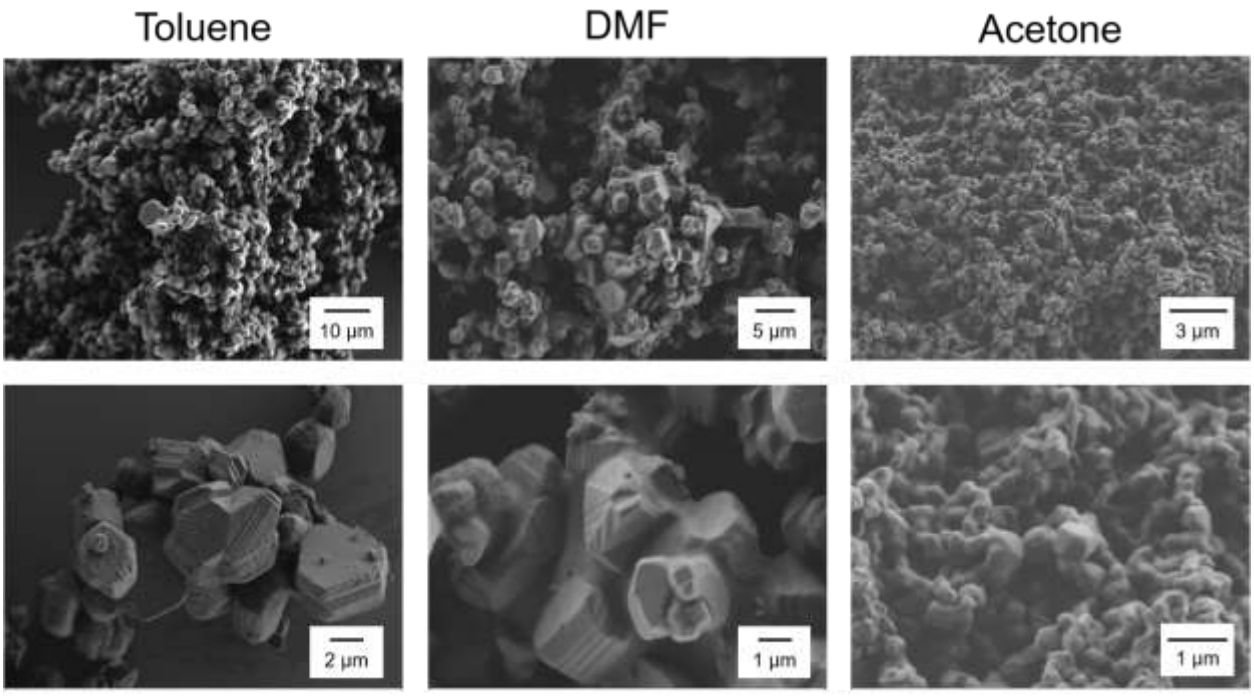

Figure 5.1. NCTs assembled in toluene (left), DMF (center), and acetone (right). NCTs in all three solvents underwent a phase transition during the collapse process, and exhibit the expected twinning caused by transitioning from FCC to BCC while maintaining the FCC crystal habit. NCT crystallites assembled in acetone are the smallest and show the least faceting, due to the very fast rate of assembly (minutes) in comparison to toluene (hours) and DMF (~1 day).

practical self-assembly system. Ideally, the materials and chemistries used in NCTs would be simple to synthesize and scale up so as to increase their viability for use in functional materials.

Results and Discussion

Experiments were conducted using previously established NCT designs, consisting of an iron oxide (IO) nanoparticle core grafted with a dense layer of polystyrene (PS) chains, with each polymer chain terminating in a diaminopyridine (DAP) group. Of the existing NCT binding groups, DAP was selected for initial tests due to its lack of self-complementarity (unlike thymine (Thy)), thus ensuring that no assembly would occur as a result of binding group interactions.

To establish a baseline for the stability of IO NCTs in solvents of varying polarity and quality for polystyrene, DAP IO NCTs were prepared in solutions of toluene, tetrahydrofuran (THF), acetone, dimethylformamide (DMF), and decane, then monitored for assembly over a span of 5 days using Small Angle X-Ray Scatttering (SAXS) (Figure S5.3). As expected, NCTs remained suspended in solution for both THF and toluene, both of which are good solvents for PS, and rapidly precipitated to form an amorphous aggregate in decane, a nonsolvent for PS. Interestingly, NCTs not only assembled into face-centered cubic (FCC) crystals in DMF (Figure 5.2) after 1 day, over the course of 5 days, NCTs underwent a phase transition from FCC to body-centered cubic (BCC), along with a decrease in the interparticle spacing, similar to the order-to-order FCC-BCC phase transition exhibited by the Thy-mel NCT system with the introduction of nonsolvent (see Chapter 4).

This assembly behavior is unlikely to be due to the presence of DAP binding groups, as both the polarity of the DMF and the non-self-complementarity of DAP would prevent binding. However, to confirm that NCT assembly in DMF was not driven by binding group interactions, additional samples using different NCT binding groups were prepared in DMF and monitored over 5 days with SAXS (Figure 5.2). Regardless of the type of binding group present – DAP, Thy, DAP and Thy – or if a binding group was even present, all IO NCTs in DMF assembled first into FCC structures, then underwent a phase transition to a BCC structure. Had binding groups been dictating the assembly behavior, Thy NCTs should have remained FCC, the mixture of DAP and Thy NCTs should have resulted in BCC crystals, and the NCTs without any binding groups should not have assembled at all.[76] Thus, binding chemistry is ruled out as the driving force behind NCT assembly in polar solvents.

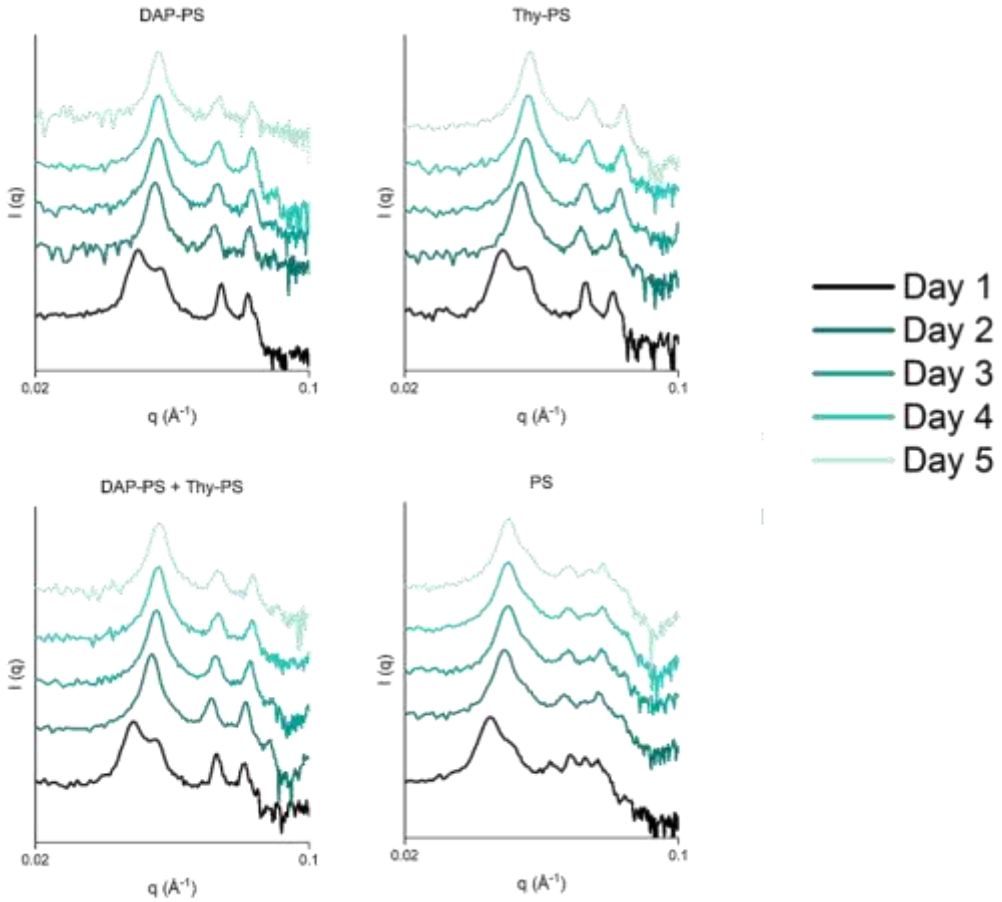

Figure 5.2. 10 nm IO NCTs in DMF were monitored with SAXS over a five day period. NCTs initially assemble into FCC structures, followed by a transition to BCC along with a reduction in the interparticle spacing, regardless of the binding chemistry present, confirming that the DAP and Thy supramolecular binding groups are not directing assembly. Given the polarity of DMF, this is to be expected. NCTs functionalized with PS without binding groups also assembled, further confirming that binding chemistry is not the reason for assembly. The title of each graph indicates the NCT polymer composition(s) used.

To further determine the extent to which and how NCTs assemble in polar solvent, DAP IO NCTs assembly behavior was also monitored in acetone, a solvent that, like DMF, is polar and a relatively good solvent for PS, although not as good a solvent as toluene or THF. Typically, IO NCTs are purified with multiple centrifugation rounds in toluene (see SI), with a final resuspension in toluene. To prepare NCTs in another solvent, one can either directly resuspend NCTs in the solvent of choice after NCTs have been spun down in the final purification centrifuge cycle in

toluene, or run an additional centrifugation cycle in the solvent of choice before the final resuspension to ensure full toluene removal. Interestingly, while no difference was seen between either protocol for NCTs in good solvents (particles were easily resuspended after centrifugation), NCTs following the former protocol remained stable in acetone, while NCTs that had been centrifuged in acetone formed a dense pellet that required sonication to break up, after which NCTs visibly assembled in minutes to form stable FCC crystallites (Figure S5.3, Figure 5.3).

Given the results above, it was hypothesized that magnetic interactions between IO cores could be the driving force behind NCT assembly in polar solvents. Centrifuging IO NCTs in acetone concentrates them into a dense pellet, resulting in a much smaller interparticle distance compared to when particles are dispersed in solution. This forced particle aggregation is important from the magnetic perspective as dipole-dipole coupling between IO NCTs that are well-dispersed in solution is too weak to induce aggregation. However, at reduced interparticle distances the strength of the magnetic dipole coupling between neighboring particles becomes strong enough to strengthen any existing assembly.[78] To test this hypothesis, Au NCTs were processed in acetone using the same centrifuge-sonicate protocol as for IO NCTs and monitored with SAXS (Figure 5.3). Au NCTs assembled into stable FCC structures in acetone, disproving the hypothesis that magnetic interactions are the driving force behind NCT assembly in polar solvents, as no such interaction is present when the core material is gold. Au NCTs did assemble at a slower rate in comparison to IO NCTs, thus it is likely that magnetic interactions facilitate further assembly once a critical interparticle distance has been reached, but the ability of Au NCTs to assemble in acetone eliminates magnetic interactions as the primary driving force behind assembly in polar solvents.

Having ruled out binding chemistries and magnetic interactions in the elucidation of the assembly mechanism, given the clear effect that solvent quality had on the stability of NCTs in

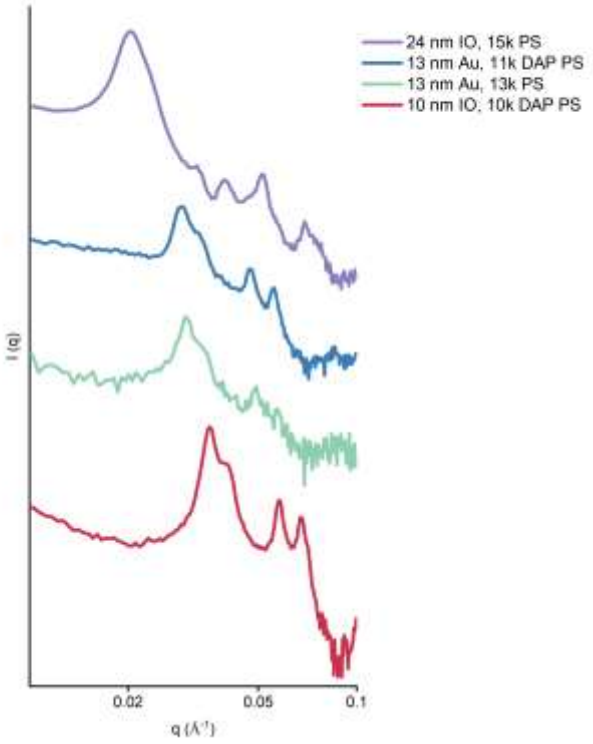

Figure 5.3. IO and Au NCTs of varying particle and polymer compositions were all successfully assembled into FCC superlattices in acetone. Both gold and iron oxide nanoparticle cores were used, as well as polymer brush with and without functional groups, demonstrating the versatility of this assembly method. Unlike in DMF, NCTs assembled in acetone did not undergo a phase transition from FCC to BCC, remaining FCC over the 5-day monitoring period.

solution (Figure S5.3), ligand-solvent interactions were the next focus of study. It is well-established that for functionalized nanoparticles, ligand-solvent interactions are key for achieving colloidal stability and controlling nanoparticle stability.[236,264] To isolate the effect of the NCT polymer brush on NCT assembly, "bare" (oleic acid-capped) IO nanoparticles without polymer functionalization were subjected to the same solvent and centrifuging protocols and monitored for assembly. Nanoparticles either remained suspended in solution or immediately aggregated and precipitated out of solution, but no ordered assembly was observed, confirming that the polymer brush is necessary for the ordered NCT assembly observed in DMF and acetone.

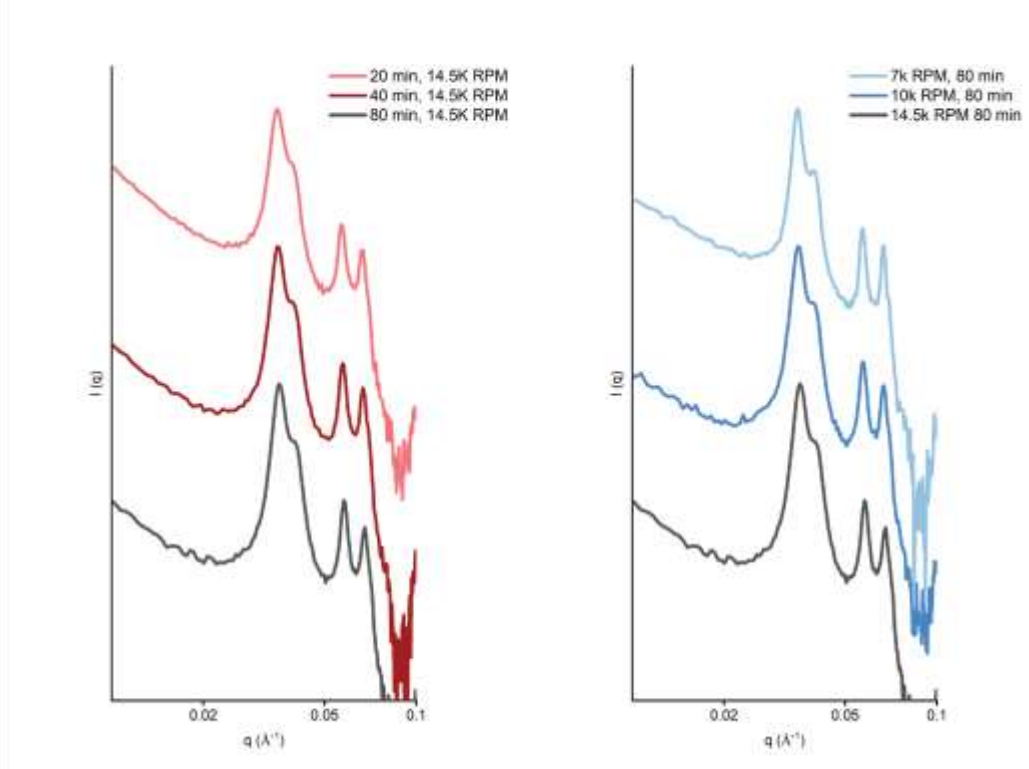

Figure 5.4. 10 nm IO NCTs functionalized with 10 kDa DAP-PS were centrifuged in acetone at varying rates and times to study the effect of centrifuging on the final nanostructure. (Left) NCTs centrifuged at a fixed rate (14.5K RPM) and varying times showed no difference in the nanostructure – all samples formed FCC crystals of the same quality. (Right) Centrifuging NCTs at a fixed time (80 minutes) and varying the centrifuging rate reduced the final NCT yield, as more particles remained suspended in solution, but also had no effect on the nanostructure quality.

Polymer-solvent interactions in colloidal systems are a balance between various factors, among them the enthalpic favorability of polymer-solvent interactions versus polymer-polymer interactions and entropic considerations from the degree of polymer conformational freedom. In a good solvent, polymer-solvent interactions are enthalpically favored and polymers swell with solvent. In a poor solvent, polymer-solvent interactions are enthalpically disfavored and polymers collapse to maximize polymer-polymer contact and expel solvent. Thus, in a good solvent, without the presence of binding groups to drive assembly, the polymer brush is nicely solvated and NCTs remain dispersed in solution. In contrast, in a poor solvent, the polymer brush collapses, resulting

in NCTs aggregating and precipitating out of solution without any opportunity to rearrange into ordered structures. Between these two extremes lies what might be called an "intermediate solvent," one in which NCTs are stable enough to not immediately precipitate out of solution, but also not so stable that they remain fully dispersed. Such conditions make it possible for NCTs to assemble into ordered structures, as seen in DMF and acetone. To quantify the solvent quality, we can compare the lattice parameters of NCT crystals in different solvents composed of NCTs of the same core size and polymer molecular weight (Table 5.1). NCTs in toluene (a good solvent) have the largest lattice parameter, while NCTs in decane (a poor solvent) have the smallest lattice parameter, with NCTs in the other three solvents and solvent blends falling in between those two, as expected for "intermediate" solvents.

In addition to involving polymer-solvent interactions, solvent-mediated NCT assembly in acetone involves centrifugation to achieve the initial aggregation. To study the effect of centrifuging conditions on the final nanostructure, IO NCTs were centrifuged at varying spin rates (7-14.5K RPM) and times (20-80 min) before sonication and assembly (Figure 5.4.). While shorter or lower rate centrifuge protocols resulted in lower yield (more NCTs remained in the supernatant), SAXS showed no difference in the nanostructure, with all 5 samples showing FCC crystals of the same quality and structural parameters (Table S5.3), indicating that NCTs in acetone are tolerant of a range of centrifuge processing conditions, eliminating the need for very precise centrifuge protocols. Since NCTs are sonicated after centrifugation to break up the main pellet and allow NCTs to assemble, this is likely why no significant difference is seen in the nanostructure.

However, if NCTs were only centrifuged and not resuspended, the centrifuge protocols would be expected to have a significant impact on both the nanostructure and the microstructure of the resulting NCT solid, since all assembly would have to occur during the centrifuging process

(Figure S5.4). In such a case, a long, slow centrifuge cycle would likely result in higher quality ordering in comparison to a short, fast centrifuge cycle where particles have less time to rearrange and thus are more likely to be caught in kinetic traps.

Table 5.1. Structural parameters for 10 nm/10 kDa IO NCTs in varying solvents

Solvent	d (nm)	a (nm)	Crystal Structure
Toluene	27.4	38.8	FCC
40% Decane, 60% Toluene	23.7	33.5	FCC
DMF	22.0	31.1	FCC
Acetone	21.7	30.7	FCC
Decane	17.71	20.45	BCC

Conclusion

NCTs are a modular nanocomposite building block whose three distinct components – nanoparticle core, polymer brush, supramolecular binding group – make it possible to independently modify structure and composition in assembled NCTs. The larger the library of accessible materials is for a given self-assembly system, the more potential utility that system has as a method for fabricating advanced functional materials, which require precise control over structure and composition to achieve the desired properties. In addition to precise structural control and materials selection, an ideal self-assembly system would also be able to achieve fast and

scalable assembly without requiring overly complex chemistries – this increases the likelihood of commercial viability. In this work, we present a fast and simple method for making ordered NCT crystallites without requiring the use of supramolecular binding groups or thermal annealing to achieve assembly. By processing NCTs in a medium-quality solvent for the polymer brush, we can utilize solvent-ligand interactions to drive NCT assembly into ordered FCC superlattices at ambient temperatures. By eliminating the need for supramolecular binding groups, we greatly simplify the synthesis for the NCT polymer brush. Furthermore, this introduces the possibility of further expanding the NCT materials library with polymer compositions that might have otherwise been incompatible with existing NCT binding chemistries. Future avenues of exploration include studying how the assembly methods introduced in this work can be combined with NCT sintering methods for the further development of NCT bulk solids.

Chapter 6: Future Studies

In Situ TEM of NCT Assembly

Studies of solid-state NCT superlattice crystallites have shown that crystallite size is a function of both NCT concentration and cooling rate, with larger crystallites forming at higher concentrations and slower cooling rates, the former of which runs counter to classical nucleation.[80] Being able to control NCT crystallite size during the assembly process is key, as it determines the grain size and thus affects the microstructure in sintered NCT solids. In situ thermal SAXS can be used to observe the emergence of ordering during the assembly process, but since it averages over all particles in solution, it is unable to provide information on how individual crystallites form.

In situ liquid cell thermal TEM, which has the ability to observe NCT assembly in solution in real time with nanoparticle-level resolution, would provide important information on the dynamics and mechanism of assembly, including when and how nucleation, growth, and rearrangement occur. Beyond contributing to a greater understanding of colloidal self-assembly, such information also has a practical application in aiding improved processing techniques. For example, during the NCT assembly process, there exists a rearrangement temperature slightly below the melting temperature (the temperature at which assembled NCTs dissociate into free particles), at which particles have enough thermal energy to rearrange into the thermodynamically favored structure without fully dissociating. Since the rearrangement temperature is close to the melting temperature, it is difficult to identify using conventional methods (UV-Vis, SAXS), but should be identifiable using in situ liquid cell thermal TEM. Sintering (see next section) NCTs at their rearrangement temperature may potentially facilitate grain boundary diffusion, minimize defects at grain boundaries, and even promote grain fusion by increasing NCT mobility within the bulk.

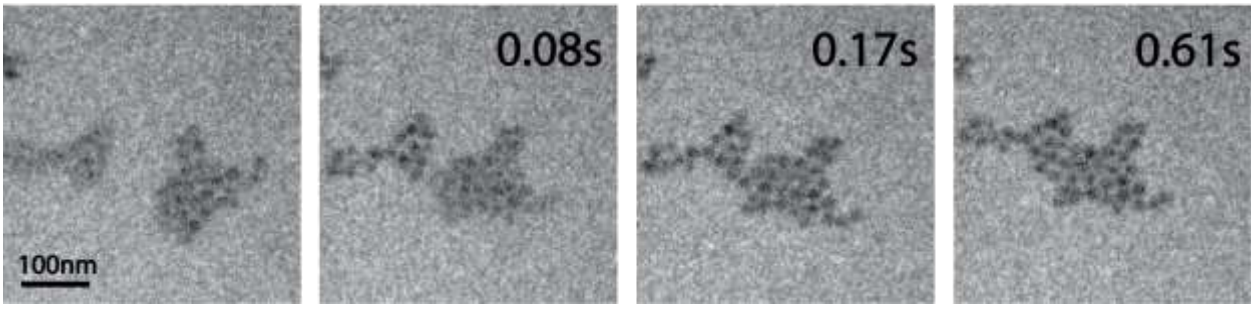

Figure 6.1. Snapshots from a video showing NCT clusters assembling after being heated and cooled back to room temperature. Individual clusters did not bind through random collision. Instead, clusters reoriented (note the position of the cluster on the right and how it rotates to match the interface of the cluster on the left) to achieve alignment before binding, as was expected given the complementary DAP and Thy binding groups present driving assembly.

Preliminary studies done in collaboration with the Frances Ross Group confirm that NCTs can be imaged in solution with in situ thermal TEM (Figure 6.1), although both sample preparation and the imaging process require some optimization. Samples were prepared by using Layer-by-Layer (LbL) deposition to deposit alternating layers of DAP and Thy NCTs on a Si_3N_4 liquid cell TEM chip (no significant difference in NCT coverage was observed between polymer-functionalized gold-coated chips and standard Si_3N_4 chips), with 3 layers of NCTs deposited in total. Deposited NCTs were collapsed in decane before drying for easier handling and storage, and resolvated with toluene before imaging. NCTs were deposited in layers to provide more even coverage and thickness, as the interior of the liquid cell has a height of just 100-200 nm, which precludes depositing NCT crystallites (500+ nm).

Initial experiments were performed with a static cell setup, although a flow cell setup is also possible. The flow cell setup is of interest because it allows for the introduction of various solvents, making it possible to study the effect of solvent quality on NCT behavior. However, the adhesive in the current flow cell setup is incompatible with toluene, anisole and DMF, the three primary solvents used with NCTs, and no suitable alternative adhesive has been found yet. One

additional drawback to liquid cell TEM as a characterization method is the inherent fragility of liquid cell TEM chips. The NCT deposition process itself is straightforward, but care must be taken when handling the TEM chips throughout the deposition and liquid cell assembly processes to reduce chip breakage or leakage.

A possible variation would be to run these experiments with Programmable Atom Equivalents (PAEs), DNA-functionalized gold nanoparticles, instead of NCTs. This would allow the solvent to be switched from toluene to water, eliminating the solvent compatibility issue. One potential drawback to using PAEs is the reduced stability of DNA when exposed to e-beam irradiation in comparison to PS, which will reduce the possible imaging time.

Controlling Microstructure in Sintered NCT Solids

The sintering process allows individual NCT crystallites to be processed into a macroscopic solid with a grain size corresponding to that of the initial crystallite size. While the sintering process itself is simple to execute, there are numerous variables within both the NCT composition and the sintering process itself. Understanding how each of these parameters affects NCT microstructure is key to being able to tailor and optimize the microstructure in sintered NCT solids, which will in turn improve their mechanical properties and processability (Figure 6.2).

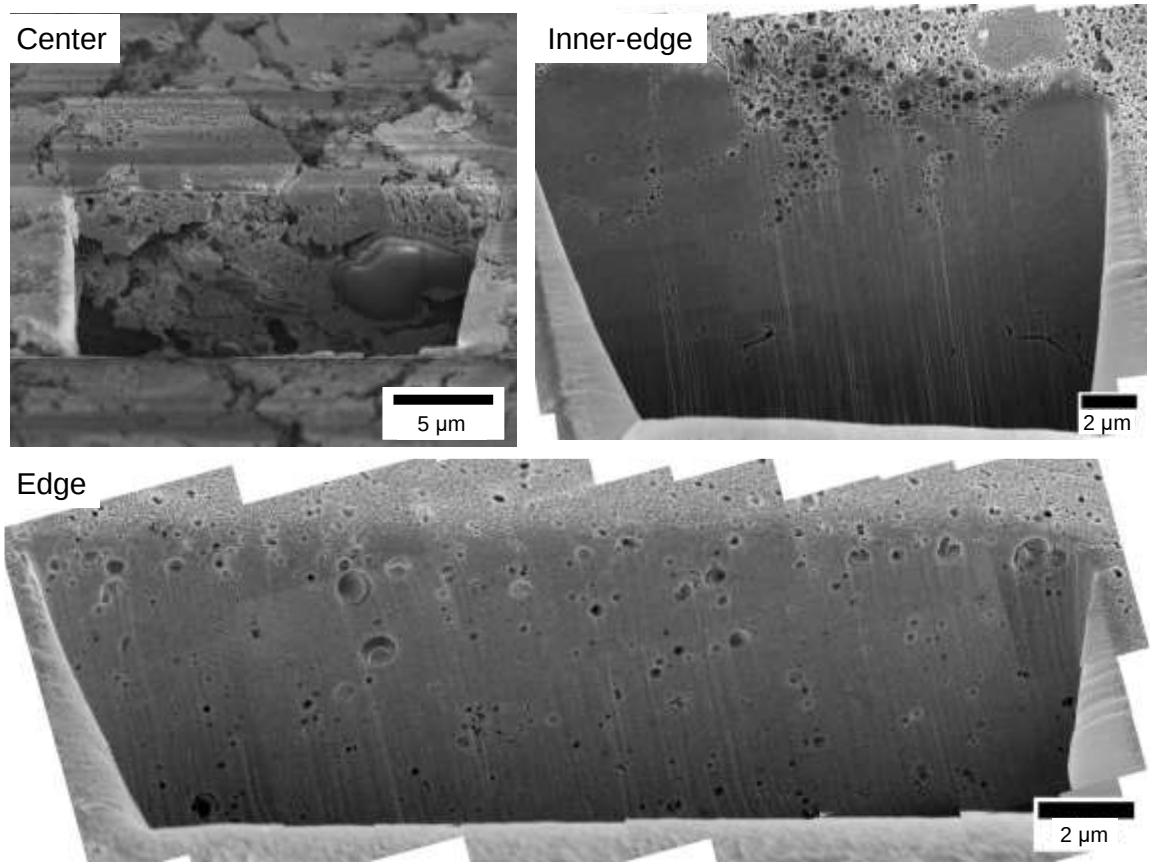

Figure 6.2. Cross-sections of an NCT solid prepared using 30 nm Au/14 kDa DAP/Thy PS NCTs annealed at 0.1 °C/min, followed by sintering at 15k rpm/1 min. The microstructure varies throughout the pellet. The center, where the pellet is the thickest, exhibits significant cracking and amorphous areas. Ordering quality improves and defect frequency lowers closer to the edge, where the pellet is thinner.

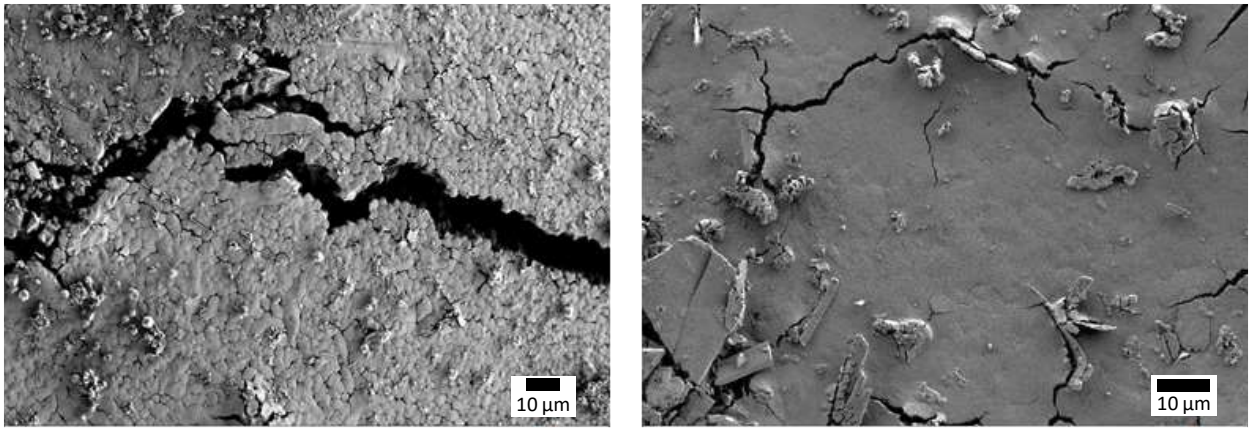

Figure 6.3. Sintered NCT solids prepared using 24 nm IO/10 kDa DAP/Thy PS NCTs (left) and 24 nm IO/10 kDa Thy-mel PS NCTs (right). The sample on the left contains a binary DAP/Thy NCT system, and the shapes of the initial crystallites remain distinct in the final sintered solid. In contrast, the sample on the right, which is composed of a single NCT type and small molecule linker, has a much smoother surface, and grain boundaries are less distinct. The self-complementarity of Thy-NCTs as well as the mobility of the small molecule linker likely contributes to improved diffusion and densification during sintering.

In the current sintering process, NCT crystallites in toluene are centrifuged at high speed (15k RPM) for a brief amount of time (1-10 minutes) to obtain a dense, compact pellet. Hypotheses include (1) increasing the centrifuging speed and time can be used to increase densification in bulk NCTs, (2) centrifuging at the rearrangement temperature will result in grain growth in bulk NCTs and can be used to generate large domains or single crystals, and (3) the labile nature of the supramolecular chemistry is what facilitates particle rearrangement. Metrics with which the efficacy of a given sintering procedure can be judged include grain size, void space, defects (dislocations, vacancies, etc.). The ideal sintering procedure should minimize void space and defects in the resulting bulk NCT solid. Variables for studying how NCT composition affects sintering include initial crystallite size, core size, polymer length, grafting density, and binding chemistry (Figure 6.3). Variables in the sintering process itself include the solvent, centrifuging time, centrifuging speed, centrifuging temperature, and centrifuging container. Follow-up studies include studying how the non-solvent collapse and drying process affects the microstructure of

sintered solids. Being able to eliminate defects in the microstructure also introduces the possibility of being able to controllably introduce desired defects into a microstructure, which could be useful for preparing NCTs with novel properties.

Mechanical Properties of NCT Single Crystals

NCTs have potential both as a model system for studying structure-property relationships in hierarchically structured materials, and as a class of building blocks for creating functional materials. A key step towards both of these futures is being able to study the mechanical properties and deformation behavior of NCTs.

A current collaboration with the Portela Group focuses on studying the deformation behavior and mechanical properties of single crystal NCTs, including FCC NCT Winterbottom structures (Figure 6.4) and pillars fabricated from FCC NCT Winterbottom structures. In situ deformation makes it possible to observe deformation behavior such as crack formation in real time, and can be combined with SEM analysis of crystal structure pre- and post-compression to gain further insights into how NCTs respond to compression. FCC NCT Winterbottom structures show a Young's modulus of 2.7 ± 0.5 GPa and yield strength of 184.0 ± 101.8 MPa, while FCC NCT pillars exhibit a significantly higher Young's modulus of 26.3 ± 11.8 GPa and yield strength of 552.4 ± 173.0 MPa. Mechanical measurements with pillars of varying surface area-to-volume ratio show that as the size decreases, the stiffness and strength increase, and that the mechanical properties of these materials have a strong correlation to the surface area-to-volume ratio of the tested material. Additional avenues of exploration include studying how modifying NCT size, composition, binding chemistry, and ordering affect the measured mechanical properties of the single crystal, as well as particle tracking and modeling to better understand deformation behavior, including failure modes and the effect of defects.

Once the mechanical properties of single crystal NCTs are understood, that knowledge can be used to study how single crystal properties influence mechanical properties in bulk NCT materials. This knowledge will also be useful in studying how processing methods affect

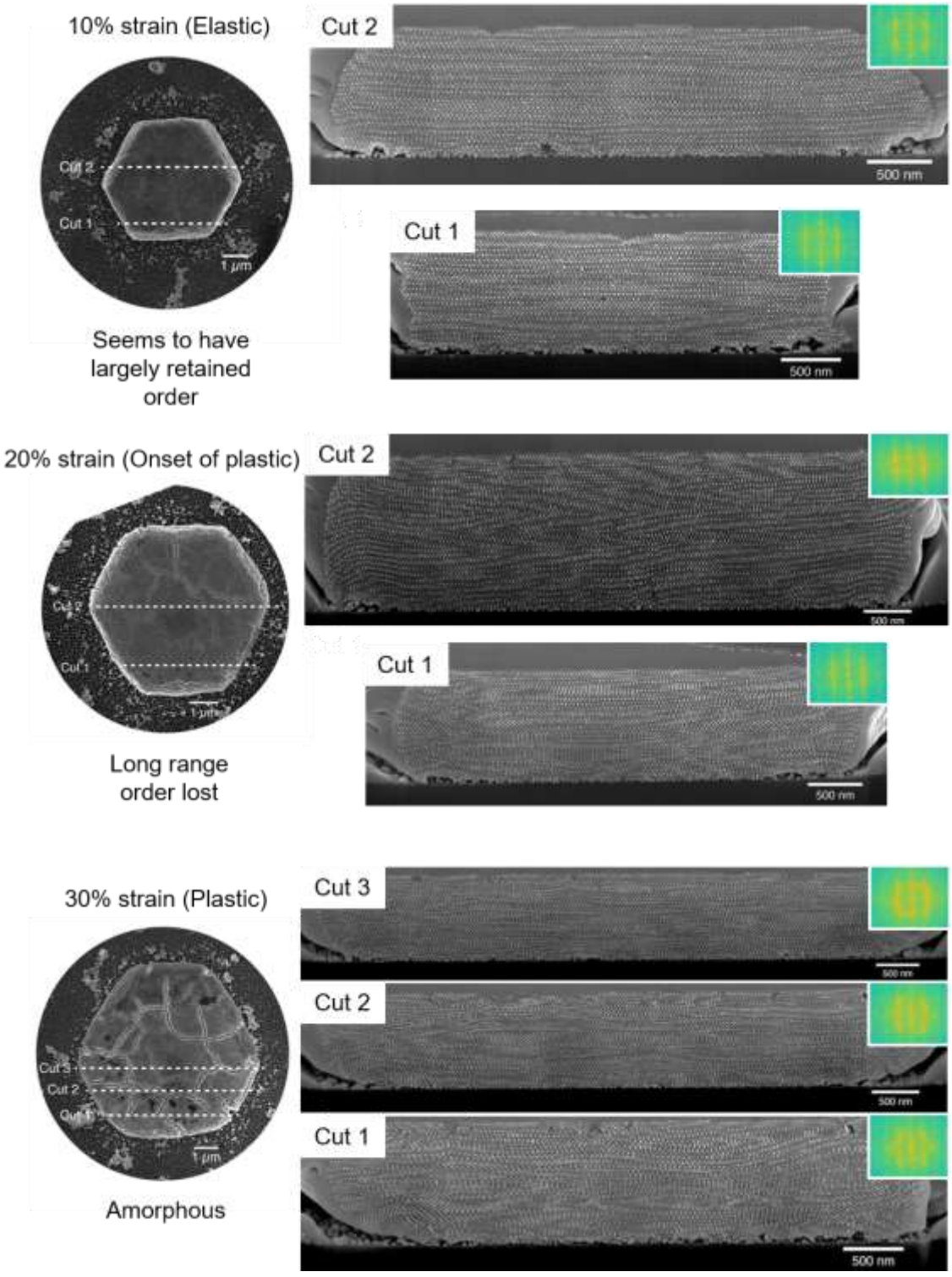

Figure 6.4. Analysis of the cross-sections of a compressed FCC NCT Winterbottom structure at three different levels of strain show how NCTs deform first elastically, then plastically, in response to compressive force. Long range ordering is initially retained, then lost as NCTs experience increased strain.

mechanical properties in bulk NCT solids, providing a performance baseline that makes it possible to separate contributions from processing, contributions from the microstructure, and contributions from the constituent crystallites in the overall mechanical performance. There are processing variables to consider at all stages, including during sintering, the collapse and drying process, and pressing. Such information will be important for developing design rules that can be used to tailor NCT solid microstructure to achieve the desired mechanical performance.

Appendix 1: Publications

1. Lee, M. S.; Kubiak, J. M.; Yee, D. W.; Santos, P. J.; Macfarlane, R. J. Improving Nanoparticle Superlattice Stability with Deformable Polymer Gels. In preparation, 2022.

2. Yee, D. W.*; Lee, M. S.*; An, J.; Macfarlane, R. J. Reversible Diffusionless Phase Transitions in 3D Nanoparticle Superlattices. In preparation, 2022.

3. Xia, J.; Lee, M. S.; *et al.* Nanocomposite tectons as unifying systems for nanoparticle assembly. *Soft Matter* (2022) doi:10.1039/D1SM01738A.

4. Lee, M. S., Yee, D. W., Ye, M. & Macfarlane, R. J. Nanoparticle Assembly as a Materials Development Tool. *J. Am. Chem. Soc.* **144**, 8, 3330–3346 (2022).

5. Santos, P. J., Gabrys, P. A., Zornberg, L. Z., Lee, M. S. & Macfarlane, R. J. Macroscopic materials assembled from nanoparticle superlattices. *Nature* **591**, 586–591 (2021).

6. Lee, M. S., Alexander-Katz, A. & Macfarlane, R. J. Nanoparticle Assembly in High Polymer Concentration Solutions Increases Superlattice Stability. *Small* **17**, 2102107 (2021).

7. Gibson, K. J.; Prominski, A.; Lee, M. S.; *et al.* Discrete pH-Responsive Plasmonic Actuators via Site-Selective Encoding of Nanoparticles with DNA Triple Helix Motif. *Cell Reports Physical Science* **1**, 100080 (2020).

8. Wang, Y. *et al.* Multistimuli Responsive Nanocomposite Tectons for Pathway Dependent Self-Assembly and Acceleration of Covalent Bond Formation. *J. Am. Chem. Soc.* **141**, 13234–13243 (2019).

9. Wang, Y.; Lee, M. S.; Kubiak, J. M.; Gabrys, P. A.; Yee, D. W.; Jia, F.; Macfarlane, R. J. "Modular Nanocomposite Superlattice Engineering by Supramolecular Chemistry Manipulation." In Preparation.

10. Jia, F.; Yee, D. W.; Kubiak, J. M.; Wang, Y.; Lee, M. S.; Macfarlane, R.J. "Linking Colloidal Crystals Through Multifunctional Polymers." In Preparation.

Appendix 2: Nanoparticle Assembly in High Polymer Concentration Solutions Increases Superlattice Stability

Materials and Instrumentation

2,6-Diaminopyridine, thymine, acetyl chloride, 11-bromo-1undecanol, 2-Bromoisobutyryl bromide, styrene, N,N,N',N",N'"-Pentamethyldiethylenetriamine (PMDETA), Tris[2-(dimethylamino)ethyl]amine (Me_6TREN), 2,2'-Azobis(2-methylpropionitrile) (AIBN), and basic alumina were purchased from Fisher Scientific. Copper bromide and pentaerythritol tetrakis(2-bromoisobutyrate) was purchased from Sigma Aldrich. Aminoethanethiol was purchased from TCI America. General solvents were purchased from Fisher Scientific. Hydrogen tetrachloroaurate(III) trihydrate was purchased from Beantown Chemical. All chemicals, including solvents, were used without further purification, except styrene, which was passed through a short column of basic alumina to remove inhibitor prior to polymerization.

Centrifugation was performed with an Eppendorf 5424 centrifuge. Thermal annealing was performed in a Techne Prime Thermal Cycler. Gel permeation chromatography (GPC) characterizations were performed on an Agilent Technologies GPC system, with THF as the eluent at 1.0 mL/min, and monodisperse polystyrene as the standard. UV-vis spectra and measurements were obtained on a Cary-5000 spectrophotometer. Transmission electron microscopy (TEM) was performed with a FEI Tecnai G2 Spirit TWIN transmission electron microscope. Small angle X-ray scattering (SAXS) measurements were performed at MIT on a SAXSLAB instrument with a Pilatus3R 300K detector and x-rays of wavelength 1.5409 Å. SAXS measurements were also performed at beamline 12-ID-B at the Advanced Photon Source at Argonne National Laboratory. Samples were probed using a Pilatus 2 M detector and 14 keV (0.8856 Å) x-rays. Both systems were calibrated using silver behenate as a standard.

Synthesis

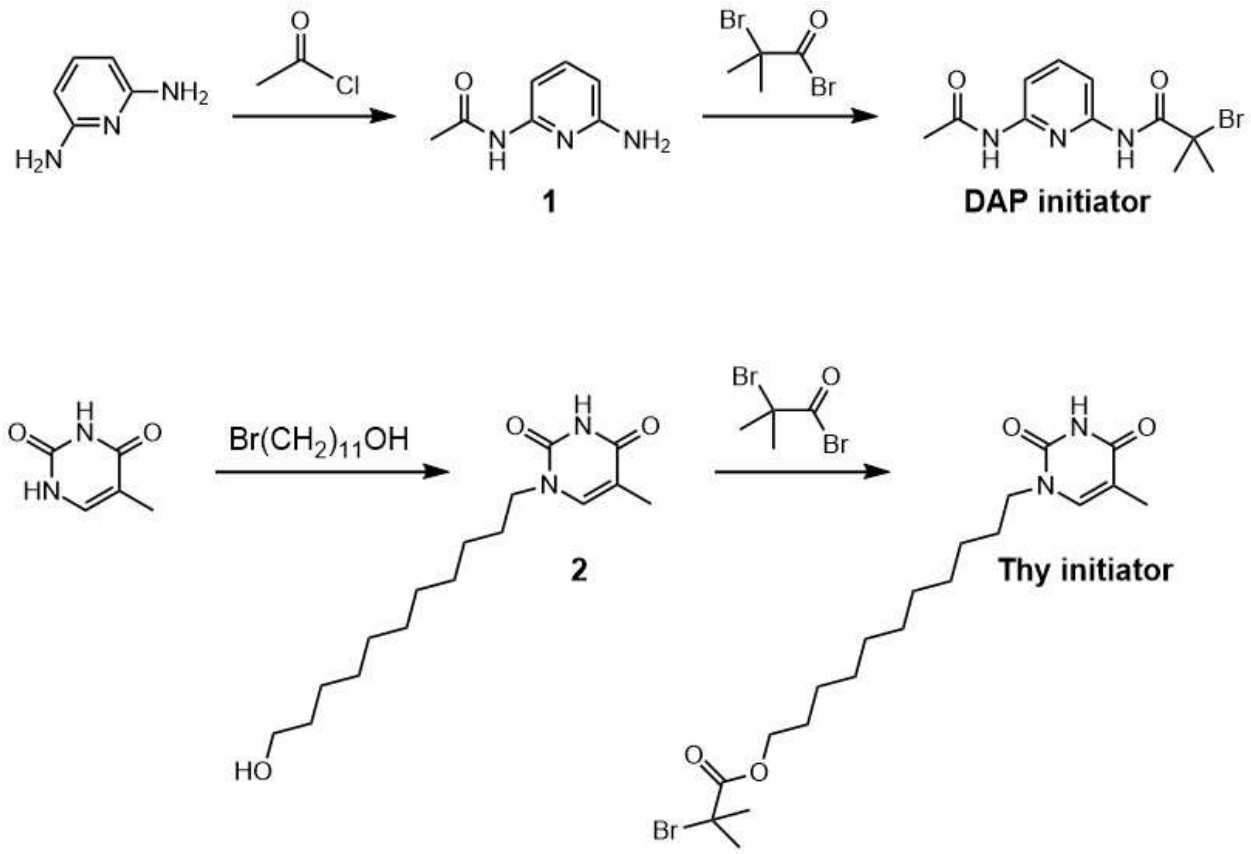

Scheme S2.1. Synthetic scheme for DAP initiator and Thy initiator

Gold Nanoparticle Synthesis

Gold nanoparticles (AuNPs) were synthesized using a modification of the Turkevich method to produce low dispersity, citrate-stabilized AuNPs.[18,274,275] All glassware and stir bars were cleaned with aqua regia before use. 800 mL of 2.75 mM 75/25 sodium citrate/citric acid buffer solution was prepared with Milli-Q purified water and heated to boiling for 15 minutes in a 1L flask. 6.08 mg of ethylenediaminetetraacetic acid tetrasodium salt hydrate (EDTA salt) was dissolved in water and added to the boiling solution to bring the overall concentration of EDTA salt to 0.02 mM. Gold precursor solution was prepared by dissolving 157.5 mg $HAuCl_4$ in 9 mL of Milli-Q purified water. After 10 minutes, 3 mL of gold precursor solution was swiftly injected into the boiling, stirring solution. A color change from clear to dark red was observed, beginning ~30 seconds after the addition of gold precursor. The reaction was boiled for 30 minutes before being allowed to gradually cool to 90 °C. After 30 minutes for temperature equilibration, another 3 mL of gold precursor was swiftly injected, followed 30 minutes later by the final 3 mL gold precursor addition. The reaction was ended after 30 minutes to obtain 16-18 nm AuNPs. Nanoparticles were characterized by TEM and their size and dispersity were analyzed using ImageJ.

DAP Initiator Synthesis

5.5 g 2,6-diaminopyridine (50 mmol) was dissolved in 40 mL of dry THF in a 3-necked round bottom flask. At 0 ºC, a solution of 1.96 g (25 mmol) acetyl chloride in 15 mL of dry THF was added dropwise under a nitrogen atmosphere. The reaction mixture was allowed to warm to room temperature and stirred for 12 hours. The insoluble content was filtered off, and the solvent was removed under reduced pressure. The resulting white solid was recrystallized in a mixture of

ethanol and toluene, to afford **1** (Scheme S2.1). 1.9 g **1** (12.6 mmol) was dissolved in 80 mL dichloromethane, and then 3.5 mL triethylamine (25 mmol) was added to this solution. The mixture was cooled to 0 ºC, and a solution of 3.22 g 2-bromoisobutyryl bromide (17.6 mmol) in dichloromethane (~10 mL) was added dropwise under a nitrogen atmosphere. The reaction mixture was allowed to warm to room temperature and stirred for 12 hours. The insoluble content was filtered off, and the filtrate was washed with a solution of sodium carbonate (x1) and brine (x3). The organic phase was dried with sodium sulfate, the solvent was removed under reduced pressure, and the product was then purified by flash chromatography (CH_2Cl_2/EtOAc 4:1). The product was further purified by recrystallization in CH_2Cl_2/EtOAc/hexanes to obtain the final DAP-initiator product. All characterization matches previous literature reports.

Thy Initiator Synthesis

5.0 g thymine (40 mmol), 1.0 g 11-bromo-1-undecanol (4 mmol), 1.1 g potassium carbonate (8 mmol) and 200 mL of DMSO were added to a 500 mL round bottom flask. The mixture was stirred and bubbled with nitrogen for 2 minutes, and then sealed with a septum and stirred for 48 hours. The resulting mixture was poured into water and chloroform for extraction. The organic phase was dried with sodium sulfate, and the solvent was removed under reduced pressure. The resulting white solid was recrystallized in EtOAc/hexanes to afford **2** (Scheme S2.1). Using very gentle heat, 592 mg **2** (2 mmol) was dissolved in 150 mL of dichloromethane, and 0.39 mL of trimethylamine (2.8 mmol) was added to the solution. The mixture was cooled to 0 ºC, and a solution of 552 mg 2-bromoisobutyryl bromide (2.4 mmol) in dichloromethane (~10 mL) was added dropwise under a nitrogen atmosphere. The reaction mixture was allowed to warm to room temperature and stirred for 14 hours, and then washed with sodium carbonate (x2) and brine (x2).

The organic phase was dried with sodium sulfate, and the solvent was removed under reduced pressure. The resulting mixture was purified by flash chromatography (CH_2Cl_2/EtOAc 8:3), to obtain the final Thy-initiator product. All characterization matches previous literature reports.

DAP-PS Polymer Synthesis

DAP-initiator (1.0 eq), Me_6TREN (0.83 eq), styrene (100-200 eq depending on target molecular weight), copper (II) bromide (0.1 eq), and anisole (0.8:1 v/v to styrene) were added to an oven-dried 100 mL Schlenk flask with stir bar. The reaction flask was then sealed with a rubber septum and 3 freeze-pump-thaw cycles were performed before filling the flask with nitrogen. Simultaneously, tin(II) 2-ethylhexanoate (0.15 eq) and anisole (0.2:1 v/v to styrene) were combined in a vial and bubbled with nitrogen. After the reaction flask finished returning to room temperature, the tin(II) 2-ethylhexanoate mixture was injected. The reaction mixture was stirred at 105 °C and quenched with liquid nitrogen at different time points to obtain polymers of the desired molecular weights. The reaction mixture was then added dropwise to methanol and the precipitated polymer was collected, redissolved in dichloromethane, and precipitated in methanol. 3 precipitations were done, ending with a polymer with a chain end bromine. The polymer was dissolved in minimal DMF with trimethylamine (40 eq) and bubbled with nitrogen for 15 minutes, followed by the addition of 2-aminoethanethiol (15 eq). The mixture was left to stir for 60 hours, and 3 precipitations were done to obtain a white powder, which was dried under vacuum to yield the final DAP-PS product.

Thy-PS Polymer Synthesis

Thy-initiator (1.0 eq), PMDETA (1.0 eq), styrene (200-300 eq depending on target molecular weight), and anhydrous anisole (30 v% to styrene) were added to an oven-dried 100 mL Schlenk flask with stir bar. The reaction flask was then sealed with a rubber septum and 3 freeze-pump-thaw cycles were performed before filling the flask with nitrogen. The septum was removed to add CuBr (1.0 eq) and the flask was quickly resealed, purged, refilled with nitrogen, and returned to room temperature. The reaction mixture was stirred at 110 °C and quenched with liquid nitrogen at different time points to obtain polymers of the desired molecular weights. The reaction mixture was then added dropwise to methanol and the precipitated polymer was collected, redissolved in dichloromethane, and precipitated in methanol. 3 precipitations were done, ending with a polymer with a chain end bromine. The polymer was dissolved in minimal DMF with trimethylamine (40 eq) and bubbled with nitrogen for 15 minutes, followed by the addition of 2-aminoethanethiol (15 eq). The mixture was left to stir for 60 hours, and 3 precipitations were done to obtain a white powder, which was dried under vacuum to yield the final Thy-PS product.

NCT Synthesis

In a 20 mL glass vial, DAP-PS or Thy-PS was dissolved in 8 mL of acetone (1 mg/mL). While stirring, 8 mL of citrate-capped AuNPs (Figure S2.1) was quickly added and the resulting suspension was allowed to stir for 30 minutes, forming a dark red/pink precipitate. The functionalized nanoparticles were recovered by a brief (2 minute) centrifugation, and purified and concentrated by three cycles of centrifugation (8k, 40 minutes), with redispersion in 8 mL of DMF, 1 mL of DMF and 1 mL of toluene before each respective centrifugation, with a final dispersion in toluene.

NCT Assembly

NCT assemblies were formed by mixing 0.2 mL each of 20 nM DAP NCTs and 20 nM Thy NCTs in toluene. To obtain crystalline structures, after assembly, samples were heated to above their melting temperature and then cooled to room temperature at a rate of 0.1 °C/minute.

4-arm Star PS Polymer Synthesis

Pentaerythritol tetrakis(2-bromoisobutyrate) (1.0 eq), PMDETA (1.2 eq), and styrene (400-1500 eq depending on target molecular weight) were added to an oven-dried 100 mL Schlenk flask with stir bar. The reaction flask was then sealed with a rubber septum and 3 freeze-pump-thaw cycles were performed before filling the flask with nitrogen. The septum was removed to add CuBr (1.2 eq) and the flask was quickly resealed, purged, refilled with nitrogen, and returned to room temperature. The reaction mixture was stirred at 100 °C and quenched with liquid nitrogen at different time points to obtain polymers of the desired molecular weights. The reaction mixture was then added dropwise to methanol and the precipitated polymer was collected, redissolved in dichloromethane, and precipitated in methanol. 3 precipitations were done, ending with a polymer with a chain end bromine. The polymer was dissolved in minimal DMF and bubbled with nitrogen for 15 minutes, followed by the addition of NaN3 (6 eq). The mixture was left to stir for 16 hours. The reaction mixture was then added dropwise to methanol and the precipitated polymer was collected, redissolved in a mixture of dichloromethane and DMF (8:2), and precipitated in methanol. 3 precipitations were done to obtain a white powder, which was dried under vacuum to yield the final 4-arm PS star polymer product.

Linear PS Polymer Synthesis

2,2'-Azobis(2-methylpropionitrile) (AIBN) (1.0 eq) and styrene (100-300 eq depending on target molecular weight) were added to an oven-dried 100 mL round bottom flask with stir bar. The reaction flask was then sealed with a rubber septum and stirred at 65 °C for 1 hour before quenching in liquid nitrogen. The reaction mixture was then added dropwise to methanol and the precipitated polymer was collected, redissolved in dichloromethane, and precipitated in methanol. 3 precipitations were done to obtain a white powder, which was dried under vacuum to yield the final linear PS polymer product.

Characterization

Gold Nanoparticles

Gold nanoparticles (AuNPs) were synthesized using a modification of the Turkevich method to produce low dispersity, citrate-stabilized AuNPs. To prepare samples for TEM, AuNPs were functionalized with polystyrene using the protocol for synthesizing NCTs and drop cast from toluene onto formvar coated TEM grids. AuNPs used had a measured diameter of 17.0 nm and dispersity of 8.3%. Analysis was performed in ImageJ.

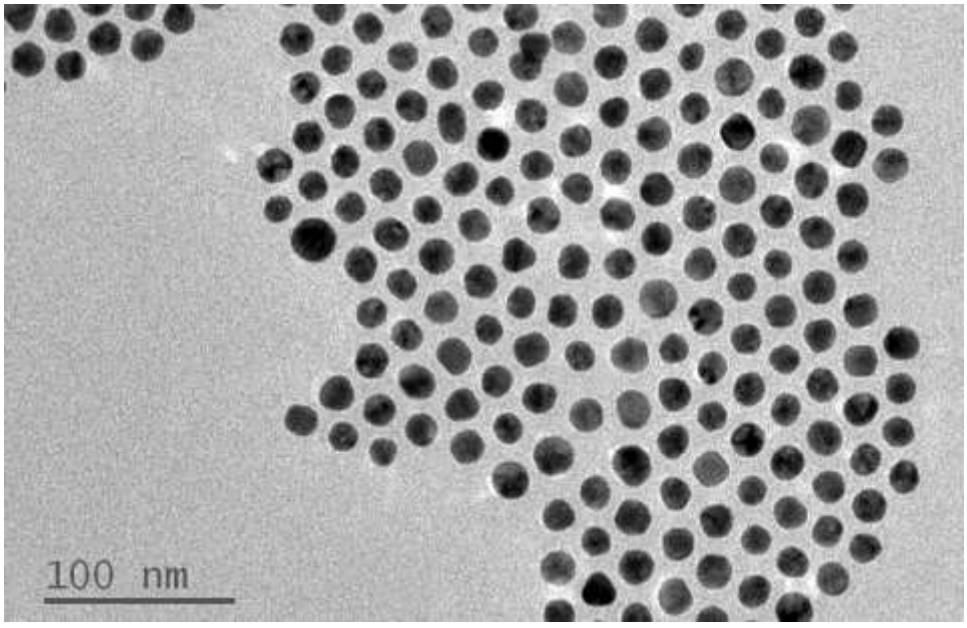

Figure S2.1. TEM micrograph of unassembled, polymer-grafted 17 nm gold nanoparticles used in this work.

Polymers

Table S2.1. Molecular weight and dispersity of the DAP-PS, Thy-PS, linear PS, and 4-arm star PS polymers used in this work.

Polymer	M_n (kDa)	Đ
DAP-PS	11.2	1.06
Thy-PS	11.2	1.03
20K Linear	20.2	1.6
26K Linear	26.5	1.4
32K Linear	31.5	1.5
35K Linear	34.6	1.4
39K Linear	39.3	1.5
46K Linear	46.4	1.3
61K Linear	61.3	1.3
26K Star	26.2	1.1
30K Star	30.1	1.1
37K Star	37.1	1.1
45K Star	45.4	1.1
60K Star	59.5	1.1

Small Angle X-Ray Scattering (SAXS) of Assembled NCTs

Assembled NCTs were prepared by thermally annealing NCTs with a grafting density of ~0.5 chains/nm^2 in a thermal cycler (60°C-50°C at 1 min/0.1 °C; 50°C-30°C at 3 min/0.1°C, 30°C-20°C at 1 min/0.1°C). Polymer was then added to assembled NCTs in toluene to obtain the desired polymer concentration. Each sample was added to a short section of 1.5mm diameter Polyimide Tubing (Cole-Parmer) and sealed at both ends with epoxy. 1-dimensional SAXS data was obtained via radial averaging of the 2-dimensional scattering pattern. Data was then transformed into profiles of scattering intensity as a function of scattering vector q. The form factor of free NCTs and background from solvent (toluene) was divided out from the raw scans to obtain the structure factor, which was used to determine peak positions and relative intensities. Body-centered cubic (BCC) ordering was confirmed, with structural parameters

$$\text{Interparticle Distance} = d = \frac{\sqrt{6}\pi}{q_0}$$

$$\text{Lattice Parameter} = a = \frac{2d}{\sqrt{3}}$$

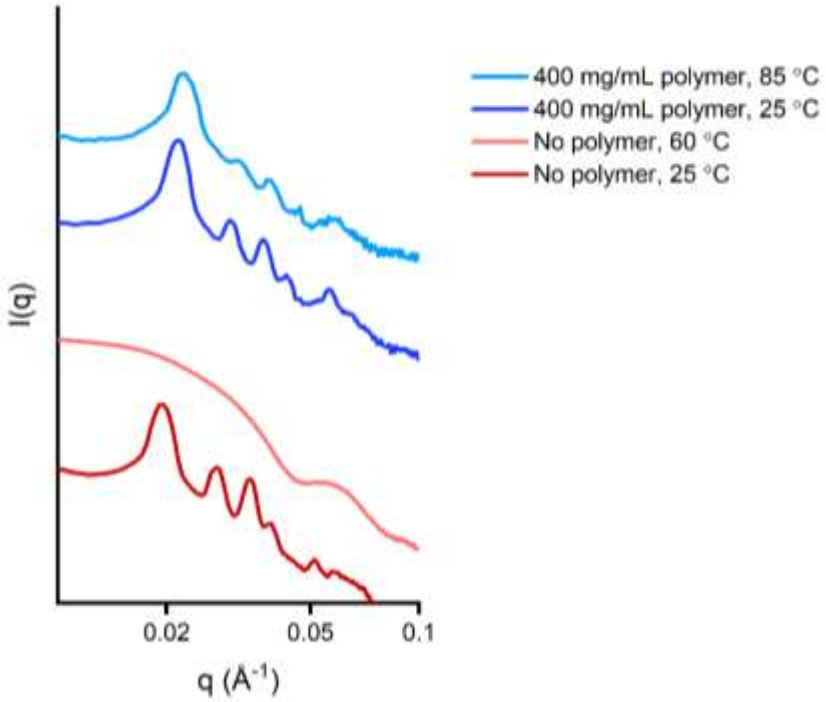

Figure S2.2. Temperature-dependent SAXS of NCTs in pure toluene (red) and NCTs in a 400 mg/mL polymer solution (blue). At 60 °C, only the form factor is present for NCTs in pure toluene, indicating that the NCTs have fully dissociated into free particles. In contrast, ordering is still present at 85 °C for NCTs in the polymer solution.

Table S2.2. Peak positions and structural parameters for the SAXS data in Figure 2.4. The lattice percent compression was determined by calculating the difference in lattice parameter between NCTs in pure toluene and NCTs in each polymer solution.

Sample	q_0 Peak Position	q_1/q_0	q_2/q_0	d (nm)	a (nm)	Lattice % Compression
No polymer	0.0209	1.45	1.73	36.7	42.4	-
26K Linear, 25 mg/mL	0.0215	1.44	1.74	25.7	41.3	2.60%
26K Linear, 50 mg/mL	0.0219	1.44	1.74	35.1	40.5	4.46%
26K Linear, 100 mg/mL	0.0230	1.41	1.75	33.5	38.6	8.92%
26K Linear, 200 mg/mL	0.0244	1.41	1.74	31.5	36.4	14.28%
26K Star, 25 mg/mL	0.0214	1.40	1.73	36.0	41.6	1.89%
26K Star, 50 mg/mL	0.0217	1.44	1.74	35.5	41.0	3.32%
26K Star, 100 mg/mL	0.0220	1.44	1.74	35.0	40.4	4.72%
26K Star, 200 mg/mL	0.0238	1.38	1.73	32.4	37.4	11.91%
Ideal BCC	-	1.41	1.73	-	-	-

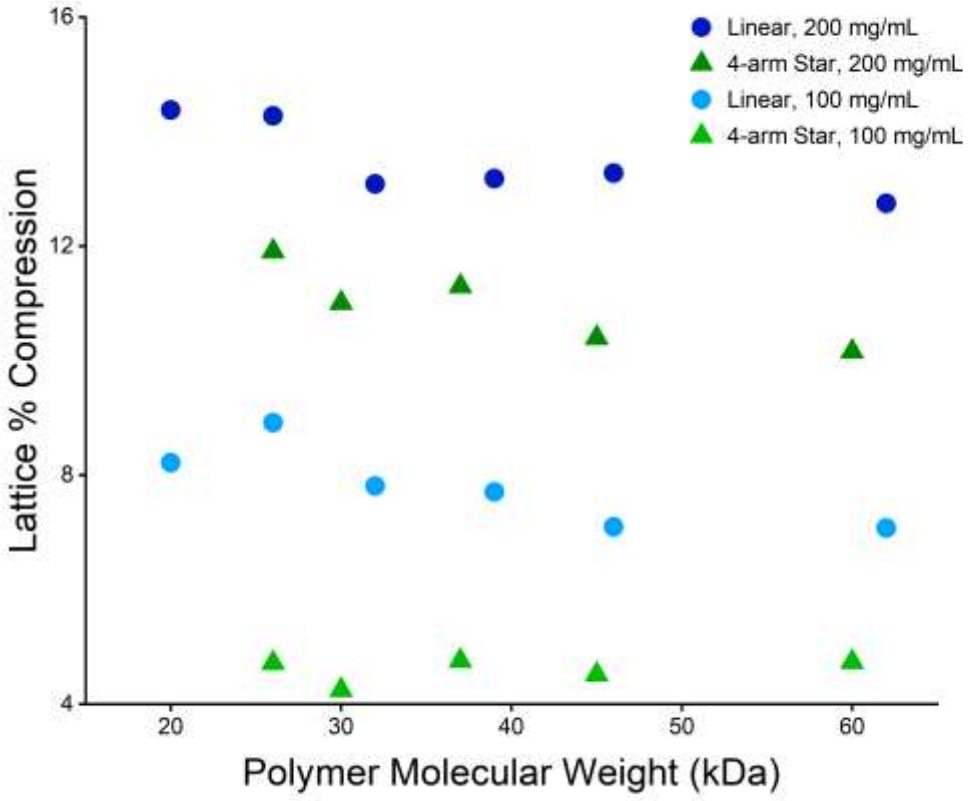

Figure S2.3. NCT lattice % compression in the presence of free polymer in solution. The % compression increases with polymer concentration but decreases as molecular weight increases. For the same molecular weight and concentration, linear polymers cause greater compression than star polymers.

Fixed-Rate Melts of Assembled NCTs

Before each melt, quartz cuvettes were cleaned with aqua regia and tetrahydrofuran to remove residual gold and polymer, respectively, followed by five water rinses. Cuvettes were then placed in a sealed chamber containing a 1:1 HMDS:n-hexane solution at room temperature overnight before use. Samples were prepared by adding equal volumes of complementary NCTs in toluene to a cuvette and waiting for an hour, followed by the addition of polymer. Samples were then given another hour to stir to ensure full assembly. The absorbance of each sample was measured at 520 nm and heated at a rate of 0.25°C/min from 20°C – 95°C to generate melt curves. For each measurement, samples were stirred to maintain homogeneity. Experimental melt curves were normalized and fit to a sigmoidal curve, and the melting temperature (T_m) was obtained by calculating the temperature for which the derivative of the fit curve is at a maximum.

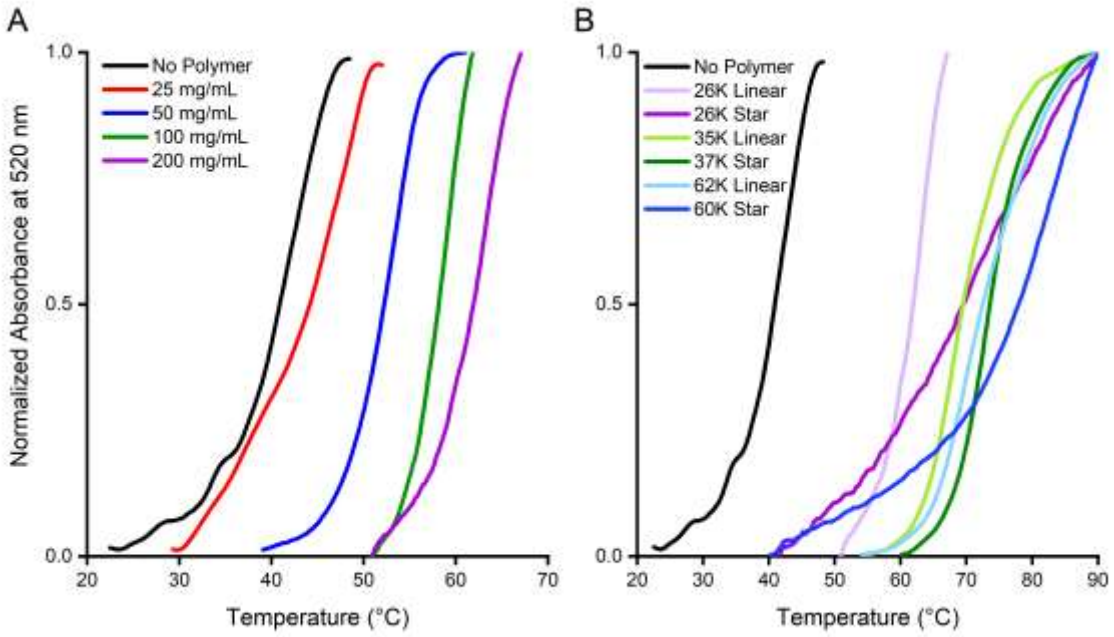

Figure S2.4. Fixed-rate melting curves for NCTs in polymer solutions of (A) varying concentrations at a constant molecular weight (26 kDa linear PS) and (B) varying molecular weight and morphology at a constant concentration (200 mg/mL).

Forced-Equilibrium Melts of Assembled NCTs

Before each melt, quartz cuvettes were cleaned with aqua regia and tetrahydrofuran to remove residual gold and polymer, respectively, followed by five water rinses. Cuvettes were then placed in a sealed chamber containing a 1:1 HMDS:n-hexane solution at room temperature overnight before use. Samples were prepared by adding equal volumes of complementary NCTs in toluene to a cuvette and waiting for an hour, followed by the addition of polymer. Samples were then given another hour to stir to ensure full assembly. The absorbance at 520 nm monitored at a set temperature until it reached equilibrium as indicated by a lack of change in absorbance. Once the sample reached equilibrium (3-5 hours), the set temperature was increased and the above process repeated until NCTs were fully disassembled. For each measurement, samples were stirred to maintain homogeneity. Changes in absorbance at each temperature were normalized and plotted to obtain forced-equilibrium melt curves. The T_m under forced-equilibrium conditions was obtained by calculating the temperature at which NCTs were 50% disassembled. The thermodynamic contribution to T_m elevation was determined for each sample by calculating the difference in T_m between NCTs in pure toluene and NCTs in each polymer solution under forced-equilibrium conditions.

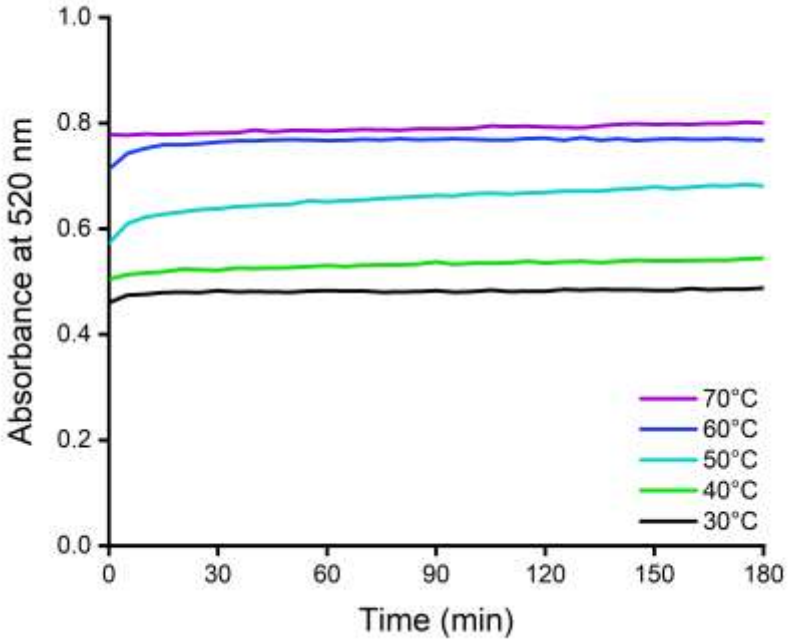

Figure S2.5. Forced-equilibrium absorbance data for a sample of NCTs in a polymer solution (26 kDa star PS, 50 mg/mL) before normalization and plotting.

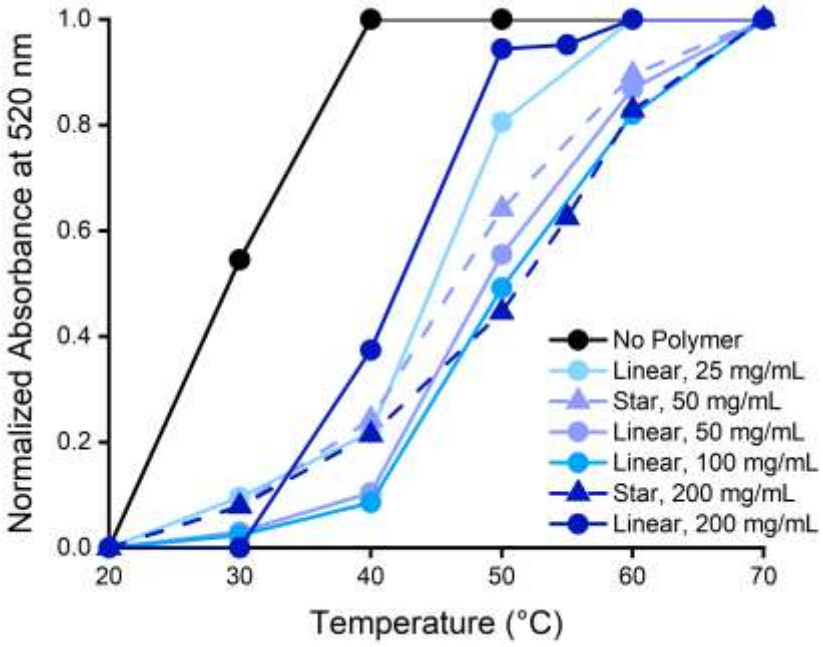

Figure S2.6. Forced-equilibrium melt curves for NCTs in polymer solutions of fixed molecular weight (26 kDa). Curves were used to calculate the thermodynamic contribution to T_m elevation in Table 2.1.

Appendix 3: Improving Nanoparticle Superlattice Stability with Deformable Polymer Gels

Materials and Instrumentation

2,6-Diaminopyridine, thymine, acetyl chloride, 11-bromoundecan-1-ol, 2-Bromoisobutyryl bromide, N,N,N',N",N'"-Pentamethyldiethylenetriamine (PMDETA), Tris[2-(dimethylamino)ethyl]amine (Me_6TREN), 2,2'-Azobis(2-methylpropionitrile) (AIBN), styrene, n-butyl acrylate, and basic alumina were purchased from Fisher Scientific. Sodium citrate, citric acid, and ethylenediaminetetraacetic acid tetrasodium salt hydrate were purchased from Acros Organics. Copper bromide and pentaerythritol tetrakis(2-bromoisobutyrate) were purchased from Sigma Aldrich. Aminoethanethiol was purchased from TCI America. General solvents were purchased from Fisher Scientific. Hydrogen tetrachloroaurate(III) trihydrate was purchased from Beantown Chemical. All chemicals, including solvents, were used without further purification, except styrene and n-butyl acrylate, which were passed through a short column of basic alumina to remove inhibitor prior to polymerization.

Centrifugation was performed with an Eppendorf 5424 centrifuge. Gel permeation chromatography (GPC) characterizations were performed on an Agilent Technologies GPC system, with tetrahydrofuran (THF) as the eluent at 1.0 mL/min, and monodisperse polystyrene as the standard. Transmission electron microscopy (TEM) was performed with a FEI Tecnai G2 Spirit TWIN transmission electron microscope. Scanning electron microsopy (SEM) and focused ion beam (FIB) milling were performed with a FEI Helios Nanolab 600 Dual Beam System. Small angle X-ray scattering (SAXS) measurements were performed at MIT on a SAXSLAB instrument with a Pilatus3R 300K detector and x-rays of wavelength 1.5409 Å. SAXS measurements were also performed at beamline 12-ID-B at the Advanced Photon Source at Argonne National

Laboratory. Samples were probed using a Pilatus 2 M detector and 14 keV (0.8856 Å) x-rays. Both systems were calibrated using silver behenate as a standard.

Synthesis

Gold Nanoparticles

Gold nanoparticles (AuNPs) were synthesized using a modification of the Turkevich method to produce low dispersity, citrate-stabilized AuNPs.[18,274,275] All glassware and stir bars were cleaned with aqua regia before use. 800 mL of 2.75 mM 75/25 sodium citrate/citric acid buffer solution was prepared with Milli-Q purified water and heated to boiling for 15 minutes in a 1 L flask. 6.08 mg of ethylenediaminetetraacetic acid tetrasodium salt hydrate (EDTA salt) was dissolved in water and added to the boiling solution to bring the overall concentration of EDTA salt to 0.02 mM. Gold precursor solution was prepared by dissolving 157.5 mg $HAuCl_4$ in 9 mL of Milli-Q purified water. After 10 minutes, 3 mL of gold precursor solution was swiftly injected into the boiling, stirring solution. A color change from clear to dark red was observed, beginning ~30 seconds after the addition of gold precursor. The reaction was boiled for 30 minutes before being allowed to gradually cool to 90 °C. After 30 minutes for temperature equilibration, another 3 mL of gold precursor was swiftly injected, followed 30 minutes later by the final 3 mL gold precursor addition. The reaction was ended after 30 minutes to obtain 16-18 nm AuNPs.

To obtain larger nanoparticles, instead of ending the reaction after the final temperature equilibration, 400 mL of the reaction mixture was removed, followed by the addition of 485.3 mg sodium citrate in 400 mL of Milli-Q purified water. A new gold precursor solution was prepared by dissolving 157.5 mg $HAuCl_4$ in 9 mL of Milli-Q purified water. After 30 minutes for temperature equilibration at 90 °C, an additional 3 rounds of swiftly injecting 3 mL of gold precursor solution into the reaction mixture was performed, with 30 minutes between injections. The reaction was ended after 30 minutes to obtain 24-27 nm AuNPs.

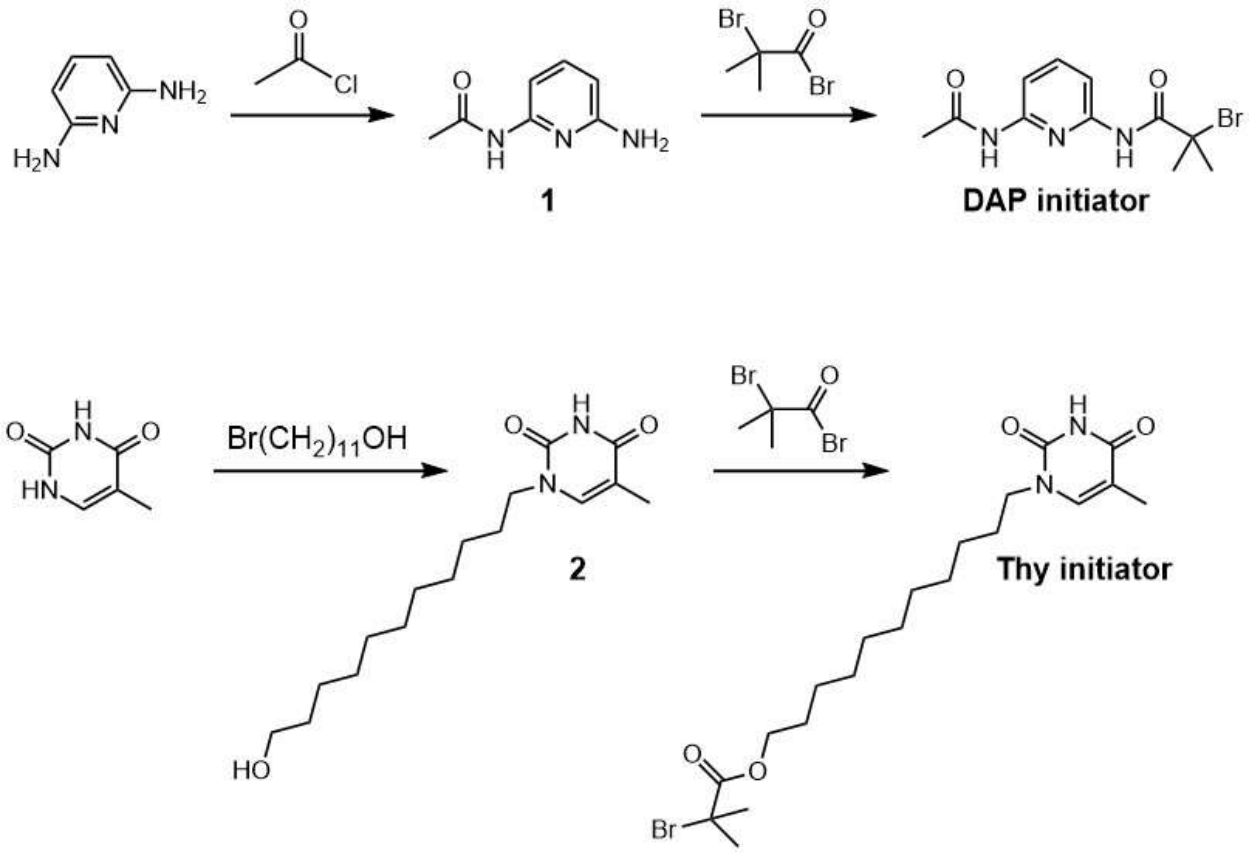

Scheme S3.1. Synthetic scheme for DAP initiator and Thy initiator

DAP Initiator

5.5 g 2,6-diaminopyridine (50 mmol) was dissolved in 40 mL of dry THF in a 3-necked round bottom flask. At 0 ºC, a solution of 1.96 g (25 mmol) acetyl chloride in 15 mL of dry THF was added dropwise under a nitrogen atmosphere. The reaction mixture was allowed to warm to room temperature and stirred for 12 hours. The insoluble content was filtered off, and the solvent was removed under reduced pressure. The resulting white solid was recrystallized in a mixture of ethanol and toluene, to afford **1** (Scheme S3.1). 1.9 g **1** (12.6 mmol) was dissolved in 80 mL dichloromethane, and then 3.5 mL triethylamine (25 mmol) was added to this solution. The mixture was cooled to 0 ºC, and a solution of 3.22 g 2-bromoisobutyryl bromide (17.6 mmol) in

dichloromethane (~10 mL) was added dropwise under a nitrogen atmosphere. The reaction mixture was allowed to warm to room temperature and stirred for 12 hours. The insoluble content was filtered off, and the filtrate was washed with a solution of sodium carbonate (x1) and brine (x3). The organic phase was dried with sodium sulfate, the solvent was removed under reduced pressure, and the product was then purified by flash chromatography (CH_2Cl_2/EtOAc 4:1). The product was further purified by recrystallization in CH_2Cl_2/EtOAc/hexanes to obtain the final DAP-initiator product. All characterization matches previous literature reports.

Thy Initiator

5.0 g thymine (40 mmol), 1.0 g 11-bromo-1-undecanol (4 mmol), 1.1 g potassium carbonate (8 mmol) and 200 mL of DMSO were added to a 500 mL round bottom flask. The mixture was stirred and bubbled with nitrogen for 2 minutes, and then sealed with a septum and stirred for 48 hours. The resulting mixture was poured into water and chloroform for extraction. The organic phase was dried with sodium sulfate, and the solvent was removed under reduced pressure. The resulting white solid was recrystallized in EtOAc/hexanes to afford **2** (Scheme S3.1). Using very gentle heat, 592 mg **2** (2 mmol) was dissolved in 150 mL of dichloromethane, and 0.39 mL of trimethylamine (2.8 mmol) was added to the solution. The mixture was cooled to 0 ºC, and a solution of 552 mg 2-bromoisobutyryl bromide (2.4 mmol) in dichloromethane (~10 mL) was added dropwise under a nitrogen atmosphere. The reaction mixture was allowed to warm to room temperature and stirred for 14 hours, and then washed with sodium carbonate (x2) and brine (x2). The organic phase was dried with sodium sulfate, and the solvent was removed under reduced pressure. The resulting mixture was purified by flash chromatography (CH_2Cl_2/EtOAc 8:3), to obtain the final Thy-initiator product. All characterization matches previous literature reports.

DAP-PS Polymer

DAP-initiator (1.0 eq), Me_6TREN (0.83 eq), styrene (100-200 eq depending on target molecular weight), copper (II) bromide (0.1 eq), and anisole (0.8:1 v/v to styrene) were added to an oven-dried 100 mL Schlenk flask with stir bar. The reaction flask was then sealed with a rubber septum and 3 freeze-pump-thaw cycles were performed before filling the flask with nitrogen. Simultaneously, tin(II) 2-ethylhexanoate (0.15 eq) and anisole (0.2:1 v/v to styrene) were combined in a vial and bubbled with nitrogen. After the reaction flask finished returning to room temperature, the tin(II) 2-ethylhexanoate mixture was injected. The reaction mixture was stirred at 105 °C and quenched with liquid nitrogen at different time points to obtain polymers of the desired molecular weights. The reaction mixture was then added dropwise to methanol and the precipitated polymer was collected, redissolved in dichloromethane, and precipitated in methanol. 3 precipitations were done, ending with a polymer with a chain end bromine. The polymer was dissolved in minimal dimethylformamide (DMF) with trimethylamine (40 eq) and bubbled with nitrogen for 15 minutes, followed by the addition of 2-aminoethanethiol (15 eq). The mixture was left to stir for 60 hours, and 3 precipitations were done to obtain a white powder, which was dried under vacuum to yield the final DAP-PS product.

Thy-PS Polymer

Thy-initiator (1.0 eq), PMDETA (1.0 eq), styrene (200-300 eq depending on target molecular weight), and anhydrous anisole (30 v% to styrene) were added to an oven-dried 100 mL Schlenk flask with stir bar. The reaction flask was then sealed with a rubber septum and 3 freeze-pump-thaw cycles were performed before filling the flask with nitrogen. The septum was removed to add CuBr (1.0 eq) and the flask was quickly resealed, purged, refilled with nitrogen, and returned

to room temperature. The reaction mixture was stirred at 110 °C and quenched with liquid nitrogen at different time points to obtain polymers of the desired molecular weights. The reaction mixture was then added dropwise to methanol and the precipitated polymer was collected, redissolved in dichloromethane, and precipitated in methanol. 3 precipitations were done, ending with a polymer with a chain end bromine. The polymer was dissolved in minimal DMF with trimethylamine (40 eq) and bubbled with nitrogen for 15 minutes, followed by the addition of 2-aminoethanethiol (15 eq). The mixture was left to stir for 60 hours, and 3 precipitations were done to obtain a white powder, which was dried under vacuum to yield the final Thy-PS product.

4-arm Star PS Polymer

Pentaerythritol tetrakis(2-bromoisobutyrate) (1.0 eq), PMDETA (1.2 eq), and styrene (400-1500 eq depending on target molecular weight) were added to an oven-dried 100 mL Schlenk flask with stir bar. The reaction flask was then sealed with a rubber septum and 3 freeze-pump-thaw cycles were performed before filling the flask with nitrogen. The septum was removed to add CuBr (1.2 eq) and the flask was quickly resealed, purged, refilled with nitrogen, and returned to room temperature. The reaction mixture was stirred at 100 °C and quenched with liquid nitrogen at different time points to obtain polymers of the desired molecular weights. The reaction mixture was passed through a short column of neutral alumina, then added dropwise to methanol. The precipitated polymer was collected, redissolved in dichloromethane, and precipitated in methanol. 3 precipitations were done, ending with a polymer with a chain end bromine. The polymer was dissolved in minimal DMF and bubbled with nitrogen for 15 minutes, followed by the addition of NaN_3 (6 eq). The mixture was left to stir for 16 hours. The reaction mixture was then added dropwise to methanol and the precipitated polymer was collected, redissolved in a mixture of

dichloromethane and DMF (8:2), and precipitated in methanol. 3 precipitations were done to obtain a white powder, which was dried under vacuum to yield the final 4-arm PS star polymer product.

4-arm Star P-nBA Polymer

Pentaerythritol tetrakis(2-bromoisobutyrate) (1.0 eq), PMDETA (1.0 eq), and n-butyl acrylate (400-1500 eq depending on target molecular weight) were added to an oven-dried 100 mL Schlenk flask with stir bar. The reaction flask was then sealed with a rubber septum and 3 freeze-pump-thaw cycles were performed before filling the flask with nitrogen. The septum was removed to add CuBr (1.0 eq) and the flask was quickly resealed, purged, refilled with nitrogen, and returned to room temperature. The reaction mixture was stirred at 100 °C and quenched with liquid nitrogen at different time points to obtain polymers of the desired molecular weights. The reaction mixture was passed through a short column of neutral alumina, then added dropwise to a cold mixture of methanol and water (9:1). The precipitated polymer was collected via centrifugation, redissolved in THF, and precipitated in a cold mixture of methanol and water (9:1). 3 precipitations were done, ending with a polymer with a chain end bromine. The polymer was dissolved in minimal DMF and bubbled with nitrogen for 15 minutes, followed by the addition of NaN_3 (24 eq). The mixture was left to stir for 16 hours. The reaction mixture was then added dropwise to a mixture of methanol and water (9:1) and the precipitated polymer was collected, redissolved in THF, and precipitated in a mixture of methanol and water (9:1). 3 precipitations were done to obtain a white solid, which was dried under vacuum to yield the final 4-arm PnBA star polymer product.

NCTs

In a 20 mL glass vial, DAP-PS or Thy-PS was dissolved in 8 mL of acetone (1 mg/mL). While stirring, 8 mL of citrate-capped AuNPs was quickly added and the resulting suspension was allowed to stir for 15 minutes, forming a dark red/pink precipitate. The functionalized nanoparticles were recovered by a brief (2 minute) centrifugation, and purified and concentrated by three cycles of centrifugation (**Table SA**), with redispersion in 8 mL of DMF, 1 mL of DMF and 1 mL of toluene before each respective centrifugation, and a final dispersion in toluene.

Table S3.1. Centrifuge protocols for the AuNPs used in this work.

Particle Diameter (nm)	Centrifuge Protocol
17	8k, 40 min
26	5.5k, 25 min

NCT Assembly

NCT assemblies were formed by mixing 0.2 mL each of 20 nM DAP NCTs and 20 nM Thy NCTs in toluene, which rapidly assembled into aggregates. To obtain crystalline structures, after assembly, samples were heated to above their melting temperature and then cooled to room temperature (60°C-50°C at 1 min/0.1 °C; 50°C-30°C at 3 min/0.1°C, 30°C-20°C at 1 min/0.1°C) in a thermal cycler.

NCT Polymer Gels

A fresh solution of 0.1 M CuCl/PPh_3 catalyst was prepared before each gelation by dissolving 9.9 mg CuCl and 26.23 mg PPh_3 in 1mL of toluene. In a 1.7 mL microcentrifuge tube, 100 mg 4-arm star polymer was dissolved in 0.25 mL toluene, followed by the addition of CuCl/PPh_3 (2.5 eq), assembled NCTs, and 1,7-octadiyne (10 eq.). Samples were mixed, sealed with Teflon tape, and heated in a heat block at 65°C for 3.5 hours to yield the final NCT polymer gel. Gelation was confirmed by the inversion test.

NCT PS Polymer Solids: UV Curing

NCT polymer gels were removed from their original tubes and sliced into discs using a single edge razor blade, then placed into new microcentrifuge tubes filled with filtered styrene. Gels were left in styrene for 24 hours to allow for styrene diffusion into the gel before excess styrene was removed, followed by the addition of AIBN (5 wt%). Samples were exposed to 2UV light (254 nm) for 12 hours to yield the final NCT polymer solid.

NCT Polymer Solids: Non-Solvent Collapse

NCT polymer gels were removed from their original tubes and sliced into discs using a single edge razor blade, then placed into new microcentrifuge tubes. n-decane was added to the tube in 30-minute intervals (**Table SB**), allowing the NCT polymer gel to gradually shrink without collapsing and losing ordering. After 24 hours, samples were dried to yield the final NCT polymer solid.

Table S3.2. Non-solvent addition procedure used in this work. After round 3, all solvent was removed and replaced with fresh n-decane in round 4.

Addition Round	n-decane Added (μL)	Total n-decane Volume (μL)
1	100	100
2	167	267
3	333	600
4	1000	1000

Characterization

Gold Nanoparticles

Gold nanoparticles (AuNPs) were synthesized using a modification of the Turkevich method to produce low dispersity, citrate-stabilized AuNPs. To prepare samples for TEM, AuNPs were functionalized with polystyrene using the protocol for synthesizing NCTs and drop cast from toluene onto formavar coated TEM grids. Size and dispersity analysis was performed in ImageJ.

Table S3.3. Particle diameter and dispersity of the AuNPs used in this work.

Nanoparticle Batch	Diameter (nm)	Dispersity
17 nm NPs	17.0	8.3%
26 nm NPs	26.2	14.89%

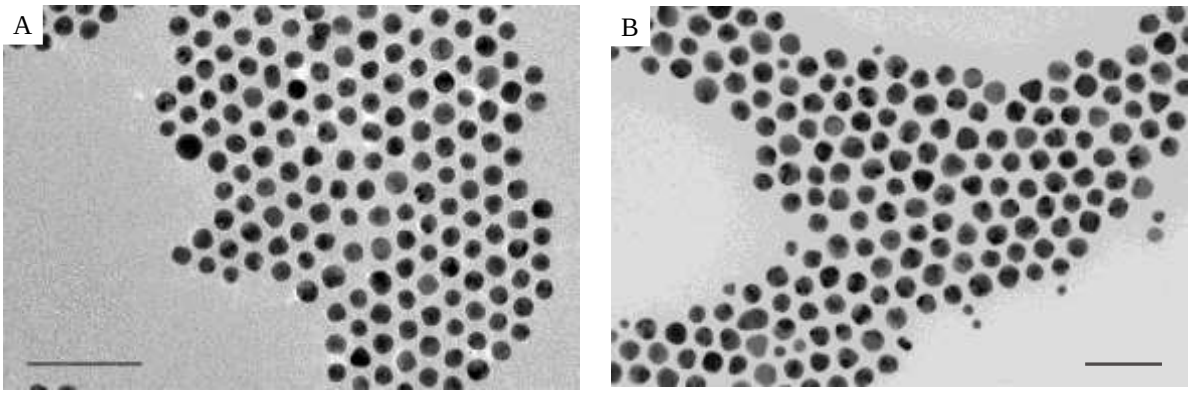

Figure S3.1. TEM micrograph of unassembled, polymer-grafted gold nanoparticles with diameters of (A) 17 nm and (B) 26 nm used in this work. Scale bars are 100 nm.

Polymers

Table S3.4. Molecular weight and dispersity of the DAP-PS, Thy-PS, and 4-arm star polymers used in this work.

Polymer	M_n (kDa)	Đ
11k DAP-PS	11.2	1.06
11k Thy-PS	11.2	1.03
15k DAP-PS	14.8	1.26
15k Thy-PS	14.0	1.14
60k PS 4-arm Star	59.5	1.08
62k PS 4-arm Star	62.1	1.105
64k PS 4-arm Star	64.2	1.06
80K PnBA 4-arm Star	79.9	1.08

SAXS of Assembled NCTs, NCT Polymer Gels, and NCT Polymer Solids

SAXS samples of assembled NCTs were prepared by adding thermally annealed NCTs in toluene to capillary tubes of 1.5mm diameter polyimide tubing (Cole-Parmer), then sealing with epoxy. SAXS samples of NCT polymer gels were prepared by adding the pre-gelation NCT mixture to capillary tubes, sealing with epoxy, then heating at 65 °C to form gels within each tube. SAXS samples of NCT polymer solids were prepared by sealing each polymer solid in polyimide tape. 1-dimensional (1-D) SAXS data was obtained via circular averaging of the 2-dimensional (2-D) scattering pattern. For mechanically compressed samples, 1-D SAXS data was obtained via averaging along orthogonal directions of the 2-D scattering pattern. Data was then transformed into profiles of scattering intensity as a function of scattering vector q. The form factor of free NCTs and background from solvent (toluene) was divided out from the raw scans to obtain the structure factor, which was used to determine peak positions and relative intensities. Body-centered cubic (BCC) ordering was confirmed, with structural parameters

$$\text{Interparticle Distance} = d = \frac{\sqrt{6}\pi}{q_0}$$

$$\text{Lattice Parameter} = a = \frac{2d}{\sqrt{3}}$$

Table S3.5. Peak positions and structural parameters for the SAXS data in Figures 3.2, 3.3, and 3.5

Figure	NCT Sample (Core (nm)/ PS (kDa))	q_0 Peak Position	q_1/q_0	q_2/q_0	d (nm)	a (nm)
2	17/11 solution	0.0200	1.43	1.75	38.49	44.43
2	17/11 gel	0.0235	1.43	1.75	32.75	37.81
2	17/15 solution	0.0185	1.41	1.70	41.60	48.03
2	17/15 gel	0.0220	1.41	1.70	34.98	40.39
2	26/11 solution	0.0150	1.43	1.73	51.30	59.24
2	26/11 gel	0.0175	1.40	1.71	43.97	50.78
3	Gel – Initial	0.0233	1.37	1.71	33.07	38.19
3	Gel – Dried 4 hrs	0.0277	1.36	1.69	27.75	32.04
3	Gel - Resolvated	0.0230	1.42	1.74	33.53	38.72
3	Gel – 25 °C	0.0226	1.40	1.70	34.13	39.40
3	Gel – 30 °C	0.0221	1.43	1.76	34.88	40.28
3	Gel – 40 °C	0.0221	1.43	1.76	34.88	40.28
3	Gel – 50 °C	0.0221	1.43	1.74	34.88	40.28
3	Gel – 60 °C	0.0221	1.43	1.74	34.88	40.28
3	Gel – 70 °C	0.0221	1.43	1.76	34.88	40.28
3	Gel – 80 °C	0.0226	1.44	1.77	34.13	39.40
3	Gel – 85 °C, 40 min hold	0.0231	1.39	1.71	33.39	38.55
5	17/11 solid (UV)	0.0245	1.40	1.71	31.38	36.24
5	17/11 solid (non-solvent)	0.0285	1.40	1.73	26.96	31.13
	Ideal BCC	-	1.41	1.73	-	-

Thermal SAXS of Assembled NCTs

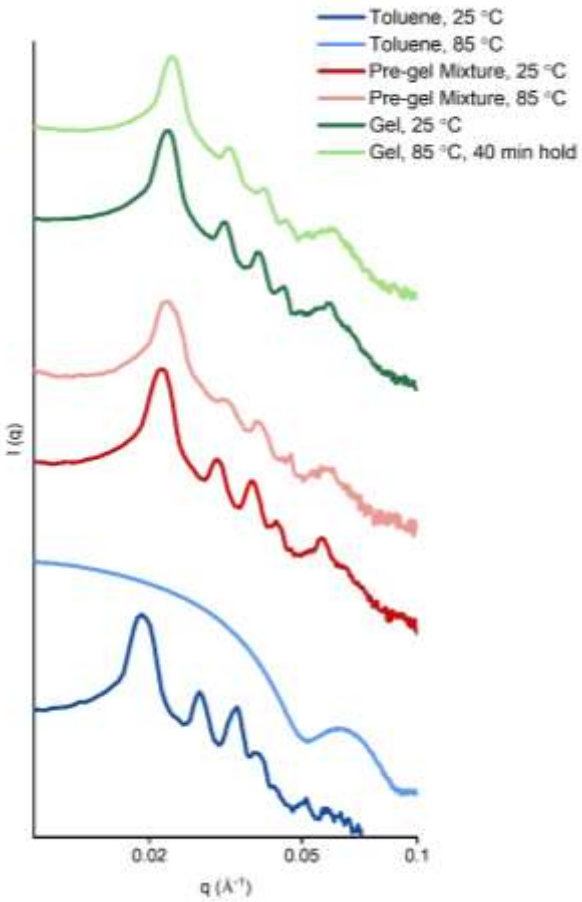

Figure S3.2. Thermal SAXS of NCTs in pure toluene (blue), NCTs in a pre-gel mixture (red), and NCTs in a PS polymer gel (green) at 25 °C (dark shade) and 85 °C (light shade). At 85 °C, only the form factor is present for NCTs in pure toluene, indicating that the NCTs have fully dissociated into free particles. While NCTs in the un-crosslinked pre-gel mixture remain assembled at 85 °C, ordering quality is diminished (indicated by the weakening intensity and loss of higher order peaks). In contrast, both NCT assembly and ordering quality are preserved even after 40 minutes at 85 °C for NCTs in the PS polymer gel.

In situ SAXS of Mechanically Deformed NCT PS Polymer Gels

Table S3.6. Structural parameters for 1D SAXS data averaged in orthogonal directions for the compression of an NCT PS polymer gel.

Compression (%)	0° a (nm)	90° a (nm)
0	39.83	39.32
35	40.81	37.75
70	41.44	36.46

Table S3.7. Structural parameters for 1D SAXS data averaged in orthogonal directions for the cyclical compression of an NCT PS polymer gel.

Cycle #	Compression (%)	0° a (nm)	90° a (nm)
1	0	39.83	39.32
	70	41.44	36.46
2	0	40.45	39.07
	70	41.40	35.95
3	0	40.35	39.10
	70	41.74	35.95
4	0	40.07	39.03
	70	42.61	36.46
5	0	40.16	38.83
	70	41.14	35.97
Final	0	40.11	39.64

NCT PnBA Polymer Gels and Polymer Solids

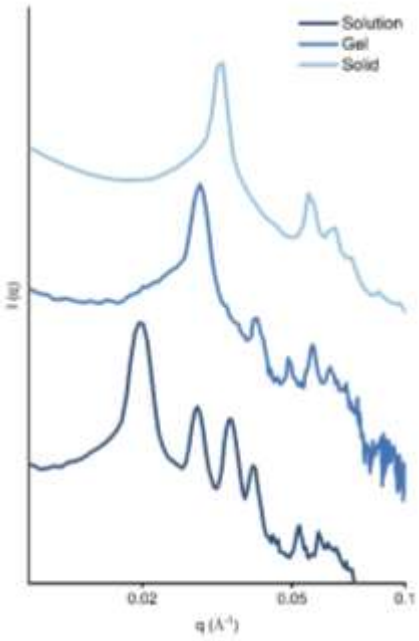

Figure S3.3. SAXS of NCTs in pure toluene, a PnBA polymer gel, and a PnBA polymer solid.

Appendix 4: Reversible Diffusionless Phase Transitions in 3D Nanoparticle Superlattices

Materials and Instrumentation

Thymine (Thy), 11-bromo-1-undecanol, 2-bromoisobutyryl bromide, sodium azide, styrene, N,N,N',N",N'"-Pentamethyldiethylenetriamine (PMDETA), and propargyl alcohol were purchased from Acros. Docosane, phosphorous acid, cyclohexamine, iodine, ferric chloride hexahydrate, oleic acid, copper (I) bromide, hydrochloric acid (HCl), melamine, and copper (II) bromide were purchased from Sigma Aldrich. 1-octadecene was purchased from Beantown Chemical. Sodium oleate was purchased from TCI America. Hexamethyldisilazane was purchased from EMD Millipore. General solvents were purchased from Fisher Scientific. All chemicals, including solvents, were used without further purification, except styrene, which was passed through a short column of basic alumina to remove inhibitor prior to polymerization. Centrifugation was performed with an Eppendorf 5424 centrifuge. UV-vis spectra and measurements were obtained on a Cary-5000 spectrophotometer. Thermal annealing was performed with a Techne Gradient Thermal Cycler. Gel permeation chromatography (GPC) characterizations were performed on an Agilent Technologies GPC system, with THF as the eluent at 1.0 mL/min, and monodisperse polystyrene as the standard. Transmission electron microscopy (TEM) was performed with a FEI Tecnai G2 Spirit TWIN transmission electron microscope. Small angle X-ray scattering (SAXS) measurements were performed on a SAXSLAB instrument with a Pilatus3R 300K detector and x-rays of wavelength 1.5409 Å. The system was calibrated using silver behenate as a standard. Scanning electron microscopy (SEM) was performed with a Zeiss Merlin High-resolution SEM at an accelerating voltage of 1kV.

Material Synthesis

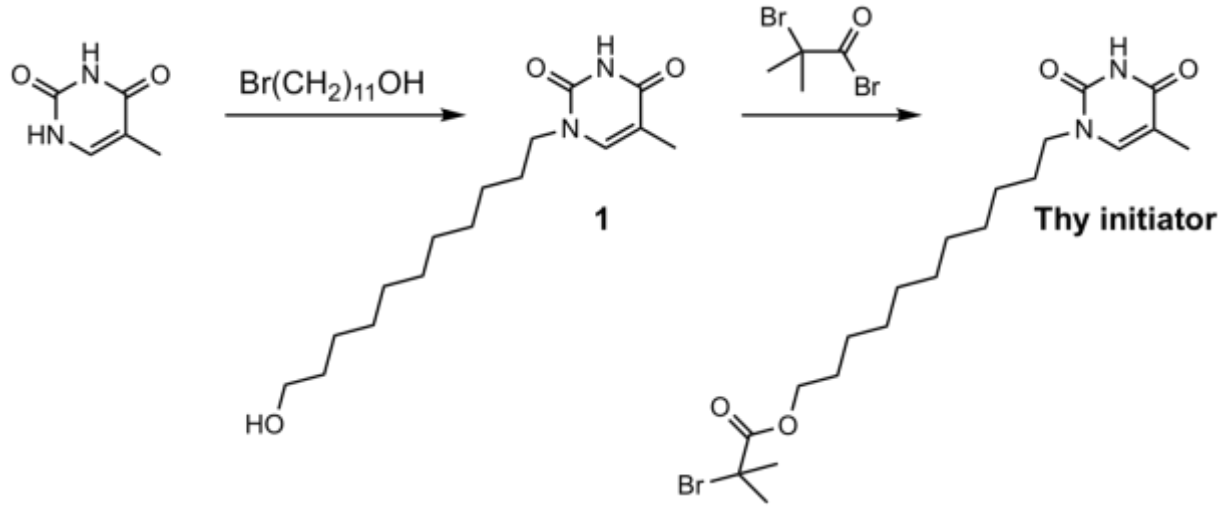

Scheme S4.1. Synthetic scheme for the Thy initiator

Thymine (Thy) Initiator Synthesis

5.0 g thymine (40 mmol), 1.0 g 11-bromo-1-undecanol (4 mmol), 1.1 g potassium carbonate (8 mmol) and 200 mL of dimethyl sulfoxide (DMSO) were added to a 500 mL round bottom flask. The mixture was stirred and bubbled with nitrogen for 2 minutes, and then sealed with a septum and stirred for 48 hours. The resulting mixture was poured into water and chloroform for extraction. The organic phase was dried with sodium sulfate, and the solvent was removed under reduced pressure. The resulting white solid was recrystallized in ethyl acetate/hexanes to afford **1** (Scheme S4.1). Using very gentle heat, 592 mg **1** (2 mmol) was dissolved in 150 mL of dichloromethane, and 0.39 mL of trimethylamine (2.8 mmol) was added to the solution. The mixture was cooled to 0 ºC, and a solution of 552 mg 2-bromoisobutyryl bromide (2.4 mmol) in dichloromethane (~ 10 mL) was added dropwise under a nitrogen atmosphere. The reaction mixture was allowed to warm to room temperature and stirred for 14 hours, and then washed with sodium carbonate (x2) and brine (x2). The organic phase was dried with sodium sulfate, and the

solvent was removed under reduced pressure. The resulting mixture was purified by flash chromatography (dichloromethane/ethyl acetate 8:3), to obtain the final Thy-initiator product. All characterization matches previous literature reports.

Propargyl Phosphonate Anchor Synthesis

The phosphonate group to anchor the Thy polymers onto iron oxide nanoparticles was synthesized according to a literature procedure.[276] Briefly, 0.41 g phosphorous acid (5 mmol, 1 eq), 10 mL propargyl alcohol (142 mmol, 34.4 eq), and 2.5 mL trimethylamine (18 mmol, 3.6 eq) were combined in a 100 mL round bottom flask. 1.9 g iodine (7.5 mmol, 1.5 eq) was slowly added with a spatula over several minutes. After reacting for 30 minutes, the mixture was precipitated in 200 mL acetone with 5 mL cyclohexamine and allowed to rest for 2 hours without stirring. The fine powder was recovered through filtration, dissolved in 30 mL hot ethanol, with 500 μL cyclohexamine and recrystallized overnight to yield the propargyl phosphate cyclohexamine salt as a white powder. Characterization matches previous literature reports.

Thy-Polystyrene Synthesis

Thy-initiator (1.0 eq), PMDETA (1.0 eq), styrene (200-300 eq depending on target molecular weight), and anhydrous anisole (30 v% to styrene) were added to an oven-dried 100 mL Schlenk flask with stir bar. The reaction flask was then sealed with a rubber septum and 3 freeze-pump-thaw cycles were performed before filling the flask with nitrogen. The septum was removed to add CuBr (1.0 eq) and the flask was quickly resealed, purged, refilled with nitrogen, and returned to room temperature. The reaction mixture was stirred at 110 °C and quenched with liquid nitrogen at different time points to obtain polymers of the desired molecular weights. The reaction mixture

was then added dropwise to methanol and the precipitated polymer was collected, redissolved in dichloromethane, and precipitated in methanol. 3 precipitations were done, ending with a polymer with a chain end bromine. The polymer was dissolved in minimal N,N-dimethylformamide (DMF) with sodium azide (4 eq) and left to stir overnight. The reaction mixture was then added dropwise to methanol and the precipitated polymer was collected, redissolved in dichloromethane, and precipitated in methanol. 3 precipitations were done, ending with an azide-terminated polymer. The alkyl functionalized phosphonate was added to the polymer through an azide-alkyne cycloaddition. The polymer (1 eq) was dissolved in DMF with the propargyl phosphate (3 eq) and PMDETA (1 eq). Three freeze-pump-thaw cycles were performed, and upon the third freeze the flask was opened under a strong nitrogen flow, and copper (I) bromide (1 eq) was added. The flask was evacuated and refilled with nitrogen twice, evacuated, thawed, and refilled with nitrogen, and heated at 30 ℃ for 48 hours. The polymer was then precipitated in methanol with 1% HCl, filtered and redissolved in dichloromethane and precipitated in methanol two more times before drying under vacuum to yield the final Thy-PS product.

Iron Oxide Nanoparticle Synthesis

Iron oxide nanoparticles (IO NP) were synthesized through the thermal decomposition of an iron oleate precursor.[277] Iron oleate precursor was first prepared by combining 10.8 g ferric chloride hexahydrate (40 mmol, 1 eq) and 36.5g sodium oleate (120 mmol, 3 eq) in a mixture of 60 mL water, 80 mL ethanol, and 140 mL hexanes. The reaction mixture was heated and allowed to reflux for 4 hours. The organic layer was then extracted 3 times with water, hexanes were removed on a rotary evaporator, and the product dried under vacuum while gradually heating to

120 °C to yield the iron oleate precursor in the form of a thick dark orange oil. Care must be taken to avoid excessive foaming during drying.

To synthesize nanoparticles, 6.4 g iron oleate precursor, oleic acid, and solvent were combined in a 250 mL three-necked flask equipped with a reflux condenser and temperature probe. The flask was heated to 120℃ while stirring, evacuated and refilled with nitrogen three times, and then heated to reflux at a controlled rate of 6℃/min. After refluxing for 1 hour, the reaction mixture was allowed to cool, transferred to a storage container, and stored as a solid in the refrigerator.

The size of the nanoparticles could be controlled by varying the solvent and amount of oleic acid. 10 nm particles were synthesized using 100 mL 1-octadecene and 2.0 g oleic acid and 24 nm particles were synthesized using 25 mL docosane and 2.0 g oleic acid.

Iron Oxide NCT Synthesis

10 nm NCTs

In a 20 mL glass vial, 750 mg 10 nm IO NP reaction mixture in 1-octadecene (a solid) was dissolved in 12 mL of tetrahydrofuran (THF). The nanoparticles were centrifuged (70 minutes, 13.5k rpm) and redispersed in THF 2 times to remove residual solvent and reaction byproducts, and concentrated to 1 mL THF. Concentrated nanoparticles were added to 25 mg of Thy-polystyrene, and the solution briefly sonicated before being shaken (600 rpm) at room temperature overnight. The next day, functionalized NCTs were diluted 4-fold with THF and were centrifuged (80 minutes, 14.5k rpm) and redispersed 3 times in THF, THF, and toluene, and concentrated to 1 mL in toluene.

24 nm NCTs

In a 20 mL glass vial, 450 mg 24 nm IO NP reaction mixture in 1-octadecene (a solid) was dissolved in 20 mL of THF. The nanoparticles were centrifuged (40 minutes, 8.0k rpm) and redispersed in THF 2 times to remove residual solvent and reaction byproducts, and concentrated to 1 mL THF. Concentrated nanoparticles were added to 15 mg of Thy-polystyrene, and the solution briefly sonicated before being shaken (600 rpm) at room temperature overnight. The next day, functionalized NCTs were diluted 4-fold with THF and were centrifuged (40 minutes, 8.5k rpm) and redispersed 3 times in THF, THF, and toluene, and concentrated to 1 mL in toluene.

Thy-Melamine NCT Assembly

A fresh melamine stock solution was prepared prior to assembly by dissolving 25 mg of melamine in a solution of 1 mL DMSO and 1 mL DMF. A 495 µM melamine solution in toluene was then prepared by mixing 5 µL of the melamine stock solution with 995 µL of toluene for immediate use. Thy-Melamine NCT assemblies were formed in a 0.5 mL centrifuge tube by mixing 200 µL of solvent (toluene, anisole, or a combination of toluene and anisole, see Figure S4.4), 100 µL of concentrated Thy NCTs in toluene, and 100 µL of 495 µM melamine solution in toluene. To obtain crystalline structures, after assembly, samples were heated to 65 °C and then cooled to 25 °C at a rate of 0.1 °C/min.

NCT Solvent Exchange and Drying

Assembled NCTs in toluene were allowed to settle to the bottom of the centrifuge tube. The supernatant was then replaced with 100 µL toluene to remove any excess free particles or melamine. A non-solvent for IO NCTs, n-decane, was gradually added to increase the % n-decane

in solution by 10% every 20 minutes. After reaching 90% n-decane, the supernatant was removed and replaced with 100 μL n-decane.

NCT solutions containing at least 40% n-decane were dried ambiently or under vacuum at room temperature to obtain ordered BCC solids. NCT solutions containing 40% n-decane were rapidly dried at 110 °C to obtain ordered FCC solids,

Additional Characterization and Discussion

Iron Oxide Nanoparticles

To prepare samples for TEM, IO NPs were centrifuged and redispersed twice in 50/50 acetone/THF and toluene to remove remove residual solvent and reaction byproducts. Particles were them dropcast onto formvar coated TEM grids. Analysis was performed in ImageJ.

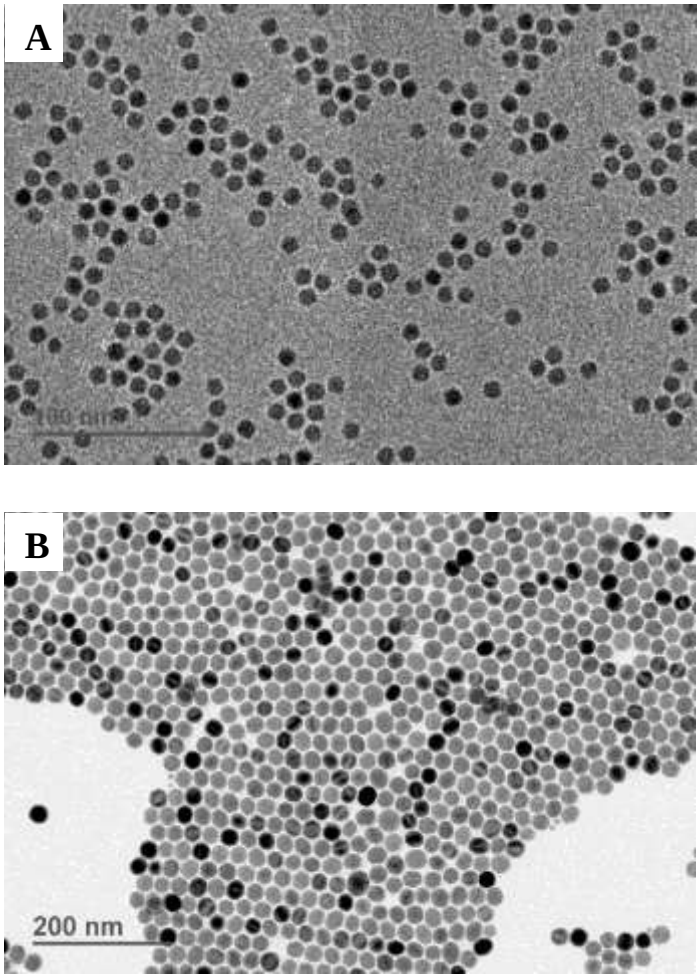

Figure S4.1. TEM images of the iron oxide nanoparticles used in this work. (A) IO NPs with an average diameter of 9.8 nm (B) IO NPs with an average diameter of 24.2 nm.

Table S4.1. Size and dispersity of the iron oxide nanoparticles used in this work

Nanoparticles	Diameter (nm)	RSD (%)
10 nm IO NP	9.8	7.4
24 nm IO NP	24.2	6.5

.Polymers

Gel permeation chromatography (GPC) characterizations were performed on an Agilent Technologies GPC system, with THF as the eluent at 1.0 mL/min, and monodisperse polystyrene as the standard.

Table S4.2. Molecular weight and dispersity of the Thy-PS polymers used in this work

Polymer	M_n (kDa)	Đ
8K Thy-PS	7.9	1.03
10K Thy-PS	9.7	1.01
13K Thy-PS	12.6	1.02

Rapid Assembly of Thy-MA NCT Assemblies

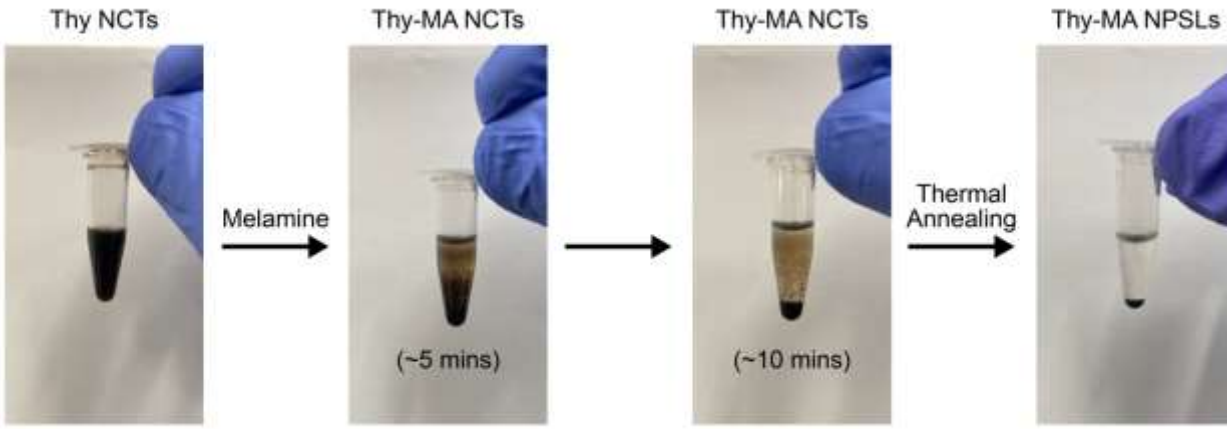

Figure S4.2. The addition of melamine to the Thy-NCTs in toluene resulted in the rapid formation of aggregates within minutes, which upon thermal annealing formed NPSLs with FCC symmetry.

SAXS of NCT Assemblies

Assembled NCTs were prepared by thermally annealing NCTs (65 °C-25 °C at 1 min/0.1 °C) in a thermal cycler. Each sample was added to a short section of 1.5mm diameter Polyimide Tubing (Cole-Parmer) and sealed at both ends with epoxy. 1-dimensional SAXS data was obtained via radial averaging of the 2-dimensional scattering pattern. Data was then transformed into profiles of scattering intensity as a function of scattering vector q. Body-centered cubic (BCC) and face-centered cubic (FCC) ordering were confirmed, with structural parameters

$$a_{BCC} = \frac{2\pi\sqrt{2}}{q_0}$$

$$a_{FCC} = \frac{2\pi\sqrt{3}}{q_0}$$

$$d_{BCC} = d_{FCC} = \frac{\pi\sqrt{6}}{q_0}$$

SAXS of Thy-MA NCT Assemblies in Toluene

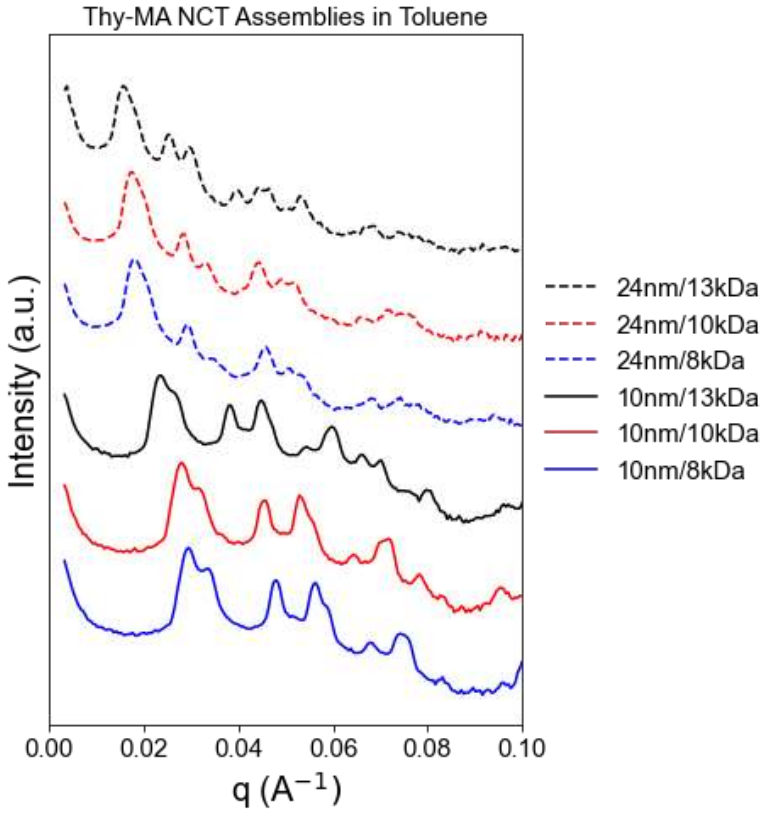

Figure S4.3. SAXS data of Thy-MA NCT assemblies in toluene. Indexing of peaks (Table S4.3) indicate that the NCT assemblies have FCC symmetry.

Table S4.3. Peak positions and structural parameters for the SAXS data in Figure S4.3. As the q_1 peaks in the 24nm NCT assemblies appeared as faint shoulders in the q_0 peaks, they were difficult to measure accurately and were thus omitted in the peak position calculations.

Sample	q_0 Peak Position	q_1/q_0	q_2/q_0	q_3/q_0	d (nm)	a (nm)	Structure
10nm/8kDa	0.030	1.13	1.62	1.91	26.05	36.83	FCC
10nm/10kDa	0.028	1.12	1.62	1.88	27.43	38.79	FCC
10nm/13kDa	0.024	1.13	1.61	1.90	32.62	46.14	FCC
24nm/8kDa	0.018	-	1.60	1.90	42.45	60.03	FCC
24nm/10kDa	0.018	-	1.63	1.88	43.72	61.83	FCC
24nm/13kDa	0.016	-	1.60	1.89	49.18	69.55	FCC
Ideal FCC	-	1.15	1.63	1.91	-	-	-

Table S4.4. Peak positions and structural parameters for the 10nm/10kDa SAXS data in Figure 4.2a.

% n-Decane	q_0 Peak Position	q_1/q_0	q_2/q_0	q_3/q_0	d (nm)	a (nm)	Structure
0	0.028	1.14	1.62	1.88	27.43	38.79	FCC
10	0.029	-	1.63	1.90	26.95	38.11	FCC
20	0.030	-	1.62	1.90	26.05	36.83	FCC
30	0.031	-	1.62	1.90	24.80	35.07	FCC
40	0.033	-	1.64	1.92	23.66	33.46	FCC
50	0.036	1.41	1.73	1.99	21.38	24.68	BCC
60	0.038	1.42	1.73	1.99	20.25	23.39	BCC
70	0.040	1.41	1.72	1.99	19.24	22.21	BCC
80	0.041	1.41	1.73	1.98	18.59	21.46	BCC
90	0.042	1.40	1.72	1.99	18.32	21.16	BCC
100	0.043	1.42	1.74	2.01	17.71	20.45	BCC
Ideal FCC	-	1.15	1.63	1.91	-	-	-
Ideal BCC	-	1.41	1.73	2.00	-	-	-

Table S4.5. Peak positions and structural parameters for the 24nm/10kDa SAXS data in Figure 4.2b. As the q_1 peaks in the 24nm/10kDa NCT NPSLs appeared as faint shoulders in the q_0 peaks, they were difficult to measure accurately and were thus omitted in the peak position calculations.

% n-Decane	q_0 Peak Position	q_1/q_0	q_2/q_0	q_3/q_0	d (nm)	a (nm)	Structure
0	0.018	-	1.63	1.88	43.72	61.83	FCC
10	0.018	-	1.65	1.93	43.64	61.72	FCC
20	0.018	-	1.63	1.91	42.52	60.13	FCC
30	0.019	-	1.64	1.99	41.37	58.51	FCC
40	0.020	-	1.61	1.96	39.26	55.52	FCC
50	0.020	-	1.62	1.96	38.29	54.14	FCC
60	0.021	-	1.61	1.92	36.47	51.58	FCC
70	0.022	-	1.61	1.92	34.82	49.24	FCC
80	0.023	-	1.62	1.90	34.06	48.16	FCC
90	0.023	-	1.62	1.90	33.32	47.13	FCC
100	0.023	-	1.64	1.92	33.37	47.19	FCC
Ideal FCC	-	1.15	1.63	1.91	-	-	-
Ideal BCC	-	1.41	1.73	2.00	-	-	-

Thermoreversibility of Thy-MA NCT Assembly

During the thermal annealing process, NCTs are first heated above their melting temperature (T_m), then gradually cooled below the T_m to obtain ordered NCT assemblies. To determine the annealing protocol, NCT T_m was obtained for each NCT core/polymer combination by measuring the solution absorbance while heating at a fixed rate (0.25 °C/min) to generate a melt curve. The T_m is the temperature at which the melt curve is the steepest. The 10 nm series of NCTs all exhibited a T_m below 60 °C in toluene. To reduce the T_m of the 24 nm series of NCTs to match that of the 10 nm series, anisole was added to toluene to increase the polarity of the solvent. The higher the solvent polarity, the weaker the Thy-MA binding becomes, resulting in a lower T_m.

Before each melt, quartz cuvettes were cleaned with hydrochloric acid to remove residual iron oxide, followed by five water rinses. Cuvettes were then placed in a sealed chamber containing a 1:1 hexamethyldisilazane:n-hexane solution at room temperature overnight before use. Samples were prepared by adding equal volumes of complementary NCTs in toluene to a cuvette, then given 20 minutes to stir to ensure full assembly. The absorbance of each sample was measured at 325 nm and heated at a rate of 0.25°C/min from 20°C – 95°C to generate melt curves. For each measurement, samples were stirred during heating to maintain homogeneity. Experimental melt curves were normalized and plotted in Figure S4.4 below.

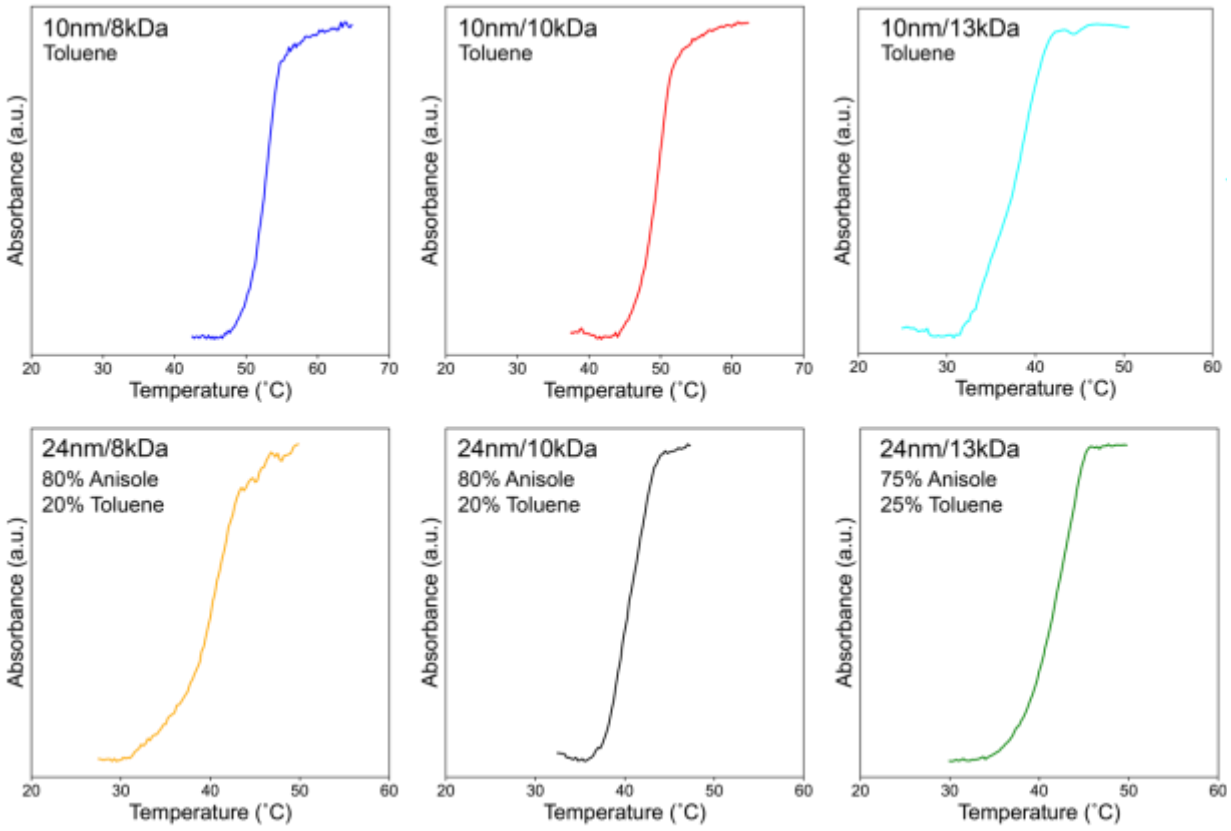

Figure S4.4. Melting curves for the NCTs used in this work. Anisole was used to lower the T_m of the 24 nm NCTs to allow the same thermal annealing protocol to be used for the assembly of both 10 nm and 24 nm NCTs.

SAXS Data of the 10 nm Thy-MA NCT Assemblies in Solutions with Varying Vol% of n-Decane

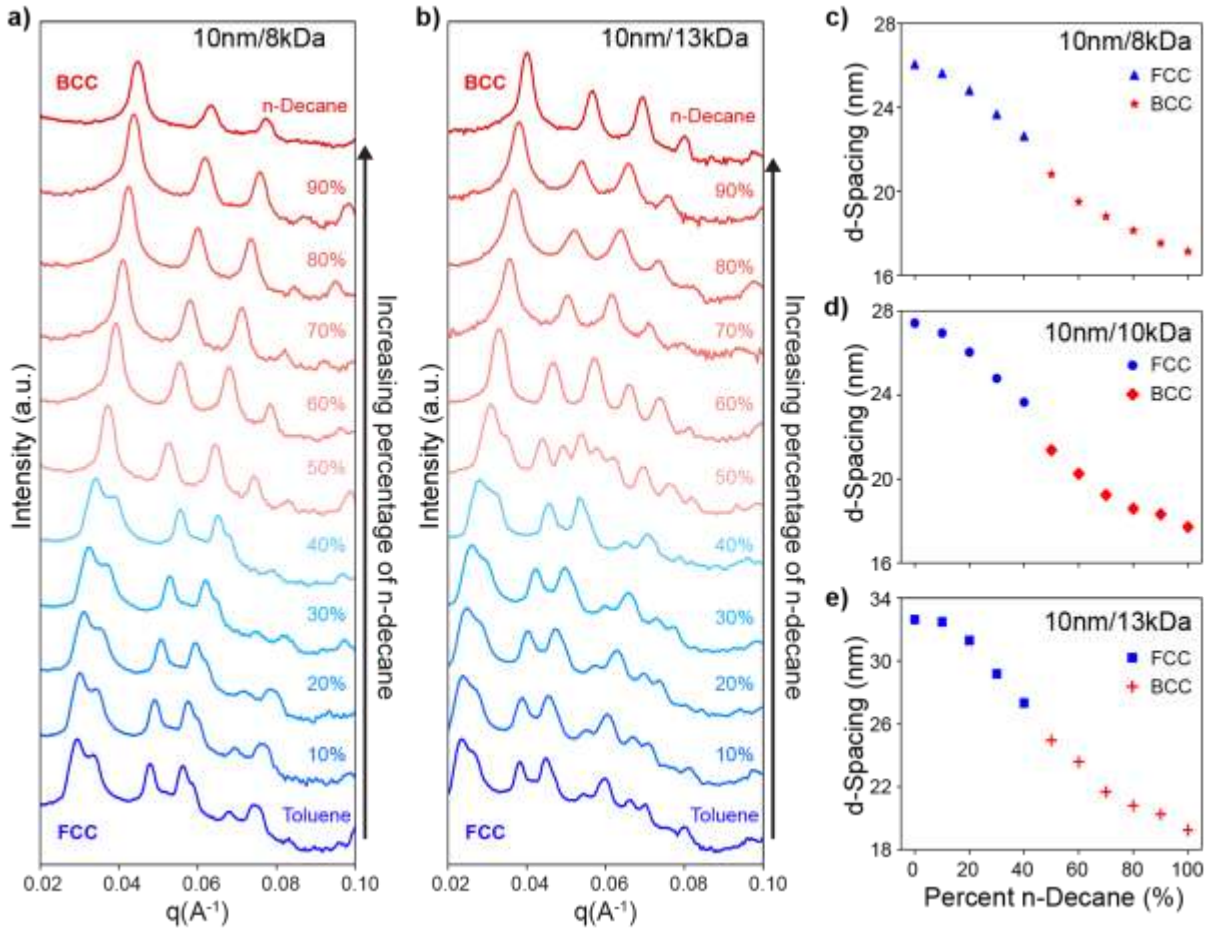

Figure S4.5. SAXS data showing the phase transition of the a) 10nm/8kDa and b) 10nm/13kDa Thy-MA assemblies from FCC (blue) to BCC (red) as a function of n-decane vol%. d-Spacing values of the c) 10nm/8kDa, d) 10nm/10kDa, and e) 10nm/13kDa Thy-MA NCT assemblies as a function of percent n-decane. The decrease in the d-spacing is due to the collapse of the polymer brush with increasing amounts of n-decane.

SAXS Data of the FCC and BCC Coexistence Points in the 10nm Thy-MA NCT Assemblies

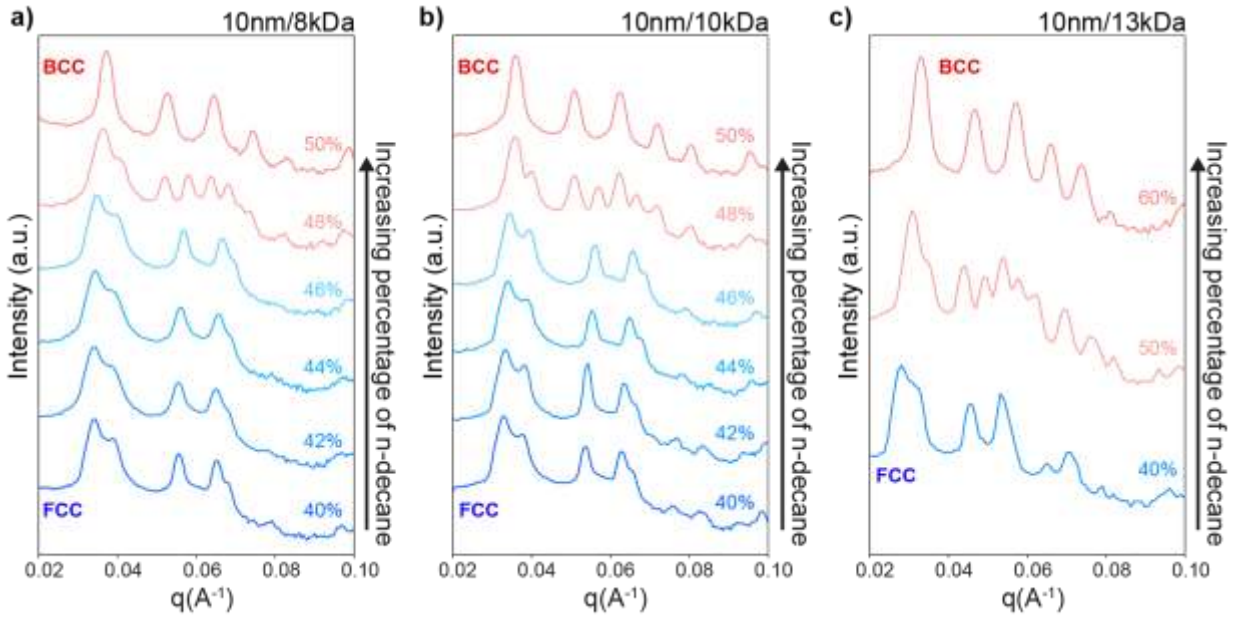

Figure S4.6. SAXS data showing the emergence of the FCC and BCC coexistence point at a particular n-decane vol%. a) 10nm/8kDa at 48 vol%, b) 10nm/10kDa at 48 vol%, and c) 10nm/13kDa at 50 vol%.

SAXS Data of the 24 nm Thy-MA NCT Assemblies in Solutions with Varying Vol% of n-Decane

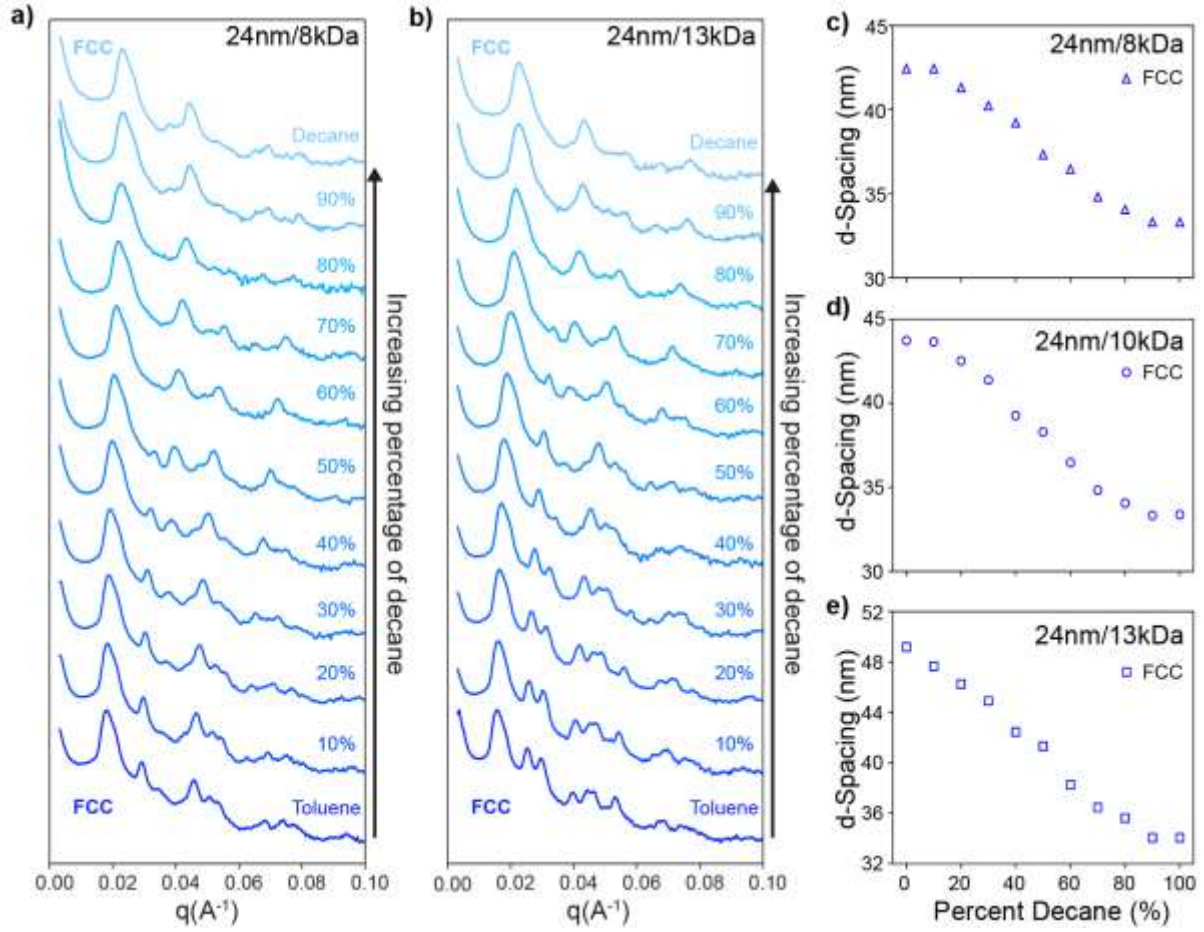

Figure S4.7. SAXS data showing that the a) 24nm/8kDa and b) 24nm/13kDa Thy-MA assemblies formed FCC in toluene and remained FCC regardless of the vol% of n-decane introduced. d-Spacing values of the c) 24nm/8kDa, d) 24nm/10kDa, and e) 24nm/13kDa Thy-MA NCT assemblies as a function of percent n-decane. The decrease in the d-spacing is due to the collapse of the polymer brush with increasing amounts of n-decane.

Thermoreversible Phase Transitions in the 10nm Thy-MA NCT Assemblies

To demonstrate the thermoreversibility of the phase transition, NCT assemblies that had already undergone a phase transition were heated in-situ during SAXS measurement. n-Decane was first added to the 10nm Thy-MA NCT assemblies in toluene until the transition point was reached (50 – 60 vol% n-decane). The phase transitioned samples were then added to a short section of 1.5mm diameter Polyimide Tubing and sealed at both ends with epoxy. SAXS data was then collected as the samples were heated in-situ inside the chamber.

10nm/10kDa

As shown in Figure S4.8a and Figure 3a, the 10nm/10kDa Thy-MA NCT assemblies in 50 vol% n-decane underwent a BCC to FCC phase transition at 60˚C. Holding the NCT assemblies at 110˚C for 60 minutes resulted in no change to the crystal structure, indicating that the FCC phase was the equilibrium phase at this temperature. When cooled back to room temperature, the NCT assemblies remained FCC, although they reverted back to BCC within 24 hours. When these thermal transition experiments were repeated in a poorer solvent for polystyrene (60 vol% n-decane), a much higher temperature was required to initiate the phase transition. The mixed FCC and BCC phases were only observed at 110 ˚C, with complete transformation to the FCC equilibrium phase only occurring after holding at 110˚C for 20 minutes (Figure S4.8b, c). Similar to the 50 vol% n-decane assemblies, the FCC phase also persisted below the transformation temperature due to kinetic effects. However, the larger driving force to adopt the more stable BCC phase meant that complete reversion to the BCC phase occurred immediately as the assemblies were cooled to 40 ˚C.

10nm/8kDa

The phase behavior of the 10nm/8kDa Thy-MA NCT assemblies in 50 vol% n-decane as a function of temperature is shown in Figure S4.9. Similar to the 10nm/10kDa NCT assemblies, the 10nm/8kDA NCT assemblies underwent a BCC to FCC phase transition at 60˚C. Holding the assemblies at 110˚C for 60 minutes resulted in no change to the crystal structure. Upon cooling to RT, the assemblies remained in the FCC phase but reverted back to the BCC phase within a day.

10nm/13kDa

The phase behavior of the 10nm/13kDa Thy-MA NCT assemblies in 60 vol% n-decane as a function of temperature is shown in Figure S4.10. The assemblies remained BCC until heated to 80˚C where both BCC and FCC phases were detected. Upon further heating, the assemblies transformed completely to the FCC phase and remained as such even after heating at 110˚C for 60 minutes. Cooling the assemblies to 50˚C resulted in the reversion of the FCC phase back to the BCC phase, with the detection of both FCC and BCC phases. Further cooling resulted in the complete reversion to the equilibrium BCC phase.

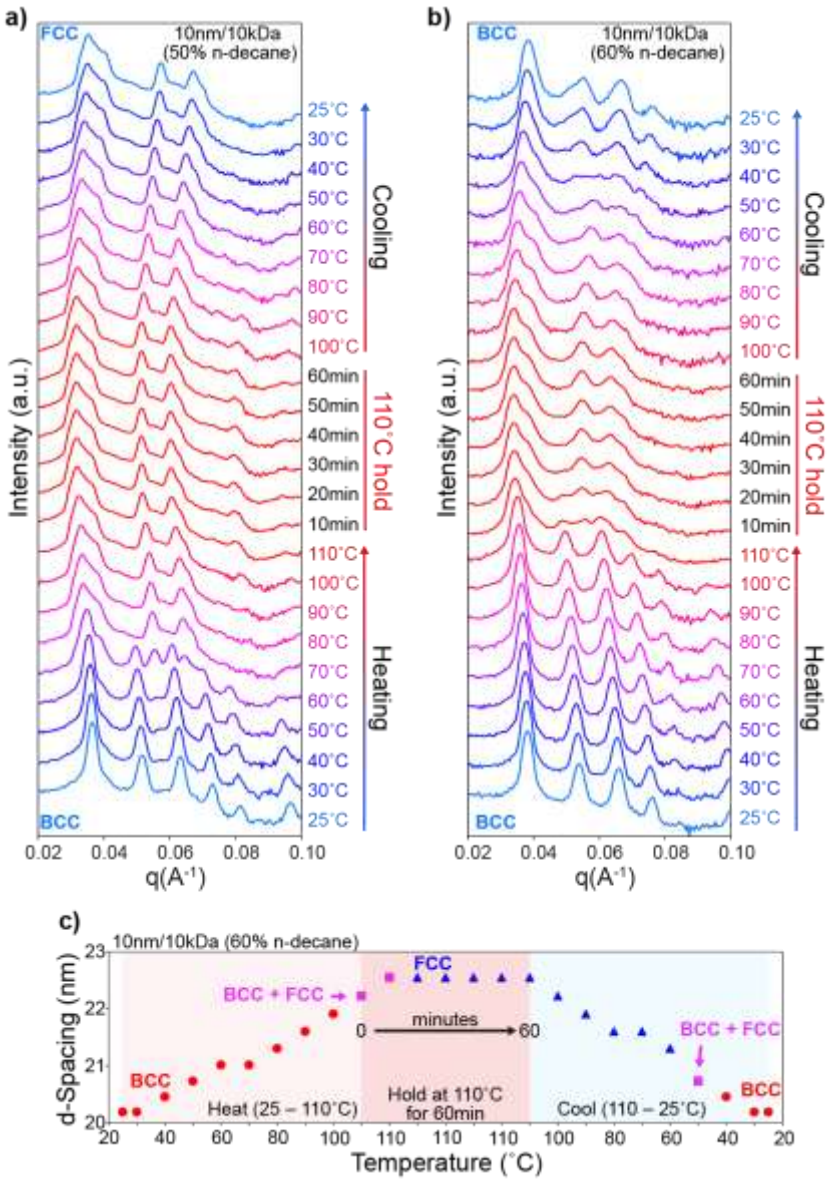

Figure S4.8. SAXS data showing the phase behavior of the 10nm/10kDa Thy-MA NCT assemblies in a) 50 vol% n-decane and b) 60 vol% n-decane as a function of temperature. c) d-Spacing and crystal symmetry of the 10nm/10kDa Thy-MA NCT assemblies in 60 vol% n-decane.

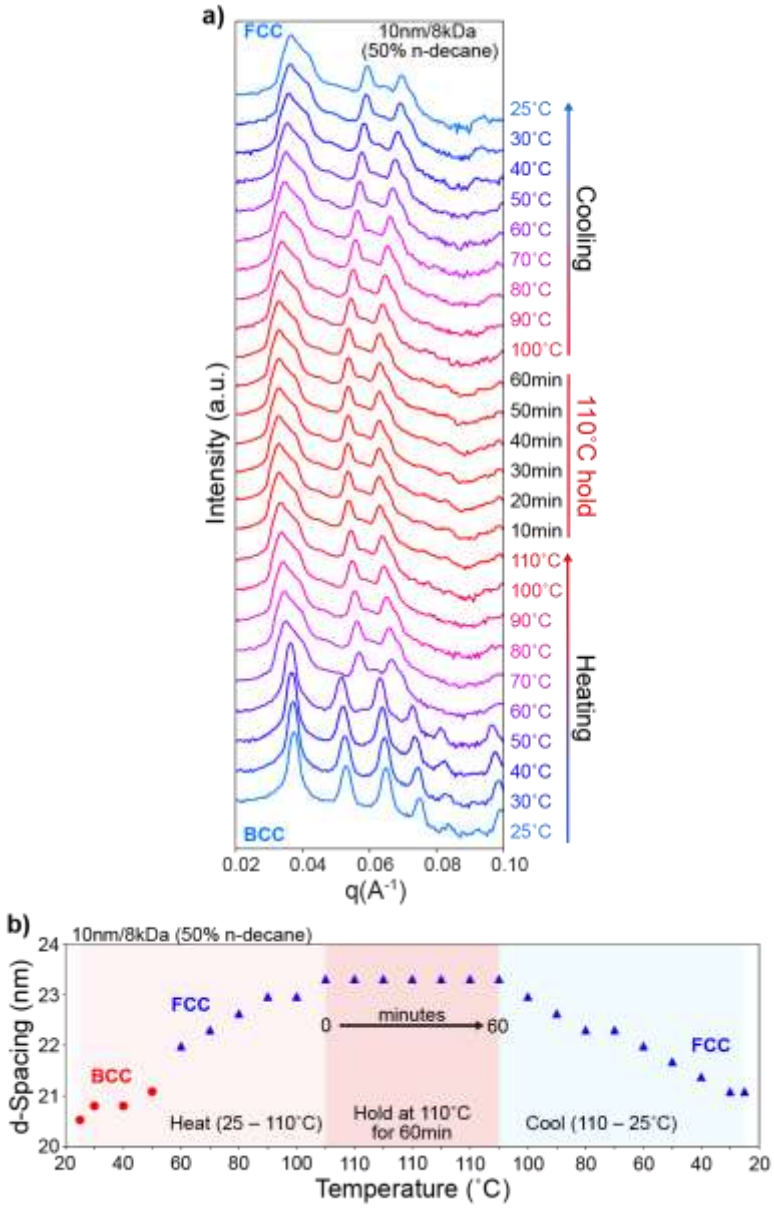

Figure S4.9. a) SAXS data showing the phase behavior of the 10nm/8kDa Thy-MA NCT assemblies in 50 vol% n-decane as a function of temperature. b) d-Spacing and crystal symmetry of the 10nm/8kDa Thy-MA NCT assemblies in 50 vol% n-decane.

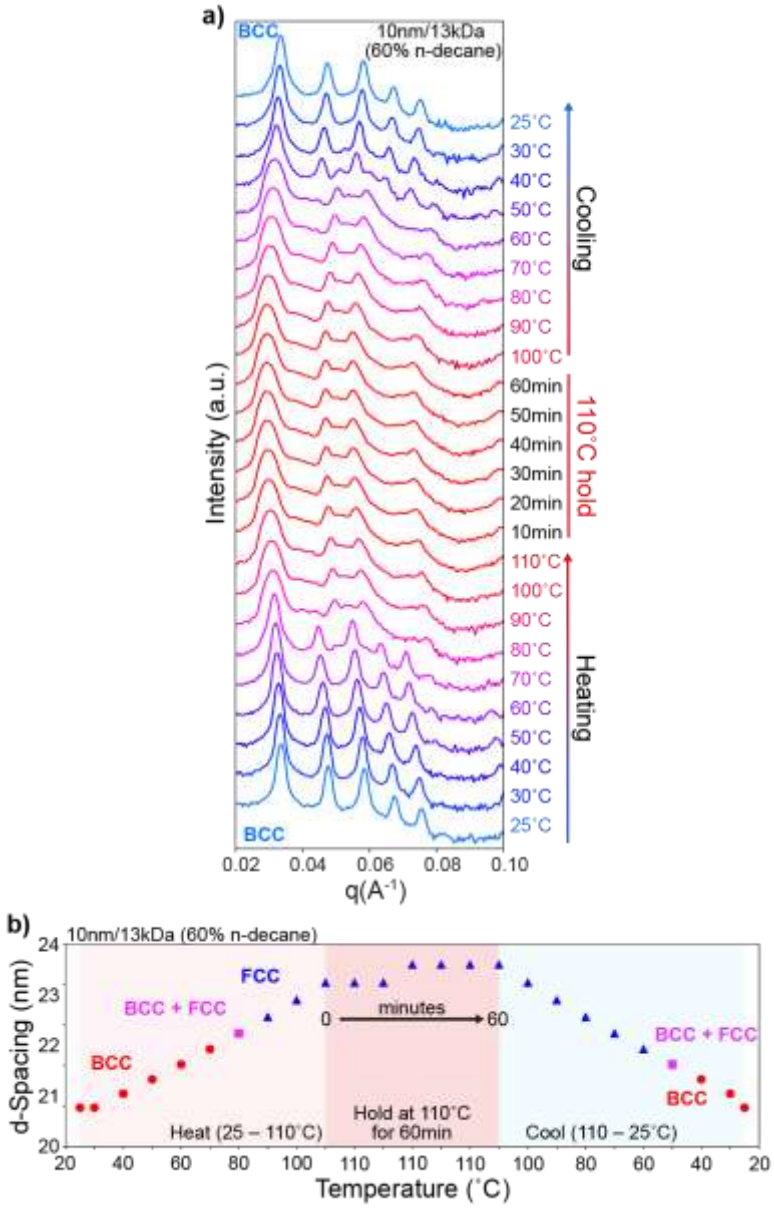

Figure S4.10. a) SAXS data showing the phase behavior of the 10nm/13kDa Thy-MA NCT assemblies in 60 vol% n-decane as a function of temperature. b) d-Spacing and crystal symmetry of the 10nm/13kDa Thy-MA NCT assemblies in 60 vol% n-decane.

Using Solvent Quality to Reverse the Phase Transition of the 10nm/8kDa and 10nm/13kDa NCT Assemblies

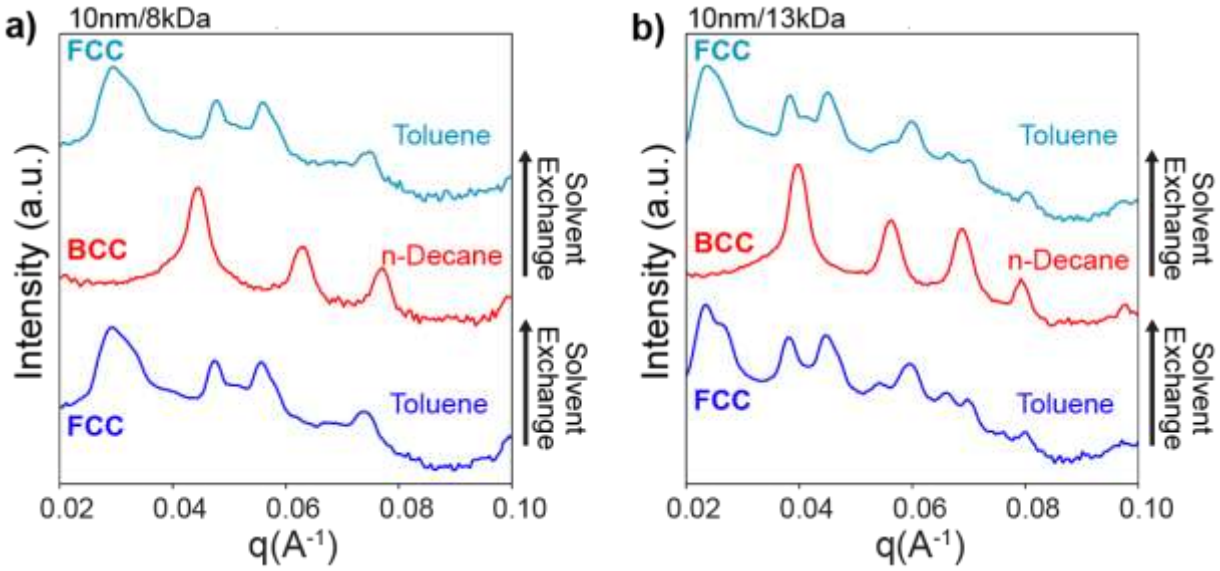

Figure S4.11. SAXS data showing that the phase transitions observed in the a) 10nm/8kDa and b) 10nm/13kDA NCT assemblies are reversible with respect to solvent quality. Replacing n-decane with toluene resulted in the reversion of the BCC assemblies to FCC.

Drop Casting of the 10 nm NCT Assemblies at Elevated Temperatures

To determine the solvent removal temperature, we conducted in-situ thermal SAXS to find the maximum temperature at which the assemblies remained stable (Figures S12). We observed that drop casting the partially collapsed NCT assemblies onto a substrate preheated to the maximum stability temperature (100˚C) allowed us to obtain the FCC phase. It is important to note the changing composition of the solvent during the drying process. As toluene evaporates faster than n-decane, the solvent gets poorer during the process; the elevated temperature thus also improves polymer-solvent interactions, which maintains the FCC phase. Interestingly, we found that for the 10nm/13kDa assemblies, we had to pre-collapse the chains more (50 vol% n-decane) prior to heating in order to obtain the dried FCC phase (Figure S4.13). However, when the solvent was rapidly removed from the 10nm/8kDa assemblies, only amorphous structures were obtained (Figure S4.13), indicating that there may be a minimum polymer length required for kinetic trapping.

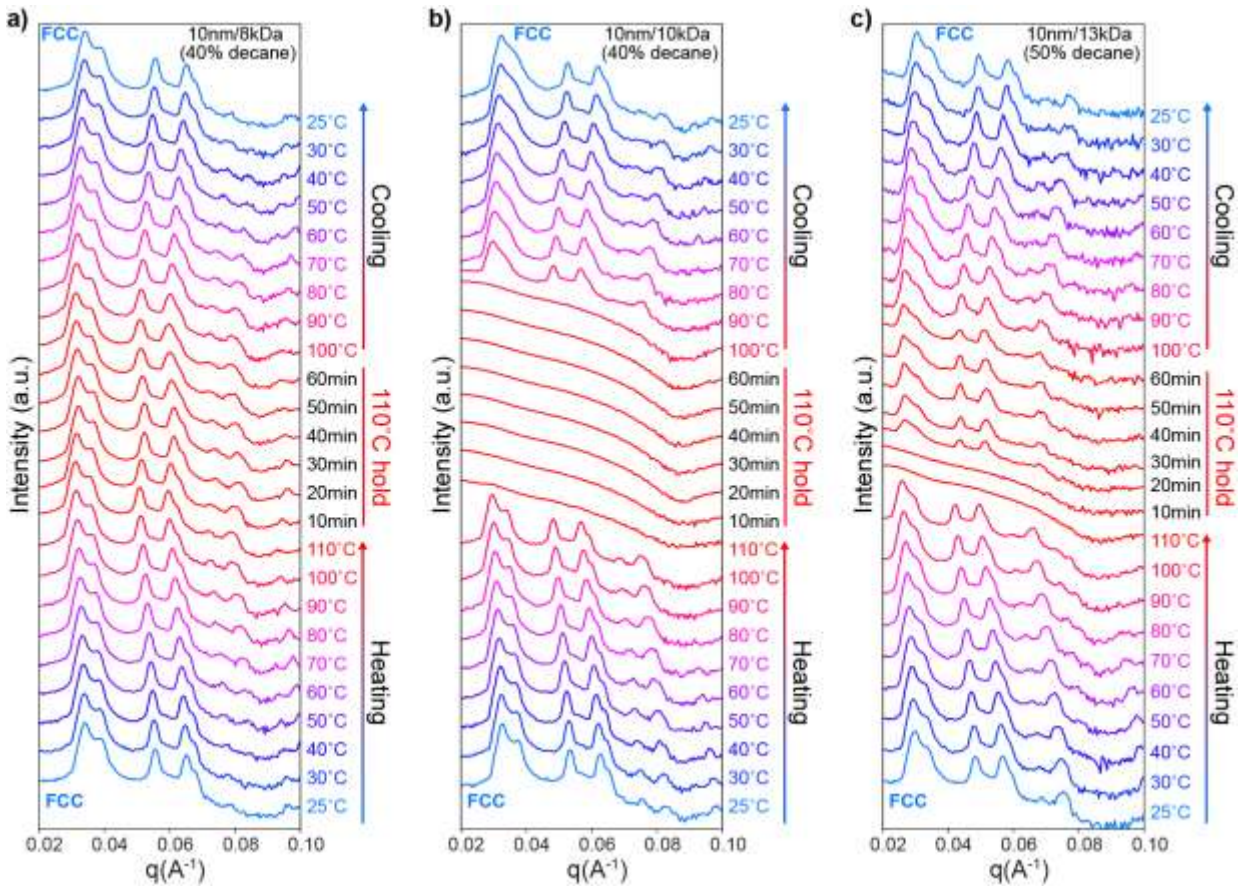

Figure S4.12. SAXS data showing the phase behavior of the a) 10nm/8kDa Thy-MA NCT assemblies in 40 vol% n-decane, b) 10nm/10kDa NCT assemblies in 40 vol% n-decane, and c) 10nm/13kDa NCT in 50 vol% n-decane as a function of temperature. For the 10nm/10kDa assemblies, melting was observed at 110˚C, so a drop casting temperature of 100˚C was selected.

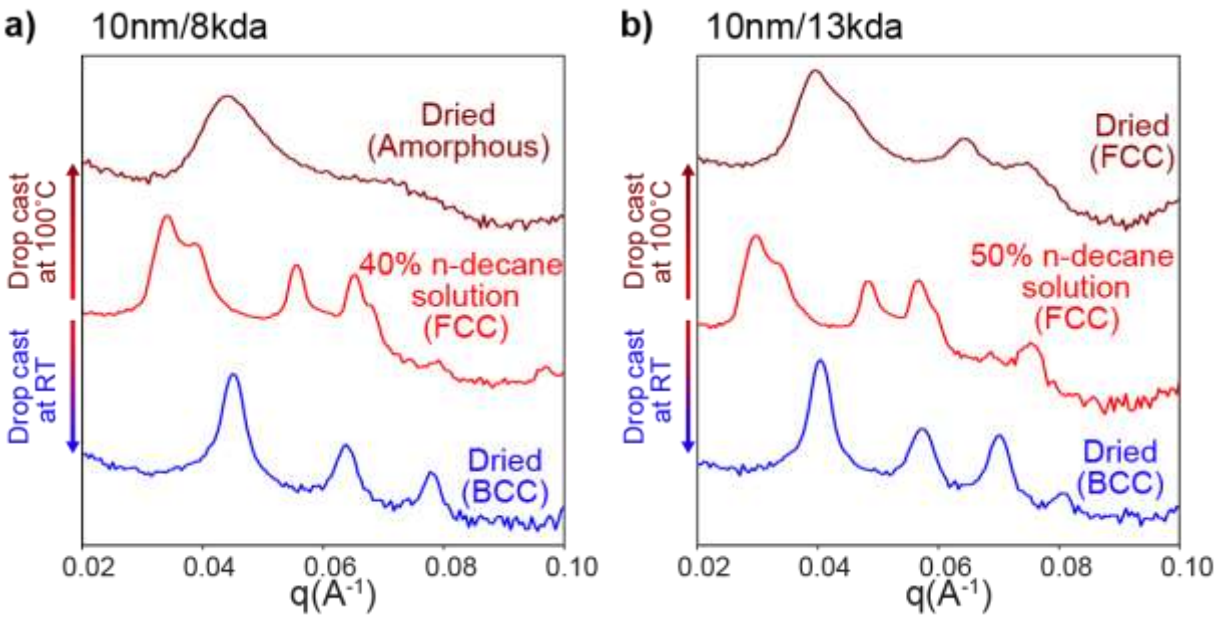

Figure S4.13. a) SAXS data of 10nm/8kDa NCT assemblies in 40 vol% n-decane dried rapidly at 100˚C and slowly at room temperature. Room temperature and rapid drying yielded BCC and amorphous structures respectively. b) SAXS data of 10nm/13kDa NCT assemblies in 50 vol% n-decane dried rapidly at 100˚C and slowly at room temperature. Room temperature and rapid drying yield BCC and FCC structures respectively.

Table S4.6. Peak positions and structural parameters for the SAXS data of the dried assemblies in Figure 4.4a and S4.13

Sample	q_0 Peak Position	q_1/q_0	q_2/q_0	q_3/q_0	d (nm)	a (nm)	Structure
10nm/8kDa (Drop cast RT)	0.045	1.42	1.73	-	17.13	19.77	BCC
10nm/8kDa (Drop cast 100˚C)	0.044	-	-	-	14.30	-	Amorphous
10nm/10kDa (Drop cast RT)	0.043	1.40	1.72	-	17.71	20.45	BCC
10nm/10kDa (Drop cast 100˚C)	0.042	1.16	1.63	1.89	18.13	25.64	FCC
10nm/13kDa (Drop cast RT)	0.040	1.42	1.74	1.98	19.02	21.96	BCC
10nm/13kDa (Drop cast 100˚C)	0.039	1.16	1.62	1.89	19.49	27.57	FCC
Ideal FCC	-	1.15	1.63	1.91	-	-	-
Ideal BCC	-	1.41	1.73	2.00	-	-	-

SEM Images of the Thy-MA NCT Assemblies

10nm/10kDa FCC

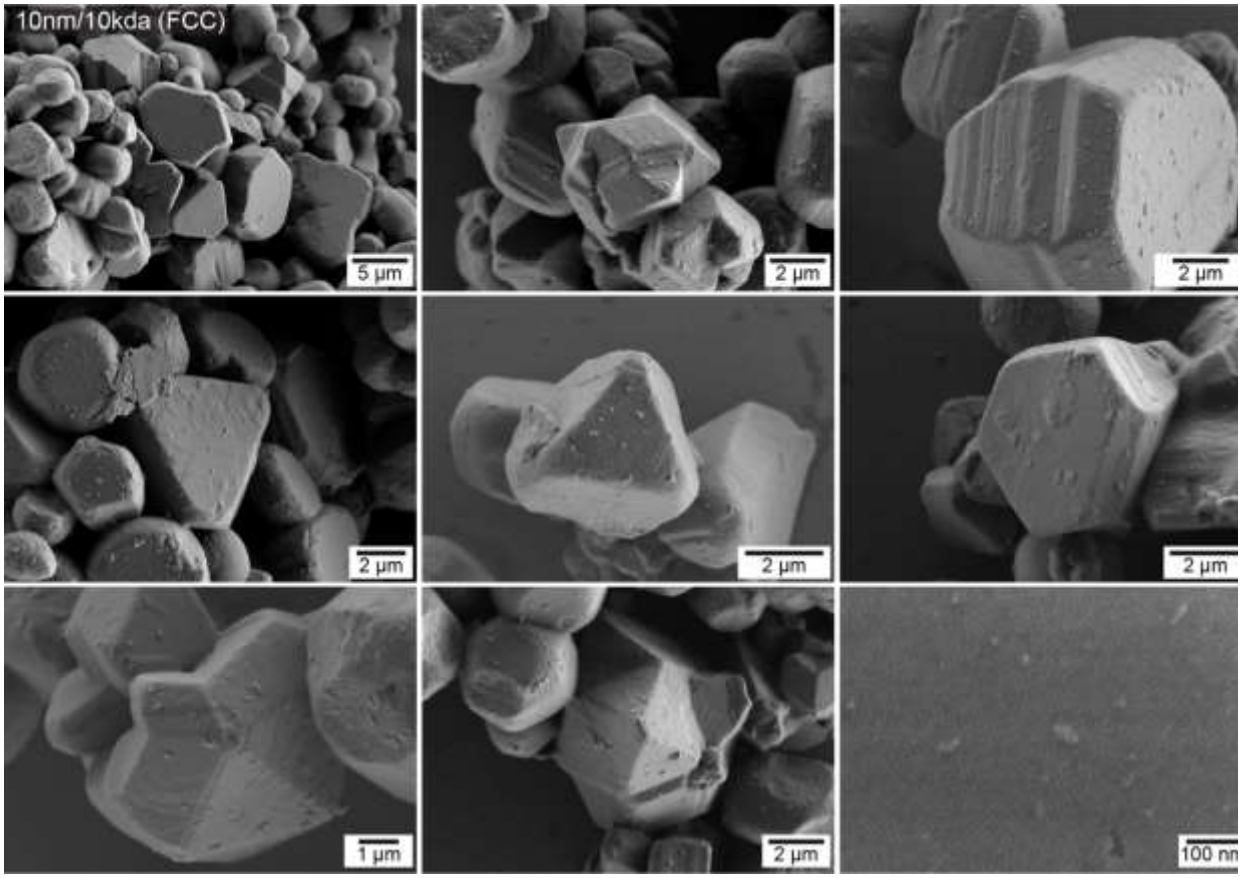

Figure S4.14. SEM images of the 10nm/10kDa FCC NCT assemblies. Stacking faults, twins, and multiply twinned structures were observed in the dried assemblies. Close-packed (111) planes could also be observed on the faces of the structures.

10nm/13kDa FCC

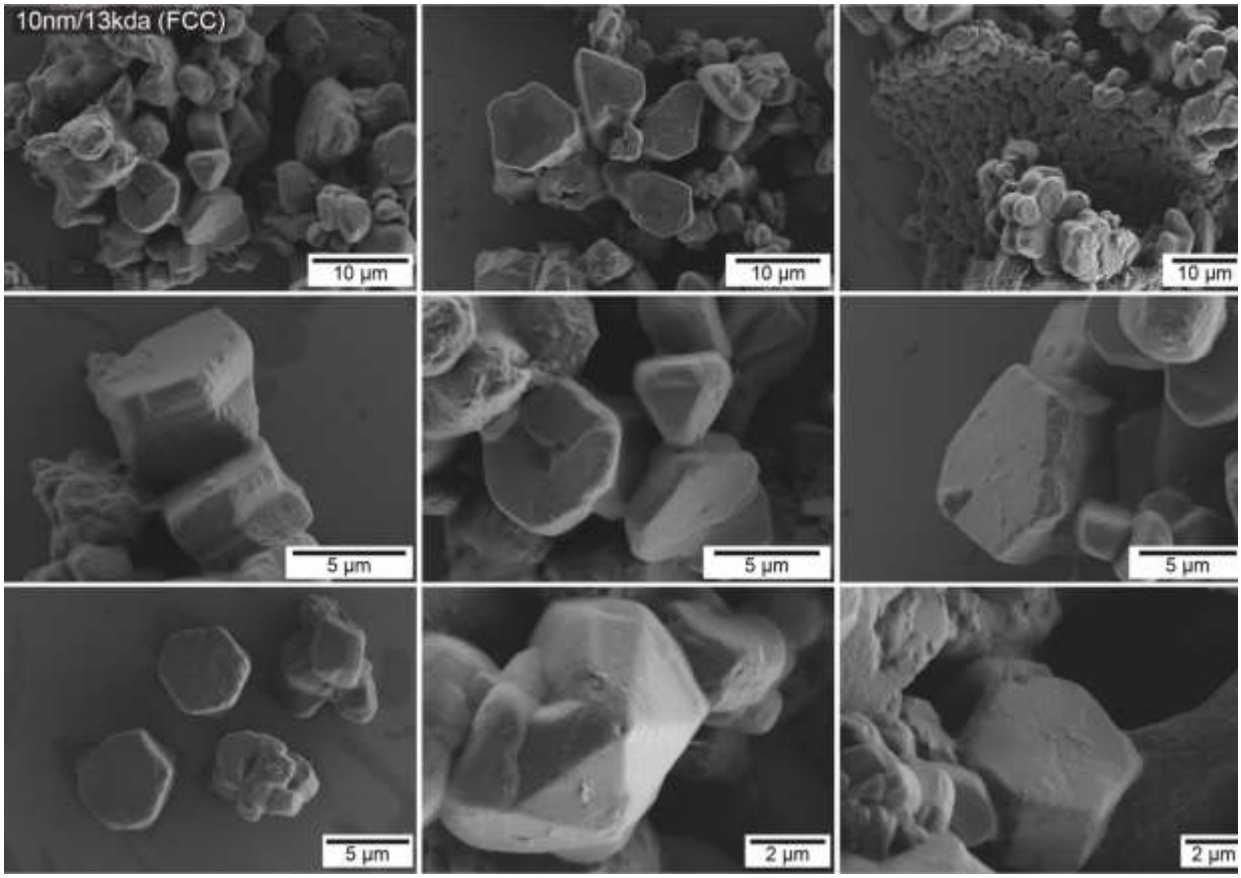

Figure S4.15. SEM images of the 10nm/13kDa FCC NCT assemblies. Stacking faults, twins, and multiply twinned structures were observed in the dried assemblies. Close-packed (111) planes could also be observed on the faces of the structures.

24nm/8kDa FCC

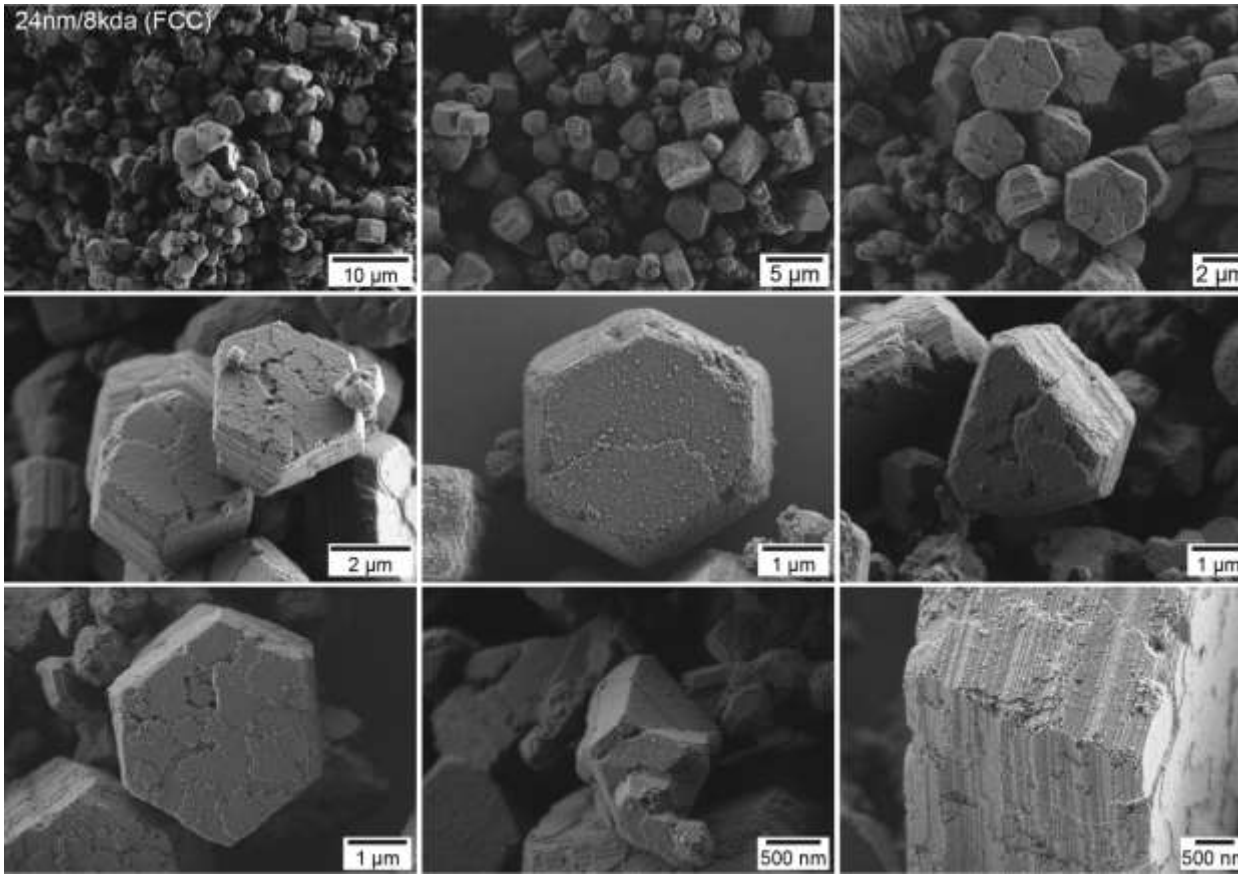

Figure S4.16. SEM images of the 24nm/8kDa FCC NCT assemblies. Stacking faults, twins, and multiply twinned structures were observed in the dried assemblies. Close-packed (111) planes could also be observed on the faces of the structures.

24nm/10kDa FCC

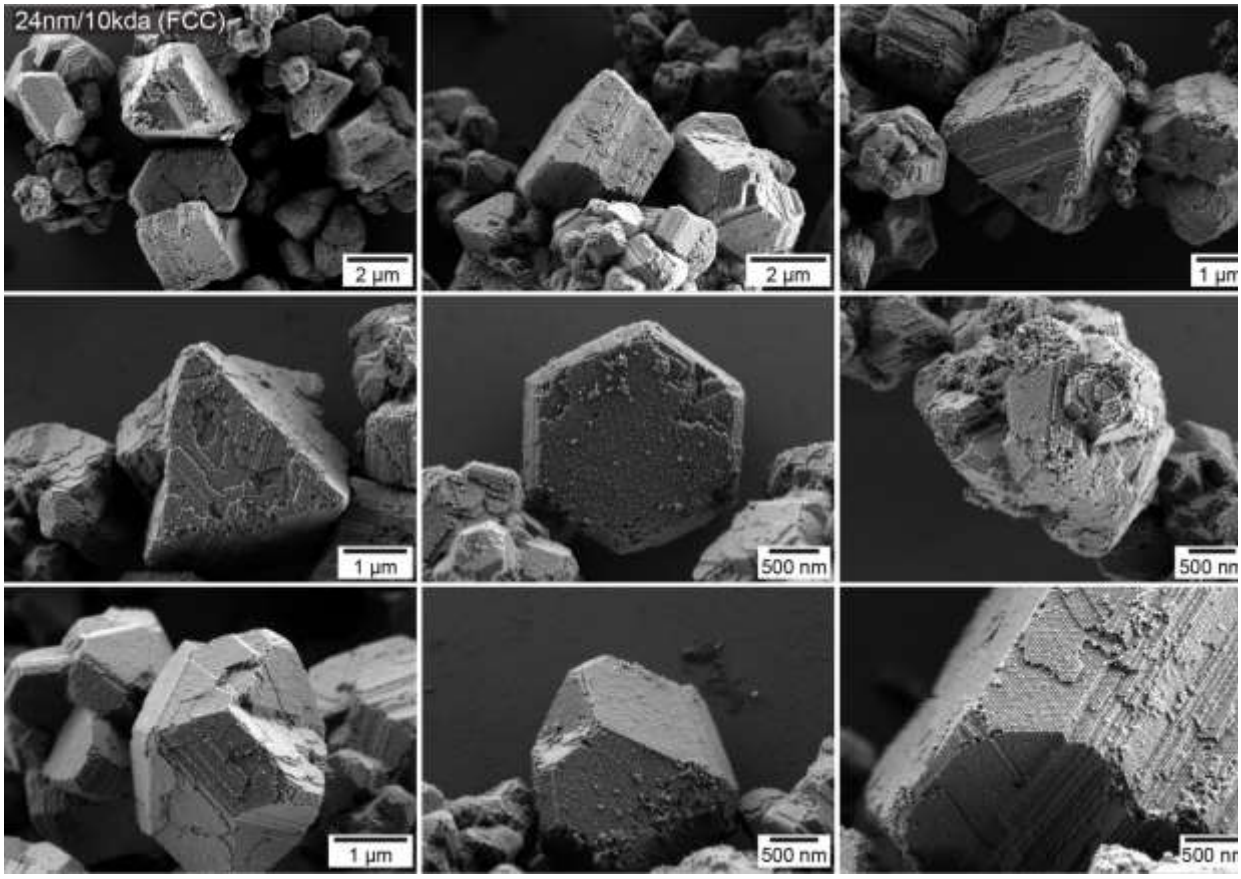

Figure S4.17. SEM images of the 24nm/10kDa FCC NCT assemblies. Stacking faults, twins, and multiply twinned structures were observed in the dried assemblies. Close-packed (111) planes could also be observed on the faces of the structures.

24nm/13kDa FCC

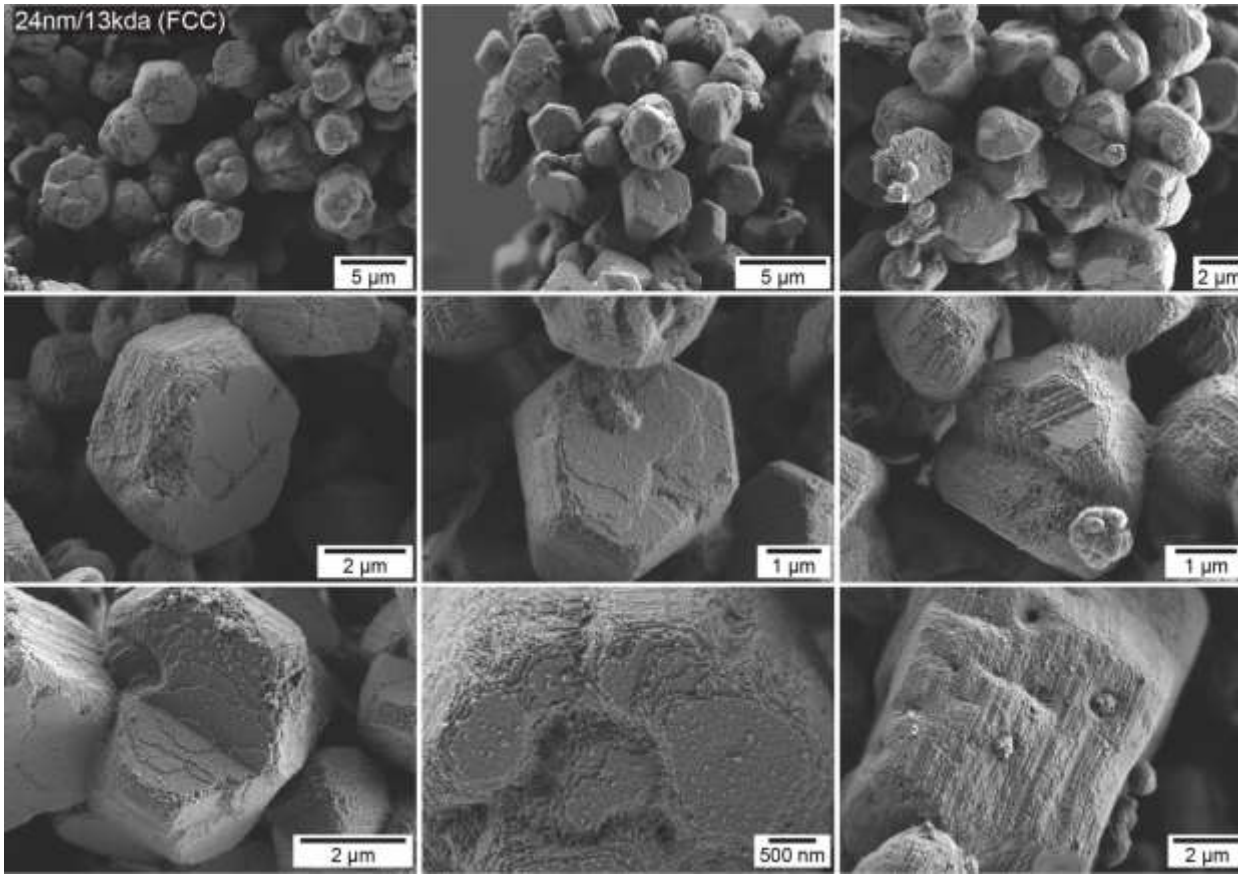

Figure S4.18. SEM images of 24nm/13kDa FCC NCT assemblies. Stacking faults, twins, and multiply twinned structures were observed in the dried assemblies. Close-packed (111) planes could also be observed on the faces of the structures.

10nm/8kDa BCC (drop cast immediately from n-decane)

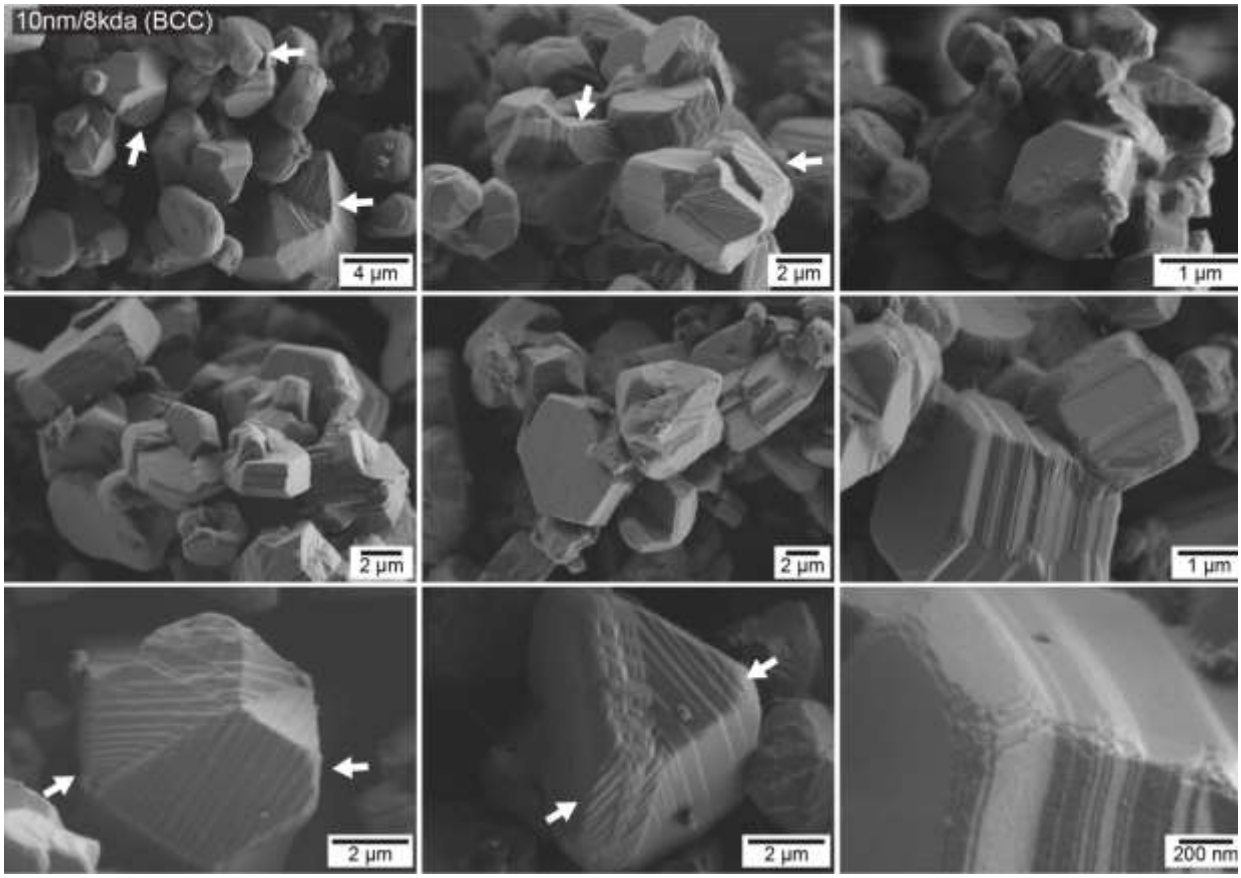

Figure S4.19. SEM images of the 10nm/8kDa BCC NCT assemblies drop cast immediately from n-decane. The assemblies have the same crystal habits as that seen in the FCC assemblies but are accompanied by the presence of transformation twins on the faces of the structures. White arrows denote the internal twins.

10nm/10kDa BCC (drop cast immediately from 40 vol% n-decane)

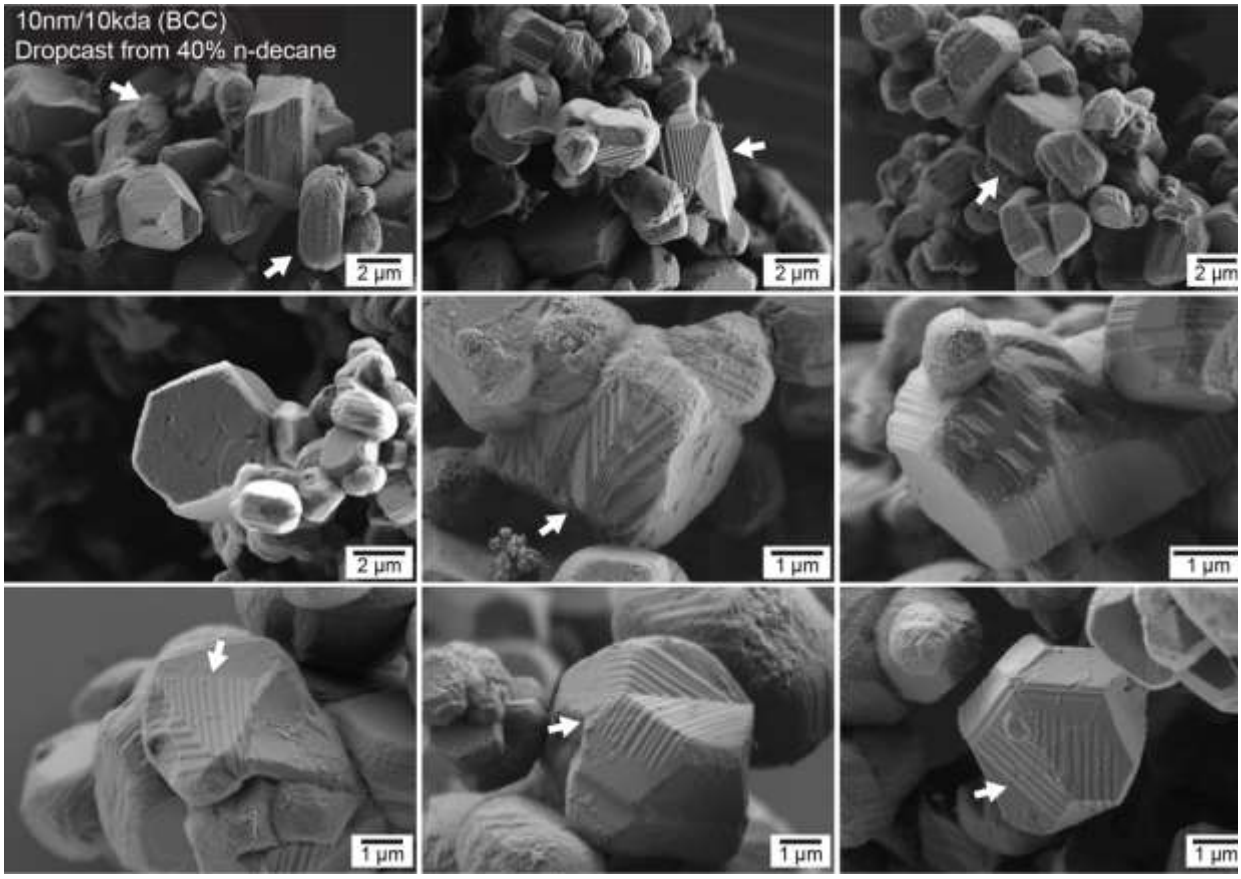

Figure S4.20. SEM images of the 10nm/10kDa BCC NCT assemblies drop cast immediately from 40 vol% n-decane. The assemblies have the same crystal habits as that seen in the FCC assemblies but are accompanied by the presence of transformation twins on the faces of the structures. White arrows denote the internal twins.

10nm/10kDa BCC (drop cast after 2 months in n-decane)

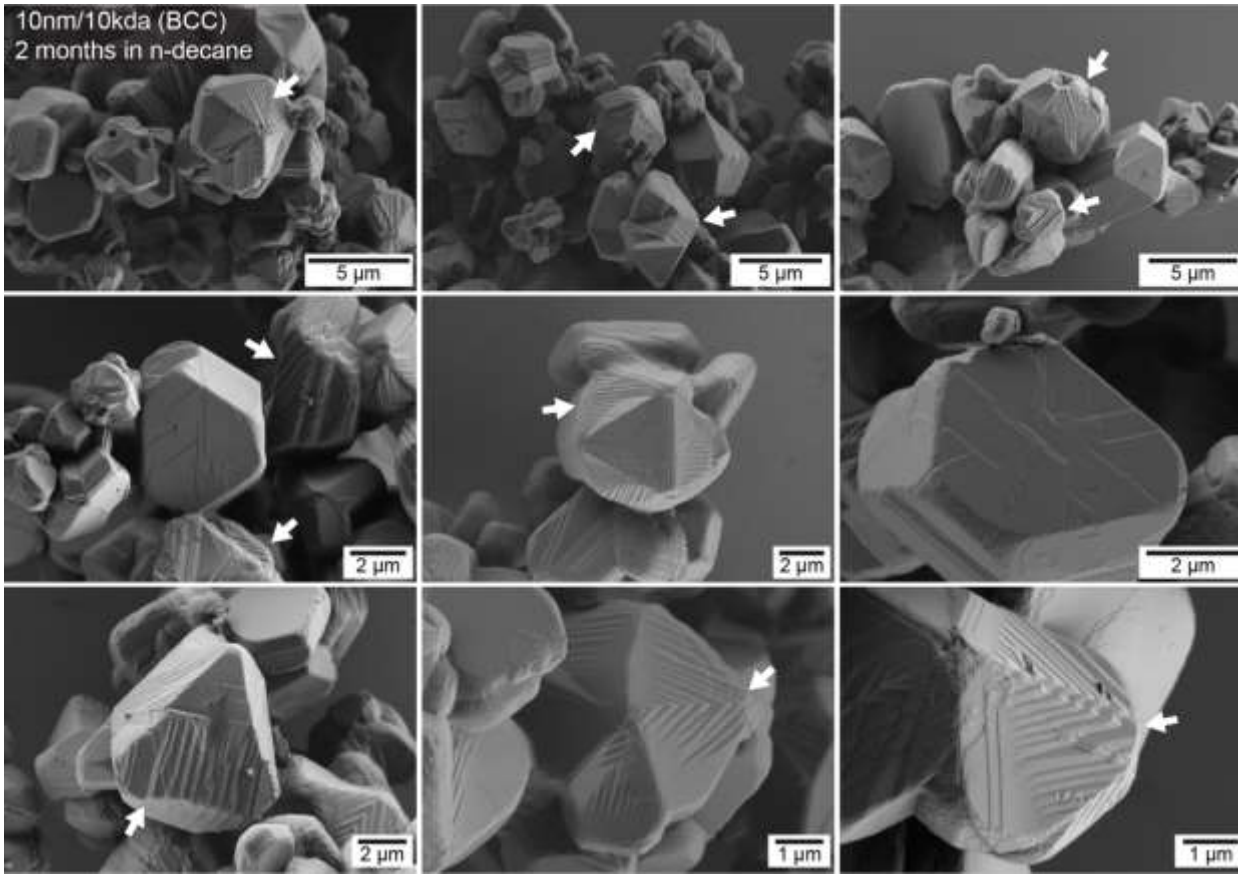

Figure S4.21. SEM images of the 10nm/10kDa BCC NCT assemblies drop cast after 2 months in n-decane. The assemblies have the same crystal habits as that seen in the FCC assemblies but are accompanied by the presence of transformation twins on the faces of the structures. White arrows denote the internal twins. The assemblies left in n-decane for 2 months were qualitatively observed to have more internal twins that the assemblies immediately drop cast from 40 vol% n-decane (Figure S4.20).

10nm/13kDa BCC (drop cast immediately from n-decane)

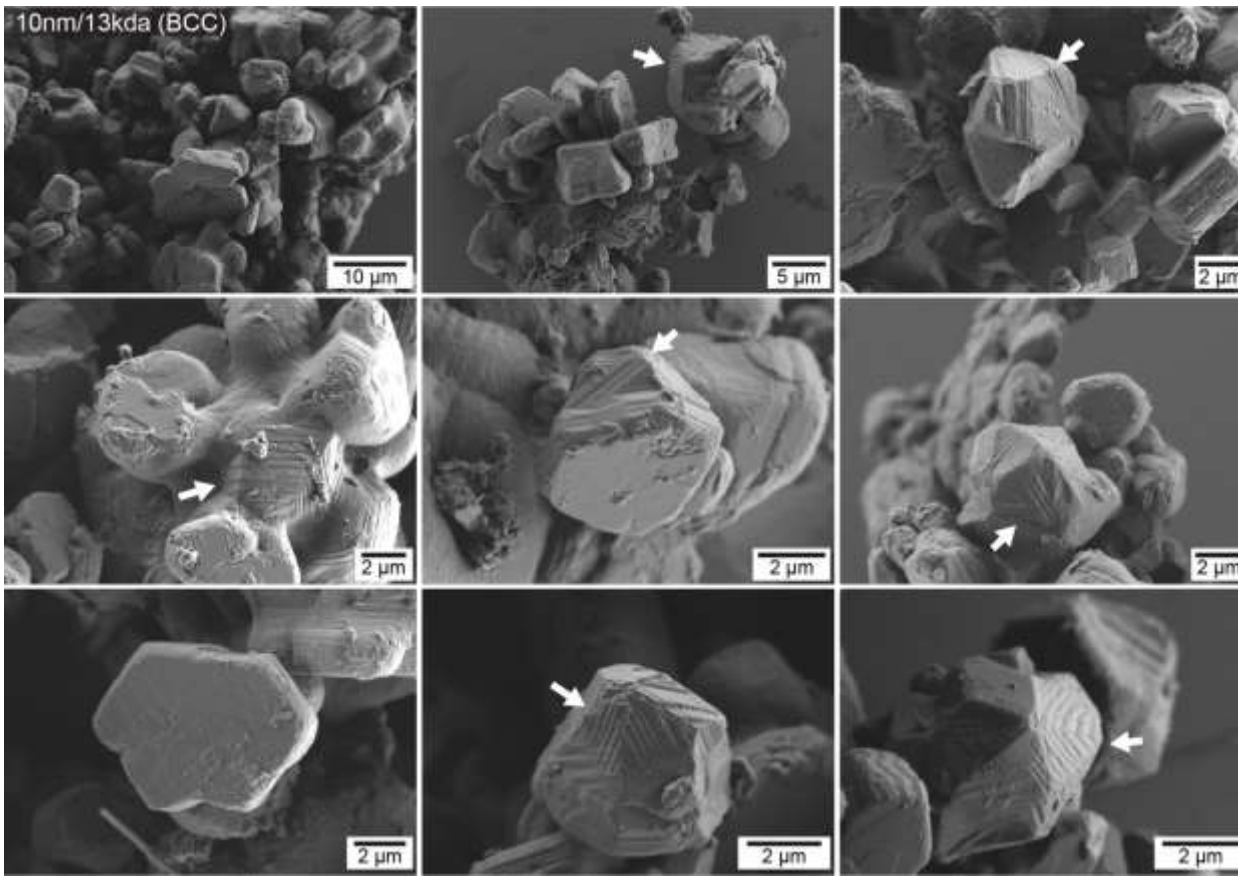

Figure S4.22. SEM images of the 10nm/13kDa BCC NCT assemblies drop cast immediately from n-decane. The assemblies have the same crystal habits as that seen in the FCC assemblies but are accompanied by the presence of transformation twins on the faces of the structures. White arrows denote the internal twins.

Transformation Twins

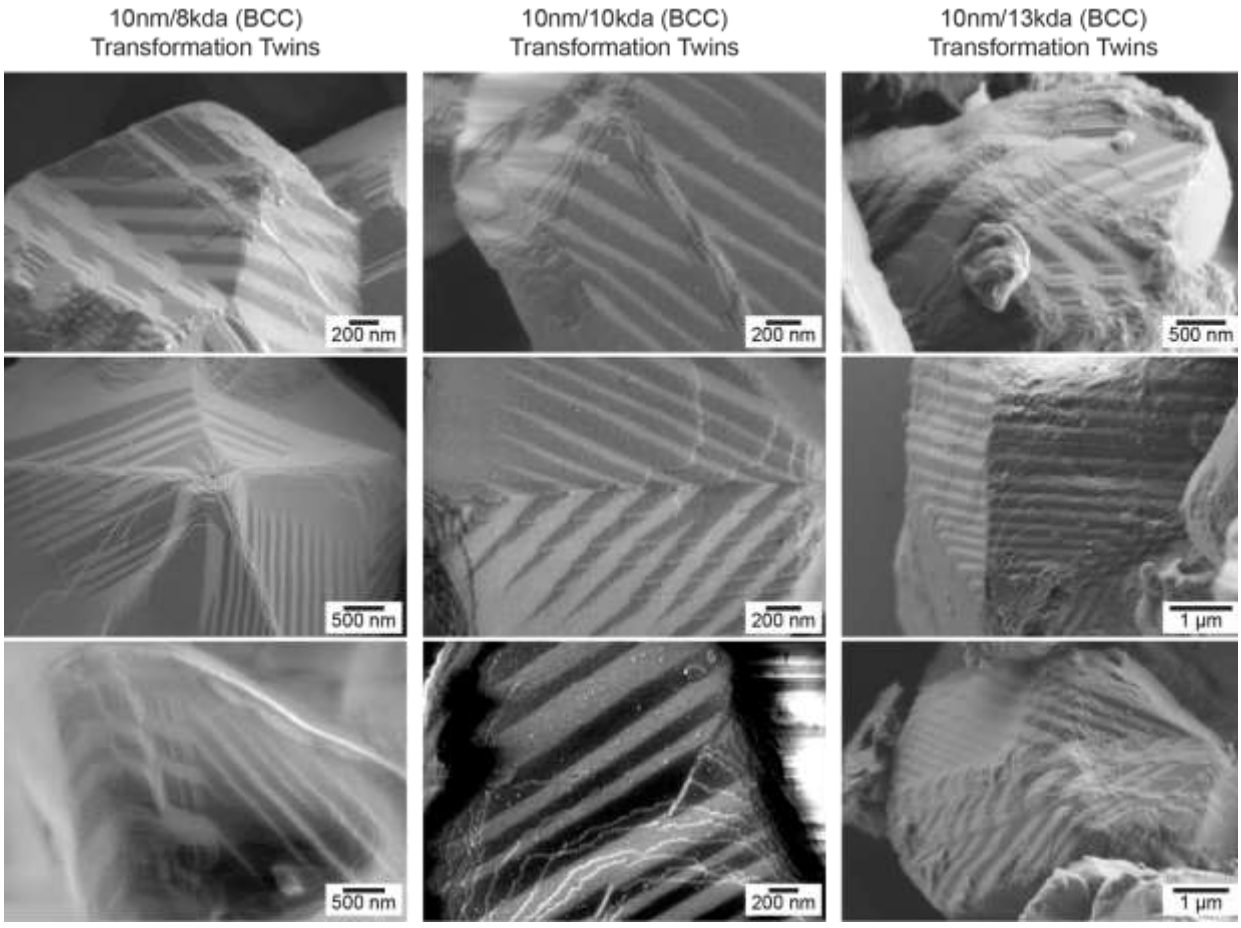

Figure S4.23. Magnified SEM images of the transformation twins observed in the 10nm NCT assemblies that underwent an FCC-to-BCC phase transition.

Appendix 5: Using Solvent Quality to Drive Nanoparticle Self-Assembly

Materials and Instrumentation

2,6-Diaminopyridine, thymine, acetyl chloride, 11-bromo-1-undecanol, 2-Bromoisobutyryl bromide, propargyl alcohol, N,N,N',N",N'"-Pentamethyldiethylenetriamine (PMDETA), and Tris[2-(dimethylamino)ethyl]amine (Me_6TREN) were purchased from Acros. Docosane, phosphorous acid, cyclohexamine, iodine, ferric chloride hexahydrate, oleic acid, copper (I) bromide, hydrochloric acid (HCl), melamine, Bis[2-(2-bromoisobutyryloxy)ethyl]disulfide (BIBOEDS), and copper (II) bromide were purchased from Sigma Aldrich. Sodium citrate, citric acid, and ethylenediaminetetraacetic acid tetrasodium salt hydrate were purchased from Acros Organics. Hydrogen tetrachloroaurate(III) trihydrate and 1-octadecene were purchased from Beantown Chemical. Aminoethanethiol and sodium oleate were purchased from TCI America. General solvents were purchased from Fisher Scientific. All chemicals, including solvents, were used without further purification, except styrene, which was passed through a short column of basic alumina to remove inhibitor prior to polymerization. Centrifugation was performed with an Eppendorf 5424 centrifuge. Gel permeation chromatography (GPC) characterizations were performed on an Agilent Technologies GPC system, with THF as the eluent at 1.0 mL/min, and monodisperse polystyrene as the standard. Transmission electron microscopy (TEM) was performed with a FEI Tecnai G2 Spirit TWIN transmission electron microscope. Small angle X-ray scattering (SAXS) measurements were performed on a SAXSLAB instrument with a Pilatus3R 300K detector and x-rays of wavelength 1.5409 Å. The system was calibrated using silver behenate as a standard. Scanning electron microscopy (SEM) was performed with a Zeiss Merlin High-resolution SEM at an accelerating voltage of 1kV.

Synthesis

Gold Nanoparticles

Gold nanoparticles (AuNPs) were synthesized using a modification of the Turkevich method to produce low dispersity, citrate-stabilized AuNPs.[18,274,275] All glassware and stir bars were cleaned with aqua regia before use. 800 mL of 2.75 mM 75/25 sodium citrate/citric acid buffer solution was prepared with Milli-Q purified water and heated to boiling for 15 minutes in a 1 L flask. 6.08 mg of ethylenediaminetetraacetic acid tetrasodium salt hydrate (EDTA salt) was dissolved in water and added to the boiling solution to bring the overall concentration of EDTA salt to 0.02 mM. Gold precursor solution was prepared by dissolving 157.5 mg $HAuCl_4$ in 9 mL of Milli-Q purified water. After 10 minutes, 3 mL of gold precursor solution was swiftly injected into the boiling, stirring solution. A color change from clear to dark red was observed, beginning ~30 seconds after the addition of gold precursor. The reaction was boiled for 30 minutes before being allowed to gradually cool to 90 °C. After 30 minutes for temperature equilibration, another 3 mL of gold precursor was swiftly injected, followed 30 minutes later by the final 3 mL gold precursor addition. The reaction was ended after 30 minutes to obtain 16-18 nm AuNPs.

To obtain larger nanoparticles, instead of ending the reaction after the final temperature equilibration, 400 mL of the reaction mixture was removed, followed by the addition of 485.3 mg sodium citrate in 400 mL of Milli-Q purified water. A new gold precursor solution was prepared by dissolving 157.5 mg $HAuCl_4$ in 9 mL of Milli-Q purified water. After 30 minutes for temperature equilibration at 90 °C, an additional 3 rounds of swiftly injecting 3 mL of gold precursor solution into the reaction mixture was performed, with 30 minutes between injections. The reaction was ended after 30 minutes to obtain 24-27 nm AuNPs.

Iron Oxide Nanoparticle Synthesis

Iron oxide nanoparticles (IO NP) were synthesized through the thermal decomposition of an iron oleate precursor.[277] Iron oleate precursor was first prepared by combining 10.8 g ferric chloride hexahydrate (40 mmol, 1 eq) and 36.5g sodium oleate (120 mmol, 3 eq) in a mixture of 60 mL water, 80 mL ethanol, and 140 mL hexanes. The reaction mixture was heated and allowed to reflux for 4 hours. The organic layer was then extracted 3 times with water, hexanes were removed on a rotary evaporator, and the product dried under vacuum while gradually heating to 120 °C to yield the iron oleate precursor in the form of a thick dark orange oil. Care must be taken to avoid excessive foaming during drying.

To synthesize nanoparticles, 6.4 g iron oleate precursor, oleic acid, and solvent were combined in a 250 mL three-necked flask equipped with a reflux condenser and temperature probe. The flask was heated to 120℃ while stirring, evacuated and refilled with nitrogen three times, and then heated to reflux at a controlled rate of 6℃/min. After refluxing for 1 hour, the reaction mixture was allowed to cool, transferred to a storage container, and stored as a solid in the refrigerator.

The size of the nanoparticles could be controlled by varying the solvent and amount of oleic acid. 10 nm particles were synthesized using 100 mL 1-octadecene and 2.0 g oleic acid and 24 nm particles were synthesized using 25 mL docosane and 2.0 g oleic acid.

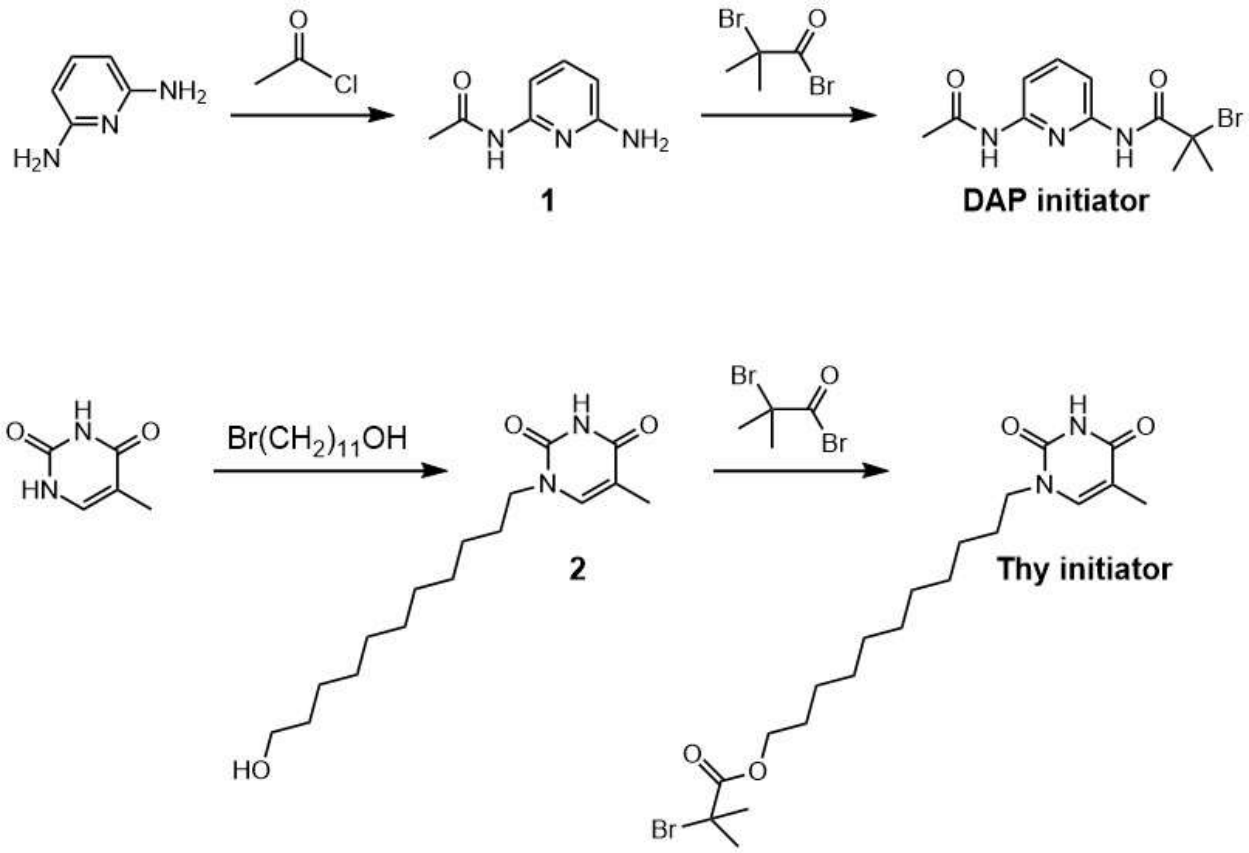

Scheme S5.1. Synthetic scheme for DAP initiator and Thy initiator

DAP Initiator

5.5 g 2,6-diaminopyridine (50 mmol) was dissolved in 40 mL of dry THF in a 3-necked round bottom flask. At 0 ºC, a solution of 1.96 g (25 mmol) acetyl chloride in 15 mL of dry THF was added dropwise under a nitrogen atmosphere. The reaction mixture was allowed to warm to room temperature and stirred for 12 hours. The insoluble content was filtered off, and the solvent was removed under reduced pressure. The resulting white solid was recrystallized in a mixture of ethanol and toluene, to afford **1** (Scheme S5.1). 1.9 g **1** (12.6 mmol) was dissolved in 80 mL dichloromethane, and then 3.5 mL triethylamine (25 mmol) was added to this solution. The mixture was cooled to 0 ºC, and a solution of 3.22 g 2-bromoisobutyryl bromide (17.6 mmol) in

dichloromethane (~10 mL) was added dropwise under a nitrogen atmosphere. The reaction mixture was allowed to warm to room temperature and stirred for 12 hours. The insoluble content was filtered off, and the filtrate was washed with a solution of sodium carbonate (x1) and brine (x3). The organic phase was dried with sodium sulfate, the solvent was removed under reduced pressure, and the product was then purified by flash chromatography (CH_2Cl_2/EtOAc 4:1). The product was further purified by recrystallization in CH_2Cl_2/EtOAc/hexanes to obtain the final DAP-initiator product. All characterization matches previous literature reports.

Thy Initiator

5.0 g thymine (40 mmol), 1.0 g 11-bromo-1-undecanol (4 mmol), 1.1 g potassium carbonate (8 mmol) and 200 mL of DMSO were added to a 500 mL round bottom flask. The mixture was stirred and bubbled with nitrogen for 2 minutes, and then sealed with a septum and stirred for 48 hours. The resulting mixture was poured into water and chloroform for extraction. The organic phase was dried with sodium sulfate, and the solvent was removed under reduced pressure. The resulting white solid was recrystallized in EtOAc/hexanes to afford **2** (Scheme S5.1). Using very gentle heat, 592 mg **2** (2 mmol) was dissolved in 150 mL of dichloromethane, and 0.39 mL of trimethylamine (2.8 mmol) was added to the solution. The mixture was cooled to 0 ºC, and a solution of 552 mg 2-bromoisobutyryl bromide (2.4 mmol) in dichloromethane (~10 mL) was added dropwise under a nitrogen atmosphere. The reaction mixture was allowed to warm to room temperature and stirred for 14 hours, and then washed with sodium carbonate (x2) and brine (x2). The organic phase was dried with sodium sulfate, and the solvent was removed under reduced pressure. The resulting mixture was purified by flash chromatography (CH_2Cl_2/EtOAc 8:3), to obtain the final Thy-initiator product. All characterization matches previous literature reports.

Propargyl Phosphonate Anchor Synthesis

The phosphonate group to anchor polymers onto iron oxide nanoparticles was synthesized according to a literature procedure.[276] Briefly, 0.41 g phosphorous acid (5 mmol, 1 eq), 10 mL propargyl alcohol (142 mmol, 34.4 eq), and 2.5 mL trimethylamine (18 mmol, 3.6 eq) were combined in a 100 mL round bottom flask. 1.9 g iodine (7.5 mmol, 1.5 eq) was slowly added with a spatula over several minutes. After reacting for 30 minutes, the mixture was precipitated in 200 mL acetone with 5 mL cyclohexamine and allowed to rest for 2 hours without stirring. The fine powder was recovered through filtration, dissolved in 30 mL hot ethanol, with 500 μL cyclohexamine and recrystallized overnight to yield the propargyl phosphate cyclohexamine salt as a white powder. Characterization matches previous literature reports.

DAP-PS Polymer

DAP-initiator (1.0 eq), Me_6TREN (0.83 eq), styrene (100-200 eq depending on target molecular weight), copper (II) bromide (0.1 eq), and anisole (0.8:1 v/v to styrene) were added to an oven-dried 100 mL Schlenk flask with stir bar. The reaction flask was then sealed with a rubber septum and 3 freeze-pump-thaw cycles were performed before filling the flask with nitrogen. Simultaneously, tin(II) 2-ethylhexanoate (0.15 eq) and anisole (0.2:1 v/v to styrene) were combined in a vial and bubbled with nitrogen. After the reaction flask finished returning to room temperature, the tin(II) 2-ethylhexanoate mixture was injected. The reaction mixture was stirred at 105 °C and quenched with liquid nitrogen at different time points to obtain polymers of the desired molecular weights. The reaction mixture was then added dropwise to methanol and the precipitated polymer was collected, redissolved in dichloromethane, and precipitated in methanol. 3 precipitations were done, ending with a polymer with a chain end bromine.

To obtain the thiol-anchored polymer for use with AuNPs, the polymer was dissolved in minimal dimethylformamide (DMF) with trimethylamine (40 eq) and bubbled with nitrogen for 15 minutes, followed by the addition of 2-aminoethanethiol (15 eq). The mixture was left to stir for 60 hours, and 3 precipitations were done to obtain a white powder, which was dried under vacuum to yield the final DAP-PS-PS product.

To obtain the phosphonate-anchored polymer for use with IO NPs, the polymer was dissolved in minimal N,N-dimethylformamide (DMF) with sodium azide (4 eq) and left to stir overnight. The reaction mixture was then added dropwise to methanol and the precipitated polymer was collected, redissolved in dichloromethane, and precipitated in methanol. 3 precipitations were done, ending with an azide-terminated polymer. The alkyl functionalized phosphonate was added to the polymer through an azide-alkyne cycloaddition. The polymer (1 eq) was dissolved in DMF with the propargyl phosphate (3 eq) and PMDETA (1 eq). Three freeze-pump-thaw cycles were performed, and upon the third freeze the flask was opened under a strong nitrogen flow, and copper (I) bromide (1 eq) was added. The flask was evacuated and refilled with nitrogen twice, evacuated, thawed, and refilled with nitrogen, and heated at 30 ℃ for 48 hours. The polymer was then precipitated in methanol with 1% HCl, filtered and redissolved in dichloromethane and precipitated in methanol two more times before drying under vacuum to yield the final DAP-PS-Phos product.

Thy-PS Polymer

Thy-initiator (1.0 eq), PMDETA (1.0 eq), styrene (200-300 eq depending on target molecular weight), and anhydrous anisole (30 v% to styrene) were added to an oven-dried 100 mL Schlenk flask with stir bar. The reaction flask was then sealed with a rubber septum and 3 freeze-

pump-thaw cycles were performed before filling the flask with nitrogen. The septum was removed to add CuBr (1.0 eq) and the flask was quickly resealed, purged, refilled with nitrogen, and returned to room temperature. The reaction mixture was stirred at 110 °C and quenched with liquid nitrogen at different time points to obtain polymers of the desired molecular weights. The reaction mixture was then added dropwise to methanol and the precipitated polymer was collected, redissolved in dichloromethane, and precipitated in methanol. 3 precipitations were done, ending with a polymer with a chain end bromine.

To obtain the phosphonate-anchored polymer for use with IO NPs, the polymer was dissolved in minimal N,N-dimethylformamide (DMF) with sodium azide (4 eq) and left to stir overnight. The reaction mixture was then added dropwise to methanol and the precipitated polymer was collected, redissolved in dichloromethane, and precipitated in methanol. 3 precipitations were done, ending with an azide-terminated polymer. The alkyl functionalized phosphonate was added to the polymer through an azide-alkyne cycloaddition. The polymer (1 eq) was dissolved in DMF with the propargyl phosphate (3 eq) and PMDETA (1 eq). Three freeze-pump-thaw cycles were performed, and upon the third freeze the flask was opened under a strong nitrogen flow, and copper (I) bromide (1 eq) was added. The flask was evacuated and refilled with nitrogen twice, evacuated, thawed, and refilled with nitrogen, and heated at 30 ℃ for 48 hours. The polymer was then precipitated in methanol with 1% HCl, filtered and redissolved in dichloromethane and precipitated in methanol two more times before drying under vacuum to yield the final Thy-PS-Phos product.

PS-SH Polymer

BIBOEDS, (1.0 eq), PMDETA (1.2 eq), and styrene (400-1500 eq depending on target molecular weight) were added to an oven-dried 100 mL Schlenk flask with stir bar. The reaction flask was then sealed with a rubber septum and 3 freeze-pump-thaw cycles were performed before filling the flask with nitrogen. The septum was removed to add CuBr (1.2 eq) and the flask was quickly resealed, purged, refilled with nitrogen, and returned to room temperature. The reaction mixture was stirred at 100 °C and quenched with liquid nitrogen at different time points to obtain polymers of the desired molecular weights. The reaction mixture was passed through a short column of neutral alumina, then added dropwise to methanol. The precipitated polymer was collected, redissolved in dichloromethane, and precipitated in methanol. 3 precipitations were done, ending with a polymer with a chain end bromine. The polymer was dissolved in minimal DMF and bubbled with nitrogen for 15 minutes, followed by the addition of NaN_3 (6 eq). The mixture was left to stir for 16 hours. The reaction mixture was then added dropwise to methanol and the precipitated polymer was collected, redissolved in a mixture of dichloromethane and DMF (8:2), and precipitated in methanol. 3 precipitations were done to obtain a white powder, which was dried under vacuum to yield the final disulfide PS polymer.

PS-Phos Polymer

Methyl α-bromoisobutyrate (1.0 eq), PMDETA (1.2 eq), and styrene (400-1500 eq depending on target molecular weight) were added to an oven-dried 100 mL Schlenk flask with stir bar. The reaction flask was then sealed with a rubber septum and 3 freeze-pump-thaw cycles were performed before filling the flask with nitrogen. The septum was removed to add CuBr (1.2 eq) and the flask was quickly resealed, purged, refilled with nitrogen, and returned to room

temperature. The reaction mixture was stirred at 100 °C and quenched with liquid nitrogen at different time points to obtain polymers of the desired molecular weights. The reaction mixture was passed through a short column of neutral alumina, then added dropwise to methanol. The precipitated polymer was collected, redissolved in dichloromethane, and precipitated in methanol. 3 precipitations were done, ending with a polymer with a chain end bromine. The polymer was dissolved in minimal DMF and bubbled with nitrogen for 15 minutes, followed by the addition of NaN_3 (6 eq). The mixture was left to stir for 16 hours. The reaction mixture was then added dropwise to methanol and the precipitated polymer was collected, redissolved in a mixture of dichloromethane and DMF (8:2), and precipitated in methanol. 3 precipitations were done, ending with an azide-terminated polymer. The alkyl functionalized phosphonate was added to the polymer through an azide-alkyne cycloaddition. The polymer (1 eq) was dissolved in DMF with the propargyl phosphate (3 eq) and PMDETA (1 eq). Three freeze-pump-thaw cycles were performed, and upon the third freeze the flask was opened under a strong nitrogen flow, and copper (I) bromide (1 eq) was added. The flask was evacuated and refilled with nitrogen twice, evacuated, thawed, and refilled with nitrogen, and heated at 30 ℃ for 48 hours. The polymer was then precipitated in methanol with 1% HCl, filtered and redissolved in dichloromethane and precipitated in methanol two more times before drying under vacuum to yield the final PS-Phos polymer.

Gold NCT Synthesis

13 nm NCTs

In a 20 mL glass vial, DAP-PS-SH, Thy-PS-SH, or PS-SH was dissolved in 8 mL of acetone (1 mg/mL). While stirring, 8 mL of citrate-capped AuNPs was quickly added and the resulting suspension was allowed to stir for 15 minutes, forming a dark red/pink precipitate. The functionalized nanoparticles were recovered by a brief (2 minute) centrifugation, and purified and concentrated by three cycles of centrifugation (9k, 50 minutes), with redispersion in 8 mL of DMF, 1 mL of DMF and 1 mL of toluene before each respective centrifugation, and a final dispersion in toluene.

20 nm NCTs

In a 20 mL glass vial, DAP-PS-SH, Thy-PS-SH, or PS-SH was dissolved in 8 mL of acetone (1 mg/mL). While stirring, 8 mL of citrate-capped AuNPs was quickly added and the resulting suspension was allowed to stir for 15 minutes, forming a dark red/pink precipitate. The functionalized nanoparticles were recovered by a brief (2 minute) centrifugation, and purified and concentrated by three cycles of centrifugation (7k, 40 minutes), with redispersion in 8 mL of DMF, 1 mL of DMF and 1 mL of toluene before each respective centrifugation, and a final dispersion in toluene.

Iron Oxide NCT Synthesis

10 nm NCTs

In a 20 mL glass vial, 750 mg 10 nm IO NP reaction mixture in 1-octadecene (a solid) was dissolved in 12 mL of tetrahydrofuran (THF). The nanoparticles were centrifuged (70 minutes,

13.5k rpm) and redispersed in THF 2 times to remove residual solvent and reaction byproducts, and concentrated to 1 mL THF. Concentrated nanoparticles were added to 25 mg of DAP-PS-Phos, Thy-PS-Phos, or PS-Phos, and the solution briefly sonicated before being shaken (600 rpm) at room temperature overnight. The next day, functionalized NCTs were diluted 4-fold with THF and were centrifuged (80 minutes, 14.5k rpm) and redispersed 3 times in THF, THF, and toluene, and concentrated to 1 mL in toluene.

24 nm NCTs

In a 20 mL glass vial, 450 mg 24 nm IO NP reaction mixture in 1-octadecene (a solid) was dissolved in 20 mL of THF. The nanoparticles were centrifuged (40 minutes, 8.0k rpm) and redispersed in THF 2 times to remove residual solvent and reaction byproducts, and concentrated to 1 mL THF. Concentrated nanoparticles were added to 15 mg of DAP-PS-Phos, Thy-PS-Phos, or PS-Phos, and the solution briefly sonicated before being shaken (600 rpm) at room temperature overnight. The next day, functionalized NCTs were diluted 4-fold with THF and were centrifuged (40 minutes, 8.5k rpm) and redispersed 3 times in THF, THF, and toluene, and concentrated to 1 mL in toluene.

NCT Assembly in DMF

0.1 mL NCTs in toluene were diluted 10-fold with DMF, centrifuged according to size (see section on NCT preparation above), and redispersed in 0.1 mL of DMF with gentle mixing. NCTs were then sealed in Kapton capillary tubes and left to sit at room temperature to assemble.

NCT Assembly in Acetone

0.1 mL NCTs in toluene were diluted 10-fold with acetone, centrifuged according to size (see section on NCT preparation above) to obtain a dense pellet of NCTs, and redispersed in 0.1 mL of acetone with sonication. NCTs were then left to sit at room temperature to assemble.

Characterization

Gold Nanoparticles

Gold nanoparticles (AuNPs) were synthesized using a modification of the Turkevich method to produce low dispersity, citrate-stabilized AuNPs. To prepare samples for TEM, AuNPs were functionalized with polystyrene using the protocol for synthesizing NCTs and drop cast from toluene onto formvar coated TEM grids. AuNPs used had a measured diameter of 12.7 nm and dispersity of 7.5%. Analysis was performed in ImageJ.

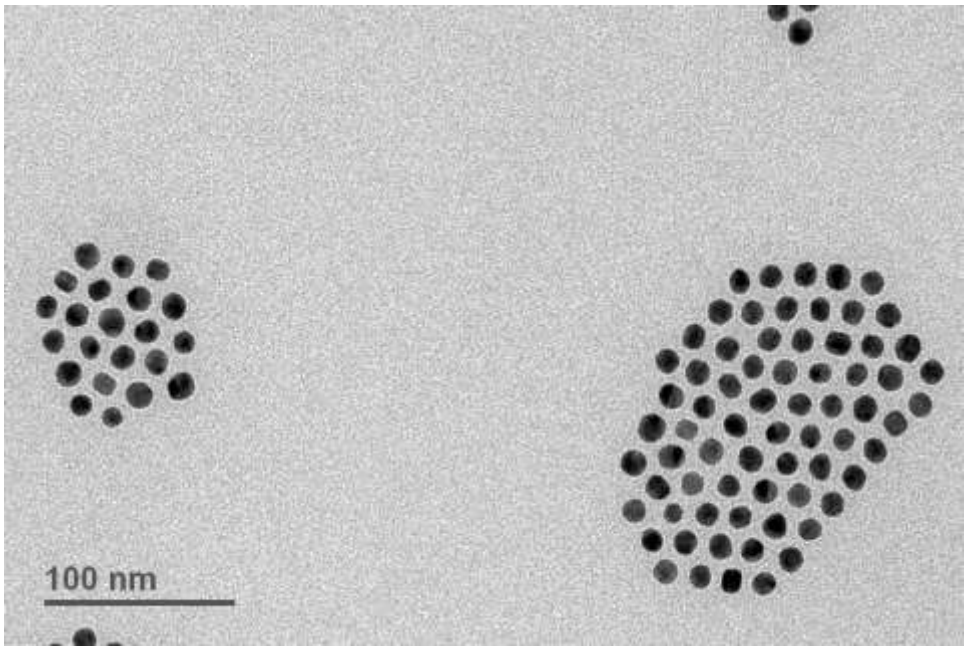

Figure S5.1. TEM micrograph of unassembled, polymer-grafted 13 nm gold nanoparticles used in this work.

Iron Oxide Nanoparticles

To prepare samples for TEM, IO NPs were centrifuged and redispersed twice in 50/50 acetone/THF and toluene to remove remove residual solvent and reaction byproducts. Particles were them dropcast onto formvar coated TEM grids. Analysis was performed in ImageJ.

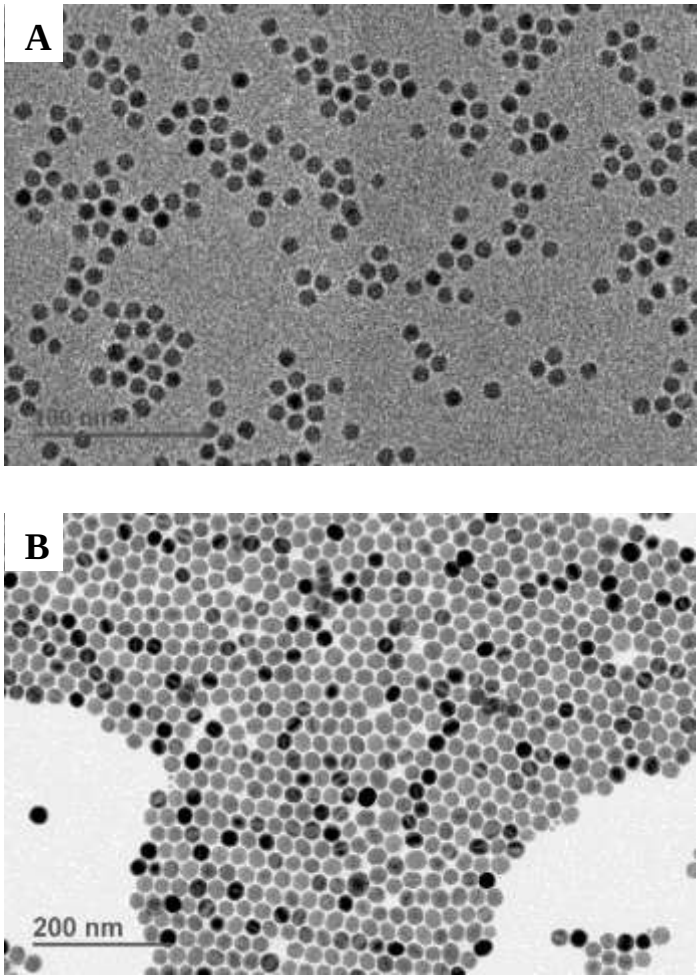

Figure S5.2. TEM images of the iron oxide nanoparticles used in this work. (A) IO NPs with an average diameter of 9.8 nm (B) IO NPs with an average diameter of 24.2 nm.

Polymers

Table S5.1. Molecular weight and dispersity of the polymers used in this work.

Polymer	M_n (kDa)	Đ
11k DAP-PS-SH	11.2	1.06
13k PS-SH	25.0 (12.5k per arm)	1.04
10k DAP-PS-Phos	9.5	1.03
10k Thy-PS-Phos	9.7	1.01
15k PS-Phos	14.9	1.15

SAXS of NCT Assemblies

Each NCT sample was added to a short section of 1.5mm diameter Polyimide Tubing (Cole-Parmer) and sealed at both ends with epoxy. 1-dimensional SAXS data was obtained via radial averaging of the 2-dimensional scattering pattern. Data was then transformed into profiles of scattering intensity as a function of scattering vector q. Body-centered cubic (BCC) and face-centered cubic (FCC) ordering were confirmed, with structural parameters

$$a_{BCC} = \frac{2\pi\sqrt{2}}{q_0}$$

$$a_{FCC} = \frac{2\pi\sqrt{3}}{q_0}$$

$$d_{BCC} = d_{FCC} = \frac{\pi\sqrt{6}}{q_0}$$

Table S5.2. Peak positions and structural parameters for the SAXS data in Figure 5.3

Sample	q_0 Peak Position	q_1/q_0	q_2/q_0	d (nm)	a (nm)	Crystal Structure
10 nm IO, 10k DAP-PS	0.0355	1.14	1.63	21.67	25.03	FCC
13 nm Au, 11k DAP-PS	0.03	1.13	-	25.65	29.62	FCC
13 nm Au, 13k PS	0.0296	1.13	1.59	26.04	30.07	FCC
24 nm IO, 15k PS	0.0201	-	1.62	38.27	44.19	FCC
Ideal FCC	-	1.15	1.63	-	-	

Table S5.3. Peak positions and structural parameters for the SAXS data in Figure 5.4

Sample	q_0 Peak Position	q_1/q_0	q_2/q_0	d (nm)	a (nm)	Crystal Structure
20 min, 14.5K RPM	0.0350	1.13	1.62	21.98	25.38	FCC
40 min, 14.5K RPM	0.0350	1.14	1.64	21.98	25.38	FCC
80 min, 14.5K RPM	0.0355	1.14	1.63	21.68	25.03	FCC
80 min, 10K RPM	0.0350	1.14	1.64	21.98	25.38	FCC
80 min, 7K RPM	0.0350	1.13	1.62	21.98	25.38	FCC
Ideal FCC	-	1.15	1.63	-	-	-

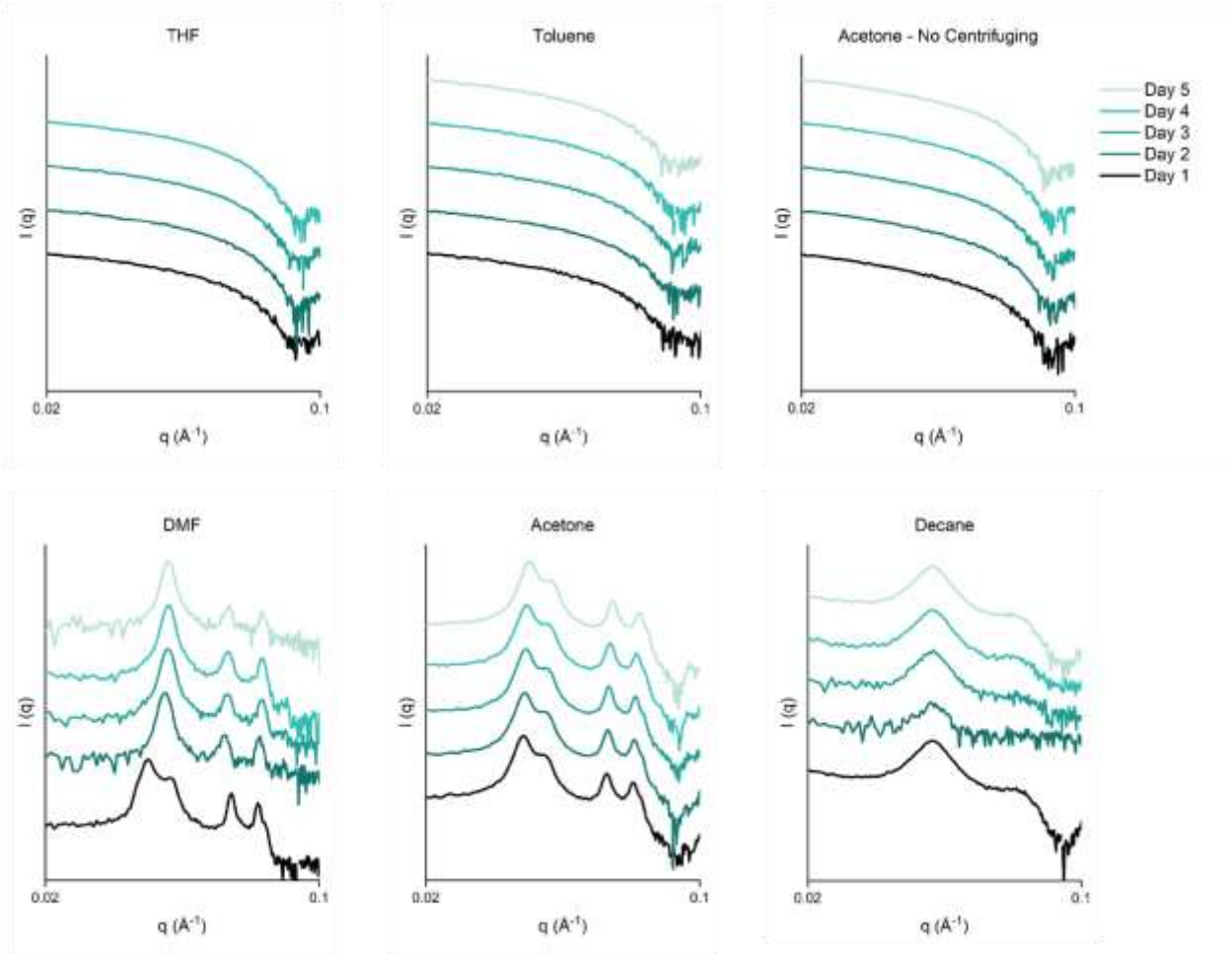

Figure S5.3. SAXS of 10 nm/10 kDa IO-DAP NCTs dispersed in various solvents and monitored over a span of 5 days. NCTs stay dispersed in good solvents (toluene, THF, uncentrifuged in acetone), assemble into ordered structures in medium-quality solvents (DMF, centrifuged in acetone) and precipitate in amorphous aggregates in poor solvents (decane).

SEM

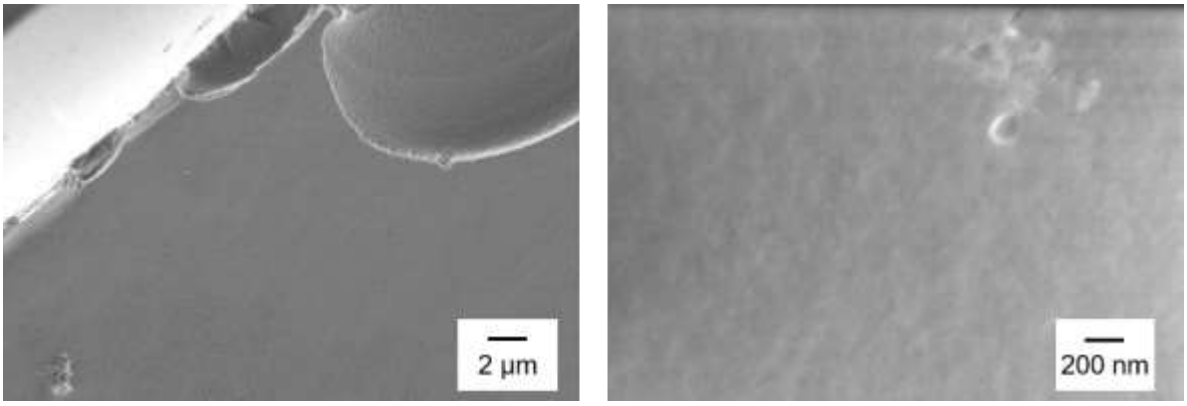

Figure S5.4. SEM of 20 nm/6 kDa Au NCTs sintered in acetone (centrifuging in acetone without subsequent resuspension). NCTs within the solid did not possess ordering on the nanoscale, but did exhibit a surface that was smooth and mostly defect-free, without noticeable grain boundaries. This is likely due to the fact that the solid was directly sintered with unassembled NCTs in solution, as opposed to traditional NCT solids obtained by sintering pre-assembled NCT crystallites. These NCT solids are ordered on the nanoscale but exhibit significantly more defects on the microscale and noticeable grain boundaries due to imperfect packing (Figure 6.2). Thus, the acetone sintering process could potentially be used to obtain sintered NCT solids that possess both ordering on the nanoscale and uniform, single-crystal-like microstructure.

References

1. Choi, C. L. & Alivisatos, A. P. From artificial atoms to nanocrystal molecules: preparation and properties of more complex nanostructures. *Annu Rev Phys Chem* **61**, 369–389 (2010).
2. Mannhart, J., Boschker, H., Kopp, T. & Valentí, R. Artificial atoms based on correlated materials. *Rep. Prog. Phys.* **79**, 084508 (2016).
3. Smith, A. M. & Nie, S. Semiconductor Nanocrystals: Structure, Properties, and Band Gap Engineering. *Acc. Chem. Res.* **43**, 190–200 (2010).
4. Ashoori, R. C. Electrons in artificial atoms. *Nature* **379**, 413–419 (1996).
5. Steigerwald, M. L. & Brus, L. E. Semiconductor crystallites: a class of large molecules. *Acc. Chem. Res.* **23**, 183–188 (1990).
6. Xue, Z., Yan, C. & Wang, T. From Atoms to Lives: The Evolution of Nanoparticle Assemblies. *Advanced Functional Materials* **29**, 1807658 (2019).
7. Macfarlane, R. J., O'Brien, M. N., Petrosko, S. H. & Mirkin, C. A. Nucleic Acid-Modified Nanostructures as Programmable Atom Equivalents: Forging a New "Table of Elements". *Angewandte Chemie International Edition* **52**, 5688–5698 (2013).
8. Talapin, D. V., Lee, J.-S., Kovalenko, M. V. & Shevchenko, E. V. Prospects of Colloidal Nanocrystals for Electronic and Optoelectronic Applications. *Chem. Rev.* **110**, 389–458 (2010).
9. Boles, M. A., Engel, M. & Talapin, D. V. Self-Assembly of Colloidal Nanocrystals: From Intricate Structures to Functional Materials. *Chem. Rev.* **116**, 11220–11289 (2016).
10. Jones, M. R., Seeman, N. C. & Mirkin, C. A. Programmable materials and the nature of the DNA bond. *Science* **347**, 1260901 (2015).

11. Cai, Z. *et al.* From colloidal particles to photonic crystals: advances in self-assembly and their emerging applications. *Chemical Society Reviews* **50**, 5898–5951 (2021).

12. Vogel, N., Retsch, M., Fustin, C.-A., del Campo, A. & Jonas, U. Advances in Colloidal Assembly: The Design of Structure and Hierarchy in Two and Three Dimensions. *Chem. Rev.* **115**, 6265–6311 (2015).

13. Sacanna, S., J. Pine, D. & Yi, G.-R. Engineering shape: the novel geometries of colloidal self-assembly. *Soft Matter* **9**, 8096–8106 (2013).

14. Mroczkowski, T. S. Tire tread rubber composition. (1992).

15. Boonstra, B. B. Role of particulate fillers in elastomer reinforcement: a review. *Polymer* **20**, 691–704 (1979).

16. Balazs, A. C., Emrick, T. & Russell, T. P. Nanoparticle Polymer Composites: Where Two Small Worlds Meet. *Science* **314**, 1107–1110 (2006).

17. Nath, N. & Chilkoti, A. A Colorimetric Gold Nanoparticle Sensor To Interrogate Biomolecular Interactions in Real Time on a Surface. *Anal. Chem.* **74**, 504–509 (2002).

18. Turkevich, J., Stevenson, P. C. & Hillier, J. A study of the nucleation and growth processes in the synthesis of colloidal gold. *Discuss. Faraday Soc.* **11**, 55–75 (1951).

19. Grzelczak, M., Pérez-Juste, J., Mulvaney, P. & M. Liz-Marzán, L. Shape control in gold nanoparticle synthesis. *Chemical Society Reviews* **37**, 1783–1791 (2008).

20. Hotze, E. M., Phenrat, T. & Lowry, G. V. Nanoparticle Aggregation: Challenges to Understanding Transport and Reactivity in the Environment. *Journal of Environmental Quality* **39**, 1909–1924 (2010).

21. Kim, T., Lee, C.-H., Joo, S.-W. & Lee, K. Kinetics of gold nanoparticle aggregation: Experiments and modeling. *Journal of Colloid and Interface Science* **318**, 238–243 (2008).

22. Huynh, K. A. & Chen, K. L. Aggregation Kinetics of Citrate and Polyvinylpyrrolidone Coated Silver Nanoparticles in Monovalent and Divalent Electrolyte Solutions. *Environ. Sci. Technol.* **45**, 5564–5571 (2011).

23. Itoh, H., Tahara, A., Naka, K. & Chujo, Y. Photochemical Assembly of Gold Nanoparticles Utilizing the Photodimerization of Thymine. *Langmuir* **20**, 1972–1976 (2004).

24. Wang, D., Tejerina, B., Lagzi, I., Kowalczyk, B. & Grzybowski, B. A. Bridging Interactions and Selective Nanoparticle Aggregation Mediated by Monovalent Cations. *ACS Nano* **5**, 530–536 (2011).

25. Storhoff, J. J. *et al.* What Controls the Optical Properties of DNA-Linked Gold Nanoparticle Assemblies? *J. Am. Chem. Soc.* **122**, 4640–4650 (2000).

26. J. Stark, W., R. Stoessel, P., Wohlleben, W. & Hafner, A. Industrial applications of nanoparticles. *Chemical Society Reviews* **44**, 5793–5805 (2015).

27. O'Regan, B. & Grätzel, M. A low-cost, high-efficiency solar cell based on dye-sensitized colloidal TiO2 films. *Nature* **353**, 737–740 (1991).

28. Paul, S. *et al.* Langmuir−Blodgett Film Deposition of Metallic Nanoparticles and Their Application to Electronic Memory Structures. *Nano Lett.* **3**, 533–536 (2003).

29. Ling, X. Y., Phang, I. Y., Vancso, G. J., Huskens, J. & Reinhoudt, D. N. Stable and Transparent Superhydrophobic Nanoparticle Films. *Langmuir* **25**, 3260–3263 (2009).

30. Choi, B., Lee, H.-H., Jin, S., Chun, S. & Kim, S.-H. Characterization of the optical properties of silver nanoparticle films. *Nanotechnology* **18**, 075706 (2007).

31. Lee, D., Rubner, M. F. & Cohen, R. E. All-Nanoparticle Thin-Film Coatings. *Nano Lett.* **6**, 2305–2312 (2006).

32. Deegan, R. D. *et al.* Capillary flow as the cause of ring stains from dried liquid drops. *Nature* **389**, 827–829 (1997).

33. Layani, M. *et al.* Transparent Conductive Coatings by Printing Coffee Ring Arrays Obtained at Room Temperature. *ACS Nano* **3**, 3537–3542 (2009).

34. Talapin, D. V. & Murray, C. B. PbSe Nanocrystal Solids for n- and p-Channel Thin Film Field-Effect Transistors. *Science* **310**, 86–89 (2005).

35. Sau, T. K. & Murphy, C. J. Self-Assembly Patterns Formed upon Solvent Evaporation of Aqueous Cetyltrimethylammonium Bromide-Coated Gold Nanoparticles of Various Shapes. *Langmuir* **21**, 2923–2929 (2005).

36. Ming, T. *et al.* Ordered Gold Nanostructure Assemblies Formed By Droplet Evaporation. *Angewandte Chemie International Edition* **47**, 9685–9690 (2008).

37. Ryan, K. M., Mastroianni, A., Stancil, K. A., Liu, H. & Alivisatos, A. P. Electric-Field-Assisted Assembly of Perpendicularly Oriented Nanorod Superlattices. *Nano Lett.* **6**, 1479–1482 (2006).

38. Dong, A., Chen, J., Vora, P. M., Kikkawa, J. M. & Murray, C. B. Binary nanocrystal superlattice membranes self-assembled at the liquid–air interface. *Nature* **466**, 474–477 (2010).

39. Shevchenko, E. V., Talapin, D. V., Kotov, N. A., O'Brien, S. & Murray, C. B. Structural diversity in binary nanoparticle superlattices. *Nature* **439**, 55–59 (2006).

40. Shevchenko, E. V., Talapin, D. V., Murray, C. B. & O'Brien, S. Structural Characterization of Self-Assembled Multifunctional Binary Nanoparticle Superlattices. *J. Am. Chem. Soc.* **128**, 3620–3637 (2006).

41. Boles, M. A. & Talapin, D. V. Many-Body Effects in Nanocrystal Superlattices: Departure from Sphere Packing Explains Stability of Binary Phases. *J. Am. Chem. Soc.* **137**, 4494–4502 (2015).

42. Travesset, A. Topological structure prediction in binary nanoparticle superlattices. *Soft Matter* **13**, 147–157 (2017).

43. Ye, X. *et al.* Structural diversity in binary superlattices self-assembled from polymer-grafted nanocrystals. *Nature Communications* **6**, 10052 (2015).

44. Dong, A., Ye, X., Chen, J. & Murray, C. B. Two-Dimensional Binary and Ternary Nanocrystal Superlattices: The Case of Monolayers and Bilayers. *Nano Lett.* **11**, 1804–1809 (2011).

45. Evers, W. H., Friedrich, H., Filion, L., Dijkstra, M. & Vanmaekelbergh, D. Observation of a Ternary Nanocrystal Superlattice and Its Structural Characterization by Electron Tomography. *Angewandte Chemie International Edition* **48**, 9655–9657 (2009).

46. Mayoral, R. *et al.* 3D Long-range ordering in ein SiO2 submicrometer-sphere sintered superstructure. *Advanced Materials* **9**, 257–260 (1997).

47. Waterhouse, G. I. N. & Waterland, M. R. Opal and inverse opal photonic crystals: Fabrication and characterization. *Polyhedron* **26**, 356–368 (2007).

48. Suzuki, Y., Sawada, T. & Tamura, K. Colloidal crystallization by a centrifugation method. *Journal of Crystal Growth* **318**, 780–783 (2011).

49. Rupich, S. M., Shevchenko, E. V., Bodnarchuk, M. I., Lee, B. & Talapin, D. V. Size-Dependent Multiple Twinning in Nanocrystal Superlattices. *J. Am. Chem. Soc.* **132**, 289–296 (2010).

50. Baranov, D. *et al.* Assembly of Colloidal Semiconductor Nanorods in Solution by Depletion Attraction. *Nano Lett.* **10**, 743–749 (2010).

51. Kim, J. *et al.* Polymorphic Assembly from Beveled Gold Triangular Nanoprisms. *Nano Lett.* **17**, 3270–3275 (2017).

52. O'Brien, M. N., Jones, M. R. & Mirkin, C. A. The nature and implications of uniformity in the hierarchical organization of nanomaterials. *Proc Natl Acad Sci U S A* **113**, 11717–11725 (2016).

53. Mirkin, C. A., Letsinger, R. L., Mucic, R. C. & Storhoff, J. J. A DNA-based method for rationally assembling nanoparticles into macroscopic materials. *Nature* **382**, 607–609 (1996).

54. Macfarlane, R. J. *et al.* Nanoparticle Superlattice Engineering with DNA. *Science* **334**, 204–208 (2011).

55. Auyeung, E. *et al.* DNA-mediated nanoparticle crystallization into Wulff polyhedra. *Nature* **505**, 73–77 (2014).

56. Lewis, D. J., Zornberg, L. Z., Carter, D. J. D. & Macfarlane, R. J. Single-crystal Winterbottom constructions of nanoparticle superlattices. *Nat. Mater.* **19**, 719–724 (2020).

57. Cheng, W. *et al.* Free-standing nanoparticle superlattice sheets controlled by DNA. *Nature Mater* **8**, 519–525 (2009).

58. Wang, M. X. *et al.* Epitaxy: Programmable Atom Equivalents Versus Atoms. *ACS Nano* **11**, 180–185 (2017).

59. Jones, M. R. *et al.* DNA-nanoparticle superlattices formed from anisotropic building blocks. *Nature Materials* **9**, 913–917 (2010).

60. A, J. A. D., Oh, J. S., Yi, G.-R. & Pine, D. J. Photo-printing of faceted DNA patchy particles. *PNAS* **117**, 10645–10653 (2020).

61. Liu, W. *et al.* Diamond family of nanoparticle superlattices. *Science* **351**, 582–586 (2016).

62. Rogers, W. B., Shih, W. M. & Manoharan, V. N. Using DNA to program the self-assembly of colloidal nanoparticles and microparticles. *Nat Rev Mater* **1**, 16008 (2016).

63. Branden, C. I. & Tooze, J. *Introduction to Protein Structure*. (Garland Science, 2012).

64. Kostiainen, M. A. *et al.* Electrostatic assembly of binary nanoparticle superlattices using protein cages. *Nature Nanotech* **8**, 52–56 (2013).

65. Mark, S. S. *et al.* Bionanofabrication of Metallic and Semiconductor Nanoparticle Arrays Using S-Layer Protein Lattices with Different Lateral Spacings and Geometries. *Langmuir* **22**, 3763–3774 (2006).

66. McMillan, R. A. *et al.* Ordered nanoparticle arrays formed on engineered chaperonin protein templates. *Nature Mater* **1**, 247–252 (2002).

67. Fyfe, M. C. T. & Stoddart, J. F. Synthetic Supramolecular Chemistry. *Acc. Chem. Res.* **30**, 393–401 (1997).

68. Jaffar, S. *et al.* Layer-by-Layer Surface Modification and Patterned Electrostatic Deposition of Quantum Dots. *Nano Lett.* **4**, 1421–1425 (2004).

69. Kalsin, A. M. *et al.* Electrostatic Self-Assembly of Binary Nanoparticle Crystals with a Diamond-Like Lattice. *Science* **312**, 420–424 (2006).

70. Leunissen, M. E. *et al.* Ionic colloidal crystals of oppositely charged particles. *Nature* **437**, 235–240 (2005).

71. Hueckel, T., Hocky, G. M., Palacci, J. & Sacanna, S. Ionic solids from common colloids. *Nature* **580**, 487–490 (2020).

72. Künzle, M., Eckert, T. & Beck, T. Binary Protein Crystals for the Assembly of Inorganic Nanoparticle Superlattices. *J. Am. Chem. Soc.* **138**, 12731–12734 (2016).

73. Han, L. *et al.* Novel Interparticle Spatial Properties of Hydrogen-Bonding Mediated Nanoparticle Assembly. *Chem. Mater.* **15**, 29–37 (2003).

74. Williams, G. A. *et al.* Mechanically Robust and Self-Healable Superlattice Nanocomposites by Self-Assembly of Single-Component "Sticky" Polymer-Grafted Nanoparticles. *Advanced Materials* **27**, 3934–3941 (2015).

75. Santos, P. J., Cao, Z., Zhang, J., Alexander-Katz, A. & Macfarlane, R. J. Dictating Nanoparticle Assembly via Systems-Level Control of Molecular Multivalency. *J. Am. Chem. Soc.* **141**, 14624–14632 (2019).

76. Zhang, J. *et al.* Self-Assembling Nanocomposite Tectons. *J. Am. Chem. Soc.* **138**, 16228–16231 (2016).

77. Santos, P. J., Cheung, T. C. & Macfarlane, R. J. Assembling Ordered Crystals with Disperse Building Blocks. *Nano Lett.* **19**, 5774–5780 (2019).

78. Santos, P. J. & Macfarlane, R. J. Reinforcing Supramolecular Bonding with Magnetic Dipole Interactions to Assemble Dynamic Nanoparticle Superlattices. *J. Am. Chem. Soc.* **142**, 1170–1174 (2020).

79. Wang, Y. *et al.* Multistimuli Responsive Nanocomposite Tectons for Pathway Dependent Self-Assembly and Acceleration of Covalent Bond Formation. *J. Am. Chem. Soc.* **141**, 13234–13243 (2019).

80. Santos, P. J., Gabrys, P. A., Zornberg, L. Z., Lee, M. S. & Macfarlane, R. J. Macroscopic materials assembled from nanoparticle superlattices. *Nature* **591**, 586–591 (2021).

81. Lee, M. S., Alexander-Katz, A. & Macfarlane, R. J. Nanoparticle Assembly in High Polymer Concentration Solutions Increases Superlattice Stability. *Small* **17**, 2102107 (2021).

82. Crespo-Biel, O., Dordi, B., Reinhoudt, D. N. & Huskens, J. Supramolecular Layer-by-Layer Assembly: Alternating Adsorptions of Guest- and Host-Functionalized Molecules and Particles Using Multivalent Supramolecular Interactions. *J. Am. Chem. Soc.* **127**, 7594–7600 (2005).

83. Ling, X. Y., Reinhoudt, D. N. & Huskens, J. Reversible Attachment of Nanostructures at Molecular Printboards through Supramolecular Glue. *Chem. Mater.* **20**, 3574–3578 (2008).

84. Nagaoka, Y., Chen, O., Wang, Z. & Cao, Y. C. Structural Control of Nanocrystal Superlattices Using Organic Guest Molecules. *J. Am. Chem. Soc.* **134**, 2868–2871 (2012).

85. Hiemenz, P. C. & Lodge, T. P. *Polymer Chemistry, Second Edition*. (Taylor & Francis, 2007).

86. Chiu, J. J., Kim, B. J., Kramer, E. J. & Pine, D. J. Control of Nanoparticle Location in Block Copolymers. *J. Am. Chem. Soc.* **127**, 5036–5037 (2005).

87. Bockstaller, M. R., Lapetnikov, Y., Margel, S. & Thomas, E. L. Size-Selective Organization of Enthalpic Compatibilized Nanocrystals in Ternary Block Copolymer/Particle Mixtures. *J. Am. Chem. Soc.* **125**, 5276–5277 (2003).

88. Zhao, Y. *et al.* Small-molecule-directed nanoparticle assembly towards stimuli-responsive nanocomposites. *Nature Mater* **8**, 979–985 (2009).

89. Pyun, J. *et al.* Synthesis of Well-Defined Block Copolymers Tethered to Polysilsesquioxane Nanoparticles and Their Nanoscale Morphology on Surfaces. *J. Am. Chem. Soc.* **123**, 9445–9446 (2001).

90. Guo, Y., Harirchian-Saei, S., Izumi, C. M. S. & Moffitt, M. G. Block Copolymer Mimetic Self-Assembly of Inorganic Nanoparticles. *ACS Nano* **5**, 3309–3318 (2011).

91. He, J., Liu, Y., Babu, T., Wei, Z. & Nie, Z. Self-Assembly of Inorganic Nanoparticle Vesicles and Tubules Driven by Tethered Linear Block Copolymers. *J. Am. Chem. Soc.* **134**, 11342–11345 (2012).

92. Haynes, C. L. & Van Duyne, R. P. Nanosphere Lithography: A Versatile Nanofabrication Tool for Studies of Size-Dependent Nanoparticle Optics. *J. Phys. Chem. B* **105**, 5599–5611 (2001).

93. Mendes, P. M. *et al.* Gold Nanoparticle Patterning of Silicon Wafers Using Chemical e-Beam Lithography. *Langmuir* **20**, 3766–3768 (2004).

94. Le, J. D. *et al.* DNA-Templated Self-Assembly of Metallic Nanocomponent Arrays on a Surface. *Nano Lett.* **4**, 2343–2347 (2004).

95. Zhang, J., Liu, Y., Ke, Y. & Yan, H. Periodic Square-Like Gold Nanoparticle Arrays Templated by Self-Assembled 2D DNA Nanogrids on a Surface. *Nano Lett.* **6**, 248–251 (2006).

96. Okuda, M. *et al.* Self-Organized Inorganic Nanoparticle Arrays on Protein Lattices. *Nano Lett.* **5**, 991–993 (2005).

97. Klajn, R., Bishop, K. J. M. & Grzybowski, B. A. Light-controlled self-assembly of reversible and irreversible nanoparticle suprastructures. *PNAS* **104**, 10305–10309 (2007).

98. De Fazio, A. F. *et al.* Light-Induced Reversible DNA Ligation of Gold Nanoparticle Superlattices. *ACS Nano* (2019) doi:10.1021/acsnano.9b01294.

99. Ahniyaz, A., Sakamoto, Y. & Bergström, L. Magnetic field-induced assembly of oriented superlattices from maghemite nanocubes. *Proc. Natl. Acad. Sci. U.S.A* **104**, 17570–17574 (2007).

100. Park, S. S. *et al.* DNA- and Field-Mediated Assembly of Magnetic Nanoparticles into High-Aspect Ratio Crystals. *Adv. Mater.* **32**, 1906626 (2019).

101. Singh, G. *et al.* Self-assembly of magnetite nanocubes into helical superstructures. *Science* **345**, 1149–1153 (2014).

102. Petryayeva, E. & Krull, U. J. Localized surface plasmon resonance: Nanostructures, bioassays and biosensing—A review. *Analytica Chimica Acta* **706**, 8–24 (2011).

103. Anker, J. N. *et al.* Biosensing with plasmonic nanosensors. in *Nanoscience and Technology* 308–319 (Co-Published with Macmillan Publishers Ltd, UK, 2009). doi:10.1142/9789814287005_0032.

104. Stiles, P. L., Dieringer, J. A., Shah, N. C. & Van Duyne, R. P. Surface-Enhanced Raman Spectroscopy. *Annual Review of Analytical Chemistry* **1**, 601–626 (2008).

105. Maier, S. A., Brongersma, M. L., Kik, P. G. & Atwater, H. A. Observation of near-field coupling in metal nanoparticle chains using far-field polarization spectroscopy. *Phys. Rev. B* **65**, 193408 (2002).

106. Prodan, E., Radloff, C., Halas, N. J. & Nordlander, P. A Hybridization Model for the Plasmon Response of Complex Nanostructures. *Science* **302**, 419–422 (2003).

107. Tao, A., Sinsermsuksakul, P. & Yang, P. Tunable plasmonic lattices of silver nanocrystals. *Nature Nanotech* **2**, 435–440 (2007).

108. Ye, X., Chen, J., Diroll, B. T. & Murray, C. B. Tunable Plasmonic Coupling in Self-Assembled Binary Nanocrystal Superlattices Studied by Correlated Optical Microspectrophotometry and Electron Microscopy. *Nano Lett.* **13**, 1291–1297 (2013).

109. Tong, L., Xu, H. & Käll, M. Nanogaps for SERS applications. *MRS Bulletin* **39**, 163–168 (2014).

110. Zhan, C. *et al.* From plasmon-enhanced molecular spectroscopy to plasmon-mediated chemical reactions. *Nat Rev Chem* **2**, 216–230 (2018).

111. Wang, X., Huang, S.-C., Hu, S., Yan, S. & Ren, B. Fundamental understanding and applications of plasmon-enhanced Raman spectroscopy. *Nat Rev Phys* **2**, 253–271 (2020).

112. Lim, D.-K., Jeon, K.-S., Kim, H. M., Nam, J.-M. & Suh, Y. D. Nanogap-engineerable Raman-active nanodumbbells for single-molecule detection. *Nature Mater* **9**, 60–67 (2010).

113. Alvarez-Puebla, R. A. *et al.* Gold nanorods 3D-supercrystals as surface enhanced Raman scattering spectroscopy substrates for the rapid detection of scrambled prions. *Proceedings of the National Academy of Sciences* **108**, 8157–8161 (2011).

114. Bodelón, G. *et al.* Detection and imaging of quorum sensing in Pseudomonas aeruginosa biofilm communities by surface-enhanced resonance Raman scattering. *Nature Mater* **15**, 1203–1211 (2016).

115. Miao, Y., Yang, K., Zong, S., Wang, Z. & Cui, Y. Au/Ag Bimetallic Nanocuboid Superlattices Coated with Ti3C2 Nanosheets for Surface-Enhanced Raman Spectroscopy Detection of Fish Drug Residues in Pond Water. *ACS Appl. Nano Mater.* **4**, 6844–6851 (2021).

116. Xia, Y., Gates, B. & Li, Z.-Y. Self-Assembly Approaches to Three-Dimensional Photonic Crystals. *Advanced Materials* **13**, 409–413 (2001).

117. Liu, P. *et al.* Self-assembled colloidal arrays for structural color. *Nanoscale Advances* **1**, 1672–1685 (2019).

118. Park, D. J. *et al.* Plasmonic photonic crystals realized through DNA-programmable assembly. **112**, 977–981 (2014).

119. Ross, M. B., Ku, J. C., Vaccarezza, V. M., Schatz, G. C. & Mirkin, C. A. Nanoscale form dictates mesoscale function in plasmonic DNA–nanoparticle superlattices. *Nature Nanotech* **10**, 453–458 (2015).

120. Sun, L., Lin, H., Kohlstedt, K. L. & Mirkin, C. A. Design principles for photonic crystals based on plasmonic nanoparticle superlattices. *PNAS* **115**, (2018).

121. Ross, M. B., Blaber, M. G. & Schatz, G. C. Using nanoscale and mesoscale anisotropy to engineer the optical response of three-dimensional plasmonic metamaterials. *Nat Commun* **5**, 4090 (2014).

122. Kim, S. *et al.* Mie-Resonant Three-Dimensional Metacrystals. *Nano Lett.* **20**, 8096–8101 (2020).

123. Kirakosyan, A., Kim, D. & Choi, J. Self-assembled polymer-grafted nanoparticles for photonic coating applications. *Macromol. Res.* **24**, 1030–1035 (2016).

124. Kravets, V. G., Kabashin, A. V., Barnes, W. L. & Grigorenko, A. N. Plasmonic Surface Lattice Resonances: A Review of Properties and Applications. *Chem. Rev.* **118**, 5912–5951 (2018).

125. Le-Van, Q. *et al.* Enhanced Quality Factors of Surface Lattice Resonances in Plasmonic Arrays of Nanoparticles. *Advanced Optical Materials* **7**, 1801451 (2019).

126. Volk, K., Fitzgerald, J. P. S. & Karg, M. In-Plane Surface Lattice and Higher Order Resonances in Self-Assembled Plasmonic Monolayers: From Substrate-Supported to Free-Standing Thin Films. *ACS Appl. Mater. Interfaces* **11**, 16096–16106 (2019).

127. Ponomareva, E., Volk, K., Mulvaney, P. & Karg, M. Surface Lattice Resonances in Self-Assembled Gold Nanoparticle Arrays: Impact of Lattice Period, Structural Disorder, and Refractive Index on Resonance Quality. *Langmuir* **36**, 13601–13612 (2020).

128. Bedanta, S. & Kleemann, W. Supermagnetism. *J. Phys. D: Appl. Phys.* **42**, 013001 (2008).

129. Lisiecki, I., Parker, D., Salzemann, C. & Pileni, M. P. Face-Centered Cubic Supra-Crystals and Disordered Three-Dimensional Assemblies of 7.5 nm Cobalt Nanocrystals: Influence of the Mesoscopic Ordering on the Magnetic Properties. *Chem. Mater.* **19**, 4030–4036 (2007).

130. Russier, V. *et al.* Phase diagram of a three-dimensional dipolar model on an fcc lattice. *Phys. Rev. B* **102**, 174410 (2020).

131. Giuntini, D. *et al.* Iron oxide-based nanostructured ceramics with tailored magnetic and mechanical properties: development of mechanically robust, bulk superparamagnetic materials. *Nanoscale Advances* **1**, 3139–3150 (2019).

132. Parker, D., Lisiecki, I. & Pileni, M. P. Do 8 nm Co Nanocrystals in Long-Range-Ordered Face-Centered Cubic (fcc) Supracrystals Show Superspin Glass Behavior? *J. Phys. Chem. Lett.* **1**, 1139–1142 (2010).

133. Luttinger, J. M. & Tisza, L. Theory of Dipole Interaction in Crystals. *Phys. Rev.* **70**, 954–964 (1946).

134. Yamamoto, K. *et al.* Direct visualization of dipolar ferromagnetic domain structures in Co nanoparticle monolayers by electron holography. *Appl. Phys. Lett.* **93**, 082502 (2008).

135. *New Trends in Nanoparticle Magnetism*. vol. 308 (Springer International Publishing, 2021).

136. Jia, C.-J. & Schüth, F. Colloidal metal nanoparticles as a component of designed catalyst. *Physical Chemistry Chemical Physics* **13**, 2457–2487 (2011).

137. Lu, L., Zou, S. & Fang, B. The Critical Impacts of Ligands on Heterogeneous Nanocatalysis: A Review. *ACS Catal.* **11**, 6020–6058 (2021).

138. Xiao, M. *et al.* Plasmon-enhanced chemical reactions. *Journal of Materials Chemistry A* **1**, 5790–5805 (2013).

139. Ro, I., Resasco, J. & Christopher, P. Approaches for Understanding and Controlling Interfacial Effects in Oxide-Supported Metal Catalysts. *ACS Catal.* **8**, 7368–7387 (2018).

140. Kang, Y. *et al.* Design of Pt–Pd Binary Superlattices Exploiting Shape Effects and Synergistic Effects for Oxygen Reduction Reactions. *J. Am. Chem. Soc.* **135**, 42–45 (2013).

141. Kang, Y. *et al.* Engineering Catalytic Contacts and Thermal Stability: Gold/Iron Oxide Binary Nanocrystal Superlattices for CO Oxidation. *J. Am. Chem. Soc.* **135**, 1499–1505 (2013).

142. Li, J. *et al.* Nanoparticle Superlattices as Efficient Bifunctional Electrocatalysts for Water Splitting. *J. Am. Chem. Soc.* **137**, 14305–14312 (2015).

143. Yamada, Y. *et al.* Nanocrystal bilayer for tandem catalysis. *Nature Chem* **3**, 372–376 (2011).

144. Sahoo, L. & Gautam, U. K. Boosting Bifunctional Oxygen Reduction and Methanol Oxidation Electrocatalytic Activity with 2D Superlattice-Forming Pd Nanocubes Generated by Precise Acid Etching. *ACS Appl. Nano Mater.* **3**, 8117–8125 (2020).

145. Wu, L. *et al.* Stable Cobalt Nanoparticles and Their Monolayer Array as an Efficient Electrocatalyst for Oxygen Evolution Reaction. *J. Am. Chem. Soc.* **137**, 7071–7074 (2015).

146. Gu, X. W. Mechanical Properties of Architected Nanomaterials Made from Organic–Inorganic Nanocrystals. *JOM* **70**, 2205–2217 (2018).

147. Lewis, D. J., Carter, D. J. D. & Macfarlane, R. J. Using DNA to Control the Mechanical Response of Nanoparticle Superlattices. *J. Am. Chem. Soc.* **142**, 19181–19188 (2020).

148. Bor, B., Giuntini, D., Domènech, B., Swain, M. V. & Schneider, G. A. Nanoindentation-based study of the mechanical behavior of bulk supercrystalline ceramic-organic nanocomposites. *Journal of the European Ceramic Society* **39**, 3247–3256 (2019).

149. Podsiadlo, P. *et al.* The Role of Order, Nanocrystal Size, and Capping Ligands in the Collective Mechanical Response of Three-Dimensional Nanocrystal Solids. *J. Am. Chem. Soc.* **132**, 8953–8960 (2010).

150. Mueggenburg, K. E., Lin, X.-M., Goldsmith, R. H. & Jaeger, H. M. Elastic membranes of close-packed nanoparticle arrays. *Nature Mater* **6**, 656–660 (2007).

151. K. Patra, T. *et al.* Ligand dynamics control structure, elasticity, and high-pressure behavior of nanoparticle superlattices. *Nanoscale* **11**, 10655–10666 (2019).

152. Gu, X. W. *et al.* Tolerance to structural disorder and tunable mechanical behavior in self-assembled superlattices of polymer-grafted nanocrystals. *Proc Natl Acad Sci U S A* **114**, 2836–2841 (2017).

153. Gauvin, M., Yang, N., Yang, Z., Arfaoui, I. & Pileni, M.-P. Hierarchical mechanical behavior of cobalt supracrystals related to nanocrystallinity. *Nano Res.* **8**, 3480–3487 (2015).

154. Yan, C. *et al.* Assessing the relevance of building block crystallinity for tuning the stiffness of gold nanocrystal superlattices. *Nanoscale* **5**, 9523–9527 (2013).

155. Liu, X. P., Ni, Y. & He, L. H. Elastic properties of gold supracrystals: Effects of nanocrystal size, ligand length, and nanocrystallinity. *J. Chem. Phys.* **144**, 144507 (2016).

156. Çolak, A., Wei, J., Arfaoui, I. & Pileni, M.-P. Coating agent-induced mechanical behavior of 3D self-assembled nanocrystals. *Physical Chemistry Chemical Physics* **19**, 23887–23897 (2017).

157. Yoon, B. *et al.* Hydrogen-bonded structure and mechanical chiral response of a silver nanoparticle superlattice. *Nature Mater* **13**, 807–811 (2014).

158. Yang, Y. *et al.* Scalable Assembly of Crystalline Binary Nanocrystal Superparticles and Their Enhanced Magnetic and Electrochemical Properties. *J. Am. Chem. Soc.* **140**, 15038–15047 (2018).

159. Kim, D. K., Lai, Y., Diroll, B. T., Murray, C. B. & Kagan, C. R. Flexible and low-voltage integrated circuits constructed from high-performance nanocrystal transistors. *Nat Commun* **3**, 1216 (2012).

160. Choi, J.-H. *et al.* Exploiting the colloidal nanocrystal library to construct electronic devices. *Science* **352**, 205–208 (2016).

161. Dreyer, A. *et al.* Organically linked iron oxide nanoparticle supercrystals with exceptional isotropic mechanical properties. *Nature Mater* **15**, 522–528 (2016).

162. Cho, H. *et al.* Direct Optical Patterning of Quantum Dot Light-Emitting Diodes via In Situ Ligand Exchange. *Advanced Materials* **32**, 2003805 (2020).

163. Gao, B., Arya, G. & Tao, A. R. Self-orienting nanocubes for the assembly of plasmonic nanojunctions. *Nature Nanotech* **7**, 433–437 (2012).

164. Murray, C. B., Kagan, C. R. & Bawendi, M. G. Synthesis and Characterization of Monodisperse Nanocrystals and Close-Packed Nanocrystal Assemblies. *Annual Review of Materials Science* **30**, 545–610 (2000).

165. Tao, A. R., Habas, S. & Yang, P. Shape Control of Colloidal Metal Nanocrystals. *Small* **4**, 310–325 (2008).

166. Personick, M. L. & Mirkin, C. A. Making Sense of the Mayhem behind Shape Control in the Synthesis of Gold Nanoparticles. *J. Am. Chem. Soc.* **135**, 18238–18247 (2013).

167. Skrabalak, S. E. & Brutchey, R. L. Going with the Flow: Continuous Flow Routes to Colloidal Nanoparticles. *Chem. Mater.* **28**, 1003–1005 (2016).

168. Długosz, O. & Banach, M. Inorganic nanoparticle synthesis in flow reactors – applications and future directions. *Reaction Chemistry & Engineering* **5**, 1619–1641 (2020).

169. Huang, Y. *et al.* Metal Nanoparticle Harvesting by Continuous Rotating Electrodeposition and Separation. *Matter* **3**, 1294–1307 (2020).

170. Wang, Y. *et al.* Modulation of Multiscale 3D Lattices through Conformational Control: Painting Silk Inverse Opals with Water and Light. *Advanced Materials* **29**, 1702769 (2017).

171. Callister, W. D. & Rethwisch, D. G. *Materials Science and Engineering: An Introduction, 10th Edition | Wiley*. (Wiley-VCH, 2012).

172. Van de Walle, C. G. & Neugebauer, J. First-principles calculations for defects and impurities: Applications to III-nitrides. *Journal of Applied Physics* **95**, 3851–3879 (2004).

173. Xie, C. *et al.* Defect Chemistry in Heterogeneous Catalysis: Recognition, Understanding, and Utilization. *ACS Catal.* **10**, 11082–11098 (2020).

174. Gabrys, P. A. *et al.* Lattice Mismatch in Crystalline Nanoparticle Thin Films. *Nano Lett.* **18**, 579–585 (2018).

175. Auyeung, E. *et al.* Synthetically programmable nanoparticle superlattices using a hollow three-dimensional spacer approach. *Nature Nanotech* **7**, 24–28 (2012).

176. Cargnello, M. *et al.* Substitutional doping in nanocrystal superlattices. *Nature* **524**, 450–453 (2015).

177. Zornberg, L. Z., Gabrys, P. A. & Macfarlane, R. J. Optical Processing of DNA-Programmed Nanoparticle Superlattices. *Nano Lett.* **19**, 8074–8081 (2019).

178. Schall, P., Weitz, D. A. & Spaepen, F. Structural Rearrangements That Govern Flow in Colloidal Glasses. *Science* **318**, 1895–1899 (2007).

179. Zhang, Horsch, M. A., Lamm, M. H. & Glotzer, S. C. Tethered Nano Building Blocks: Toward a Conceptual Framework for Nanoparticle Self-Assembly. *Nano Lett.* **3**, 1341–1346 (2003).

180. van Ravensteijn, B. G. P., Voets, I. K., Kegel, W. K. & Eelkema, R. Out-of-Equilibrium Colloidal Assembly Driven by Chemical Reaction Networks. *Langmuir* **36**, 10639–10656 (2020).

181. Zhao, H. *et al.* Reversible trapping and reaction acceleration within dynamically self-assembling nanoflasks. *Nature Nanotech* **11**, 82–88 (2016).

182. Hatton, B., Mishchenko, L., Davis, S., Sandhage, K. H. & Aizenberg, J. Assembly of large-area, highly ordered, crack-free inverse opal films. *Proc Natl Acad Sci U S A* **107**, 10354–10359 (2010).

183. Tan, A. T. L., Beroz, J., Kolle, M. & Hart, A. J. Direct-Write Freeform Colloidal Assembly. *Advanced Materials* **30**, 1803620 (2018).

184. Klajn, R. *et al.* Plastic and Moldable Metals by Self-Assembly of Sticky Nanoparticle Aggregates. *Science* **316**, 261–264 (2007).

185. Liu, Q. *et al.* Self-Alignment of Plasmonic Gold Nanorods in Reconfigurable Anisotropic Fluids for Tunable Bulk Metamaterial Applications. *Nano Lett.* **10**, 1347–1353 (2010).

186. Malaquin, L., Kraus, T., Schmid, H., Delamarche, E. & Wolf, H. Controlled Particle Placement through Convective and Capillary Assembly. *Langmuir* **23**, 11513–11521 (2007).

187. Ding, T., Song, K., Clays, K. & Tung, C.-H. Fabrication of 3D Photonic Crystals of Ellipsoids: Convective Self-Assembly in Magnetic Field. *Advanced Materials* **21**, 1936–1940 (2009).

188. Tan, A. T. L. *et al.* In-Plane Direct-Write Assembly of Iridescent Colloidal Crystals. *Small* **16**, 1905519 (2020).

189. Varga, Z. *et al.* Hydrodynamics control shear-induced pattern formation in attractive suspensions. *PNAS* **116**, 12193–12198 (2019).

190. Palazon, F., Akkerman, Q. A., Prato, M. & Manna, L. X-ray Lithography on Perovskite Nanocrystals Films: From Patterning with Anion-Exchange Reactions to Enhanced Stability in Air and Water. *ACS Nano* **10**, 1224–1230 (2016).

191. Wei, Y. *et al.* In Situ Light-Initiated Ligands Cross-Linking Enables Efficient All-Solution-Processed Perovskite Light-Emitting Diodes. *J. Phys. Chem. Lett.* **11**, 1154–1161 (2020).

192. Lee, S., Zheng, C. Y., Bujold, K. E. & Mirkin, C. A. A Cross-Linking Approach to Stabilizing Stimuli-Responsive Colloidal Crystals Engineered with DNA. *J. Am. Chem. Soc.* **141**, 11827–11831 (2019).

193. Auyeung, E., Macfarlane, R. J., Choi, C. H. J., Cutler, J. I. & Mirkin, C. A. Transitioning DNA-Engineered Nanoparticle Superlattices from Solution to the Solid State. *Advanced Materials* **24**, 5181–5186 (2012).

194. Kubiak, J. M., Morje, A. P., Lewis, D. J., Wilson, Sara. L. & Macfarlane, R. J. Dynamic Manipulation of DNA-Programmed Crystals Embedded in a Polyelectrolyte Hydrogel. *ACS Appl. Mater. Interfaces* **13**, 11215–11223 (2021).

195. Jiao, Y. *et al.* Fabrication of three-dimensionally interconnected nanoparticle superlattices and their lithium-ion storage properties. *Nat Commun* **6**, 6420 (2015).

196. Kim, B. J., Chiu, J. J., Yi, G.-R., Pine, D. J. & Kramer, E. J. Nanoparticle-Induced Phase Transitions in Diblock-Copolymer Films. *Advanced Materials* **17**, 2618–2622 (2005).

197. Kagan, C. R., Lifshitz, E., Sargent, E. H. & Talapin, D. V. Building devices from colloidal quantum dots. *Science* **353**, aac5523 (2016).

198. Grason, G. M. Perspective: Geometrically frustrated assemblies. *J. Chem. Phys.* **145**, 110901 (2016).

199. Grötsch, R. K. *et al.* Pathway Dependence in the Fuel-Driven Dissipative Self-Assembly of Nanoparticles. *J. Am. Chem. Soc.* **141**, 9872–9878 (2019).

200. Rahedi, A. J., Douglas, J. F. & Starr, F. W. Model for reversible nanoparticle assembly in a polymer matrix. *J. Chem. Phys.* **128**, 024902 (2008).

201. Wang, Y. *et al.* Crystallization of DNA-coated colloids. *Nat Commun* **6**, 7253 (2015).

202. Ou, Z., Wang, Z., Luo, B., Luijten, E. & Chen, Q. Kinetic pathways of crystallization at the nanoscale. *Nat. Mater.* **19**, 450–455 (2020).

203. Macfarlane, R. J. *et al.* Importance of the DNA 'bond' in programmable nanoparticle crystallization. *Proc Natl Acad Sci U S A* **111**, 14995–15000 (2014).

204. Kim, Y., Macfarlane, R. J., Jones, M. R. & Mirkin, C. A. Transmutable nanoparticles with reconfigurable surface ligands. *Science* **351**, 579–582 (2016).

205. Maye, M. M., Kumara, M. T., Nykypanchuk, D., Sherman, W. B. & Gang, O. Switching binary states of nanoparticle superlattices and dimer clusters by DNA strands. *Nature Nanotech* **5**, 116–120 (2010).

206. Grzelczak, M., Vermant, J., Furst, E. M. & Liz-Marzán, L. M. Directed Self-Assembly of Nanoparticles. *ACS Nano* **4**, 3591–3605 (2010).

207. Severoni, E. *et al.* Plasmon-Enhanced Optical Chirality through Hotspot Formation in Surfactant-Directed Self-Assembly of Gold Nanorods. *ACS Nano* **14**, 16712–16722 (2020).

208. Euliss, L. E. *et al.* Cooperative Assembly of Magnetic Nanoparticles and Block Copolypeptides in Aqueous Media. *Nano Lett.* **3**, 1489–1493 (2003).

209. Hobbie, E. K. Metastability and Depletion-Driven Aggregation. *Phys. Rev. Lett.* **81**, 3996–3999 (1998).

210. Hore, M. J. A. & Composto, R. J. Using Miscible Polymer Blends To Control Depletion–Attraction Forces between Au Nanorods in Nanocomposite Films. *Macromolecules* **45**, 6078–6086 (2012).

211. Ng, K. C. *et al.* Free-Standing Plasmonic-Nanorod Superlattice Sheets. *ACS Nano* **6**, 925–934 (2012).

212. Kim, H. J., Wang, W., Travesset, A., Mallapragada, S. K. & Vaknin, D. Temperature-Induced Tunable Assembly of Columnar Phases of Nanorods. *ACS Nano* **14**, 6007–6012 (2020).

213. Kim, H. J., Wang, W., Mallapragada, S. K. & Vaknin, D. The Effects of Temperature on the Assembly of Gold Nanoparticle by Interpolymer Complexation. *J. Phys. Chem. Lett.* **12**, 1461–1467 (2021).

214. Choi, J., Hore, M. J. A., Clarke, N., Winey, K. I. & Composto, R. J. Nanoparticle Brush Architecture Controls Polymer Diffusion in Nanocomposites. *Macromolecules* **47**, 2404–2410 (2014).

215. Bayliss, K., Duijneveldt, J. S. van, A. Faers, M. & P. Vermeer, A. W. Comparing colloidal phase separation induced by linear polymer and by microgel particles. *Soft Matter* **7**, 10345–10352 (2011).

216. Louis, A. A., Bolhuis, P. G., Meijer, E. J. & Hansen, J. P. Density profiles and surface tension of polymers near colloidal surfaces. *J. Chem. Phys.* **116**, 10547–10556 (2002).

217. Winslow, S. W., Swan, J. W. & Tisdale, W. A. The Importance of Unbound Ligand in Nanocrystal Superlattice Formation. *J. Am. Chem. Soc.* (2020) doi:10.1021/jacs.0c01809.

218. Edwards, T. D. & Bevan, M. A. Depletion-Mediated Potentials and Phase Behavior for Micelles, Macromolecules, Nanoparticles, and Hydrogel Particles. *Langmuir* **28**, 13816–13823 (2012).

219. Ligon, S. C., Liska, R., Stampfl, J., Gurr, M. & Mülhaupt, R. Polymers for 3D Printing and Customized Additive Manufacturing. *Chem. Rev.* **117**, 10212–10290 (2017).

220. Valino, A. D. *et al.* Advances in 3D printing of thermoplastic polymer composites and nanocomposites. *Progress in Polymer Science* **98**, 101162 (2019).

221. Parandoush, P. & Lin, D. A review on additive manufacturing of polymer-fiber composites. *Composite Structures* **182**, 36–53 (2017).

222. Tang, W., Santare, M. H. & Advani, S. G. Melt processing and mechanical property characterization of multi-walled carbon nanotube/high density polyethylene (MWNT/HDPE) composite films. *Carbon* **41**, 2779–2785 (2003).

223. Karmaker, A. C. & Youngquist, J. A. Injection molding of polypropylene reinforced with short jute fibers. *Journal of Applied Polymer Science* **62**, 1147–1151 (1996).

224. Lafleur, P. G. & Vergnes, B. Co-Rotating Twin-Screw Extrusion. in *Polymer Extrusion* 109–210 (John Wiley & Sons, Ltd, 2014). doi:10.1002/9781118827123.ch4.

225. Tadmor, Z. & Gogos, C. G. *Principles of Polymer Processing*. (John Wiley & Sons, 2013).

226. Vlassopoulos, D., Fytas, G., Pakula, T. & Roovers, J. Multiarm star polymers dynamics. *J. Phys.: Condens. Matter* **13**, R855 (2001).

227. Marzi, D. *et al.* Depletion, melting and reentrant solidification in mixtures of soft and hard colloids. *Soft Matter* **11**, 8296–8312 (2015).

228. Rudin, A. & Choi, P. Chapter 3 - Practical Aspects of Molecular Weight Measurements. in *The Elements of Polymer Science & Engineering (Third Edition)* (eds. Rudin, A. & Choi, P.) 89–148 (Academic Press, 2013). doi:10.1016/B978-0-12-382178-2.00003-1.

229. Douglas, J. F., Roovers, J. & Freed, K. F. Characterization of branching architecture through ‘universal’ ratios of polymer solution properties. *Macromolecules* **23**, 4168–4180 (1990).

230. Götzelmann, B., Evans, R. & Dietrich, S. Depletion forces in fluids. *Phys. Rev. E* **57**, 6785–6800 (1998).

231. Karas, A. S., Glaser, J. & Glotzer, S. C. Using depletion to control colloidal crystal assemblies of hard cuboctahedra. *Soft Matter* **12**, 5199–5204 (2016).

232. Asakura, S. & Oosawa, F. On Interaction between Two Bodies Immersed in a Solution of Macromolecules. *J. Chem. Phys.* **22**, 1255–1256 (1954).

233. Asakura, S. & Oosawa, F. Interaction between particles suspended in solutions of macromolecules. *Journal of Polymer Science* **33**, 183–192 (1958).

234. Edwards, T. D. & Bevan, M. A. Polymer Mediated Depletion Attraction and Interfacial Colloidal Phase Behavior. *Macromolecules* **45**, 585–594 (2012).

235. Wijmans, C. M., Zhulina, E. B. & Fleer, G. J. Effect of Free Polymer on the Structure of a Polymer Brush and Interaction between Two Polymer Brushes. *Macromolecules* **27**, 3238–3248 (1994).

236. Lee, M. S., Yee, D. W., Ye, M. & Macfarlane, R. J. Nanoparticle Assembly as a Materials Development Tool. *J. Am. Chem. Soc.* **144**, 3330–3346 (2022).

237. Quan, Z. *et al.* Solvent-Mediated Self-Assembly of Nanocube Superlattices. *J. Am. Chem. Soc.* **136**, 1352–1359 (2014).

238. Hong, L., Cacciuto, A., Luijten, E. & Granick, S. Clusters of Amphiphilic Colloidal Spheres. *Langmuir* **24**, 621–625 (2008).

239. Liang, L. & Astruc, D. The copper(I)-catalyzed alkyne-azide cycloaddition (CuAAC) "click" reaction and its applications. An overview. *Coordination Chemistry Reviews* **255**, 2933–2945 (2011).

240. Hein, J. E. & Fokin, V. V. Copper-catalyzed azide–alkyne cycloaddition (CuAAC) and beyond: new reactivity of copper(i) acetylides. *Chem Soc Rev* **39**, 1302–1315 (2010).

241. Gonda, Z. & Novák, Z. Highly active copper-catalysts for azide-alkyne cycloaddition. *Dalton Trans.* **39**, 726–729 (2009).

242. Gabrys, P. A., Zornberg, L. Z. & Macfarlane, R. J. Programmable Atom Equivalents: Atomic Crystallization as a Framework for Synthesizing Nanoparticle Superlattices. *Small* **15**, 1805424 (2019).

243. Jones, M. R. *et al.* DNA-nanoparticle superlattices formed from anisotropic building blocks. *Nature Mater* **9**, 913–917 (2010).

244. van Anders, G., Ahmed, N. K., Smith, R., Engel, M. & Glotzer, S. C. Entropically Patchy Particles: Engineering Valence through Shape Entropy. *ACS Nano* **8**, 931–940 (2014).

245. Girard, M. *et al.* Particle analogs of electrons in colloidal crystals. *Science* **364**, 1174–1178 (2019).

246. Wang, S. *et al.* The emergence of valency in colloidal crystals through electron equivalents. *Nat. Mater.* (2022) doi:10.1038/s41563-021-01170-5.

247. Kagan, C. R. & Murray, C. B. Charge transport in strongly coupled quantum dot solids. *Nature Nanotech* **10**, 1013–1026 (2015).

248. Young, K. L. *et al.* Using DNA to Design Plasmonic Metamaterials with Tunable Optical Properties. *Adv. Mater.* **26**, 653–659 (2014).

249. Bian, K., Wang, Z. & Hanrath, T. Comparing the Structural Stability of PbS Nanocrystals Assembled in fcc and bcc Superlattice Allotropes. *J. Am. Chem. Soc.* **134**, 10787–10790 (2012).

250. Casey, M. T. *et al.* Driving diffusionless transformations in colloidal crystals using DNA handshaking. *Nat Commun* **3**, 1209 (2012).

251. Zhang, Y. *et al.* Selective transformations between nanoparticle superlattices via the reprogramming of DNA-mediated interactions. *Nature Mater* **14**, 840–847 (2015).

252. Wang, Z., Bian, K., Nagaoka, Y., Fan, H. & Cao, Y. C. Regulating Multiple Variables To Understand the Nucleation and Growth and Transformation of PbS Nanocrystal Superlattices. *J. Am. Chem. Soc.* **139**, 14476–14482 (2017).

253. Winslow, S. W., Smilgies, D.-M., Swan, J. W. & Tisdale, W. A. Reversible Temperature-Induced Structural Transformations in PbS Nanocrystal Superlattices. *J. Phys. Chem. C* **124**, 13456–13466 (2020).

254. Lee, M. S., Alexander-Katz, A. & Macfarlane, R. J. Nanoparticle Assembly in High Polymer Concentration Solutions Increases Superlattice Stability. *Small* **17**, 2102107 (2021).

255. Li, Q. *et al.* A poly(thymine)–melamine duplex for the assembly of DNA nanomaterials. *Nat. Mater.* **19**, 1012–1018 (2020).

256. Bian, K. *et al.* Shape-Anisotropy Driven Symmetry Transformations in Nanocrystal Superlattice Polymorphs. *ACS Nano* **5**, 2815–2823 (2011).

257. Huang, X. *et al.* In Situ Constructing the Kinetic Roadmap of Octahedral Nanocrystal Assembly Toward Controlled Superlattice Fabrication. *J. Am. Chem. Soc.* **143**, 4234–4243 (2021).

258. Lee, B., Littrell, K., Sha, Y. & Shevchenko, E. V. Revealing the Effects of the Non-solvent on the Ligand Shell of Nanoparticles and Their Crystallization. *J. Am. Chem. Soc.* **141**, 16651–16662 (2019).

259. Weidman, M. C., Smilgies, D.-M. & Tisdale, W. A. Kinetics of the self-assembly of nanocrystal superlattices measured by real-time in situ X-ray scattering. *Nature Mater* **15**, 775–781 (2016).

260. Wayman, C. M. The phenomenological theory of martensite crystallography: Interrelationships. *MMTA* **25**, 1787–1795 (1994).

261. Thaner, R. V. *et al.* Entropy-Driven Crystallization Behavior in DNA-Mediated Nanoparticle Assembly. *Nano Lett.* **15**, 5545–5551 (2015).

262. Kaushik, A. P. & Clancy, P. Solvent-driven symmetry of self-assembled nanocrystal superlattices-A computational study. *J. Comput. Chem.* **34**, 523–532 (2013).

263. Goodfellow, B. W., Yu, Y., Bosoy, C. A., Smilgies, D.-M. & Korgel, B. A. The Role of Ligand Packing Frustration in Body-Centered Cubic (bcc) Superlattices of Colloidal Nanocrystals. *J. Phys. Chem. Lett.* **6**, 2406–2412 (2015).

264. Si, K. J., Chen, Y., Shi, Q. & Cheng, W. Nanoparticle Superlattices: The Roles of Soft Ligands. *Adv. Sci.* **5**, 1700179 (2018).

265. Yun, H. *et al.* Softness- and Size-Dependent Packing Symmetries of Polymer-Grafted Nanoparticles. *ACS Nano* **14**, 9644–9651 (2020).

266. Korgel, B. A. & Fitzmaurice, D. Small-angle x-ray-scattering study of silver-nanocrystal disorder-order phase transitions. *Phys. Rev. B* **59**, 14191–14201 (1999).

267. Tan, T. *et al.* Resolving the stacking fault structure of silver nanoplates. *Nanoscale* **13**, 195–205 (2021).

268. Germain, V., Li, J., Ingert, D., Wang, Z. L. & Pileni, M. P. Stacking Faults in Formation of Silver Nanodisks. *J. Phys. Chem. B* **107**, 8717–8720 (2003).

269. Du, J. S., Zhou, W., Rupich, S. M. & Mirkin, C. A. Twin Pathways: Discerning the Origins of Multiply Twinned Colloidal Nanoparticles. *Angew. Chem. Int. Ed.* **60**, 6858–6863 (2021).

270. Oliver, E. C., Mori, T., Daymond, M. R. & Withers, P. J. Neutron diffraction study of stress-induced martensitic transformation and variant change in Fe–Pd. *Acta Materialia* **51**, 6453–6464 (2003).

271. Nalwa, H. S. *Encyclopedia of nanoscience and nanotechnology*. (American scientific publishers, 2004).

272. LoVerso, F., Egorov, S. A. & Binder, K. Interaction Between Polymer Brush-Coated Spherical Nanoparticles: Effect of Solvent Quality. *Macromolecules* **45**, 8892–8902 (2012).

273. Wang, Y. *et al.* Kinetically Controlled Self-Assembly of Binary Polymer-Grafted Nanocrystals into Ordered Superstructures via Solvent Vapor Annealing. *Nano Lett.* **21**, 5053–5059 (2021).

274. Schulz, F. *et al.* Little Adjustments Significantly Improve the Turkevich Synthesis of Gold Nanoparticles. *Langmuir* **30**, 10779–10784 (2014).

275. Bastús, N. G., Comenge, J. & Puntes, V. Kinetically Controlled Seeded Growth Synthesis of Citrate-Stabilized Gold Nanoparticles of up to 200 nm: Size Focusing versus Ostwald Ripening. *Langmuir* **27**, 11098–11105 (2011).

276. Lee, L. V. *et al.* A Potent and Highly Selective Inhibitor of Human α-1,3-Fucosyltransferase via Click Chemistry. *J. Am. Chem. Soc.* **125**, 9588–9589 (2003).

277. Park, J. *et al.* Ultra-large-scale syntheses of monodisperse nanocrystals. *Nature Mater* **3**, 891–895 (2004).